

Thermomagnetic studies on transition metal pnictides

Proefschrift

ter verkrijging van de graad van doctor
aan de Technische Universiteit Delft,
op gezag van de Rector Magnificus prof. ir. K.C.A.M. Luyben,
voorzitter van het College voor Promoties,
in het openbaar te verdedigen op vrijdag 17 januari 2014 om 10:00 uur

door

José Carlos VIEIRA LEITÃO
Mestre em Física, Universidade de Aveiro
geboren te Leiria, Portugal.

Dit proefschrift is goedgekeurd door de promotor:
Prof.dr. E. Brück

Copromotor Dr.ir. N.H. van Dijk

Samenstelling promotiecommissie:

Rector Magnificus,	voorzitter
Prof.dr. E.H. Brück,	Technische Universiteit Delft, promotor
Dr.ir. N.H. van Dijk,	Technische Universiteit Delft, copromotor
Prof.dr. R. Burriel Lahoz,	University of Zaragoza, Spain
Prof.dr. V.B. Sequeira Amaral,	University of Aveiro, Portugal
Prof.dr. R.A. de Groot,	Radboud Universiteit Nijmegen
Prof.dr. A. Schmidt-Ott,	Technische Universiteit Delft
Prof.dr. K.H.J. Buschow,	Universiteit van Amsterdam
Prof.dr. C. Pappas,	Technische Universiteit Delft, reservelid

The work presented in this PhD thesis is financially supported by BASF New Business and Stichting voor Fundamenteel Onderzoek der Materie (FOM), under the Industrial Partnership Programme IPP I18 of the 'Stichting voor Fundamenteel Onderzoek der Materie (FOM)' which is financially supported by the 'Nederlandse Organisatie voor Wetenschappelijk Onderzoek (NWO)'.

Casimir PhD series Delft-Leiden 2013-32
ISBN 978-90-8593-170-6

Printed by: Proefschriftmaken.nl || Uitgeverij BOXPress
Published by: Uitgeverij BOXPress, 's-Hertogenbosch

dedicavit ad nihili

Table of Contents

Chapter 1 Introduction	1
1.1 Global refrigeration.....	1
1.2 Magnetocaloric effect.....	2
1.3 Magnetocaloric materials.....	4
1.3.1 La(Fe,Si) ₁₃ based compounds.....	4
1.3.2 MnAs based compounds.....	5
1.3.3 Heusler alloys.....	5
1.3.4 Fe ₂ P based compounds.....	6
1.4 Thesis outline.....	6
References.....	7
Chapter 2 Theoretical approach	9
2.1 Basic magnetocaloric quantities.....	9
2.2 Magnetic anisotropy.....	11
2.2.1 Magnetocrystalline anisotropy.....	14
2.2.2 Anisotropy energy density according to structure.....	14
2.2.3 Estimation of anisotropy constants.....	16
References.....	22
Chapter 3 Experimental equipment	25
3.1 Introduction.....	25
3.2 High energy planetary ball mill.....	25
3.3 Arc-melting furnace.....	26
3.4 X-ray diffraction.....	27
3.5 Scanning electron microanalysis and Energy dispersive X-ray spectrometry.....	28
3.6 SQUID magnetometer.....	29
3.7 Differential scanning calorimeter.....	30
References.....	31

Chapter 4 Differential microcalorimetry setup	33
4.1 Introduction	33
4.2 Experimental setup	34
4.2.1 Cryostat and insert	34
4.2.2 Temperature control	36
4.2.3 Microcalorimetry chips	37
4.2.4 External measurement and power supply equipment	39
4.3 Measurement cycle	39
4.4 Data management	41
4.5 Conclusion	44
References	44
Chapter 5 Magnetostructural study of the (Mn,Fe)₃(P,Si) system	47
5.1 Introduction	47
5.2 Material overview	48
5.2.1 The Mn _{3-x} Fe _x Si system	48
5.2.2 The Mn _{3-x} Fe _x P system	50
5.3 Sample preparation and characterization	51
5.4 Results and discussion	51
5.4.1 Structural results	51
5.4.2 Magnetic results	54
5.5 The (Mn,Fe) ₃ (Si,P) magnetostructural phase diagram	57
5.5.1 Overall diagram description	59
5.6 (Mn,Fe) ₃ (Si,P)B compounds	62
5.6.1 Sample preparation and characterization	63
5.6.2 Results and discussion	63
5.6.3 Magnetic results	65
5.7 Conclusions	67
References	68
Chapter 6 Magnetocaloric exploration of the (Fe,Co)₃(Si,P) and (Mn,Co)₃(Si,P) systems	71
6.1 Introduction	71
6.2 Material overview	71
6.2.1 The (Fe,Co) ₃ (Si,P) system	71
6.2.2 The (Mn,Co) ₃ (Si,P) system	72

6.3 Results on the $(\text{Fe,Co})_3(\text{Si,P})$ system	73
6.3.1 Si rich samples	73
6.3.2 P rich samples	75
6.3.3 Sulfur substitution in $(\text{Fe,Co})_3(\text{P,Si})$	77
6.4 Results on the $(\text{Mn,Co})_3(\text{Si,P})$ system	79
6.4.1 Inverse magnetocaloric effect	80
6.5 Conclusions	82
References	83

Chapter 7 Magnetic and Magnetocaloric Exploration of Fe rich

$(\text{Mn,Fe})_2(\text{P,Ge})$	87
7.1 Introduction	87
7.2 Material overview	89
7.3 Sample preparation and characterization	90
7.4 Result and discussion	91
7.4.1 $(\text{Mn,Fe})_2(\text{P,Ge})$ system	91
7.4.2 $(\text{Mn,Fe})_{1.95}(\text{P,Ge})$ system	94
7.5 Permanent magnet potential	97
7.6 Conclusions	102
References	103

Chapter 8 In field microcalorimetry measurements on polycrystalline Fe_2P

8.1 Introduction	105
8.2 Material overview	106
8.3 Experimental procedure	107
8.4 Results and discussion	108
8.5 Conclusions	112
References	113

Addendum Instruction Manual for the use and handling of the microcalorimetry setup described in Chapter 4

A.1 Hardware overview	115
A.2 Wiring	120
A.2.1 Insert head	120
A.2.2 Insert body and top	125
A.2.3 Insert cables	125

A.3 Software overview	126
A.3.1 Interface software	126
A.3.2 Data visualization and extraction software	133
A.3.3 Calculation software	135
A.3.4 Data display	140
A.4 Measurement preparation protocol	141
A.5 Measurement protocol	146
A.5.1 Software handling	146
A.5.2 Temperature sweeps	152
A.5.3 Magnetic fields	154
A.5.4 Stopping a measurement	155
A.6 Data management	156
Summary	165
Samenvatting	169
Acknowledgements	173
List of Publication	179
Corriculum Vitæ	183
Epilogue	185

Chapter 1

Introduction

1.1 Global refrigeration

Whether it is for food conservation or simple comfort, the possibility to control environmental temperature is a general need in modern society. Of these two points, food conservation is without a doubt the most important one. It is obvious that our modern life style is impossible to conceive without refrigerators and food preservation.

Historically, refrigerators as we know today first came about in the early 20th century. These were mainly operated with the vapor-compression method, using steam engines with open drive compressors operating with dangerous and environmentally unfriendly refrigerants, being anyway too large, dangerous and expensive for a wide range distribution [1].

Later in 1930, this system evolved, and the use of CFCs (Chlorofluorocarbons) in refrigeration rapidly dominated the market. Still, latter research revealed that the use of uncontrolled CFCs was significantly hazardous to the stratospheric ozone layer and due to the Montreal protocol, the use of these gasses was substituted by that of HFCs (Hydrochlorofluorocarbons). Although these do not damage the ozone layer, they contribute to the rise of the earth's average temperature and to the greenhouse effect. Both of these were later targeted by the Kyoto protocol and governments around the world became committed to reducing the use of these gases [2], opening the field for a new environmentally-friendly technology to come along.

Considering that electricity consumption represents one fifth of the total energy used in Europe [3], and that modern day refrigerators work well below the optimal Carnot cycle [4], an improvement on this technology has to reflect not only environmental friendliness but also energetic efficiency. Magnetic refrigeration, based

on the magnetocaloric effect (MCE), provides a new and viable solution for the creation of a more efficient refrigeration system. Contrarily to vapor compression, this technology resorts to materials in solid form and does not use hazardous gases, being able to reach a maximum theoretical efficiency of about 60% [3], being a bright promise for the future.

1.2 Magnetocaloric effect

In simple terms, the Magnetocaloric Effect (a phenomenon already widely known since the XIXth century but only named as such in 1917/1918 by P. Weiss [5]) is the increase in temperature of a magnetic material with the application of an external magnetic field. This can be understood if we imagine a magnetic material with randomly aligned spins to which we apply an external magnetic field. Considering an ideal system, as we apply this field the spins in the material will tend to align with it, causing a reduction in the magnetic entropy of the system (ΔS) and generate a corresponding heat transfer (δQ). Both these quantities are related by the second law of thermodynamics for a reversible process.

$$\Delta S = \int \frac{\delta Q}{T} \quad (1.1)$$

The thermo-magnetic cycle is in all aspects analogous to the vapor compression cycle of the current commercial refrigerators, in which we merely substitute a gas by a magnetic material and pressure by an external magnetic field, as exemplified by Figure 1.1.

The field in question can either be applied under adiabatic or isothermal conditions, corresponding to either an adiabatic temperature change, where the temperature of the system/material in question increases/reduces, or an isothermal entropy change where the material remains at the same temperature but exchanges heat with its surrounding environment. These two processes are demonstrated in Figure 1.2.

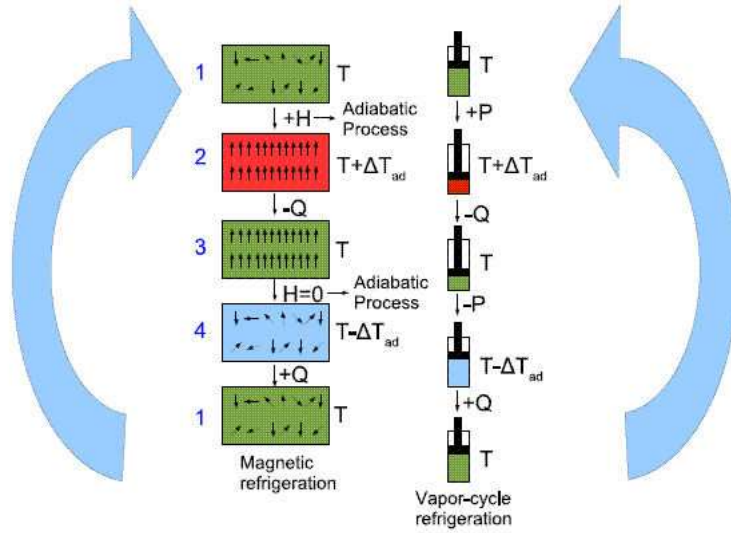


Figure 1.1 Comparison between a magnetic refrigeration cycle (left) and a gas compression cycle (right)

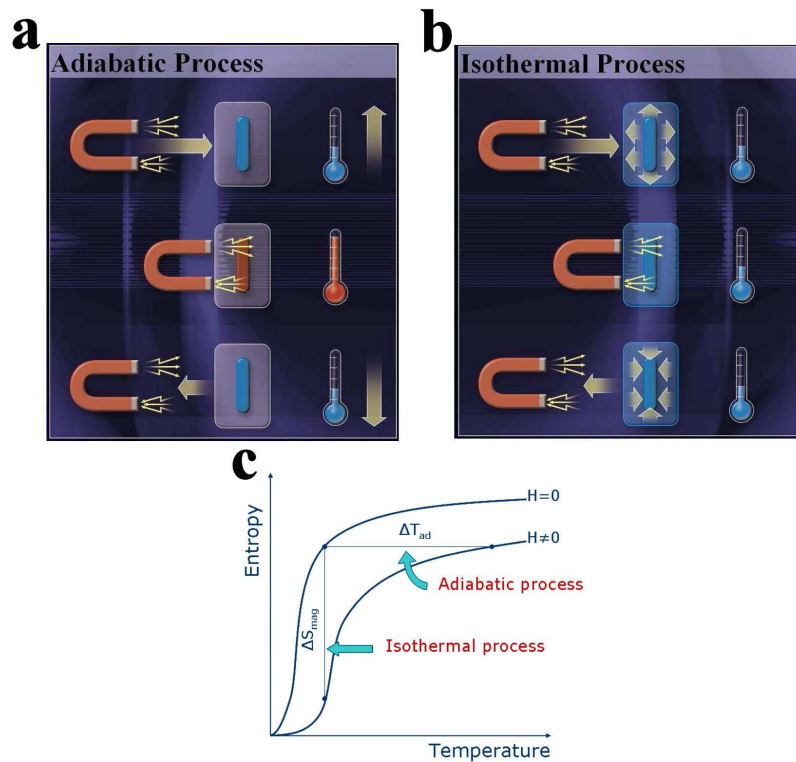


Figure 1.2 a) Example of an adiabatic temperature variation with the application of a magnetic field (Ericsson cycle); b) Example of an isothermal heat exchange with the application of magnetic field (Brayton cycle); c) Example of the adiabatic and isothermal processes between two isofield entropy curves.

The calculation of these two quantities (isothermal entropy change and adiabatic temperature change) is described in detail in Chapter 2.

The idea of a thermo-magnetic refrigerator first appeared in the late 1920s, when cooling via adiabatic demagnetization was proposed by Debye [6] and Giauque [7]. The process was later demonstrated by Giauque and MacDougall in 1933, where the remarkable temperature of 250 mK was reached [8]. This was still a long way from an actual commercially viable refrigerator which was first proposed by Brown in 1976 [9], with a refrigeration model using Gd as a cooling material. Since this point there has been a constant search for more effective, cheap and non-toxic working materials, which may solidly establish the possibility for such a working refrigerator.

1.3 Magnetocaloric materials

The field of MCE material research drastically changed when in 1997 Pecharsky and Gschneidner [10] discovered what became known as the Giant Magnetocaloric Effect (GMCE) in $\text{Gd}_5\text{Si}_2\text{Ge}_2$. This compound displays a strong magneto-structural first order phase transition below room temperature, which can be driven by temperature [11], magnetic field [12] and pressure [13]. Such a transition is most interesting for MCE applications because it represents a sharp and radical change in the entropy of the system.

This result has effectively shaped and directed the research of new MCE materials. We can currently name four particular families of compounds that are serious candidates for practical MCE applications: the $\text{La}(\text{Fe},\text{Si})_{13}$ based compounds, the MnAs based compounds, the Heusler alloys and the Fe_2P based compounds [14].

1.3.1 $\text{La}(\text{Fe},\text{Si})_{13}$ based compounds

Fe-rich $\text{La}(\text{Fe},\text{Si})_{13}$ exhibits a magnetic ordering temperature between 200 and 260 K and has a sharp 1st order phase transition that can be manipulated by adequate heat treatments [14]. These compounds can be further tuned by negative pressure (expansion of the unit cell) via insertion of hydrogen, which can shift the transition temperature up to room temperature and beyond, up until 450 K [15, 14]. On the other hand, positive pressure (compression of the unit cell), via hydrostatic pressure, increases the ΔS value, but decreases the transition temperature [16].

Furthermore, one can also substitute Fe by other elements, such as in the $\text{La(Fe,Co)}_{13-x}\text{Al}_x$ and $\text{La(Fe,Co)}_{13-x}\text{Si}_x$ systems, to increase the magnetic ordering temperature and have a significant MCE near room temperature [17, 18].

The tuning and control mechanisms of this system are somewhat elaborate, having even the necessity of the introduction of a porous architecture in order to control its mechanical properties [19], and the use of La makes it a relatively expensive candidate as a working material for a commercial MCE refrigerator.

1.3.2 MnAs based compounds

The pure MnAs compound displays two different crystal structures, a hexagonal NiAs structure, at both low and high temperatures, and an orthorhombic MnAs structure in the temperature range between 307 and 393 K. The high temperature transition between these structures is 2nd order, while the low temperature one (between ferromagnetic and paramagnetic states) is a sharp 1st order magneto-structural transition [20], displaying a significant thermal hysteresis [14]. This compound can be effectively tuned by the careful substitution of As by Sb, giving the possibility to shift T_C from 220 to 320 K, while maintaining a large entropy change [21].

The downside to this system is the use of toxic As in its composition, which offers an uncertain danger for its long-term use.

1.3.3 Heusler alloys

These compounds usually undergo a 1st order temperature-induced structural transition between a high-temperature cubic austenite and a low-temperature tetragonal martensite phase. This transition is often accompanied by a magnetic phase transition between ferromagnetism and paramagnetism [14].

For example, the Ni_2MnGa compound undergoes a structural transition around 220 K and a magnetic transition at around 376 K [22]. These transitions are easily tuned by altering the mentioned stoichiometric proportions to the point of coupling both into a single large magneto-structural one [23-25]. Some of these alloys containing In or Sn demonstrate an inverse MCE (explained in Chapter 6).

Apart from the typical large thermal hysteresis, which can be controlled by compositional tuning, processing or pressure [14], these systems also present significant difficulties since they are usually not reliable for long-term thermal cycling, unless they are produced as single crystals [14].

1.3.4 Fe₂P based compounds

Fe₂P type compounds usually undergo a 1st order transition consisting of an elastic shift of c/a with hardly any volume change accompanying a magnetic transition from a ferromagnetic to a paramagnetic phase. By the substitution of As, B and Si into the P site, and the partial substitution of Fe by Mn, it is possible to increase the transition temperature of this compound from 217 K [26] up to 450 K [14] and still maintain its hexagonal structure.

This family of compounds is the favored one by the Delft magnetocaloric group and, either directly (Chapters 7 and 8) or indirectly (Chapters 5 and 6), is the driving motivation behind most of the research presented in this thesis.

1.4 Thesis outline

This thesis is partially focused on research performed in the scope of the optimization of Fe₂P-type compounds. Apart from this, there is also a great deal of focus on the assembly and use of a home-made experimental setup for in-field microcalorimetry measurements.

More specifically, Chapter 2 covers the necessary theoretical concepts for the understanding of the MCE (as defined above). It also gives an overview of the magnetic anisotropy phenomenon, which is relevant for the understanding of certain results presented in the following chapters.

Chapter 3 covers the main experimental procedures and equipment used during sample preparation and characterization. Chapter 4 focuses particularly on the already mentioned home-made in-field microcalorimetry setup assembled during the course of this study.

Chapter 5 describes our findings in the (Mn,Fe)₃(Si,P) system, which is related to the (Mn,Fe)₂(Si,P) systems. As a result of this study, resorting to the extensive experimental characterization this system went through, a magnetostructural map was assembled, which includes the discovery of a novel hexagonal phase.

Chapter 6 continues the exploration of the novel hexagonal phase discovered in Chapter 5 in an attempt to use and tune it for MCE applications, namely through the addition of Co, resulting in the (Mn,Co)₃(Si,P) and (Fe,Co)₃(Si,P) systems. Although the results from this research did not provide us with viable MCE materials, it none the

less opened the possibility for further research in the $(\text{Fe,Co})_3(\text{P,S})$ system and the $(\text{Mn,Co})_{1.9}(\text{Si,P})$ system, which displays a substantial inverse MCE.

Chapter 7 focuses on the development of Fe_2P -type alloys, and consists of a study of the $(\text{Mn,Fe})_2(\text{P,Ge})$ system to optimize it in terms of monetary costs. This also led to the study of this system's potential for permanent magnet applications.

Chapter 8 is a fundamental investigation of the key magnetic properties of pure Fe_2P using the experimental setup described in Chapter 4, namely the change in the nature of the magnetoelastic transition of this system when put under a magnetic field.

Finally, a detailed Addendum is included in this thesis, consisting of an operator's manual for the experimental setup described in Chapter 4 and used in Chapter 8.

References

- [1] B. Nagengast, *Mech. Eng. Mag.* May (2000) 56.
- [2] W. T. Tsai, *Chemosphere* 61 (2005) 1539.
- [3] R. P. Fernandes, *Magnetocaloric effect of $\text{Pr}(\text{Ni,Co})_5$ hard magnets and $\text{Ni}_2\text{Mn}(\text{Ga,Bi})$ shape memory alloys*, Universidade de Aveiro (2007), MSc thesis, Chapter 1.
- [4] K. A. Gschneidner and V. K. Pecharsky, *Annu. Rev. Mater. Sci.* 30 (2000) 387.
- [5] A. Smith, *Eur. Phys. J. H* 38 (2013) 507.
- [6] P. Debye, *Ann. Phys.* 81 (1926) 1154.
- [7] W. F. J. Giauque, *Am. Chem. Soc* 49 (1927) 1864.
- [8] W. F. Giauque and D. P. MacDougall, *Phys. Rev.* 43 (1933) 768.
- [9] G. V. Brown, *J. Appl. Phys.*, 47 (1976) 3673.
- [10] V. K. Pecharsky and K. A. Gschneidner, *Phys. Rev. Lett.* 78 (1997) 4494.
- [11] W. Choe, V. K. Pecharsky, A. O. Pecharsky, K. A. Gschneidner Jr., V. G. Young Jr. and G. J. Miller, *Phys. Rev. Lett.* 84 (2000) 4617.
- [12] V. K. Pecharsky, A. P. Holm, K. A. Gschneidner Jr. and R. Rink, *Phys. Rev. Lett.* 91 (2003) 197204.
- [13] L. Morellon, Z. Arnold, C. Magen, C. Ritter, O. Prokhnenko, Y. Skorokhod, P. A. Algarabel, M. R. Ibarra and J. Kamarad, *Phys. Rev. Lett.* 93 (2004) 137201.
- [14] O. Gutfleisch, M. A. Willard, E. Brück, C. H. Chen, S. G. Sankar J. P. Liu, *Adv. Mater.* 23 (2011) 821.

- [15] A. Fujita, S. Fujieda, Y. Hasegawa and K. Fukamichi, *Phys. Rev. B* 67 (2003) 104416.
- [16] A. Fujita, S. Fujieda, K. Fukamichi, H. Mitamura and T. Goto, *Phys. Rev. B* 65 (2001) 014410.
- [17] F. X. Hu, B. G. Shen, J. R. Sun and Z. H. Cheng, *Phys. Rev. B* 64 (2001) 012409.
- [18] J. R. Proveti, E. C. Passamani, C. Larica, A. M. Gomes, A. Y. Takeuchi and A. Massioli, *J. Phys. D: Appl. Phys.* 38 (2005) 1531.
- [19] J. Lyubina, R. Schäfer, N. Martin, L. Schultz, and O. Gutfleisch, *Adv. Mater.* 22 (2010) 3735;
- [20] H. Wada and Y. Tanabe, *Appl. Phys. Lett.* 79 (2001) 3302.
- [21] N. K. Sun, W. B. Cui, D. Li, D. Y. Geng, F. Yang and Z. D. Zhang, *Appl. Phys. Lett.* 92 (2008) 072504.
- [22] P. J. Webster, K. R. A. Ziebeck, S. L. Town and M. S. Peak, *Philos. Mag. B* 49 (1984) 295.
- [23] F. Albertini, F. Canepa, S. Cirafici, E. Franceschi, M. Napoletano, A. Paoluzi, L. Pareti and M. Solzi, *J. Magn. Magn. Mat.* 272-276 (2003) 2111.
- [24] V. Khovailo, V. Novosad, T. Takagi, D. Filippov, R. Levitin and A. Vasil'ev, *Phys. Rev. B* 70 (2004) 174413.
- [25] A. Vasil'ev, A. Bozhko, V. Khovailo, I. Dikshtein, V. Shavron, V. Buchelnikov, M. Matsumoto, S. Suzuki, T. Takagi and J. Tani, *Phys. Rev. B* 59 (1999) 1113.
- [26] O. Beckman, L. Lundgren, P. Nordblad, P. Svedlindh, A. Törne, Y. Andersson and S. Rundqvist, *Phys. Scripta* 25 (1982) 679.

Chapter 2

Theoretical approach

2.1 Basic magnetocaloric quantities

The isothermal entropy change (ΔS) and adiabatic temperature change (ΔT_{ad}) quantities discussed in Chapter 1 can be deduced using the following mathematical steps.

Considering the Gibbs free energy G as a function of temperature (T), pressure (P) and Magnetization (M), used in an isobaric system, we can write:

$$G = U - TS + PV - MH\mu_0 \quad (2.1)$$

where S is the entropy and U the internal energy.

The total differential then becomes:

$$dG = VdP - SdT - MdH\mu_0 \quad (2.2)$$

Yielding thus the expressions:

$$S(T, H, P) = - \left(\frac{\partial G}{\partial T} \right)_{H, P} \quad (2.3a)$$

$$M(T, H, P) = - \frac{1}{\mu_0} \left(\frac{\partial G}{\partial H} \right)_{T, P} \quad (2.3b)$$

$$V(T, H, P) = \left(\frac{\partial G}{\partial P} \right)_{T, H} \quad (2.3c)$$

Through mathematical development of Equations (2.3a) and (2.3b) we obtain:

$$\frac{1}{\mu_0} \left(\frac{\partial S}{\partial H} \right)_T = \left(\frac{\partial M}{\partial T} \right)_H \quad (2.4)$$

The change in entropy ΔS , from an initial magnetic field H_i to a final magnetic field of H_f thus corresponds to:

$$\Delta S(T)_{\Delta H} = \mu_0 \int_{H_i}^{H_f} \left(\frac{\partial M(T, H)}{\partial T} \right)_H dH \quad (2.5)$$

this results in the expression for the calculation of magnetic ΔS .

From this expression we can conclude that the calculation of the magnetic entropy ΔS of a given magnetic material can be achieved through the measurement of magnetic isotherms. It can be easily observed that this quantity will be maximized around large variations in magnetization with temperature, as those that happen around the Curie temperature (T_C), the critical temperature at which a ferromagnet turns into a paramagnet. It is obvious that in the search for novel magnetic materials for commercial cooling applications, one should focus on materials with sharp transitions in the vicinity of room temperature (the temperature we wish to cool from).

Following from Equation (2.3a), through the first law of thermodynamics we can calculate the specific heat of a system with the second derivative of the Gibbs free energy

$$C_{H,P} = -T \left(\frac{\partial^2 G}{\partial T^2} \right)_{H,P} = T \left(\frac{\partial S}{\partial T} \right)_{H,P} \quad (2.6)$$

Considering entropy as a function of temperature and magnetic field, $S=S(T,H)$, a small change is represented as

$$dS = \left(\frac{\partial S}{\partial T} \right)_H dT + \left(\frac{\partial S}{\partial H} \right)_T dH \quad (2.7)$$

Considering an adiabatic process ($dS=0$) we obtain:

$$\left(\frac{\partial S}{\partial T}\right)_H dT = -\left(\frac{\partial S}{\partial H}\right)_T dH \quad (2.8)$$

Taking Equation (2.6), (2.4) and (2.8) we thus obtain:

$$\frac{C}{T} dT = -\mu_0 \left(\frac{\partial M}{\partial T}\right)_H dH \quad (2.9)$$

and consequently

$$\Delta T_{ad}(T)_{\Delta H} = \mu_0 \int_{H_i}^{H_f} \left(\frac{T}{C(T,H)}\right) \left(\frac{\partial M(T,H)}{\partial T}\right)_H dH \quad (2.10)$$

deriving the expression for the calculation of ΔT_{ad} .

Observable in Equation (2.10) is the fact that, besides the isothermal magnetization measurements already required in Equation (2.5), for ΔT_{ad} one also needs specific heat data. This means that, while in practical terms the use of the adiabatic process is more convenient, it is in fact mathematically and experimentally more difficult.

2.2 Magnetic anisotropy

Anisotropy effects in magnetism relate to the existence of energetically favored spatial dimensions [2].

Considering a volume V with uniform magnetization \vec{M} , our focus becomes the dependence of the free energy $F_{AN}(\vec{m})$ on the orientation of \vec{M} . Disregarding temperature dependent effects, making $|\vec{M}| = M_S$ (with M_S being the saturation magnetization), the state of the system is described by the magnetization unit vector as:

$$\vec{m} = \frac{\vec{M}}{M_S} \quad (2.11)$$

The Cartesian components of $\vec{m} = (m_x, m_y, m_z)$ can be expressed in terms of the spherical angles θ and ϕ by:

$$m_x = \sin \theta \cos \phi \quad (2.12a)$$

$$m_y = \sin \theta \sin \phi \quad (2.12b)$$

$$m_z = \cos \theta \quad (2.12c)$$

The energy density, simply defined as $f_{AN}(\vec{m}) = \frac{F_{AN}(\vec{m})}{\Delta V}$, can be represented as a surface where the distance from the origin along the direction \vec{m} is given by $f_{AN}(\vec{m})$. An isotropic exchange generates a surface that resembles a sphere, as depicted in Figure 2.1, indicating no particular directional preference.

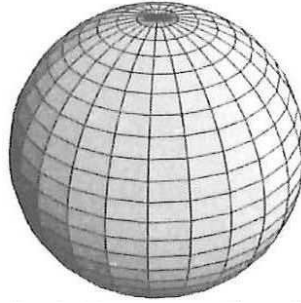


Figure 2.1 Spherical free energy surface for an isotropic exchange [2].

Assuming now that $f_{AN}(\vec{m})$ is defined as an expansion that only depends on θ :

$$f_{AN}(\vec{m}) = K_0 + K_1 \sin^2 \theta + K_2 \sin^4 \theta + K_3 \sin^6 \theta + \dots \quad (2.13)$$

where K_1 , K_2 and K_3 are anisotropy constants independent of m , having the dimensions of energy per unit of volume. For different values of these constants we obtain different energy surfaces, with depressions indicating energetically favored directions, as displayed in Figure 2.2.

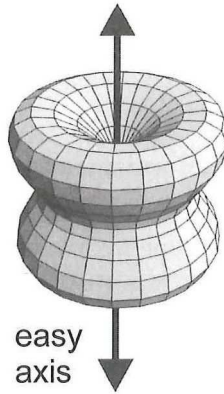


Figure 2.2 Broken spherical symmetry with the formation of an easy magnetization axis [2].

The direction with the lowest value for $f_{AN}(\vec{m})$ is referred to as easy magnetization direction, and should this be coincident with a particular crystallographic axis it may be referred to as easy magnetization axis or simply easy axis. This represents the direction in which magnetization will naturally align with in order to minimize the system's free energy and upon measuring the same magnetic sample for different orientations, a distinct magnetic behavior will be recorded depending on the orientation of the sample relatively to the applied magnetic field, as shown in Figure 2.3.

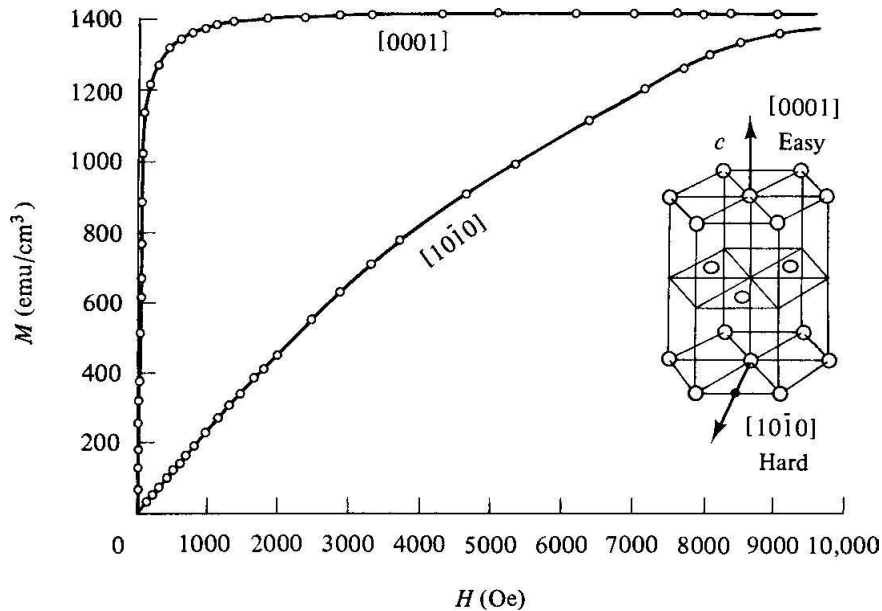


Figure 2.3 Example of magnetization curves measured along the easy direction [0001], demonstrating a rapid rise to the saturation magnetization, and hard direction [1010], demonstrating a slow saturation, for a close-packed hexagonal Cobalt structure; a , b and c represent the basal plane and d an axis perpendicular to this plane in the $[abcd]$ notation [3].

2.2.1 Magnetocrystalline anisotropy

There are several exchange interactions that play a part in magnetocrystalline anisotropy. The first is the spin-orbit coupling, which causes the electronic orbitals to be influenced by electronic spin, following it when magnetization changes orientation [2]. Even though this is a clear source of anisotropy, it is usually very weak, being easily overcome by a few hundred oersteds [4].

Shape anisotropy should also be mentioned as a relevant contributor, although this is not developed in the current thesis. This is the kind of anisotropy that arises from a magnetic body which does not have a perfect spherical shape. This means that its demagnetization field will not be equal for all direction and in this case generate a non spherical energy surface (of a shape complementary to the actual body) with preferred directions\planes.

Even though this anisotropy phenomenon arises from purely geometrical contributions, it cannot be disregarded or underestimated, as it is the driving force behind such widely used magnetic materials as the Alnico (Al-Ni-Co) magnets, which consist of FeCo-rich needles in a NiAl-rich matrix [2, 5].

The great contributor to anisotropy that will be focused upon is the orbit-lattice interaction, meaning that the electronic orbitals are coupled to the crystal lattice of the system [4]. This strongly influences the orientation of the moments with respect to the lattice, which, mathematically, translates itself as different values for the above mentioned anisotropy constants. This is referred to as magnetocrystalline anisotropy [2].

2.2.2 Anisotropy energy density according to structure

The anisotropy constants are not usually defined in theoretical terms, but rather through measurement, being in fact material-specific quantities [4]. The values of these constants have very specific effects on the energy surface defined by Equation (2.13) depending on the symmetry of the lattice [2, 3].

- Uniaxial system

Specifying the expansion of Equation (2.13) for a system with a single axis of high symmetry (assumed to be the z axis), the following expression is obtained:

$$f_{AN}(m) = K_1 \sin^2 \theta \quad (2.14)$$

When K_1 is positive, the direction of lowest energy, the easy axis, is z . When K_1 is negative we instead have an easy plane perpendicular to z [4].

- Hexagonal, Tetragonal and Rhombohedral systems

For these three cases the anisotropy energy density has the following forms:

Hexagonal

$$f_{AN}(m) = K_1 \sin^2 \theta + K_2 \sin^4 \theta + K_3 \sin^6 \theta \cos 6\phi \quad (2.15a)$$

Tetragonal [6]

$$f_{AN}(m) = K_1 \sin^2 \theta + K_2 \sin^4 \theta + K_3 \sin^4 \theta \sin 4\phi \quad (2.15b)$$

Rhombohedral [6]

$$f_{AN}(m) = K_1 \sin^2 \theta + K_2 \sin^4 \theta + K_3 \cos \theta \sin^3 \theta \cos 3\phi \quad (2.15c)$$

Considering that in most cases only K_1 and K_2 play a relevant role in the anisotropy energy density, these three equations become equivalent to the second term development of Equation (2.13). In this case their solutions in terms of K_1 and K_2 naturally become the same and the following cases can be distinguished:

- 1 – For $K_1=K_2=0$ the system is an isotropic ferromagnet;
- 2 – For $K_1>0$ and $K_2>-K_1$ we have an easy axis for $\theta=0$ (usually z);
- 3 – For $K_1>0$ and $K_2<-K_1$ or $K_1<0$ and $K_2<-K_1/2$ the plane perpendicular to the z axis is the easy plane;

4 – For $2K_2 < K_1 < 0$ the easy axis will be reached for a θ value given by the following expression [4]:

$$\sin^2 \theta = -\frac{K_1}{2K_2} \quad (2.16)$$

making in fact an easy cone aligned with the z axis [3].

- Cubic system

The Cubic case is more complex given its high symmetry, and it becomes easier to step outside of spherical coordinates. In this case our expression becomes [2]

$$f_{AN}(m) = K_1(\alpha^2 \beta^2 + \beta^2 \gamma^2 + \gamma^2 \alpha^2) + K_2 \alpha^2 \beta^2 \gamma^2 \quad (2.17)$$

with $\alpha = \cos \phi \sin \theta$, $\beta = \sin \phi \sin \theta$ and $\gamma = \cos \theta$.

In this case the anisotropy variations for different values of K_1 and K_2 are listed in Table 2.1 and 2.2 [2].

Table 2.1 Easy and hard axis for a Cubic system, taking $K_1 > 0$ and $x = K_2/K_1$

	$-\infty < x < -9$	$-9 < x < -9/4$	$-9/4 < x < +\infty$
$\langle 100 \rangle$	Medium-hard	Easy	Easy
$\langle 110 \rangle$	Hard	Hard	Medium-hard
$\langle 111 \rangle$	Easy	Medium-Hard	Hard

Table 2.2 Easy and hard axis for a Cubic system, taking $K_1 < 0$ and $x = K_2/|K_1|$

	$-\infty < x < 9/4$	$9/4 < x < 9$	$9 < x < +\infty$
$\langle 100 \rangle$	Hard	Hard	Medium-hard
$\langle 110 \rangle$	Medium-hard	Easy	Easy
$\langle 111 \rangle$	Easy	Medium-hard	Hard

2.2.3 Estimation of anisotropy constants

The determination of the values of the anisotropy constant values can be performed in various ways.

A straightforward method is by measuring the anisotropy field H_{an} . This is achieved by measuring magnetization curves with a magnetic field applied parallel and perpendicular to the easy magnetization direction. The intersection of these two curves then gives us the anisotropy field [3]. An example of such a measurement is given in Figure 2.4.

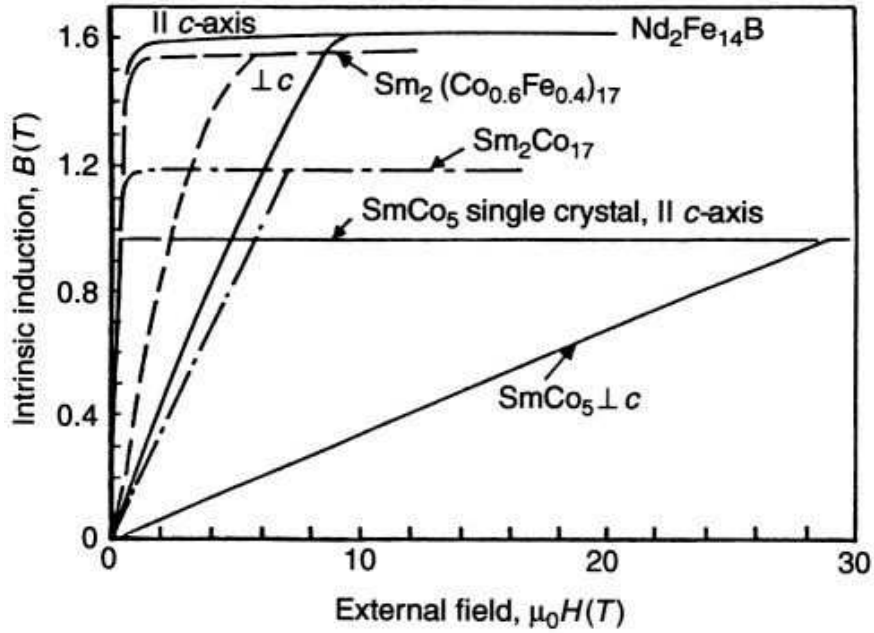


Figure 2.4 Several easy\hard magnetization curves for various compounds [7]. Intrinsic induction being $\mu_0 M$.

Supposing that a material's spontaneous magnetization M_S has an angle θ , with a field applied perpendicular to the symmetry axis, the magnetic field will exert a torque of $\mu_0 H M_S \cos \theta$, which will tend to increase with θ . The value of this torque can be obtained by differentiating the expression for the anisotropy energy.

$$\frac{df_{AN}}{d\theta} = 2K_1 \sin \theta \cos \theta + 4K_2 \sin^3 \theta \cos \theta \quad (2.18)$$

Taking the two torques into consideration we arrive at the following expression:

$$\mu_0 H = \frac{2K_1 \sin \theta + 4K_2 \sin^3 \theta}{M_S} \quad (2.19)$$

Knowing that the value of H that makes M_S parallel to the applied field is reached when $\sin \theta = 1$, the anisotropy field H_{AN} can be calculated as

$$\mu_0 H_{AN} = \frac{2K_1 + 4K_2}{M_S} \quad (2.20)$$

Given that in some materials K_2 is negligible, measurements of H_{AN} are then sufficient to determine K_1 .

- Sucksmith-Thompson method

Still, alternative methods for the determination of K_1 and K_2 have been developed. One such method, developed by Sucksmith and Thompson in 1954 [8], is based on the following relation, with $J = \mu_0 M$:

$$\frac{2K_1}{J_s^2} + \frac{4K_2}{J_s^4} J^2 = \frac{H}{J} \quad (2.21)$$

which is valid for magnetization curves of single crystals under small fields perpendicular to the easy direction. It is then possible to assume that J_s does not change with the field strength and that $\sin \theta = J / J_s$ (which, when substituted in Equation (2.19) give us Equation (2.21)). When H/J is plotted versus J^2 , the anisotropy constant K_1 can be estimated by the vertical interception of the graph with the y -axis, and K_2 by the slope of this same graph.

- Modified Sucksmith-Thompson method

Another method based on the Sucksmith-Thomson has also been proposed by Ram and Gaut in 1983 [9], which has the advantage of weeding out errors which occur when this method is used on powder samples with a misalignment.

In this modified model $H / \alpha(J - J_r)$ is plotted versus $\alpha^2(J - J_r)^2$, where J_r is the remanence in the hard direction and $\alpha = (J_s - J_r) / J_s$ has been introduced to simulate a perfect magnetic alignment of the powder particles. K_1 and K_2 can then be extracted from this graph in the same way as in the Sucksmith-Thomson method, as demonstrated in Figure 2.5.

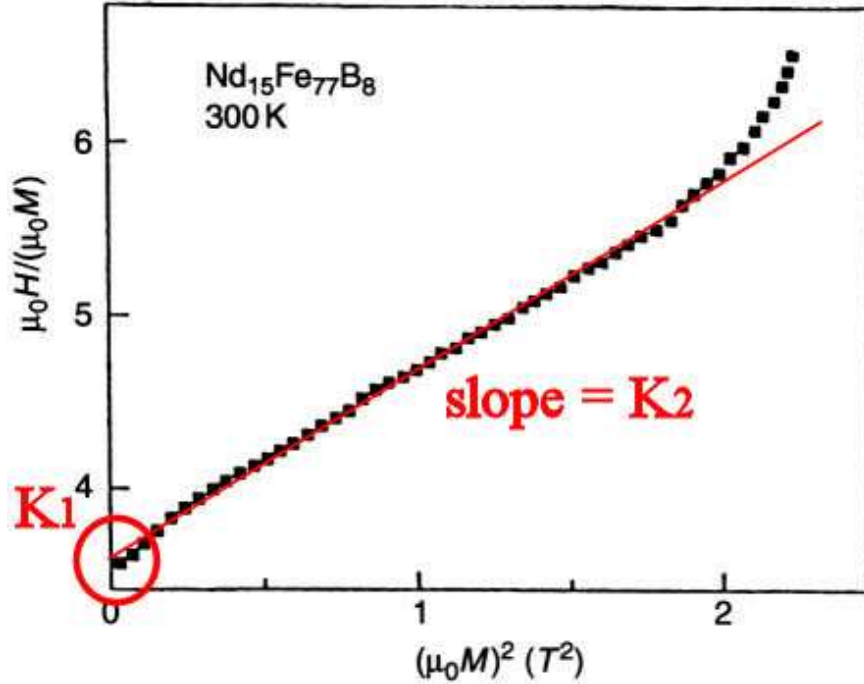


Figure 2.5 Sucksmith-Thompson plot for $\text{Nd}_{15}\text{Fe}_{77}\text{B}_8$, evidencing the extraction of the values of K_1 and K_2 [10].

- Area Method

Yet another alternative is called the Area method, which has the advantage of avoiding errors due to isotropic strains.

In a cubic structure the variation of the anisotropy energy with the direction of magnetization is commonly expressed in terms of directional cosines. Assuming OA, OB and OC to be the cubic edges of the structure, and magnetization direction to be OP, then the anisotropy energy per volume can be given by:

$$f_{AN} = K_0' + K_1'(\alpha_1^2\alpha_2^2 + \alpha_2^2\alpha_3^2 + \alpha_3^2\alpha_1^2) + K_2'(\alpha_1^2\alpha_2^2\alpha_3^2) \quad (2.22)$$

where $\alpha_1 = \cos POA$, $\alpha_2 = \cos POB$ and $\alpha_3 = \cos POC$.

The anisotropy constants can be determined by calculating the energy of magnetization as $\int \vec{H}d\vec{J}$ along the different crystal axes. This includes the measurement of the $J(\vec{H})$ curve from complete demagnetization up to magnetic saturation. The area between this curve and the J -axis may then be determined, which adds up to the energy for each crystallographic direction.

Taking as an example the [100] direction, from Equation (2.22) we obtain $\alpha_1 = 1$ and $\alpha_2 = \alpha_3 = 0$, being the end result that $E_{100} = K'_0$.

Taking the [110] direction we obtain $\alpha_1 = \alpha_2 = \frac{1}{\sqrt{2}}$ and $\alpha_3 = 0$. From these values Equation (2.22) then gives us $E_{110} = K'_0 + \frac{1}{4}K'_1$.

Similarly, for the [111] direction we will find $\alpha_1 = \alpha_2 = \alpha_3 = \frac{1}{\sqrt{3}}$, which substituting in Equation (2.22) lead up the expression of $E_{111} = K'_0 + \frac{1}{3}K'_1 + \frac{1}{27}K'_2$, which then lead to:

$$K'_1 = 4(E_{110} - E_{111}) \quad (2.23a)$$

$$K'_2 = 27(E_{111} - E_{100}) - 36(E_{110} - E_{100}) \quad (2.23b)$$

- Torque Method

This method requires the use of a torque magnetometer that can measure the torque, N , required to keep a crystal with its axis inclined at various known angles relatively to the external magnetic field. A sample, shaped like a disk or ellipsoid is rotated around an axis perpendicular to both its plane and the applied field, which should be sufficient to saturate the sample.

In a cubic lattice, the torque curves are expected to depend on the crystal plane of the sample. A sample cut perpendicularly to the [001] direction will have values of $\alpha_1 = \cos \theta$, $\alpha_2 = \sin \theta$ and $\alpha_3 = 0$, which, when applied to Equation (2.22), results in

$$f_{AN} = K'_0 + K'_1(\cos^2 \theta \sin^2 \theta) = K'_0 + \frac{K'_1}{8}(1 - \cos 4\theta) \quad (2.24)$$

The differential of Equation (2.24) then gives us the torque as

$$N = \frac{1}{2}K'_1 \sin 4\theta \quad (2.25)$$

It should be noted that Equation (2.24) is specific for the cubic case. Other expressions will need to be derived from the anisotropy energy equations corresponding to other structures.

Having the above specified torque measurements, as exemplified by Figure 2.6, after a Fourier analysis of the corresponding curves and comparison to Equation (2.25), or any other obtained from of the structure's anisotropy energy expression, one may arrive at the values of the anisotropy constants.

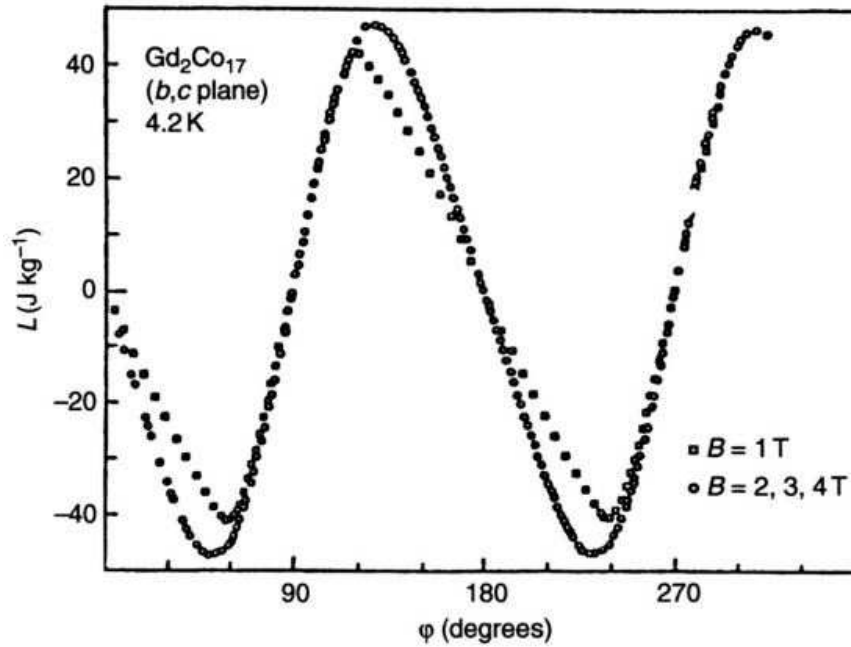


Figure 2.6 Torque measurement for the b, c plane in Gd_2Co_{17} [11].

Table 2.3 shows examples of the room temperature anisotropy constant values for several magnetic materials. As usually lower symmetry leads to larger anisotropy, materials with a hexagonal crystal structure have larger anisotropy constants than those with cubic crystal structures.

Table 2.3 Examples of anisotropy constant values at room temperature [4]

Structure	Compound	K_1 (10^4 J/m ³)	K_2 (10^4 J/m ³)
Cubic	Fe	4.8	± 0.5
	Ni	-0.5	-0.2
	FeO	-1.1	
	MnO	-0.3	
	NiO	-0.62	
	MgO	-0.25	
	CoO	20	
	Co	45	15
Hexagonal	BaO	33	
	YCo ₅	550	
	MnBi	89	27

References

- [1] A. M. Tishin and Y. I. Spichkin, *The Magnetocaloric Effect and its Applications*, Inst. of Phys. Publishing, Bristol, UK (2003).
- [2] G. Bertotti, *Hysteresis in Magnetism for Physicists, Material Scientists and Engineers*, Academic Press, San Diego, USA (1998).
- [3] B. D. Cullity and C. D. Graham, *Introduction to Magnetic Materials*, Wiley-IEEE Press, Hoboken, New Jersey (2009).
- [4] K. H. J. Buschow and F. R. de Boer, *Physics of Magnetism and Magnetic Materials*, Kluwer Academic Publishers, New York, USA (2004).
- [5] Joong Jung Kim, Hyun Soon Park, Daisuke Shindo, Satoshi Hirosawa and Hideyuki Morimoto, *Mater. Trans.* 47 (2006) 907.
- [6] L. D. Landau, L. P. Pitaevskii and E. M. Lifshitz, *Electrodynamics of Continuous Media – Volume 8*, Butterworth-Heinemann, Burlington, USA (1984).
- [7] K. J. Strnat in E. P. Wohlfarth and K. H. J. Bushow (Eds), *Ferromagnetic Materials – Volume 2*, Elsevier Science Publishers B.V., Amsterdam, Netherlands (1980).
- [8] W. Sucksmith and J. E. Thompson, *Proc. Roy. Soc.* A225 (1954) 362.
- [9] V. S. Ram and P. Gaunt, *J. Appl. Phys.* 54 (1983) 2872.

- [10] K. D. Durst and H. Kronmüller, *J. Magn. Magn. Mater.* 59 (1986) 86.
- [11] J. J. M. Franse, S. Sinnema, R. Verhoef, R. J. Radwański, F. R. de Boer, A. Menovsky, *CEAM Report*, Elsevier Science Publishers B.V., London, UK (1989).

Chapter 3

Experimental equipment

3.1 Introduction

This thesis is largely the result of experimental work of production and characterization of metallic samples. In this chapter all experimental equipment used in this process is listed and detailed.

All materials described in the next chapters were produced at the section of Fundamental Aspects of Materials and Energy (FAME) of the Faculty of Applied Sciences of the Delft University of Technology. The subsequent characterization measurements performed on these were equally performed in this same section unless mentioned otherwise.

3.2 High energy planetary ball mill

High energy ball milling has received great attention for its great range of applications, from cold welding, grain size control, synthesis of equilibrium and non-equilibrium materials and mechanical coating [1].

In the current work this technique, schematically represented in Figure 3.2, was mostly used as a pre-alloying technique and homogenizer of starting materials, turning our several elemental or binary initial compounds into an evenly homogenous powder, which could be subsequently pressed and annealed.

All ball milled samples were produced in a Fritsch Pulverisette planetary mill and were milled for 6 hours (3 hours with 5 minute breaks every 5 minutes to prevent overheating) at 360 rpm in 80 ml hardened steel crucibles, each containing fifteen 4 g

hardened steel balls and a sample mass of 5 g, amounting to a sample\ball ratio of 0.083(3).

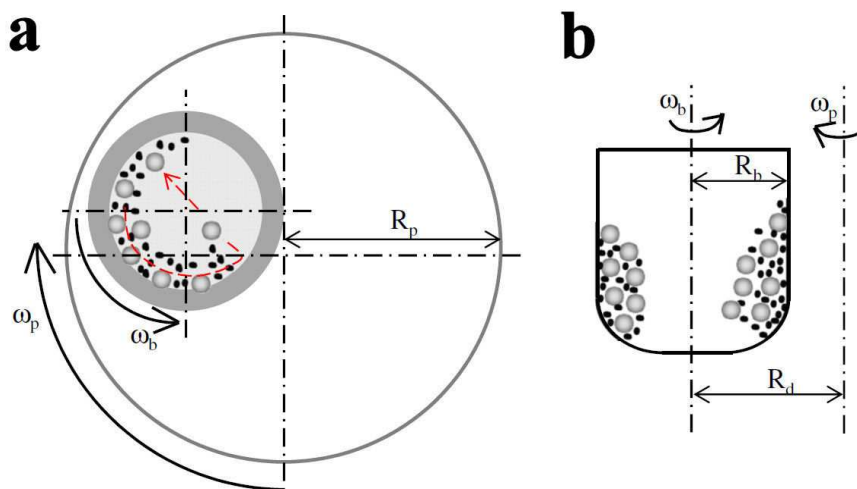


Figure 3.1 a) Arial diagram of a planetary ball mill; b) Sectional view of a planetary ball mill; Legend: ω_p) angular moment of the planetary mill; ω_b) angular moment of the crucibles inside the mill; R_p) Radius of the planetary mill; R_b) radius of the crucibles inside the planetary mill; R_d) distance between the center of rotation of the mill and the crucible [1].

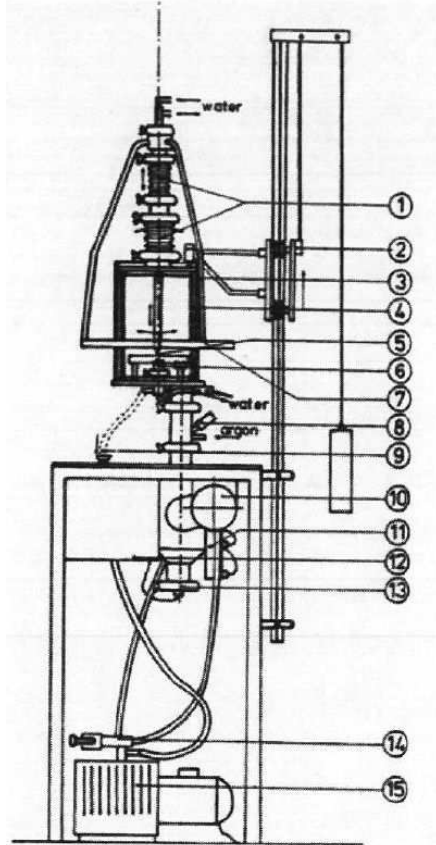
3.3 Arc-melting furnace

Arc-melting is widely used both in industry and lab-scale applications given its suitability for the rapid production of highly homogeneous metallic ingots.

The used arc-melting furnace, shown in Figure 3.2, is a home-made setup, originally produced in the Van der Waals-Zeeman Institute at the University of Amsterdam and later transferred to FAME.

This system was designed for the preparation of lab-scale intermetallic compounds with a maximal mass of 15 grams. The electrical current in this setup is tunable between 5 and 300 A [2, 3].

All samples produced with this equipment were melted on a water cooled copper crucible inside the arc-melting furnace under a 500 mbar atmosphere of purified argon. The as-melted ingots were turned over and re-melted again between 3 and 5 times to attain good homogeneity before annealing.



1. Stainless steel bellows.
2. Lift.
3. Plexyglass tube for safety.
4. Pyrex tube.
5. Water-cooled tungsten electrode.
6. Water-cooled copper crucible.
7. Manipulation ring.
8. Pressure indicator.
9. Vacuum connection for casting.
10. Turbo pump.
11. Pneumatic valve.
12. Electronic equipment.
13. Water-leak detector.
14. Three way valve.
15. Fore pump.

Figure 3.2 Schematic representation of the home made arc-melting furnace used in sample production [2].

3.4 X-ray diffraction

The crystal structure and sample homogeneity were analyzed with an X'Pert PRO X-ray diffractometer from PANalytical using Cu K_{α} radiation, schematically represented in Figure 3.3, both in ambient and non-ambient conditions (only used in Chapter 8). The resulting diffraction patterns were analyzed using the X'Pert HighScore and FullProf's software implementation of the Rietveld refinement method [4].

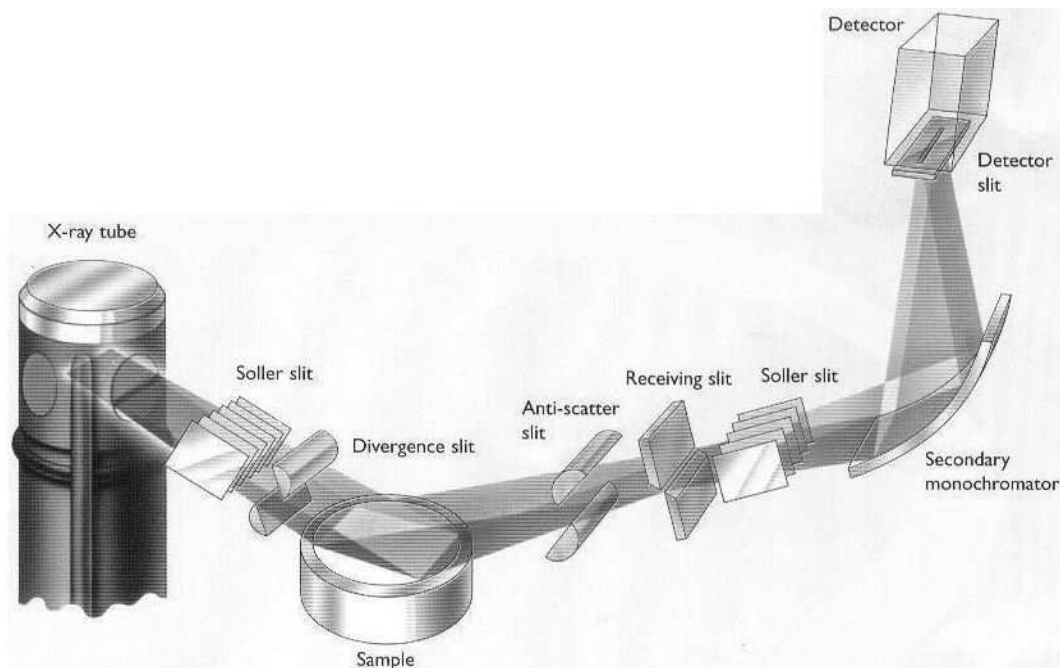


Figure 3.3 Schematic representation of an X-ray diffractometer (image from PANalytical B. V.).

3.5 Scanning electron microanalysis and Energy dispersive X-ray spectrometry

The determination of phase compositions in our $(\text{Mn,Co})_3(\text{Si,P})$ samples (Chapter 6) was conducted with a scanning electron microscope (SEM) and an energy dispersive X-ray spectrometer (EDS). Both these measurements were performed in a Jeol JSM-840A equipment at the Delft Aerospace Structures & Materials Laboratory at the Delft University of Technology. The equipment in question had an acceleration voltage of 5 to 35 kV, a magnification of 20 to 300000 \times and a resolution down to 3.5 nm.

A schematic representation of the EMP and EDS setup is given in Figure 3.4.

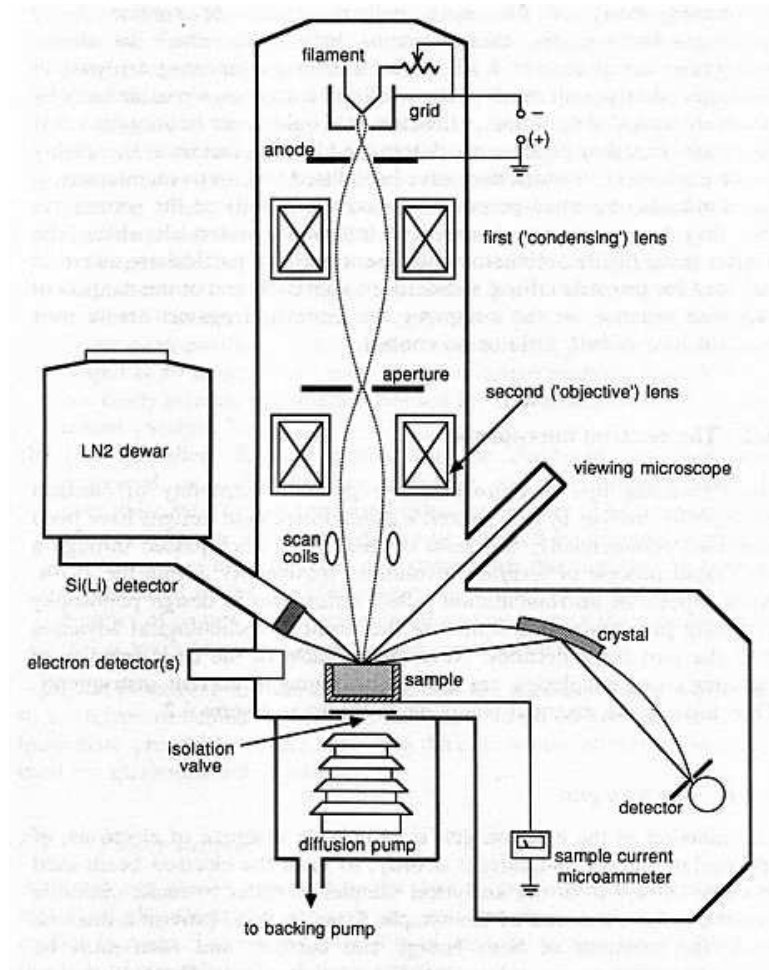


Figure 3.4 Representation of a generic EMP/EDS (image taken from the Department of Geosciences of the University of Wisconsin-Madison).

3.6 SQUID magnetometer

Superconducting quantum interference devices (SQUID) are usually used for the precise measurement of magnetic moments. This equipment resorts to a sensor ring consisting of two superconductors separated by thin insulating layers to form two parallel Josephson junctions, schematically shown in Figure 3.5a. The great sensitivity of SQUID devices originate from the detection of changes in magnetic field associated with one flux quantum:

$$\Phi_0 = \frac{h}{2e} = 2.067833636 \times 10^{-15} \text{ Wb} \quad (3.1)$$

With a constant biasing current in the SQUID device, the measured voltage will oscillate with the changes in phase at the two junctions, which depends upon the change in the magnetic flux. Counting the oscillations allows for the evaluation of the flux change.

Magnetic measurements were thus performed in two different SQUID magnetometers, a MPMS-5S and a MPMS XL model, both from Quantum Design.

The measurements taken were, unless mentioned otherwise, temperature sweeps from 5 to 370 K (MPMS-5S) or 400 K (MPMS XL) with a fixed applied magnetic field.

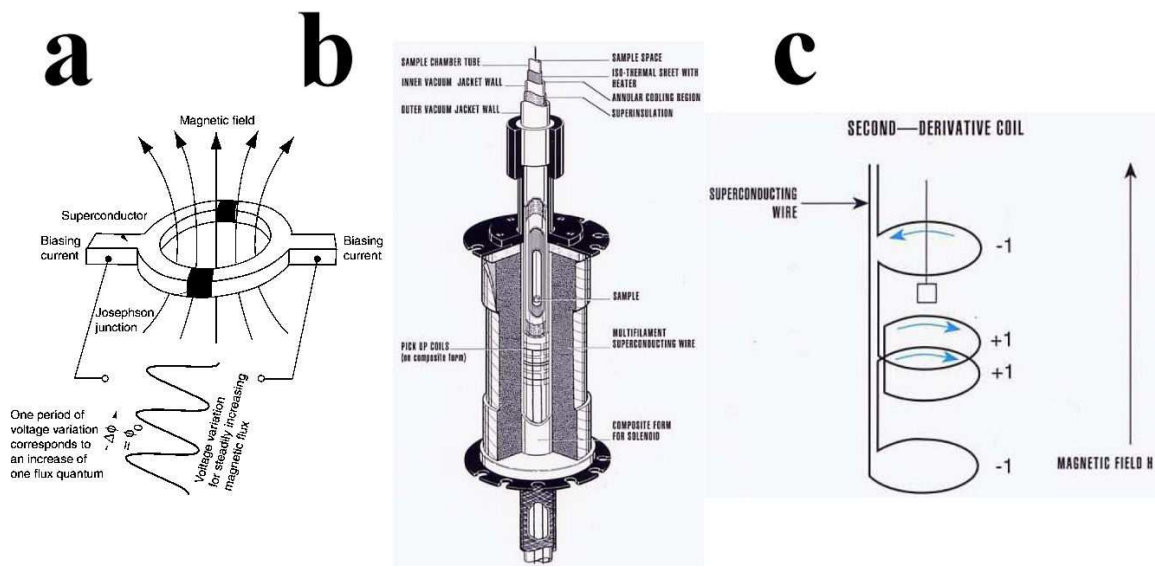


Figure 3.5 a) Schematic representation of a Josephson junction [5]; b) Schematic representation of the insert of a MPMS magnetometer; c) Schematic representation of a detection coil of a MPMS magnetometer [6]

3.7 Differential scanning calorimeter

Differential scanning calorimeter (DSC) measurements were used on those samples whose transition temperatures exceeded the temperature range of our magnetometers.

For this end a Q2000 model from TA Instruments-Waters LLC was used, performing temperature sweeps from 0 °C to 500 °C at a rate of 20 °C per minute. The functioning of this equipment relies on a sample and reference assembly connected by a low-resistance heat-flow path (a metal disc) enclosed in a single furnace. Any enthalpy or heat capacity change in the sample (as those which happen during a structural or magnetic transition) causes a difference in its temperature relatively to the

reference, which is recorded using a calibration experiment [7, 3]. A diagram of this DSC system is given in Figure 3.6.

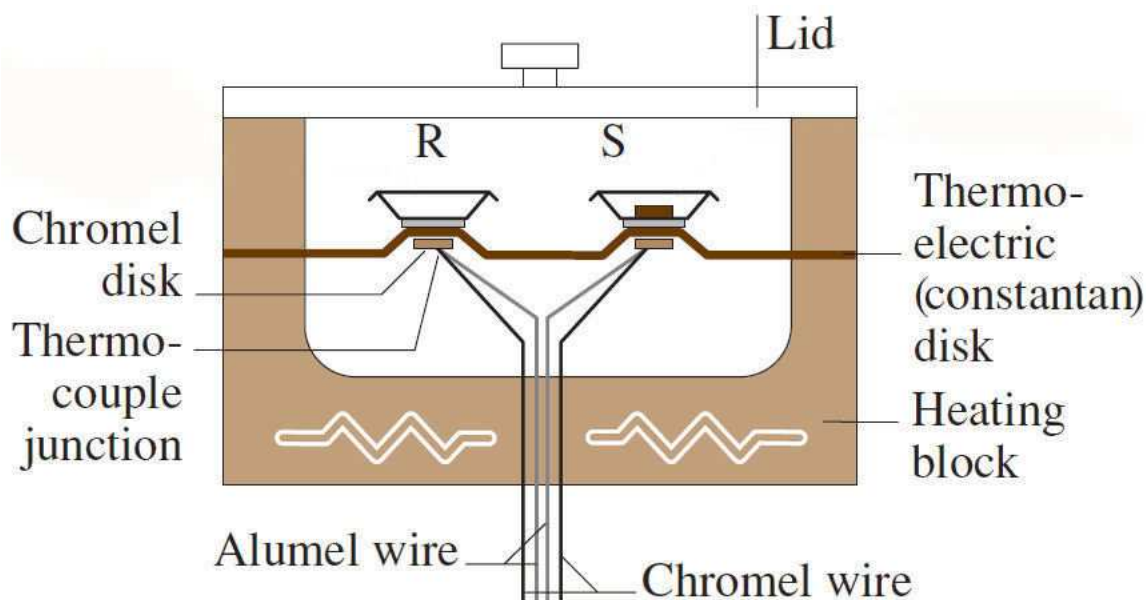


Figure 3.6 – Schematic representation of a DSC system as used in the current thesis; S stands for Sample and R for Reference [8]

References

- [1] Liang Hao, Yun Lu, Hiromasa Sato, Hiroshi Asanuma, Jie Guo, *Int. J. Miner. Process.* 212 (2013) 51.
- [2] Pham Duc Thang, *Permanent Magnets based on Iron-Platinum alloys*, University of Amsterdam (2003), PhD thesis, Chapter 2.
- [3] N. T. Trung, *First-order phase transitions and giant magnetocaloric effect*, Delft University of Technology (2010) PhD thesis, Chapter 3.
- [4] Rodriguez-Carvajal, “FULLPROF: A Program for Rietveld Refinement and Pattern Matching Analysis”, Abstracts of the Satellite Meeting on Powder Diffraction of the XV Congress of the IUCr, p. 127, Toulouse, France (1990).
- [5] M. McElfresh, *Fundamentals of Magnetism and Magnetic Measurements – Featuring Quantum Design’s Magnetic Property Measurement System*, printed by Quantum Design (1994).
- [6] <http://hyperphysics.phy-astr.gsu.edu/hbase/solids/squid.html>

- [7] H. K. D. H. Bhadeshia, *Differential scanning calorimetry*, University of Cambridge, Material Science & Metallurgy
(http://www.uzaktanegitimplatformu.com/UEP/uep_ylisans/ey2/ey2_download/DSC%20Thermal2.pdf).
- [8] S. Kasap, D. Tonchev, *Springer Handbook of Electronic and Photonic Materials*, Wemding, Springer, (2006) Chapter 19.

Chapter 4

Differential microcalorimetry setup

4.1 Introduction

As explained in Chapters 1 and 2, there are two common methods by which one may calculate the magnetocaloric effect of a given material: the isothermal process, in which we calculate the magnetic entropy change (ΔS), and the adiabatic process, in which we calculate the actual temperature change (ΔT) of a given material.

Of these two the isothermal process is by far the most commonly used, as, in practical terms, one only needs to perform a series of magnetic isothermal measurements to calculate ΔS (Equation 2.5).

The calculation of ΔT on the other hand is slightly more complex, as it relies on isofield specific heat measurements, as well as the same magnetization measurements required for the calculation ΔS (equation 2.10) [1]. Even though for a proper study of the magnetocaloric potential both these quantities are required [2, 3], the calculation of ΔT is usually made difficult by the lack of a commercial measurement systems that allows reliable specific heat measurements in applied magnetic field.

To overcome this issue, many research groups world-wide resort to assembling their own isofield specific heat measuring equipments. Among the most recent examples we may cite the setup described by Marcos *et al.* [4], consisting of an insert that can be fitted to any cryostat with the capacity to generate a magnetic field. This setup resorts to thermo-batteries, which give a voltage output in response to the heat exchange with the measured sample.

One other example described by Korolev *et al.* [5], has been specifically designed to measure magnetic colloids. Instead of using a permanent magnet it is

designed as a microcalorimetry cell placed between the two poles of an electromagnet to generate a (low-intensity) magnetic field.

The setup described by Kuepferling *et al.* [6] on the other hand resorts to commercial Peltier cells, a thermoelectric device made of a series of junctions of conductors with different thermoelectric power, acting as both sensors and actuators. In this way the system is able to achieve strict isothermal conditions. The drawback of this system is a high dependence on an accurate calibration of the Peltier cells.

The versatility of Peltier elements can also be observed in the setup described by Porcari *et al.* [7], which resorts to a power Peltier to perform the temperature control and two Peltier sensors to perform the actual DSC measurement [8], a setup quite similar to the one described by Jeppesen *et al.* [9].

Under this perspective the microcalorimetry chips from the company Xensor Integration have gained increasing relevance, due to their precision, practicality and relatively small price, as presented by Morrison *et al.* [10, 11], Minakov *et al.* [12-15] and Merzlyakov (in a non-magnetocaloric context) [16], making them a very attractive and promising component for such calorimeters.

We report the design and construction of an experimental setup that allows for specific heat measurements under high magnetic fields, using these microcalorimetry chips. We have adopted a two chip setup in our equipment, which enables us to easily bypass many bothersome calibration and equipment specific issues. This instrument's potential range is well beyond the purely magnetocaloric oriented, as it can provide invaluable information regarding any phase transition, where the application of a magnetic field may play a significant role.

4.2 Experimental setup

4.2.1 Cryostat and insert

As a base for this setup we resorted to a commercial cryostat from American Magnetics Inc. (AMI), equipped with a 9 Tesla 2 inch bore superconducting magnet (Solenoid) with its own power supply and magnetic field controller.

This cryostat has a 36 l LHe reservoir, in direct contact with the superconducting magnet to keep it at a constant temperature of 4.2 K. A separate LN₂ reservoir, with a capacity for 36 l, is also present to reduce helium evaporation.

The Variable Temperature Insert (VTI), fitted for transport measurements was removed to mount another insert with the capacity to perform specific heat

measurements, shown in Figure 4.1a. This step, made it impossible to use the original built-in temperature control system of this cryostat. A schematic diagram of the cryostat is shown in Figure 4.1b.

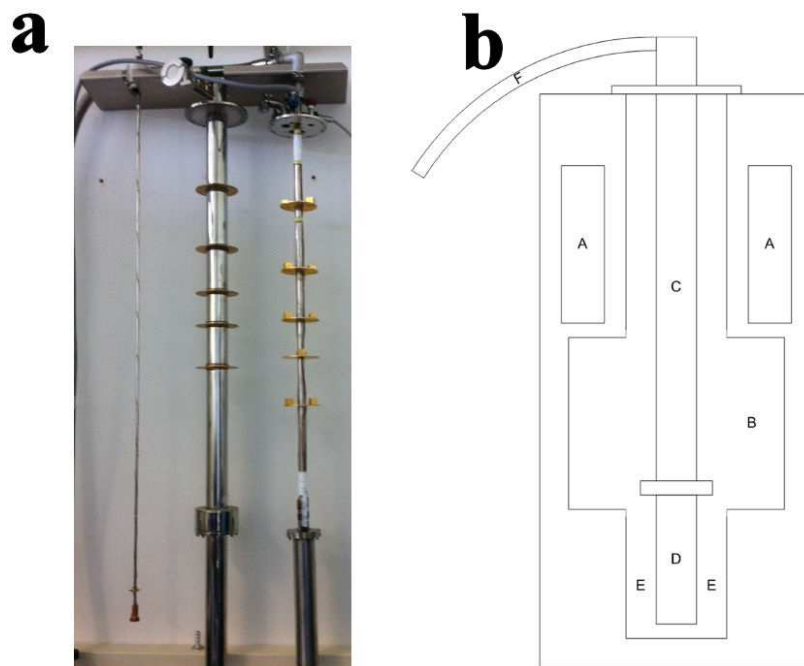


Figure 4.1 a) Comparison of the original transport measurements VTI insert and its respective casing (left and middle respectively) with the newly fashioned home made microcalorimetry insert (right); b) Schematic diagram of the AMI cryostat. Legend: A) Liquid Nitrogen reservoir; B) Liquid Helium reservoir; C) Insert; D) Magnetic field center; E) Superconducting Magnet; F) Wiring connecting the insert to the rest of the measurement equipment/vacuum pump tube.

The evacuated sample space in the tip of the newly constructed insert is in direct contact with the liquid Helium and consists of a small 25 mm wide cylinder protected by three cylindrical shields of which the first of these shield is equipped with a heater.

A scheme of the insert head is shown in Figure 4.2:

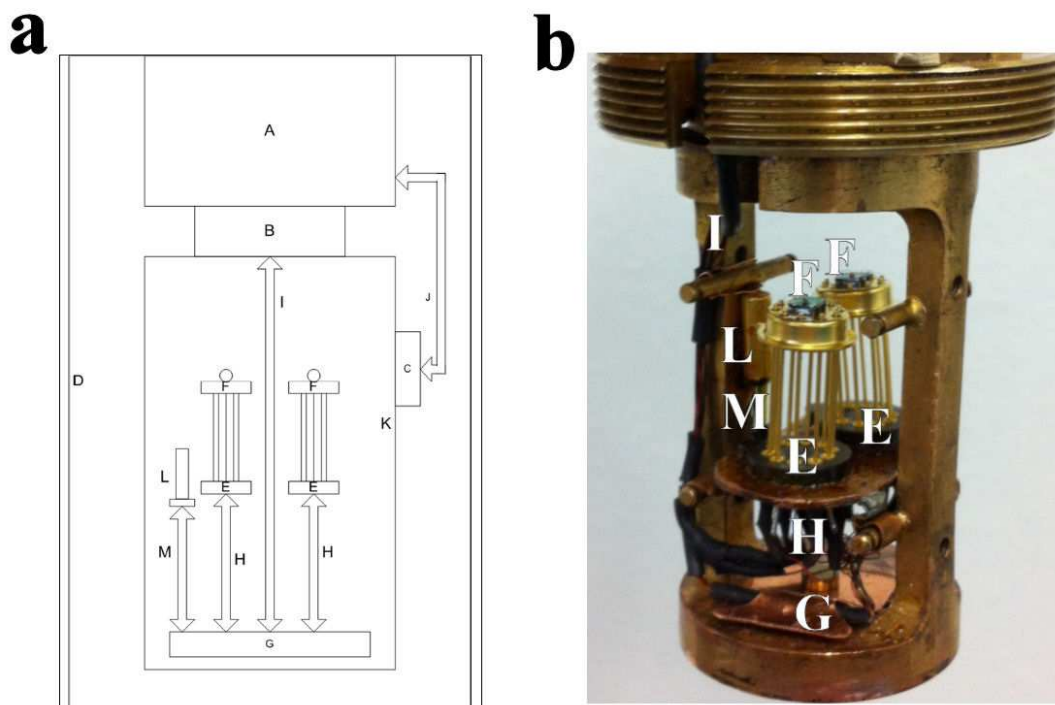


Figure 4.2 - a) Insert head scheme: b) Experimental sample space. Legend: A) Body of the insert; B) Connector, enabling the head to be detached from the insert body and easily handled; C) Wiring connection to the heating cylinder; D) Vacuum cylinder; E) Calorimetry chip socket; F) Xensor microcalorimetry chips (see below); G) Soldering platform functioning as a thermal anchor for all the wiring inside the insert head; H) Wiring between the chip sockets and the soldering platform; I) Wiring from the soldering platform to the body of the insert; J) Wiring from the heating cylinder to the body of the insert; K) Heating cylinder; L) Carbon-glass temperature dependent resistor; M) Wiring from the resistor to the soldering platform;

4.2.2 Temperature control

All aspects of temperature control in the current setup are done by a Lakeshore 331 Temperature Controller. This instrument measures the resistance of the carbon-glass temperature dependent resistor, placed next to the calorimetry chips and in thermal contact with the heating shield, using a 4-point measurement method. This resistance value is then converted into a temperature through a calibration table previously measured and displayed in figure 4.3. The determination of this table was itself performed in the early stages of the setup assembly, using a calibrated Cernox thermometer from LakeShore Cryogenics.

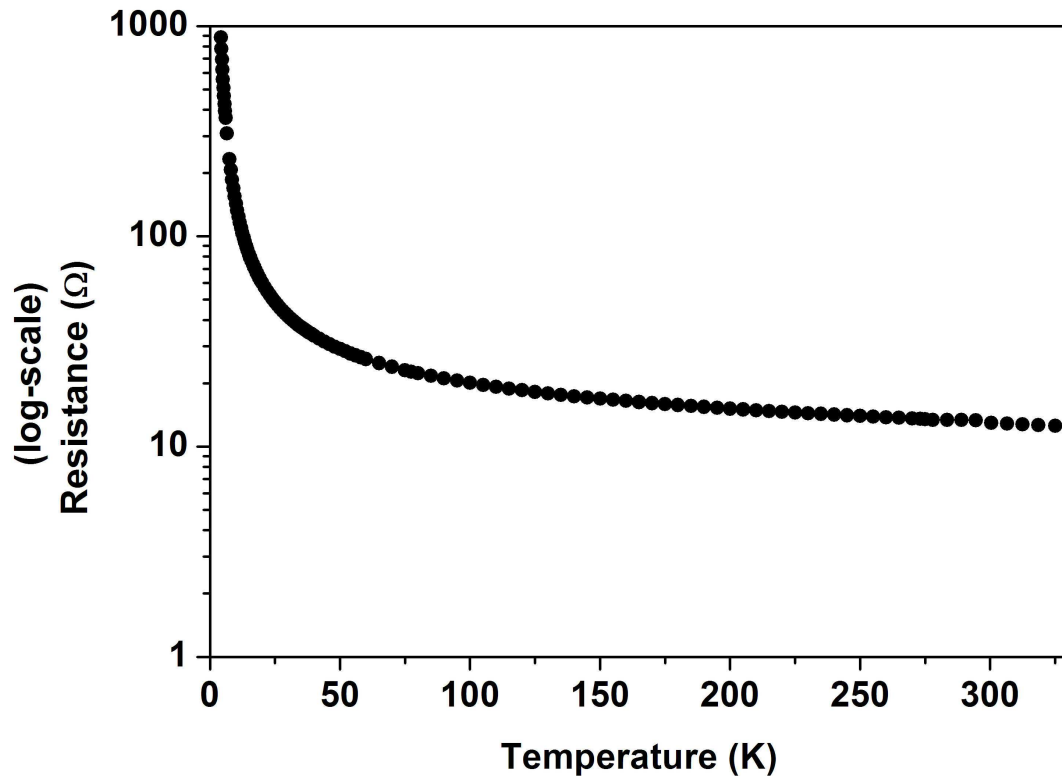


Figure 4.3 Resistance vs temperature for the carbon-glass temperature dependent resistor used to determine the temperature inside the sample space.

Furthermore, this temperature controller determines and supplies current to the heater by comparing the measured temperature with a set point temperature. As cooling is achieved passively by the simple contact of the insert with the LHe, this heater is the only active element in the temperature control.

4.2.3 Microcalorimetry chips

As the use of strong magnetic fields in ferromagnetic samples can give rise to high field gradients that can affect the measurement by moving or dislocating samples, we have decided to use small samples in the order of micrograms to minimize this effect. For this end we used two XEN-39328 microcalorimetry chips manufactured by the company Xensor Integration.

These chips consist of a thin 0.9×0.9 mm SiN membrane [17] with a sensitive thermopile and a heater. Given their small size, these chips have a high thermopile and heater accuracy. Detailed images of these chips can be observed in Figure 4.4a and 4.4b.

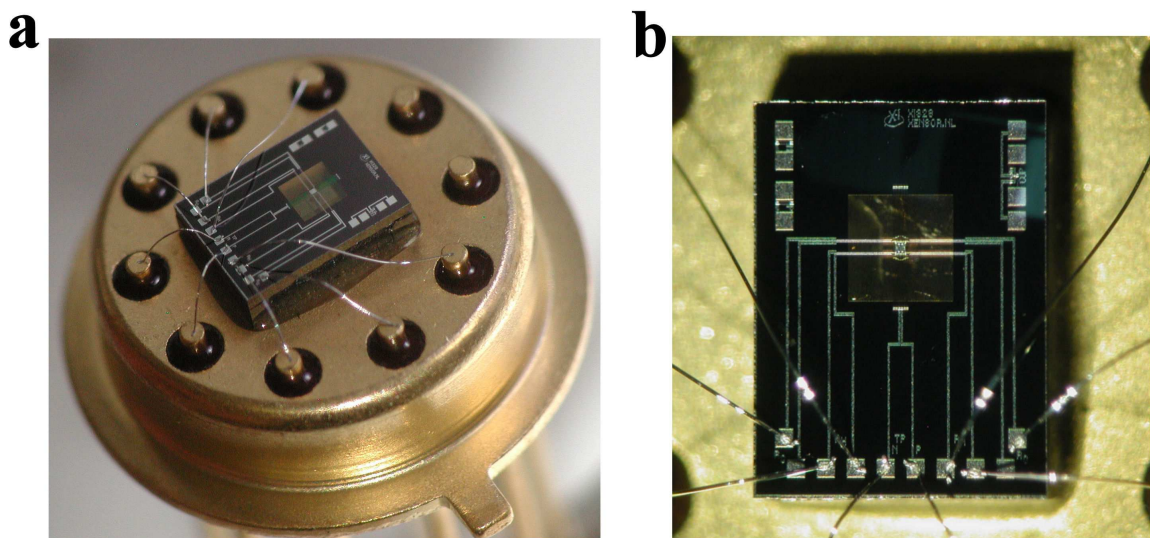


Figure 4.4 – XEN-39328 microcalorimetry chips used in the current setup; a) overall detailed view on the chip and frame; b) detailed view on the calorimetry chip itself.

Chip specifications are displayed in Table 4.1.

Table 4.1 - XEN-39328 chip manufacturer's specifications at 22 °C. These chips are largely similar to the older model XEN-39287 used in the earlier stages of the development of the current setup

Membrane dimensions	0.9x0.9 mm
Approximate thermopile sensitivity	2.0 mV K ⁻¹
Heating site dimensions (hotspot)	92x92 μm
Pins	TO-5
Heater resistance	1.2 kΩ
Heater resistance temperature coefficient	0.1 % K ⁻¹
Effective heat capacity (in air)	100 nJ K ⁻¹
Maximum heating voltage (in vacuum)	2.7 V
Membrane thermal resistance	50 – 100 kK W ⁻¹
Membrane thermal resistance temperature coefficient	0 % K ⁻¹
Thermopile resistance	30 kΩ

As is shown in Figure 4.2, in the current setup we use two of these chips: one loaded with a Cu reference and the other with our sample. In contrast with the single chip setups used by both Morrison *et al.* [10] and Minakov *et al.* [13], this two chip

setup was chosen in order to minimize any chip dependent issues that might interfere with our measurements. Assuming that the two chips used are equal in all aspects, and are under the same conditions, we can thus use the heat capacity ratio between them and disregard most of the chips' influence on the measured results, making our subsequent data analysis simpler. This approach eliminates the necessity of having to deal with the unknown Seebeck coefficient of the chip thermopiles [10], the temperature-dependent resistance of the chip heaters, and other bothersome calibrations often required for temperature scanning experiments.

To insure good thermal contact between the heaters on the chips, their sensors and the sample, Apiezon N and H greases are used, for low and high-temperature measurements respectively. This further prevents sample motion during chip handling and application of the external magnetic field.

The specific heat of Apiezon N grease has been studied extensively [18-21] and can easily be taken into consideration during the data analysis. This issue is further reduced due to the double chip setup, when the amount of grease in both chips is comparable.

4.2.4 External measurement and power supply equipment

The power supplied to the chips comes from a Keithley 2400 Source Meter. To measure and register the voltage output of the calorimetry chips' thermopiles a Keithley 2000 is used. This is equipped with a scanner card, enabling us to switch between different channels and measure different signals, thus simultaneously measuring both the reference and the sample chip.

The information supplied by the previous two modules and the Lakeshore temperature controller is then fed into a PC, via a GPIB bus, where the data is processed and analyzed via LabVIEW and MATLAB routines.

4.3 Measurement cycle

The specific heat in this setup can be determined by the so-called relaxation method. In this method, initially the sample and the chip are at the same temperature, T_1 . A current is then applied to the chip's heater, making the sample temperature rise to a new constant value, T_2 . Next, the current is cut and the sample relaxes back to its original temperature, in a relaxation time τ [22]. This cycle is achieved by supplying the chip heaters with a square wave from the Keithley 2400, and then, via the chips'

inbuilt thermopiles, measuring the temperature of the sample and reference sequentially with the Keithley 2000. To calculate one data point we need to measure both chips. Figure 4.5 shows the typical response for one relaxation period.

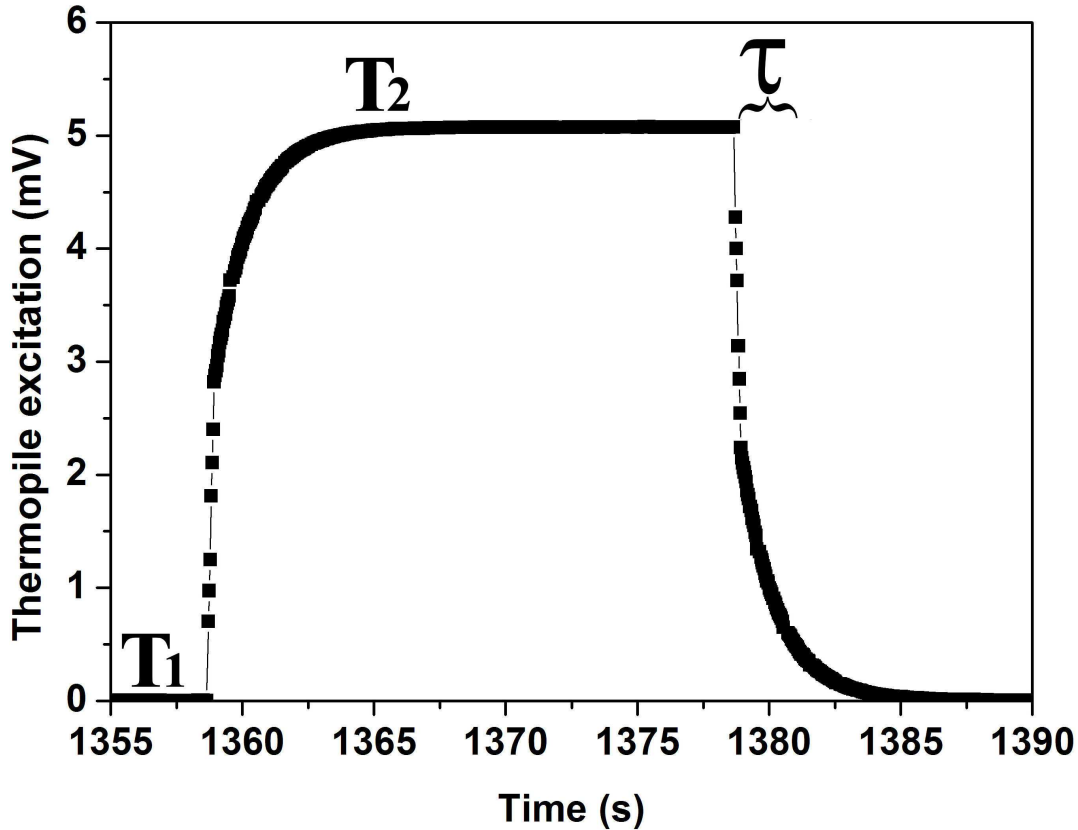


Figure 4.5 - Thermopile response to the square wave heater input used to perform a relaxation measurement.

The cooling curve has the following form:

$$V(t) = Ae^{-\frac{t}{\tau}} \quad (4.1)$$

The mentioned relaxation time is then calculated by taking the logarithm of the signal and performing a least-square fit for a straight line. The slope of this fit is equal to the inverse of the relaxation time τ . We can then calculate the heat capacity by the following simple expression:

$$C = \kappa\tau \quad (4.2)$$

where κ , the thermal conductivity:

$$\kappa = \frac{P}{T_2 - T_1} \quad (4.3)$$

and P is the power supplied to the chip.

4.4 Data management

A complete measurement taken with this set up is depicted in Figure 4.6.

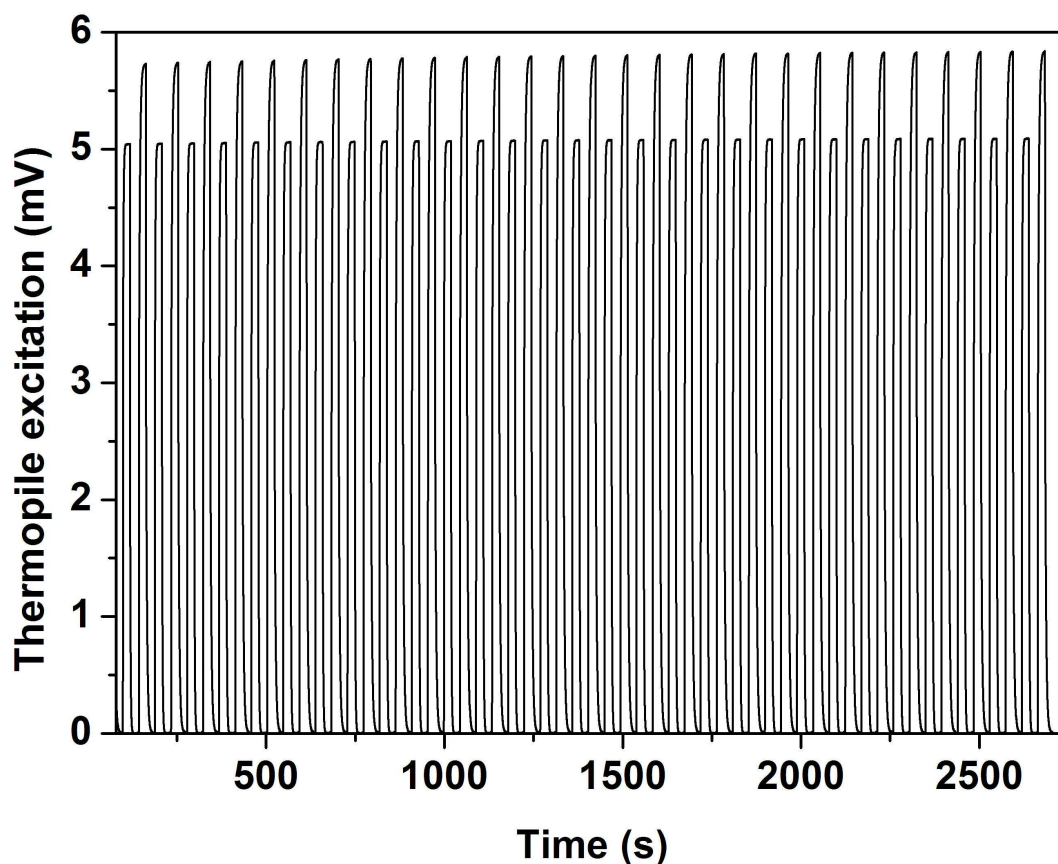


Figure 4.6 Specific heat data as acquired by the Keithley 2000. The alternating height of the relaxation cycles is due to the alternating readout between the sample and the reference chip.

The calculated relaxation is shown in Figure 4.7. For this calculation certain particularities of the measurement system need to be taken into consideration, such as an inbuilt instantaneous temperature jump that may occur in the sensor temperature readout of the microcalorimetry chips. To correct for this problem the fit is only

performed between two movable start and finish points, removing the initial points of each relaxation curve from our calculation.

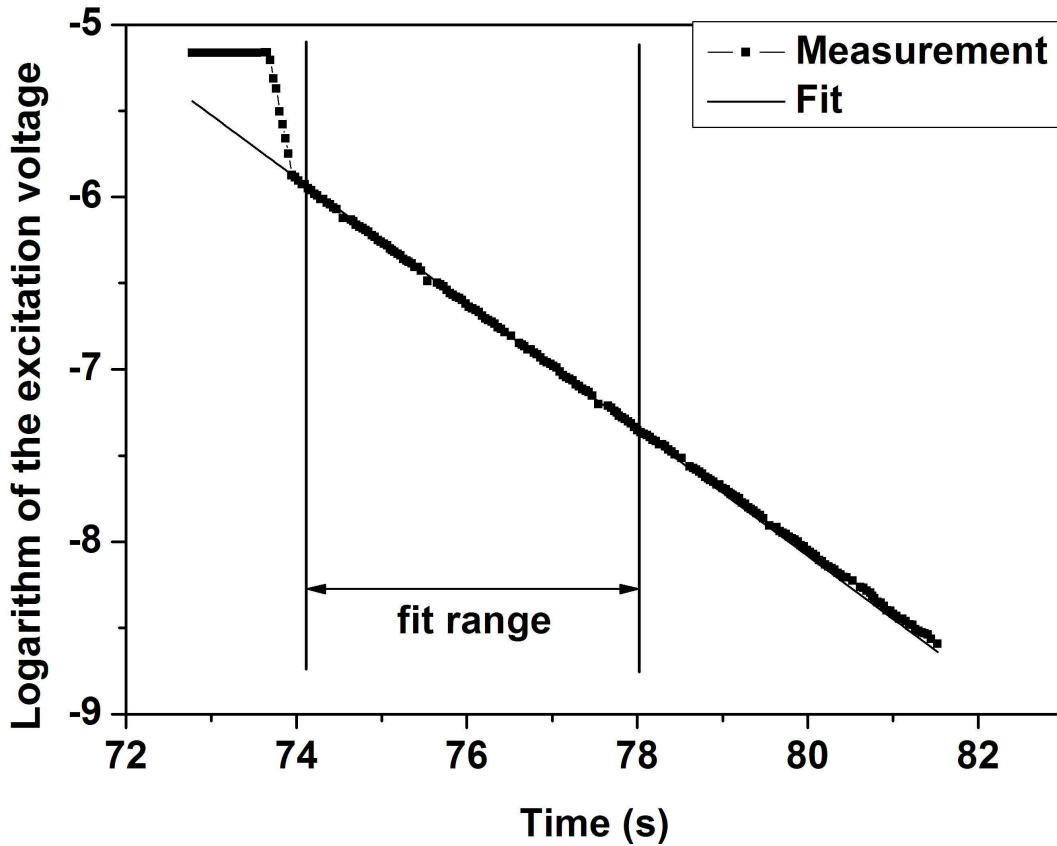


Figure 4.7 Linear fit of the logarithm of the thermopile output while relaxing.

From the calculated relaxation time and the initial voltage supplied by the Keithley 2400, the ratio of the total heat capacity between the two chips can be calculated. Knowing the masses and molar weight of both samples, together with the specific heat of the reference, this value can further worked until the heat capacity of the sample material is obtained, as displayed in Figure 4.8.

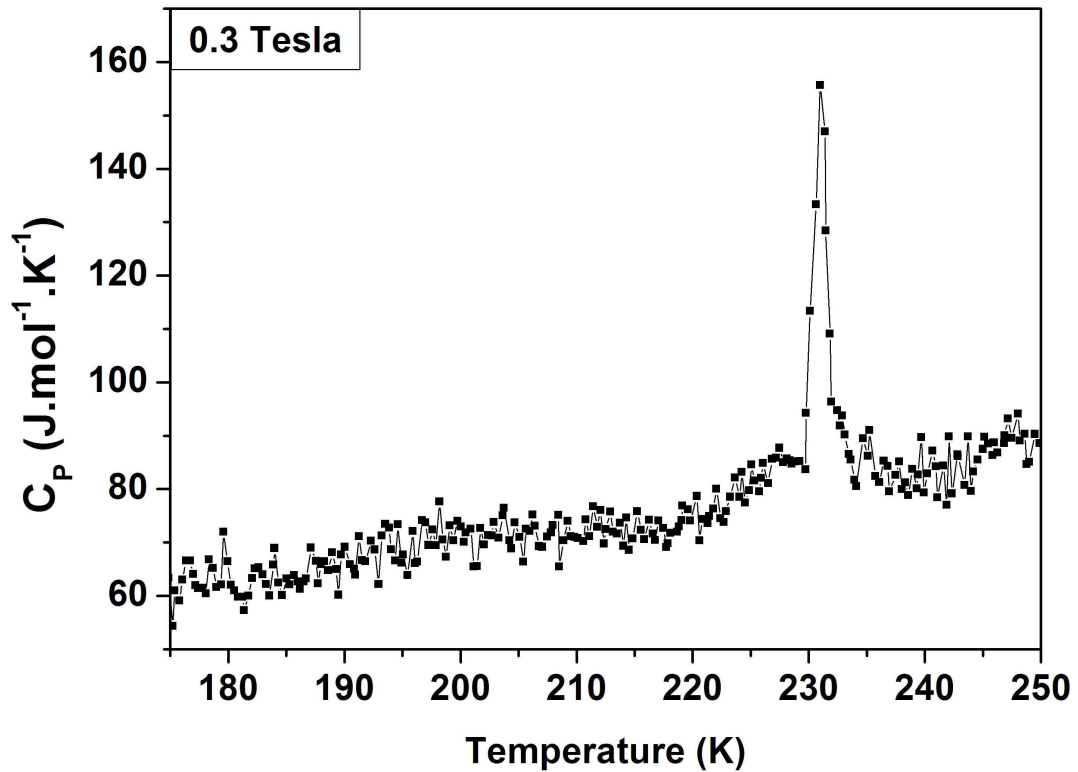


Figure 4.8 Isolated Fe_2P specific heat measurement over time for an applied field of 0.3 Tesla measured in this setup. The reference used was a Cu sample and its specific heat value was taken from ref. [23].

For this measurement the used reference was a Cu piece and the measured sample polycrystalline Fe_2P (this same sample is fully examined in Chapter 8). Their details can be found on Table 4.2.

Table 4.2 Details regarding the samples in the two chips used in the measurement displayed in Figure 4.6.

	Mass (mg)	Error (mg)	Grease (mg)	Error (mg)
Sample	0.22	0.02	Grease mass was too small to be registered by our balance, none the less we should consider a maximum value of 0.02 mg, the balance error.	
Reference	0.23	0.02		

4.5 Conclusion

A setup to measure the heat capacity of micrograms of sample has successfully been assembled using microcalorimetry chips from the company Xensor Integration. With this calorimeter it is possible to measure the specific heat capacities of samples in a magnetic field at various temperatures.

For this end we use the relaxation method where the heat capacity is calculated from the sample's relaxation time after the input of a square-wave to the chip's heaters.

This setup uses two microcalorimetry chips simultaneously to eliminate the need for thermopile calibration and concerns regarding the Seebeck coefficient in magnetic fields.

References

- [1] A.M. Tishin and Y.I. Spichkin, *The Magnetocaloric Effect and Its Applications*, Bodmin, MPG Books Ltd, 2003.
- [2] K. A. Gschneidner Jr, V. K. Pecharsky and A. O. Tsokol, *Rep. Prog. Phys.* 68 (2005) 1479.
- [3] Anders Smith, Christian R.H. Bahl, Rasmus Bjørk, Kurt Engelbrecht, Kaspar K. Nielsen and Nini Pryds, *Adv. Energy Mater.* 2 (2012) 1288.
- [4] Jordi Marcos, Fèlix Casanova, Xavier Batlle, Amílcar Labarta, Antoni Planes and Lluís Mañosa, *Rev. Sci. Instrum.* 74 (2003) 4768.
- [5] V. V. Korolev, A. S. Romanov and I. M. Aref'ev, *Russ. J. Phys. Ch.*, 80 (2006) 310.
- [6] Michaela Kuepferling, Carlo Paolo Sasso, Vittorio Basso and Laura Giudici, *IEEE T. Magn.* 43 (2007) 2764.
- [7] G. Porcari, F. Cugini, S. Fabbrici, C. Pernechele, F. Albertini, M. Buzzi, M. Mangia and M. Solzi, *Phys. Rev. B* 86 (2012) 104432.
- [8] Giacomo Porcari, *Magnetocaloric effect across first order transformations of energy conversion materials*, Università degli studi di Parma, (2013) PhD thesis, Chapter 3.
- [9] S. Jeppesen, S. Linderoth, N. Pryds, L. Theil Kuhn and J. Buch Jensen, *Rev. Sci. Instrum.* 79 (2008) 083901.
- [10] K. Morrison, Y. Miyoshi, J. D. Moore, A. Barcza, K. G. Sandeman, A. D. Caplin and L. F. Cohen, *Phys. Rev. B* 78 (2008) 134418.

- [11] K. Morrison, J. D. Moore, K. G. Sandeman, A. D. Caplin, and L. F. Cohen, *Phys. Rev. B* 79 (2009) 134408.
- [12] A. A. Minakov, S.A. Adamovsky, C. Schick, *Thermochim. Acta* 432 (2005) 177.
- [13] A. A. Minakov, S. B. Roy, Y. V. Bugoslavsky and L. F. Cohen, *Rev. Sci. Instrum.* 76 (2005) 043906.
- [14] A. A. Minakov, A.W. van Herwaarden, W. Wien, A. Wurm, C. Schick, *Thermochim. Acta* 461 (2007) 96.
- [15] S. A. Adamovsky, A.A. Minakov, C. Schick, *Thermochim. Acta*, 402 (2003) 55.
- [16] Mikhail Merzlyakov, *Thermochim. Acta* 403 (2003) 65.
- [17] Sander van Herwaarden, *Gas Nanocalorimeters, Xensor Integration*, 2010.
- [18] J. G. Bunting, T. Ashworth and H. Steeple, *Cryogenics* 9 (1969) 385.
- [19] W. Schnelle, J. Engelhardt and E. Gmelin, *Cryogenics* 39 (1999) 271.
- [20] M. Wun and N. E. Phillips, *Cryogenics* 15 (1975) 36.
- [21] H. J. Schink and H.v. Lohneysen, *Cryogenics* 21 (1981) 591.
- [22] Nhu Hoa Kim-Ngan, *Magnetic Phase Transitions in NdMn₂ and Related Compounds*, Universiteit van Amsterdam, (1993) PhD thesis, Chapter 4
- [23] N. Dass, *J. Phys. Soc. Japan* 28 (1970) 251.

Chapter 5

Magnetostructural study of the $(\text{Mn,Fe})_3(\text{P,Si})$ system

5.1 Introduction

Previous material studies performed on the $(\text{Mn,Fe})_2(\text{P,Si})$ and $(\text{Mn,Fe})_{1.95}(\text{P,Si})$ systems [1, 2] have demonstrated a clear experimental difficulty in achieving pure single phase samples in this family of compounds. In the above mentioned references a residual amount of a cubic $(\text{Mn,Fe})_3\text{Si}$ phase was consistently observed in samples belonging to these two systems.

The motivation of the research presented in the current chapter was to explore the magnetic behavior of this secondary phase, generalized as the $(\text{Mn,Fe})_3(\text{P,Si})$ system, and evaluate its magnetocaloric potential.

This study has made it possible to outline the basic properties and assemble a magnetostructural phase diagram for the $(\text{Mn,Fe})_3(\text{P,Si})$ system, which is greatly valuable for its understanding and may yet open further horizons to those areas where both the $(\text{Mn,Fe})_3\text{Si}$ and $(\text{Mn,Fe})_3\text{P}$ systems have been studied in the past. Even though several of its compositional areas presented significant magnetization shifts, none of these were sufficiently large or sharp to make this system appropriate for magnetic cooling purposes.

5.2 Material overview

5.2.1 The $\text{Mn}_{3-x}\text{Fe}_x\text{Si}$ system

The $\text{Mn}_{3-x}\text{Fe}_x\text{Si}$ system has been studied both for its properties as an itinerant-electron antiferromagnet and as a half-metallic ferromagnet (HMF), at different compositional ranges. In its antiferromagnetic phase (Mn rich) it has been studied in the context of spin-wave excitation by means of neutron inelastic scattering [3]. As a HMF (Fe rich), having a band gap in one spin at the Fermi level whereas the other spin is strongly metallic, a complete spin polarization of the conduction electrons at the Fermi level is found, which is of interest in the field of spintronics [4].

The Mn_3Si compound crystallizes in the cubic $Fm\bar{3}m$ structure (AlFe_3 prototype) [3, 5, 6]. It is a bcc structure with two distinct Mn atom sites, A (MnI) and B/B' (MnII) [3, 5], as shown in Figure 5.2a. The reported magnetic moments are $0.19 \mu_B$ and $1.7 \mu_B$ [3, 5-7] for MnI and MnII, respectively. This compound orders antiferromagnetically below a Néel Temperature (T_N) of about 25 K, being paramagnetic above this temperature [3, 5-7].

Fe_3Si crystallizes in the same cubic $Fm\bar{3}m$ structure as Mn_3Si . The Fe atoms on the A site have a magnetic moment of $2.4 \mu_B$, while those on the B/B' site exhibit a magnetic moment of $1.2 \mu_B$ [8, 9]. The moments are ordered ferromagnetically at room temperature with a T_C of about 840 K [10, 16].

The whole pseudo-binary $\text{Mn}_{3-x}\text{Fe}_x\text{Si}$ system maintains the same stable $Fm\bar{3}m$ crystal structure for $0 < x < 3$. A minor secondary phase, either tetragonal or hexagonal, has been reported by S. Yoon *et al.* for Mn contents between 1.8 and 3 [12].

Starting from the Fe_3Si compound, with increasing Mn content, T_C drops linearly from 840 to approximately 300 K at a composition $\text{Mn}_{0.7}\text{Fe}_{2.3}\text{Si}$ [16, 12]. From this composition on a transition between ferromagnetic and antiferromagnetic order is found around 50 K [13]. This ferromagnetic state was described by Miki *et al.* as canted ferromagnetism [14]. This second transition eventually fades away at a composition of $\text{Mn}_{1.8}\text{Fe}_{1.2}\text{Si}$. In this interval T_C decreases at a much slower rate, reaching a value of 65 K at the above mentioned composition, as can be observed in Figure 5.1. Further addition of Mn from this point on triggers an antiferromagnetic behavior in this system. T_N drops smoothly from the last value of T_C until it reaches 25 K at Mn_3Si [14].

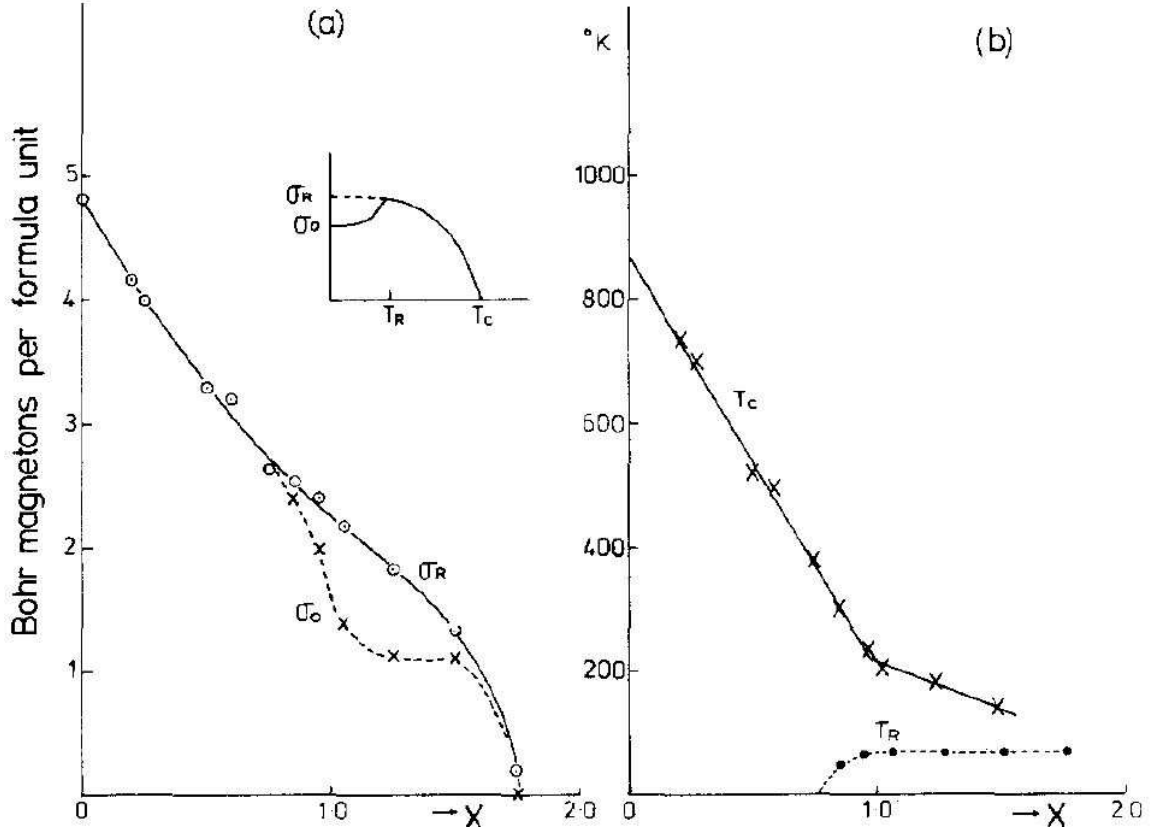


Figure 5.1 (a) Saturation magnetization and (b) transition temperature variation with composition for the $\text{Fe}_{3-x}\text{Mn}_x\text{Si}$ system. The insert in (a) represents the Typical magnetization temperature curve in the range $0.7 < x < 1.8$. In (b) T_R stands for the second transition between the antiferromagnetic and canted ferromagnetic phase [11].

Regarding site preferences of the Fe and Mn atoms: in the parent compound Fe_3Si , the addition of Mn atoms preferably occupies the A sites, for compositions between 0 and 0.75. Within this interval, T_C continuously decreases from 840 to 370 K, while the magnetic moment of this site remains relatively constant, meaning that Fe(A) and Mn(A) atoms exhibit approximately the same moment [13]. For compositions above 0.75 the Mn atoms begin to occupy half of the B sites, so that the B sublattice can be split into B and B' sites [15]. The A sites are only found to be completely filled for a Mn content above 1.5 [13].

For Mn composition between 0.75 and 1.8, we then find the already mentioned canted ferromagnetism displaying a transition between canted ferromagnetic and antiferromagnetic states [13, 14].

5.2.2 The $\text{Mn}_{3-x}\text{Fe}_x\text{P}$ system

As far as practical application goes, this system has been studied in the context of nuclear-reactor material research, mostly the Fe_3P compound [16]. Beyond this it does not seem to provoke much interest outside the academic sphere.

Both the Mn_3P and Fe_3P compounds crystallize in the tetragonal $I\bar{4}$ structure [17, 18] (Ni_3P prototype), Figure 5.2b, with three different Mn/Fe sites [18]. Mn_3P is an antiferromagnet with a T_N of about 115 K and a magnetic moment of $1.69 \mu_B$ per Mn atom [19]. Fe_3P on the other hand is a ferromagnet with a T_C of about 700 K and a magnetic moment of $1.89 \mu_B$ per Fe atom [19].

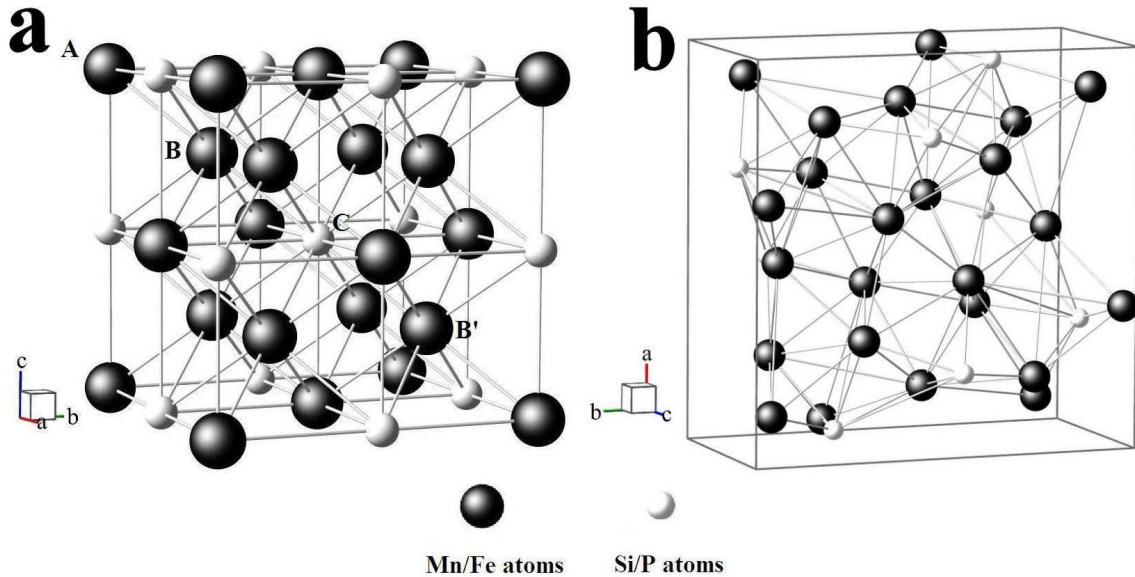


Figure 5.1 a) The Mn_3Si $Fm\bar{3}m$ cubic structure, showing the MnI atoms on the A sites, the MnII atoms on the B/B' sites and the Si atoms on the C sites; b) The Mn_3P and Fe_3P $I\bar{4}$ tetragonal structure

The $\text{Mn}_{3-x}\text{Fe}_x\text{P}$ system maintains the same $I\bar{4}$ tetragonal crystal structure for $0 < x < 1$ [20, 21] and again for $2.2 < x < 3$ [19, 21], approximately. In the gap between these two intervals an orthorhombic structure is reported [21]. In this structure the moments order antiferromagnetic with a relatively constant T_N of about 340 K [21].

Goto *et al.* [21], having studied the magnetic properties of $\text{Fe}_{3-x}\text{M}_x\text{P}$, with $M = \text{Cr}, \text{Mn}, \text{Co}, \text{Ni}$ and report that this orthorhombic structure only occurred in the Mn

compounds, all the other systems maintained the $I\bar{4}$ tetragonal structure for the studied compositions.

5.3 Sample preparation and characterization

All produced samples belonging to the $(\text{Mn,Fe})_3(\text{Si,P})$ system were prepared from the appropriate amounts of 99+% iron powder, 99.99% granular silicon, 99% red phosphorous powder and 99.9% manganese chips reduced at 600 °C under a hydrogen atmosphere in order to remove oxides.

The samples were ball milled as described in Chapter 3, then compacted into 10 mm pellets with a pressure of 150 kgf/cm² and sealed into quartz tubes with an atmosphere of 200 mbar of argon. Finally these were annealed in a vertical resistive furnace for 100 hours at 950 °C and quenched in water at room temperature.

This procedure was selected to be appropriate for all possible composition variations of the $(\text{Mn,Fe})_3(\text{Si,P})$ system. The use of an arc melting furnace (a common procedure for the production of samples belonging to the $\text{Mn}_{3-x}\text{Fe}_x\text{Si}$ system [10, 12, 22]) was found to be unsuitable for the production of samples containing Phosphorous.

Magnetic and DSC measurements were performed on all samples and homogeneity and crystal structure was checked using X-ray diffraction as described in Chapter 2.

5.4 Results and discussion

5.4.1 Structural results

All the structural information regarding the $\text{Mn}_{3-x}\text{Fe}_x\text{Si}$ and $\text{Mn}_{3-x}\text{Fe}_x\text{P}$ systems mentioned in section 5.2 was confirmed.

The $Fm\bar{3}m$ cubic structure of the Mn_3Si and Fe_3Si was found to exist up to the Phosphorous substitution of $\text{Mn}_3\text{Si}_{0.8}\text{P}_{0.2}$ on the Mn rich side of the diagram and up to $\text{Fe}_3\text{Si}_{0.4}\text{P}_{0.6}$ on the Fe rich side. The secondary tetragonal or hexagonal phases reported by Yoon *et al.* [12] in cubic samples with a Mn content above 1.8 were not observed. Such a result may be a direct consequence of the different sample preparation procedures used in the current chapter and those used by the mentioned authors, namely: arc melting, annealing for 24 hours at 800 °C, and quenching into cold water.

On the Mn rich side, the $I\bar{4}$ tetragonal phase, was found to exist up to a composition of $\text{Mn}_3\text{Si}_{0.8}\text{P}_{0.2}$. On the Fe rich side this structure was found to exist up to the Si substitution of $\text{Fe}_3\text{Si}_{0.4}\text{P}_{0.6}$.

The diffraction data from samples displaying the orthorhombic phase was found to be consistent with the $Pmmm$ space group, Figure 5.3a. This structure was also found for the $\text{MnFe}_2\text{Si}_{0.5}\text{P}_{0.5}$ composition.

A fourth crystal structure, consistent with the hexagonal $P6/mmm$ space group, was found for values in the range of $0.2 < x < 1.95$ and $0.2 < y < 0.9$, for $\text{Mn}_{3-x}\text{Fe}_x\text{Si}_{1-y}\text{P}_y$, as shown in Figure 5.3b. It is possible that this structure is the same as the one observed by Yoon *et al.* [12] as a secondary phase in cubic samples with Mn content above 1.8, but, as these authors did not provide any additional information regarding this secondary phase, we cannot confirm this hypothesis. The detection of this structure in this system can be said to be a complete novelty and has never been reported in literature.

The lattice constant a for the cubic phase has been found to decrease with the Fe content, ranging from 5.72 Å for Mn_3Si to 5.65 Å for Fe_3Si , in excellent accordance with the values found by Yoon *et al.* [12]. However, the substitution of P seems to promote an increases in the lattice parameter a , as both for $\text{Fe}_3\text{Si}_{0.8}\text{P}_{0.2}$ and $\text{Fe}_3\text{Si}_{0.5}\text{P}_{0.5}$ a value for a of about 5.66 Å was found.

The a and c lattice constants in the Mn-rich tetragonal phase is also in good accordance with the literature [20, 21], as both decrease with increasing Fe content. Si substitution increases both a and c , as $a=9.179$ Å and $c=4.568$ Å for Mn_3P while $a=9.183$ Å and $c=4.607$ Å for $\text{Mn}_3\text{Si}_{0.2}\text{P}_{0.8}$.

On the Fe-rich tetragonal phase, values $a=9.104$ Å and $c=4.4631$ Å were found for the Fe_3P compound, in accordance with literature [19, 21]. We were unable to establish whether the evolution of the lattice parameter with Mn substitution in this compositional area. The presence of an orthorhombic secondary phase in our samples, prevents us from achieving a good fit of our X-ray diffraction patterns. However, it has been determined that Si substitution strongly increases both lattice parameters. The composition of $\text{Fe}_3\text{Si}_{0.2}\text{P}_{0.8}$ shows a lattice parameters of an $a=9.1168$ Å and $c=4.4782$ Å.

The lattice parameters of the orthorhombic phase were found to be slightly smaller than those reported by Goto *et al.* [21], with $a = 8.9456$ Å, $b = 8.0079$ Å and $c = 4.3368$ Å for the $\text{Mn}_{1.5}\text{Fe}_{1.5}\text{P}$ compound. Due to the presence of secondary phases,

belonging to both the Mn and the Fe rich tetragonal phase and the hexagonal phase, we were able to make a good fitting of our other orthorhombic samples.

The hexagonal phase, for $\text{Mn}_{2.5}\text{Fe}_{0.5}\text{Si}_{0.5}\text{P}_{0.5}$, presents values of $a=8.83 \text{ \AA}$ and $c=10.89 \text{ \AA}$. The values decrease for increasing Fe content, arriving at an $a=8.77 \text{ \AA}$ and $c=10.64 \text{ \AA}$ for $\text{Mn}_{1.4}\text{Fe}_{1.6}\text{Si}_{0.5}\text{P}_{0.5}$. X-ray diffraction fitting for samples with a higher Fe content than 1.6 was found to be unreliable, as these samples presented a larger amount of secondary phases, belonging to cubic and orthorhombic structures. The same problem occurred for our samples with other Si/P ratios than the presented 0.5/0.5.

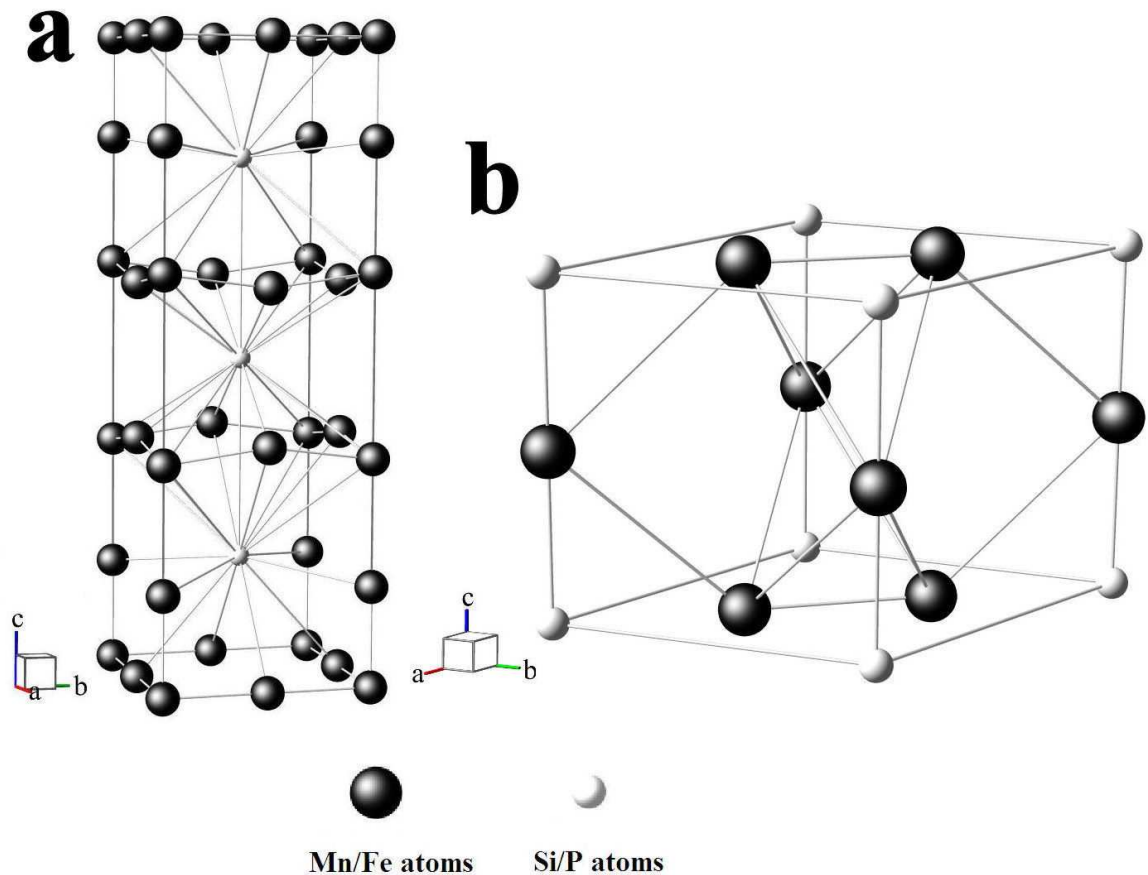


Figure 5.3 a) Pmmm orthorhombic structure of the $\text{Mn}_{3-x}\text{Fe}_x\text{P}$ (for values of x between 1 and 2, approximately); b) P6/mmm hexagonal structure of the $\text{Mn}_{3-x}\text{Fe}_x\text{Si}_{1-y}\text{P}_y$ (for $0.2 < x < 2.0$ and $0.2 < y < 0.9$)

The borders between the various structural phases in this system were found to be significantly influenced by the annealing temperature used in their production. Having tested various annealing temperatures on a set of $\text{MnFe}_2\text{Si}_{0.5}\text{P}_{0.5}$ samples (displaying cubic, hexagonal and orthorhombic phases, see Table 5.1) it was found that the hexagonal phase is promoted for increasing annealing temperature, while the cubic

phase was partially suppressed. The orthorhombic phase also appears to increase with temperature, but not strongly.

5.4.2 Magnetic results

All of the samples belonging to the *Pmmm* orthorhombic structure, in accordance with the results from Goto *et al.* [21], were found to be antiferromagnetic.

The novel hexagonal phase, similarly to the cubic phase, was found to exhibit a Ferromagnetic-Paramagnetic transition above an Fe content of 1.2. This transition, like those present in cubic and tetragonal phases of this system, also presents the characteristics of a second order phase transition.

On all border regions samples were found to exhibit multiple phases. In fact rigid borders or discontinuities between different phases aren't observed. What was found were relatively wide bands where the bordering phases coexist. Border lines can only be estimated through the analysis of phase fractions on each sample. However, by taking into consideration magnetic measurements, a much clearer monitoring of this border may be obtained.

The border between the orthorhombic and tetragonal phases was mapped through the influence of the Si content on the magnetic behavior of the sample, as there is a very clear difference between the antiferromagnetic orthorhombic phase and the ferromagnetic tetragonal phase (Figure 5.4).

Assuming that the magnetization of the (Fe rich) ferromagnetic tetragonal phase decreases linearly with Mn content, through extrapolation of the measured values of magnetization at 5 K we can then estimate the percentage of the different phases present in our samples.

At 5 K we found for our $\text{Mn}_{0.5}\text{Fe}_{2.5}\text{Si}_{0.2}\text{P}_{0.8}$ and $\text{Mn}_{0.6}\text{Fe}_{2.4}\text{Si}_{0.2}\text{P}_{0.8}$ samples a magnetization of $72.78 \text{ Am}^2/\text{kg}$ and $61.19 \text{ Am}^2/\text{kg}$, respectively. For a linear extrapolation an estimated value of around $49.6 \text{ Am}^2/\text{kg}$ should be expected for $\text{Mn}_{0.7}\text{Fe}_{2.3}\text{Si}_{0.2}\text{P}_{0.8}$. Instead we find a value of $17.52 \text{ Am}^2/\text{kg}$, showing that this sample is now predominantly antiferromagnetic. Through simple calculus we can then assume that our $\text{Mn}_{0.7}\text{Fe}_{2.3}\text{Si}_{0.2}\text{P}_{0.8}$ sample is made up of about 35% of ferromagnetic tetragonal phase and 65% antiferromagnetic orthorhombic phase.

This method of phase estimation, however useful, can only be used on borders between structures with a distinctly different magnetic behavior.

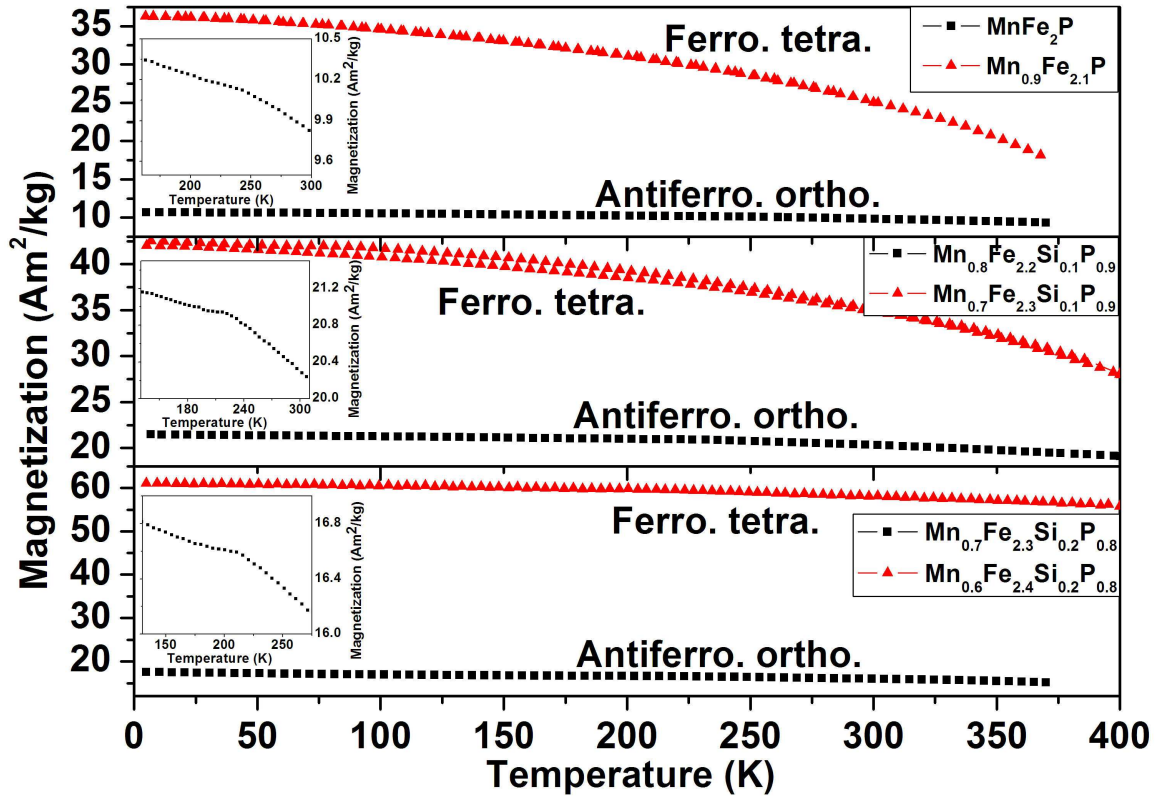


Figure 5.4 Magnetization versus temperature plots revealing the influence of Si content on the magnetic behaviors of the compositions on both sides of the border between the orthorhombic and tetragonal phases, taken with 1 Tesla of applied magnetic field. Inserts: detail on the magnetization curve of the aniferromagnetic orthorhombic samples, revealing the characteristic bump of an antiferromagnetic transition.

The temperature-induced transition from antiferromagnetism to canted ferromagnetism in compounds on the Si rich side of the structure diagram has been found to be completely independent of any compositional or magnetic field change, maintaining a relatively constant temperature of about 50 K between a Mn content of 1.8 and 1. Below this composition range it rapidly decreases until it is no longer observable at a Mn content of 0.6, a result also observed by Yoon *et al.* [11, 12]. The addition of P has proven to reduce the overall magnetic moment of the sample and widen the already broad second order phase transition between the ferromagnetic and paramagnetic phases, resulting in an increase in T_C , as seen on Figure 5.5. This effect is probably due to the increase in the lattice parameters by P substitution.

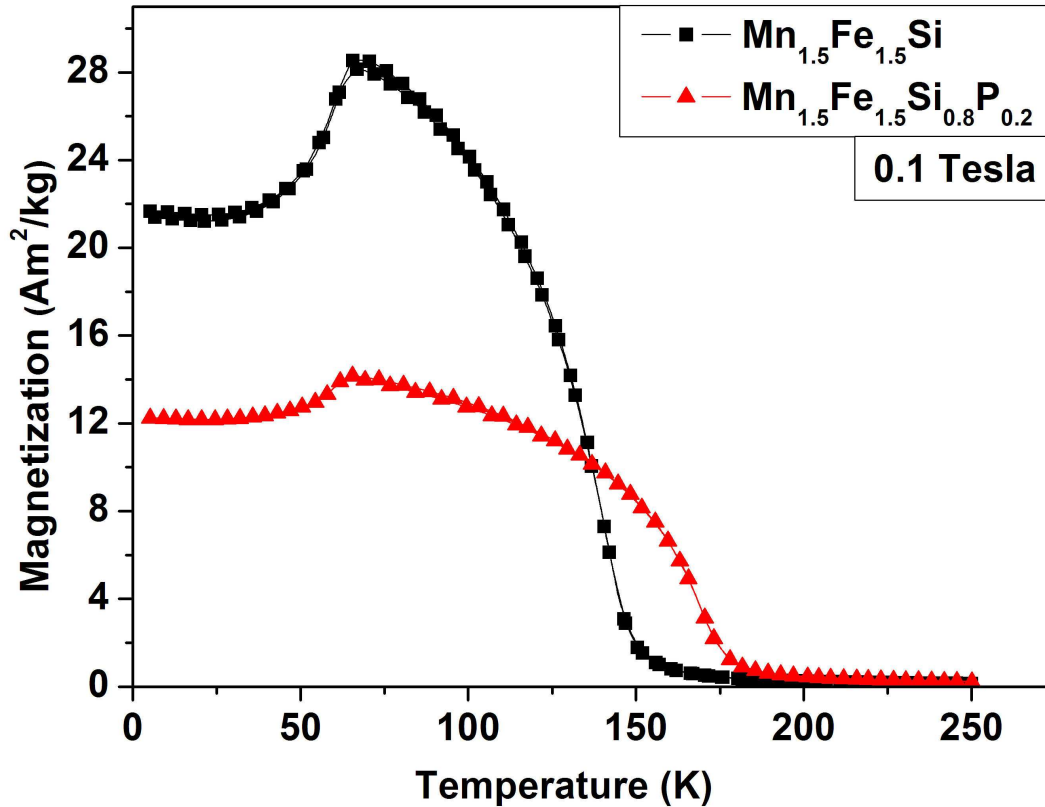


Figure 5.5 Magnetization versus temperature plot revealing the influence of P addition to the canted ferromagnetic phase of the $(\text{Mn,Fe})_3(\text{Si,P})$ system

An analysis of the temperature dependence of the magnetization for $\text{Mn}_{3-x}\text{Fe}_x\text{Si}$ samples, with $2 < x < 2.5$, revealed an unusual magnetic behavior. Instead of a continuous increase in magnetization with increasing Fe content, abrupt jumps in magnetization were clearly observed in Figure 5.6. This result can be partially explained by site preference of the Mn and Fe atoms described in section 5.2.1.

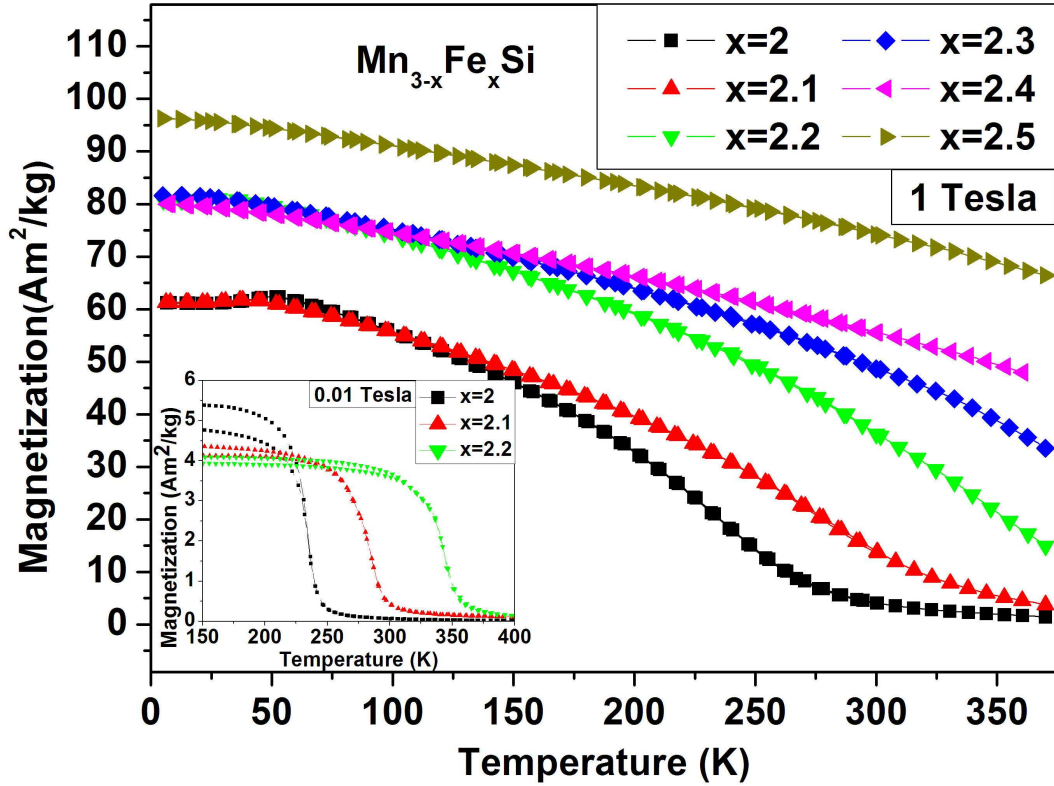


Figure 5.6 Magnetization versus temperature plot for $\text{Mn}_{3-x}\text{Fe}_x\text{Si}$, with x between 2 and 2.5, revealing the possible effects of the site preference of Mn and Fe atoms described in section 2.1 in magnetization. Insert: magnetization versus temperature measurements for low magnetic fields (0.01 T), revealing the change in T_C with Fe content.

5.5 The $(\text{Mn,Fe})_3(\text{Si,P})$ magnetostructural phase diagram

By compiling all the data from our X-ray diffraction patterns, magnetization measurements and DSC measurements, together with literature data from [12], [14], [19], [20] and [21], we can construct the magnetostructural phase diagram of the $(\text{Mn,Fe})_3(\text{Si,P})$ system shown in Figure 5.7. Details regarding the samples can be consulted in Table 5.1.

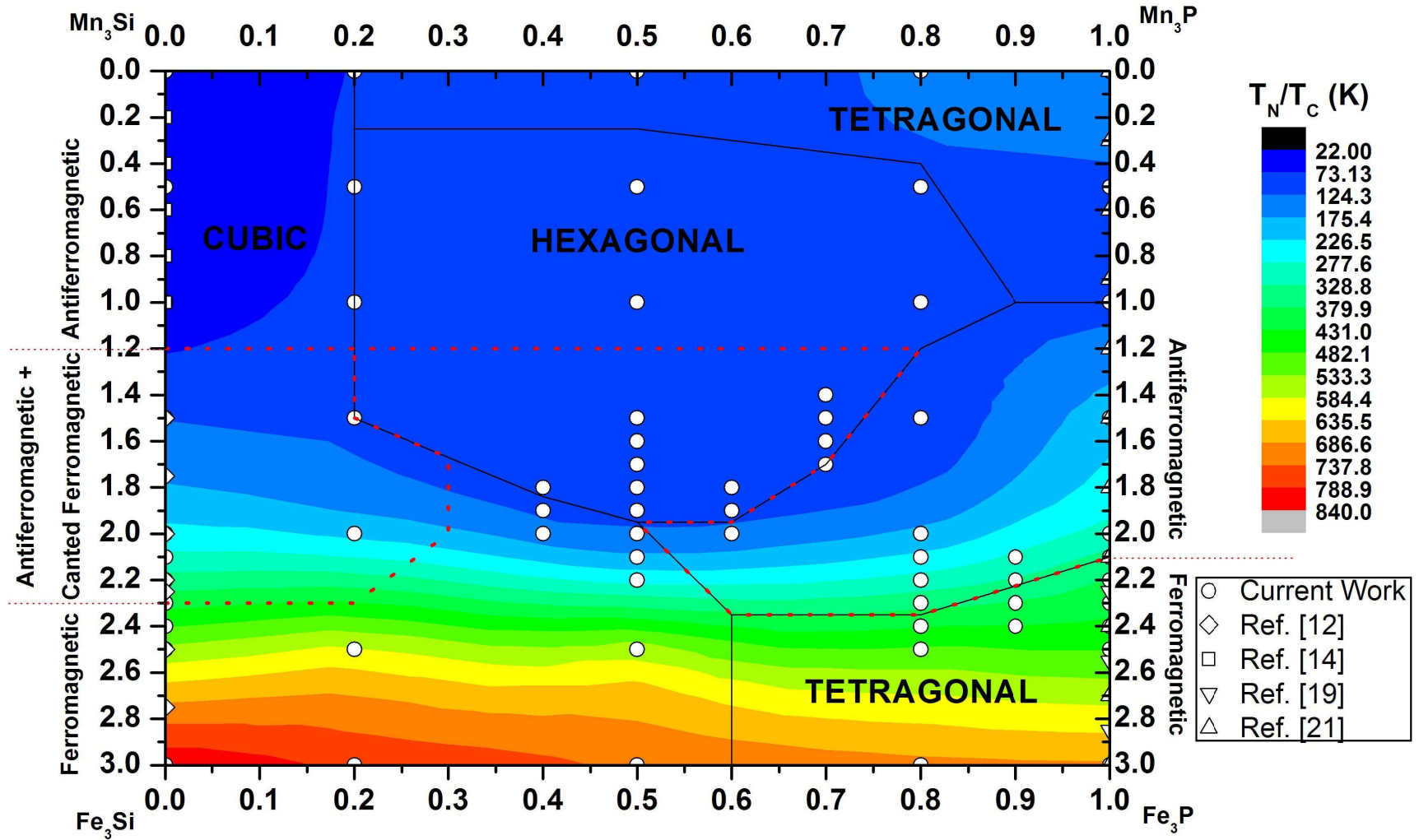


Figure 5.7 Magnetostructural phase diagram of the $(\text{Mn,Fe})_3(\text{Si,P})$ system, revealing the compositional areas of all the different crystal structures described in the current chapter and their magnetic behaviors at room temperature, for an annealing temperature of 950 °C. The color code refers to transition temperatures (T_N for the antiferromagnetic samples and T_C for the ferromagnetic samples). In the canted ferromagnetic phase area (referred to in this diagram as the “Antiferromagnetic + canted ferromagnetic” area), only the values of T_C have been inserted in the diagram, seeing as T_N here is relatively constant. It should be noted that all border lines presented are only estimates made through the analysis of phase fractions on each sample.

5.5.1 Overall diagram description

The Mn_3Si compound orders in the cubic $\text{Fm}\bar{3}\text{m}$ structure and is an antiferromagnet below a T_N of about 25 K and paramagnetic above this temperature. This behavior is maintained for P substitutions up to 0.2, where we find the tetragonal $\overline{I4}$ structure. This structure is then observed until the full substitution of Si by P, in the Mn_3P compound, with an increase in T_N up to 115 K for Mn_3P .

With increasing Fe substitution the cubic structure maintains its border along the $\text{Mn}_{3-x}\text{Fe}_x\text{Si}_{0.8}\text{P}_{0.2}$ line and displays a slow increase in T_N until a Fe content of 1.2. The tetragonal phase, however, is no longer observed at an Fe substitution of only 0.5. Instead, the hexagonal structure, consistent with the $P6/mmm$ space group, is detected. This structure is only present in the P interval between 0.2 and 0.9, bordered by the cubic phase of the Si rich side and by the tetragonal phase on the P rich side. It also exhibits antiferromagnetic behavior up to the Fe content of 1.2.

The T_N of both the hexagonal and the tetragonal structures also demonstrates a slow increase with Fe content.

At an Fe content of 1, on the P rich side of the diagram, the orthorhombic structure is observed. This structure appears to be consistently antiferromagnetic with a relatively constant T_N of 340 K, and is observed as far as the composition $\text{Mn}_{1.95}\text{Fe}_{1.05}\text{Si}_{0.5}\text{P}_{0.5}$.

At an Fe substitution of 1.2 both the cubic and hexagonal phases start to display ferromagnetic behavior. The T_C of both these phases display an increase with Fe content, although the cubic phase does so at a much higher rate.

From a Fe content of 1.2 up to 2.3 the cubic phase, besides the transition between ferromagnetic and paramagnetic phases, also displays a transition between antiferromagnetic and ferromagnetic phases, with a relatively constant T_N of 50 K. This behavior is described as canted ferromagnetism.

At an Fe content of 1.9 the hexagonal phase is no longer observed, being substituted by the cubic phase whose range can now be observed from 0 to 0.5 P substitution. From the Fe content of 1.9 to 2.35 the cubic phase borders the orthorhombic phase.

As we further increase the Fe content T_C of the cubic phase also continues to increase until it reaches its highest value of 840 K in the Fe_3Si compound.

On the P rich side, the orthorhombic phase reaches its border at an Fe content of about 2.1, and the tetragonal $I\bar{4}$ structure is once again observed until the complete substitution of Mn by Fe. In this area the tetragonal phase now displays a transition between a ferromagnetic and a paramagnetic state, with an Fe dependent increase in T_C until it reaches its maximum of 700 K in the Fe_3P compound.

In the Fe rich region the cubic and tetragonal phases display a border along the $Mn_{3-x}Fe_xSi_{0.4}P_{0.6}$ with $2.35 < x < 3$.

All paramagnetic-ferromagnetic phase transitions observed in this system present the characteristics of second order phase transitions.

Table 5.1 Details regarding crystal structure, magnetic behavior and transition temperatures for every sample produced for the current chapter

Sample Composition	Structure (at Room Temperature)	Magnetic Transitions	Trans. Temp. (K)
Mn_3Si	Fm3m	Antiferro-Para	27
$Mn_{2.5}Fe_{0.5}Si$	Fm3m	Antiferro-Para	24.5
Mn_2FeSi	Fm3m	Antiferro-Para	50
$Mn_{1.5}Fe_{1.5}Si$	Fm3m	Antiferro-Ferro-Para	62 \ 137
$MnFe_2Si$	Fm3m	Antiferro-Ferro-Para	50 \ 233
$Mn_{0.9}Fe_{2.1}Si$	Fm3m	Antiferro-Ferro-Para	40 \ 281
$Mn_{0.8}Fe_{2.2}Si$	Fm3m	Antiferro-Ferro-Para	30 \ 342
$Mn_{0.7}Fe_{2.3}Si$	Fm3m	Antiferro-Ferro-Para	12 \ 387
$Mn_{0.6}Fe_{2.4}Si$	Fm3m	Ferro-Para	397
$Mn_{0.5}Fe_{2.5}Si$	Fm3m	Ferro-Para	547
Fe_3Si	Fm3m	Ferro-Para	840
$Mn_3Si_{0.8}P_{0.2}$	Fm3m+ $I\bar{4}$	Antiferro-Para	79
$Mn_{2.5}Fe_{0.5}Si_{0.8}P_{0.2}$	Fm3m+P6/mmm	Antiferro-Para	82
$Mn_2FeSi_{0.8}P_{0.2}$	Fm3m+P6/mmm	Antiferro-Para	90
$Mn_{1.5}Fe_{1.5}Si_{0.8}P_{0.2}$	Fm3m+P6/mmm	Antiferro-Ferro-Para	58 \ 135
$MnFe_2Si_{0.8}P_{0.2}$	Fm3m	Antiferro-Ferro-Para	50 \ 173
$Mn_{0.5}Fe_{2.5}Si_{0.8}P_{0.2}$	Fm3m	Ferro-Para	657
$Fe_3Si_{0.8}P_{0.2}$	Fm3m	Ferro-Para	750
$Mn_{1.2}Fe_{1.8}Si_{0.6}P_{0.4}$	P6/mmm+Fm3m	Ferro-Para	102
$Mn_{1.1}Fe_{1.9}Si_{0.6}P_{0.4}$	P6/mmm+Fm3m+Pmmm	Ferro-Para	111

$\text{MnFe}_2\text{Si}_{0.6}\text{P}_{0.4}$	$\text{Fm}\bar{3}\text{m}+\text{P6}/\text{mmm}+\text{Pmmm}$	Ferro-Para	111
$\text{Mn}_3\text{Si}_{0.5}\text{P}_{0.5}$	$\text{I}\bar{4}$	Antiferro-Para	100
$\text{Mn}_{2.5}\text{Fe}_{0.5}\text{Si}_{0.5}\text{P}_{0.5}$	$\text{P6}/\text{mmm}$	Antiferro-Para	91
$\text{Mn}_2\text{FeSi}_{0.5}\text{P}_{0.5}$	$\text{P6}/\text{mmm}$	Antiferro-Para	107
$\text{Mn}_{1.5}\text{Fe}_{1.5}\text{Si}_{0.5}\text{P}_{0.5}$	$\text{P6}/\text{mmm}$	Ferro-Para	95
$\text{Mn}_{1.4}\text{Fe}_{1.6}\text{Si}_{0.5}\text{P}_{0.5}$	$\text{P6}/\text{mmm}$	Ferro-Para	85
$\text{Mn}_{1.3}\text{Fe}_{1.7}\text{Si}_{0.5}\text{P}_{0.5}$	$\text{P6}/\text{mmm}$	Ferro-Para	97
$\text{Mn}_{1.2}\text{Fe}_{1.8}\text{Si}_{0.5}\text{P}_{0.5}$	$\text{P6}/\text{mmm}+\text{Pmmm}$	Ferro-Para	108
$\text{Mn}_{1.1}\text{Fe}_{1.9}\text{Si}_{0.5}\text{P}_{0.5}$	$\text{P6}/\text{mmm}+\text{Pmmm}+\text{Fm}\bar{3}\text{m}$	Ferro-Para	125
$\text{MnFe}_2\text{Si}_{0.5}\text{P}_{0.5}$	$\text{Fm}\bar{3}\text{m}+\text{P6}/\text{mmm}+\text{Pmmm}$	Ferro-Para	127
$\text{Mn}_{0.9}\text{Fe}_{2.1}\text{Si}_{0.5}\text{P}_{0.5}$	$\text{Fm}\bar{3}\text{m}+\text{Pmmm}+\text{P6}/\text{mmm}$	Ferro-Para	164
$\text{Mn}_{0.8}\text{Fe}_{2.2}\text{Si}_{0.5}\text{P}_{0.5}$	$\text{Fm}\bar{3}\text{m}+\text{Pmmm}$	Ferro-Para	221
$\text{Mn}_{0.5}\text{Fe}_{2.5}\text{Si}_{0.5}\text{P}_{0.5}$	$\text{Fm}\bar{3}\text{m}+\text{I}\bar{4}$	Ferro-Para	667
$\text{Fe}_3\text{Si}_{0.5}\text{P}_{0.5}$	$\text{Fm}\bar{3}\text{m}+\text{I}\bar{4}$	Ferro-Para	697
$\text{Mn}_{1.2}\text{Fe}_{1.8}\text{Si}_{0.4}\text{P}_{0.6}$	$\text{P6}/\text{mmm}+\text{Pmmm}$	Ferro-Para	103
$\text{Mn}_{1.1}\text{Fe}_{1.9}\text{Si}_{0.4}\text{P}_{0.6}$	$\text{P6}/\text{mmm}+\text{Pmmm}$	Ferro-Para	127
$\text{MnFe}_2\text{Si}_{0.4}\text{P}_{0.6}$	$\text{Pmmm}+\text{Fm}\bar{3}\text{m}$	Antiferro-Para	84
$\text{Mn}_{1.6}\text{Fe}_{1.4}\text{Si}_{0.3}\text{P}_{0.7}$	$\text{P6}/\text{mmm}+\text{Pmmm}$	Ferro-Para	71
$\text{Mn}_{1.5}\text{Fe}_{1.5}\text{Si}_{0.3}\text{P}_{0.7}$	$\text{P6}/\text{mmm}+\text{Pmmm}$	Ferro-Para	75
$\text{Mn}_{1.4}\text{Fe}_{1.7}\text{Si}_{0.3}\text{P}_{0.7}$	$\text{Pmmm}+\text{P6}/\text{mmm}$	Ferro-Para	84
$\text{Mn}_{1.3}\text{Fe}_{1.7}\text{Si}_{0.3}\text{P}_{0.7}$	$\text{Pmmm}+\text{P6}/\text{mmm}$	Ferro-Para	88
$\text{Mn}_3\text{Si}_{0.2}\text{P}_{0.8}$	$\text{I}\bar{4}$	Antiferro-Para	133
$\text{Mn}_{2.5}\text{Fe}_{0.5}\text{Si}_{0.2}\text{P}_{0.8}$	$\text{P6}/\text{mmm}+\text{I}\bar{4}$	Antiferro-Para	117
$\text{Mn}_2\text{FeSi}_{0.2}\text{P}_{0.8}$	$\text{P6}/\text{mmm}$	Antiferro-Para	133
$\text{Mn}_{1.5}\text{Fe}_{1.5}\text{Si}_{0.2}\text{P}_{0.8}$	Pmmm	Antiferro-Para	78
$\text{MnFe}_2\text{Si}_{0.2}\text{P}_{0.8}$	$\text{Pmmm}+\text{I}\bar{4}$	Antiferro-Para	154
$\text{Mn}_{0.9}\text{Fe}_{2.1}\text{Si}_{0.2}\text{P}_{0.8}$	$\text{Pmmm}+\text{I}\bar{4}$	Antiferro-Para	233
$\text{Mn}_{0.8}\text{Fe}_{2.2}\text{Si}_{0.2}\text{P}_{0.8}$	$\text{Pmmm}+\text{I}\bar{4}$	Antiferro-Para	223
$\text{Mn}_{0.7}\text{Fe}_{2.3}\text{Si}_{0.2}\text{P}_{0.8}$	$\text{Pmmm}+\text{I}\bar{4}$	Antiferro-Para	213
$\text{Mn}_{0.6}\text{Fe}_{2.4}\text{Si}_{0.2}\text{P}_{0.8}$	$\text{I}\bar{4} + \text{Pmmm}$	Ferro-Para	-
$\text{Mn}_{0.5}\text{Fe}_{2.5}\text{Si}_{0.2}\text{P}_{0.8}$	$\text{I}\bar{4} + \text{Pmmm}$	Ferro-Para	523
$\text{Fe}_3\text{Si}_{0.2}\text{P}_{0.8}$	$\text{I}\bar{4}$	Ferro-Para	695

$\text{Mn}_{0.9}\text{Fe}_{2.1}\text{Si}_{0.1}\text{P}_{0.9}$	$\text{Pmmm}+\overline{\text{I } 4}$	Antiferro-Para	227
$\text{Mn}_{0.8}\text{Fe}_{2.2}\text{Si}_{0.1}\text{P}_{0.9}$	$\text{Pmmm}+\overline{\text{I } 4}$	Antiferro-Para	219
$\text{Mn}_{0.7}\text{Fe}_{2.3}\text{Si}_{0.1}\text{P}_{0.9}$	$\overline{\text{I } 4} +\text{Pmmm}$	Ferro-Para	-
$\text{Mn}_{0.6}\text{Fe}_{2.4}\text{Si}_{0.1}\text{P}_{0.9}$	$\overline{\text{I } 4} +\text{Pmmm}$	Ferro-Para	-
Mn_3P	$\overline{\text{I } 4}$	Antiferro-Para	150
$\text{Mn}_{2.5}\text{Fe}_{0.5}\text{P}$	$\overline{\text{I } 4}$	Antiferro-Para	117
Mn_2FeP	$\overline{\text{I } 4} +\text{Pmmm}$	Antiferro-Para	89
$\text{Mn}_{1.5}\text{Fe}_{1.5}\text{P}$	Pmmm	Antiferro-Para	233
MnFe_2P	$\text{Pmmm}+\overline{\text{I } 4}$	Antiferro-Para	240
$\text{Mn}_{0.9}\text{Fe}_{2.1}\text{P}$	$\text{Pmmm}+\overline{\text{I } 4}$	Ferro-Para	400
$\text{Mn}_{0.8}\text{Fe}_{2.2}\text{P}$	$\text{Pmmm}+\overline{\text{I } 4}$	Ferro-Para	400
$\text{Mn}_{0.7}\text{Fe}_{2.3}\text{P}$	$\overline{\text{I } 4} +\text{Pmmm}$	Ferro-Para	413
$\text{Mn}_{0.6}\text{Fe}_{2.4}\text{P}$	$\overline{\text{I } 4} +\text{Pmmm}$	Ferro-Para	42
$\text{Mn}_{0.5}\text{Fe}_{2.5}\text{P}$	$\overline{\text{I } 4} +\text{Pmmm}$	Ferro-Para	473
Fe_3P	$\overline{\text{I } 4}$	Ferro-Para	686

5.6 $(\text{Mn,Fe})_3(\text{Si,P})\text{B}$ compounds

In light of the results obtained during the study of the $(\text{Mn,Fe})_3(\text{Si,P})$ system, there was a further interest in exploring the antiferromagnetic-ferromagnetic transition observed in the cubic Si rich samples with Fe content ranging from 1.2 to 2.3.

To this end a series of samples were produced containing small amounts of B, with the intention of having this element enter interstitially into the cubic lattice and in this way possibly move the antiferromagnetic transition up from its value of $T_N \approx 50$ K.

Such a method had been previously used with great success in magnetocaloric studies for the control to key properties like T_C , magnetization and magnetic entropy change in La-Fe-Si systems [23], shape-memory alloys [24], and MnCoGe systems [25]. In contrast to the usual stoichiometric tuning, the technique of inserting interstitial atoms in a crystal lattice is meant to solely affect the inter-atomic distance, and not the electronic interactions between atoms directly (via the valence electron concentration e/a [24]).

For this end a series of $\text{Mn}_{3-x}\text{Fe}_x\text{SiB}_y$ samples (with $x=1.9, 2, 2.1$ and 2.2 , and $y=0.02, 0.05, 0.1, 0.15, 0.2, 0.3, 0.4$ and 0.5) were produced to study the tuning potential of boron doping on the antiferromagnetic-ferromagnetic phase transition of the cubic $(\text{Mn,Fe})_3(\text{Si,P})$ phase.

5.6.1 Sample preparation and characterization

All samples produced for the study of the effects of interstitial boron were made from the same starting materials as those used in the preparation of samples belonging to the $(\text{Mn,Fe})_3(\text{Si,P})$ system and previously described in section 5.3.1. The boron used consisted of crystalline pieces of 99.5% purity.

As the current samples no longer contain elemental phosphorous, an arc melting furnace was used for their preparation. The resulting metallic buttons were annealed in the exact same conditions as the samples belonging to the $(\text{Mn,Fe})_3(\text{Si,P})$ system.

The characterization of the samples was conducted in the exact same way as those described in section 5.3.2.

5.6.2 Results and discussion

X-ray diffraction measurements on boron doped samples, with boron concentration of 0.05, 0.1 and 0.15, revealed that all of these contain a minor Si peak in contrast to the undoped samples. The intensity of this peak remained stable for these three concentrations, suggesting a partial substitution of Si by boron in the sample's crystal lattice as opposed to a purely interstitial fit, as demonstrated by Figure 5.8.

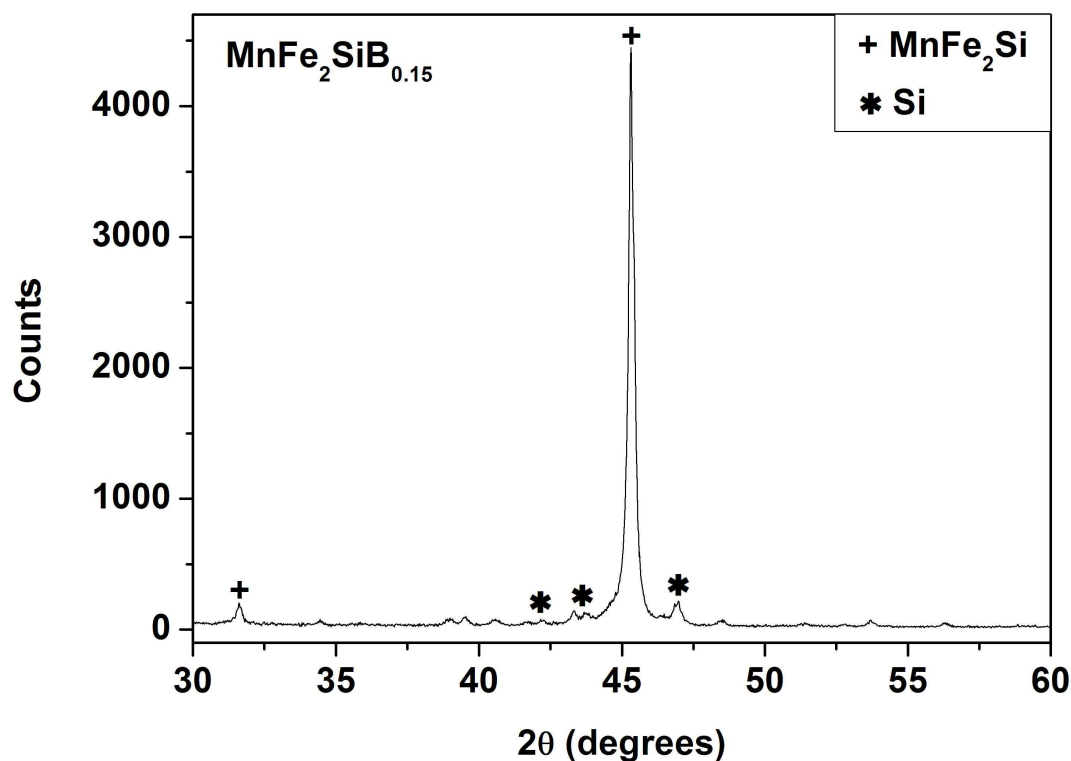


Figure 5.8 X-ray diffraction pattern for the sample $\text{MnFe}_2\text{SiB}_{0.15}$, revealing the cubic $\text{Fm}\bar{3}\text{m}$ structure of the Si rich $(\text{Mn,Fe})_3(\text{Si,P})$ system and minor peaks consistent with pure Si segregation.

Samples with a boron concentration higher than 0.15, were found to exhibit, besides the Si segregation, other minor multiple secondary phases.

The exact nature of these phases was not investigated in depth, as a preliminary observation of the X-ray diffraction patterns of these samples revealed that the formation of these secondary phases did not appear to follow a particular trend or logical evolution with increasing boron content, as demonstrated in Figure 5.9. The lattice parameter a of our doped samples increased for a boron content of 0.02, while for higher concentrations it was found to decrease in a non-linearly fashion.

These results further underline that indeed B atoms do not enter this system as an interstitial element above the content of 0.02, but are partially substituting Si in the crystal structure, which effectively limits the amount of boron that can be added to this structure.

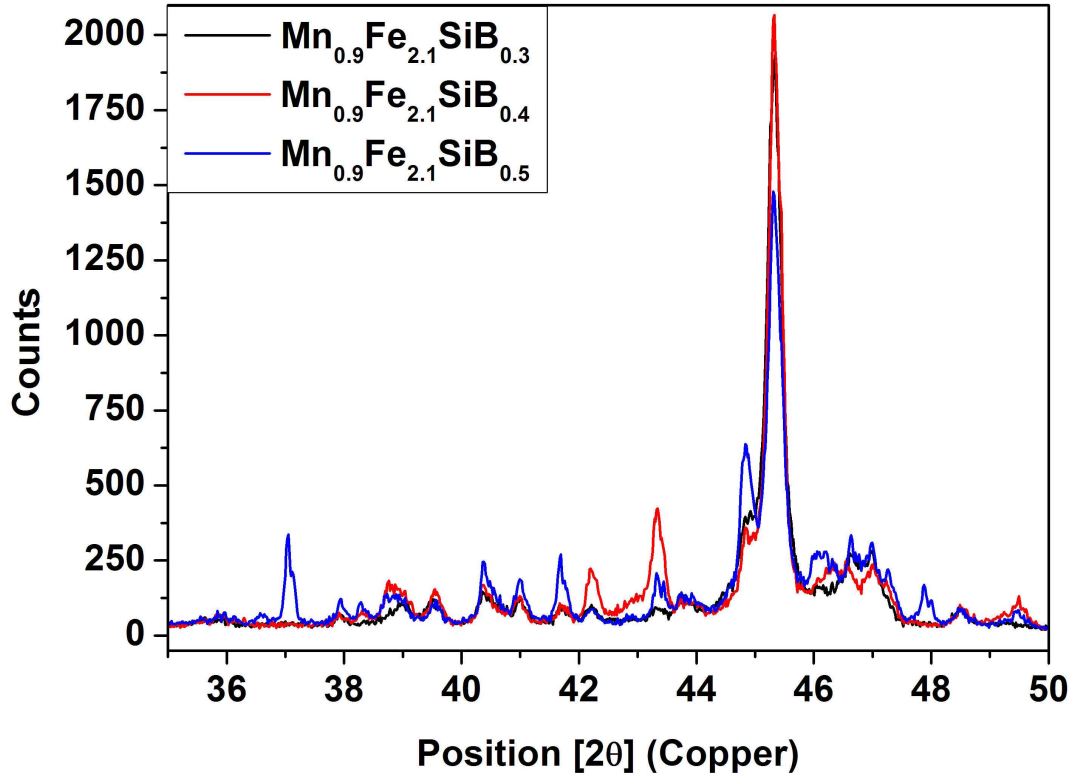


Figure 5.9 Comparison of the X-ray diffraction patterns of the samples $\text{Mn}_{0.9}\text{Fe}_{2.1}\text{SiB}_{0.3}$, $\text{Mn}_{0.9}\text{Fe}_{2.1}\text{SiB}_{0.4}$ and $\text{Mn}_{0.9}\text{Fe}_{2.1}\text{SiB}_{0.5}$, revealing an apparent random occurrence of secondary phases as a result of increasing B content among the cubic main phase.

5.6.3 Magnetic results

The antiferromagnetic-ferromagnetic transition temperature was found to increase with boron concentrations of 0.02 and 0.05. With the added boron these samples also presented a slightly higher magnetization and a sharper ferromagnetic-paramagnetic transition. For higher boron concentration however, the transition temperature not only decreased, but we also observed a loss of sharpness in the antiferromagnetic-ferromagnetic transition and an increase in the base line of the magnetization curve, indicating the increasing presence of secondary phases, as shown in Figure 5.10.

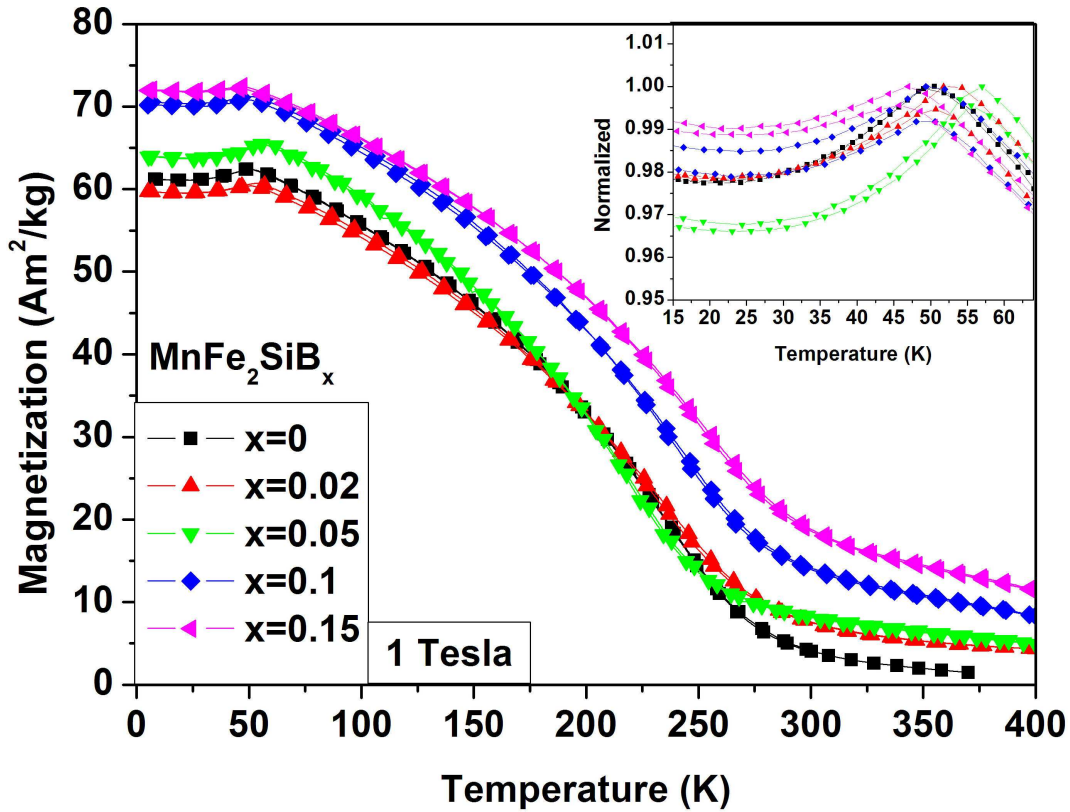


Figure 5.10 Magnetization vs temperature curves for $\text{MnFe}_2\text{SiB}_x$, with $x=0, 0.02, 0.05, 0.1$ and 0.15 demonstrating the effects of boron addition to the magnetic behavior of the cubic phase of Si rich $(\text{Mn,Fe})_3(\text{Si,P})$ system. Up to $x=0.05$ we can observe an increase in T_N , magnetization and transition sharpness, beyond this concentration all these properties lose their desirable characters. Insert: detail on the normalized antiferromagnetic-ferromagnetic transition, demonstrating the increase in T_N up to $x=0.05$ and its subsequent decrease with $x=0.1$ and 0.15 .

In Figure 5.11 the dependence of T_N and the lattice parameter a on the added boron concentration is shown. We were able to effectively increase T_N from 50.5 K, for $x=0$, to 57 K, for $x=0.05$. Further addition of B presented itself as counter productive in every aspect. Even though we were indeed able to optimize this transition we were not able to do so in a way that is beneficial for future magnetocaloric application.

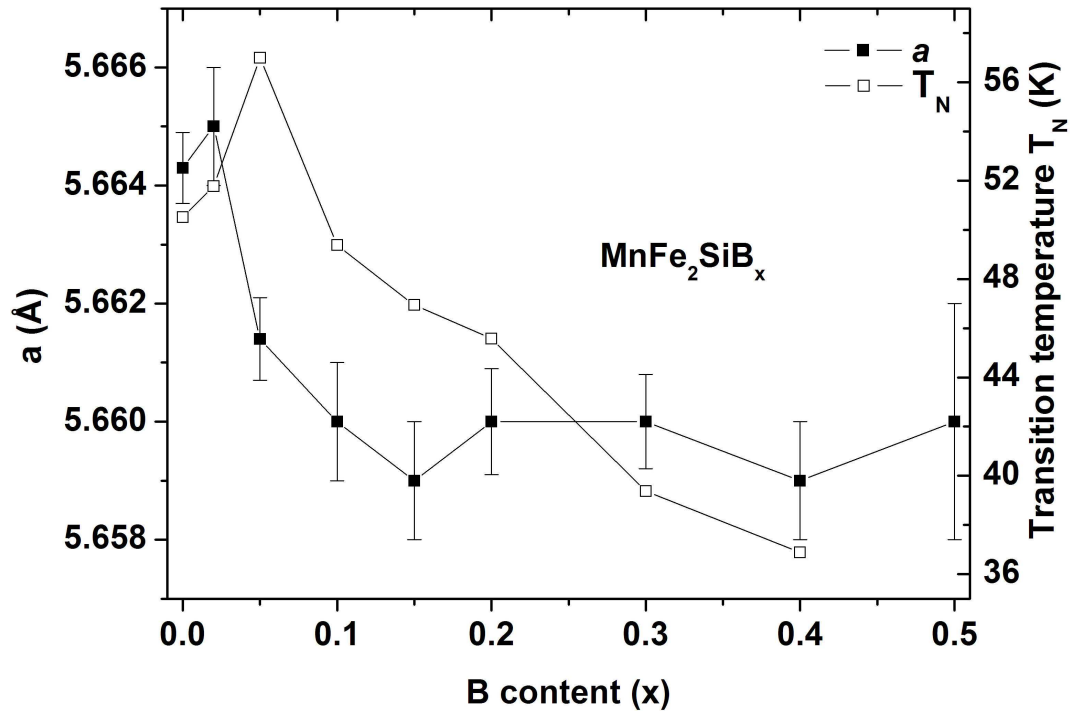


Figure 5.11 Evolution of the lattice parameter a and T_N of $MnFe_2SiB_x$ with increasing B . Given the increasing presence of undesirable secondary phases in samples with B constants above 0.15, the lattice parameter values above this composition should be regarded as rough approximations.

5.7 Conclusions

Based on the collected data and previous literature, the magnetostructural quaternary phase diagram of the $(Mn,Fe)_3(Si,P)$ system was successfully constructed, offering a rare overall view of its unique magnetic and structural properties and greatly expanding our knowledge of the already widely studied $(Mn,Fe)_3Si$ and $(Mn,Fe)_3P$ systems. Still, this diagram appears to be very particular and sensitive to the sample production procedure, as other authors have found different properties when using different annealing temperatures.

The novel hexagonal phase, observed for the first time in this system, like all other phases, shows paramagnetic behaviors at low Fe concentrations and ferromagnetic at high concentrations and may offer the possibility for further developments on those areas where both the $(Mn,Fe)_3Si$ and $(Mn,Fe)_3P$ systems have been studied in the past, such as spintronics research, in its ferromagnetic phase or on metal–metalloid compound research, an area of interest in nuclear-reactor materials science.

Further experimentation with interstitial boron was performed in an attempt to tune the antiferromagnetic-ferromagnetic transition observed in the Si rich cubic phase of the $(\text{Mn,Fe})_3(\text{Si,P})$ system. The antiferromagnetic transition could be enhanced by addition of low boron concentrations, but it decreases for higher additions.

This system was found inappropriate for magnetocaloric applications. This research and the understanding it offers may however open the possibility for further magnetocaloric studies and developments. The novel hexagonal phase still represents a new and unexplored set of compounds that may be optimized by the addition of a fifth element.

References

- [1] N. H. Dung, L. Zhang, Z. Q. Ou and E. Brück, *Appl. Phys. Lett.* 99 (2011) 092511.
- [2] N. H. Dung, L. Zhang, Z. Q. Ou, L. Zhao, L. van Eijck, A. M. Mulders, M. Avdeev, E. Suard, N. H. van Dijk and Ekkes Brück, *Phys. Rev. B* 86 (2012) 045134.
- [3] S. Tomiyoshi, Y. Yamaguchi, M. Ohashi, E. R. Cowley and G. Shirane, *Phys. Rev. B*, 36 (1987) 2118.
- [4] L. Hongzhi, Z. Zhiyong, M. Li, X. Shifeng, L. Heyan, Q. Jingping, L. Yangxian and W. Guangheng, *J. Phys. D: Appl. Phys.* 40 (2007) 7121.
- [5] S. Tomiyoshi and H. Watanabe, *J. Phys. Soc. Jpn.* 39 (1975) 295.
- [6] C. Pfleiderer, J. Boeuf and H. v. Löhneysen, *Phys. Rev. B* 65 (2002) 172404.
- [7] C. Pfleiderer, *Physica B* 329-333 (2003) 1085.
- [8] A. Go, M. Pugaczowa-Michalska and L. Dobrzyński, *Eur. Phys. J. B* 59 (2007) 1.
- [9] E. J. D. Garba and R. L. Jacobs, *J. Phys. F: Met. Phys.* 16 (1986) 1485.
- [10] G. D. Mukherjee, C. Bansal and A. Chatterjee, *Physica B* 254 (1998) 223.
- [11] S. Yoon and J. G. Booth, *Phys. Lett.* 48A (1974) 381.
- [12] S. Yoon and J. G. Booth, *J. Phys. F: Metal Phys.* 7 (1977) 1079.
- [13] V. A. Niculescu, T. J. Burch and J. I. Budnick, *J. Magn. Mater.* 39 (1983) 223-267.
- [14] H. Miki, K. Ohoyama, H. Onodera, H. Yamauchi, Y. Yamaguchi, H. Nojiri, M. Motokawa, S. Funahashi and S. Tomiyosh, *Physica B* 237-238 (1997) 465-466.
- [15] P. Mohn and E. Supanetz, *Philos. Mag. B* 78 (1998) 629.

- [16] O. A. Dubovskii, A. V. Orlov, and V. A. Semenov, *Phys. Solid State*, 45 (2003) 326.
- [17] Rundqvist, *Acta Chem. Scand.* 16 (1962) 992.
- [18] S. Rundqvist, *Acta Chem. Scand.* 16 (1962) 1.
- [19] A. Broddefalk, P. James, Hui-Ping Liu, B. Kalska, Y. Andersson, P. Granberg, P. Nordblad, L. Häggström and O. Eriksson, *Phys. Rev. B* 61 (2001) 413.
- [20] Hui-ping Liu, Y. Andersson, P. James, D. Satula, B. Kalska, L. Häggström, O. Eriksson, A. Broddefalk and P. Nordblad, *J. Magn. Magn. Mater.* 256 (2003) 117.
- [21] M. Goto, H. Tange, T. Tokunaga, H. Fujii and T. Okamoto, *Jpn. J. Appl. Phys.* 16 (1977) 2175.
- [22] T. F. Smith, G. K. Bristow, C. V. Boughton and P. R. W. Hudson, *J. Phys. F: Metal Phys.* 10 (1980) 2867.
- [23] H. C. Xuan, D. H. Wang, C. L. Zhang, Z. D. Han, B. X. Gu, and Y. W. Du, *Appl. Phys. Lett.* 92 (2008) 102503.
- [24] S. H. Xie, J. Q. Li, Y. H. Zhuang, *J. Magn. Magn. Mater.* 311 (2007) 589.
- [25] N. T. Trung, *First-order phase transitions and giant magnetocaloric effect*, Delft University of Technology (2010) PhD thesis, Chapter 6.

Chapter 6

Magnetocaloric exploration of the $(\text{Fe,Co})_3(\text{Si,P})$ and $(\text{Mn,Co})_3(\text{Si,P})$ systems

6.1 Introduction

The current study was motivated by the discovery of the novel $P6/mmm$ hexagonal phase in the $(\text{Mn,Fe})_3(\text{Si,P})$ system. Its aim was to ascertain the existence of this hexagonal phase in related systems and its potential for magnetocaloric applications.

The selection of cobalt as both a substitute for iron and manganese was due to both its elemental proximity and affordable price. The toxicity of cobalt when compared to that of manganese or iron is not irrelevant, but it is lower than that of nickel or chromium, our other options for this study.

As the hexagonal $P6/mmm$ structure was found to be sensitive to the experimental procedure used during the sample preparation, all studied samples of the $(\text{Fe,Co})_3(\text{Si,P})$ and $(\text{Mn,Co})_3(\text{Si,P})$ systems were produced by following the same experimental procedure as used for the $(\text{Mn,Fe})_3(\text{Si,P})$ system, described in Chapter 5. The used elemental cobalt in our sample preparation was 99.8% pure Co powder from Alfa Aesar.

6.2 Material overview

6.2.1 The $(\text{Fe,Co})_3(\text{Si,P})$ system

On the Si rich side, the $(\text{Fe,Co})_3(\text{Si,P})$ system has been mostly studied in the field of spintronics [1] with particular emphasis on spin-related transport properties [2]

(similarly to the $(\text{Mn,Fe})_3\text{Si}$ system). Co-based Heusler alloys, particularly the FeCo_2Si composition, exhibit remarkably high magnetic moment and T_C [3], and have been studied in lateral spin-valve devices for their giant spin signals at room temperature [2].

This system shows a unique preferential site-substitution pattern that allows a direct study of the correlation between the magnetic-field interactions and local electronic configurations [4, 5].

Similarly to the $(\text{Mn,Fe})_3\text{Si}$ system, the $(\text{Fe,Co})_3\text{Si}$ is reported to crystallize in the cubic $Fm\bar{3}m$ structure [1, 3, 4]. Contrarily to the Mn/Fe system, this structure is not found to be stable throughout the whole compositional range between Co_3Si and Fe_3Si . Those samples with Co content above 2.15 are not single phase [5]. This crystal arrangement has the particularity that those atoms found on the left of Fe in the periodic table preferentially enter into the A site of its lattice, while those to the right and beneath Fe (the current case of Co) preferentially occupy the B and B' sites [4, 6] (see Figure 5.2a).

Starting from pure Fe_3Si , the lattice parameters originally decrease with increasing Co content, dropping from 5.65 Å to below 5.64 Å for the $\text{Fe}_{1.8}\text{Co}_{1.2}\text{Si}$ compound. From this Co content on, an increase in lattice parameters is observed [7], with the Co_2FeSi compound having a lattice parameter of 5.658 Å [4].

In terms of magnetic behavior the Si rich side displays particularly high values of T_C , with 1100 K being reported for the FeCo_2Si compound [1, 3]. The saturation magnetization is also reported to increase with Co addition [4, 5].

On the P rich side of this system there seems to be little information available. Several studies claim that there is a clear compositional limit of about 30% to the amount of Co that can be effectively substituted in pure Fe_3P [8, 9], and therefore that the Co_3P compound does not exist [9, 10].

Below this Co compositional limit, this system presents the already studied $I\bar{4}$ tetragonal structure, the orthorhombic phase observed in the $(\text{Mn,Fe})_3\text{P}$ system is not present for the $(\text{Fe,Co})_3(\text{Si,P})$ system [8, 10]. In the $I\bar{4}$ structure, both a and c parameters decrease with Co addition [8]. The same is true for both T_C and the overall saturation magnetization [8-10].

6.2.2 The $(\text{Mn,Co})_3(\text{Si,P})$ system

The Si rich side of this system is once again a relevant study object for spintronics [11-14] and electronic conductivity [15], displaying a high Curie

temperature [12, 13] (as most metallic compounds containing Co) and a large gap of 0.4 eV in the minority spin channel, being a system frequently used for the fabrication of magnetic tunnel junction [11, 12, 14].

The full compositional range of this system seems to be largely disregarded as most papers simply focus on the Co_2MnSi compound, which displays quite promising properties for the already mentioned spintronics research [11-14].

This particular compound is reported as crystallizing in the $Fm\bar{3}m$ cubic structure [11-13, 15] with a lattice parameter of $a = 5.654 \text{ \AA}$. In terms of magnetic behavior, it is reported to have a T_C of 985 K, one of the highest among all known Heusler compounds [11-13, 16], and a magnetic moment of $5.01 \mu_B/\text{f.u.}$.

On all accounts the P rich side of this system appears not to exist [15], with the only study done on it consisting of theoretical calculations meant for the same spintronic applications as the Si rich side [18].

6.3 Results on the $(\text{Fe,Co})_3(\text{Si,P})$ system

6.3.1 Si rich samples

All samples produced in the $(\text{Fe,Co})_3\text{Si}$ system were single phase and show the cubic $Fm\bar{3}m$ phase. In the studied compositional range, with Co concentration ranging from 2 to 1.2, the lattice parameter a was found to increase, consistent with previous results described in section 6.2.1.

In this same Co range the addition of elemental P caused the formation of a secondary phase with the orthorhombic $Pnma$ structure, demonstrated in Figure 6.7. The rise of this secondary phase is demonstrated in Figure 6.1a. This phase becomes gradually more prominent with increasing P content, while it never becomes the single phase in our samples. This result indicates that it does not belong to the $(\text{Fe,Co})_3(\text{Si,P})$ system, but most likely to the $(\text{Co,Fe})_2\text{P}$ system.

To confirm this hypothesis we produced a sample belonging to this $(\text{Co,Fe})_2\text{P}$ system and found its X-ray diffraction pattern to be consistent with the second phase present in our P samples, as can be observed in Figure 6.1b.

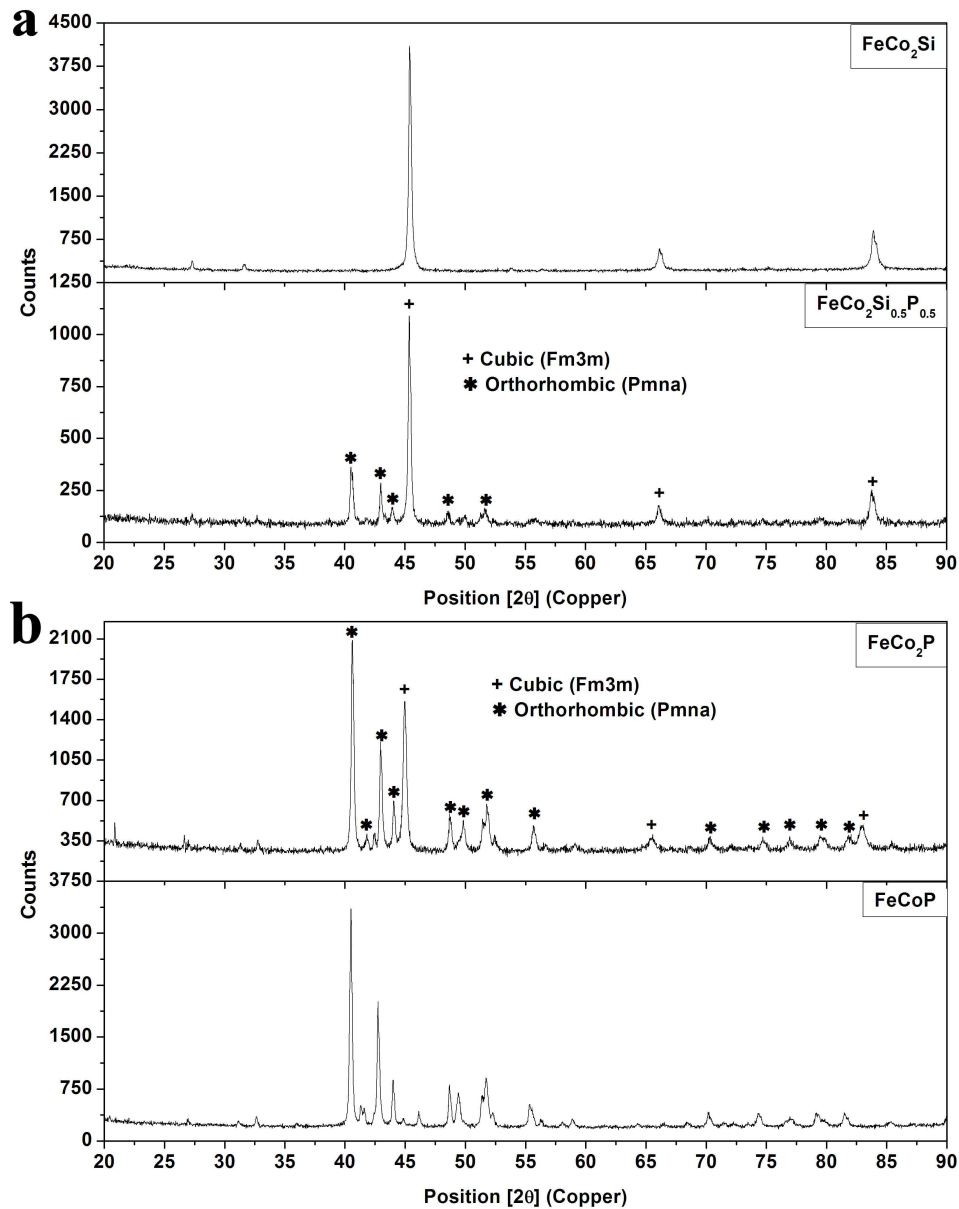


Figure 6.1 a) Comparison of the X-ray diffraction pattern of the FeCo₂Si compound, demonstrating a pure cubic single phase, and the FeCo₂Si_{0.5}P_{0.5} compound, demonstrating the rise of a secondary phase consistent with the orthorhombic *Pnma* structure; **b)** Comparison of the X-ray diffraction pattern of the FeCo₂P compound, demonstrating both the Cubic *Fm3m* and the orthorhombic *Pnma* structures, and the FeCoP compound, demonstrating a pure single phased *Pmna* structure which corresponds perfectly to the secondary orthorhombic phase observed in the FeCo₂P compound.

In terms of magnetic behavior the FeCo₂Si sample was found to have a high saturation magnetization of about 140 Am²/kg. With increasing P content the saturation magnetization steadily decreases due to the formation of the already mentioned second

phase, which displays a much lower magnetization. T_C was found to be beyond the range of both our magnetometers and our DSC measurement system, but as we increased the P content an additional weak magnetic transition became visible as a result of the formed second 2-1 phase, which exhibits a low and quite tunable T_C [19-21].

6.3.2 P rich samples

Given the high T_C of the Co and Si rich cubic phase samples, the Fe and P rich side, with a tetragonal structure is most likely to provide candidates for a successful magnetocaloric approach. Coming from the pure Fe_3P compound, with a T_C of 686 K [8-10], we explored the Co dependence of T_C in order to tune down this transition to a more accessible temperature.

In contrast to what has been reported by Goto *et al.* [8] and Liu *et al.* [9] we were able to produce single-phase samples with a Co content above 30% substitution. The results are quite close to the phase diagram presented by Raghavan [22], shown in Figure 6.2.

As such we were able to lower T_C below the reported 640 K [8, 9] to around 600 K, as shown in Figure 6.3a. To complement the results by Liu [9], we monitored the evolution of the lattice parameters a and c with increasing Co as shown in Figure 6.3b.

Further attempts to manipulate T_C by substitution of P by Si presented multiple phases. These results, and those of the Si rich side of the system, may be taken as solid evidence that the quaternary $(\text{Fe,Co})_3(\text{Si,P})$ does not in fact exist as a single-phase material. The sought after hexagonal $P6/mmm$ phase discovered for the $(\text{Mn,Fe})_3(\text{Si,P})$ is not present in the $(\text{Fe,Co})_3(\text{Si,P})$ system.

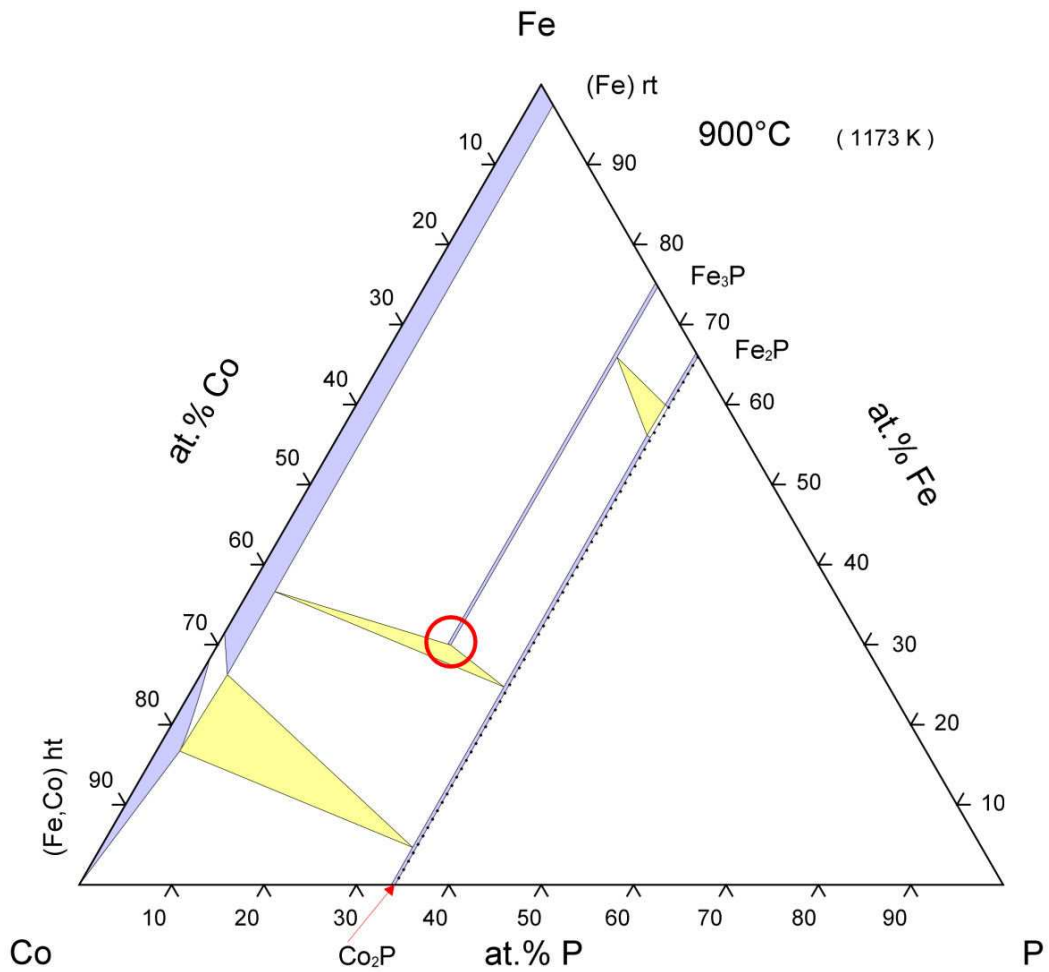


Figure 6.2 Phase diagram of the Fe-Co-P system. The circle demonstrates the compositional limit of Co substitution on the Fe₃P pure compound, contradicting the results presented by Goto *et al.* [8] and Liu *et al.* [9] (Figure taken from [23]).

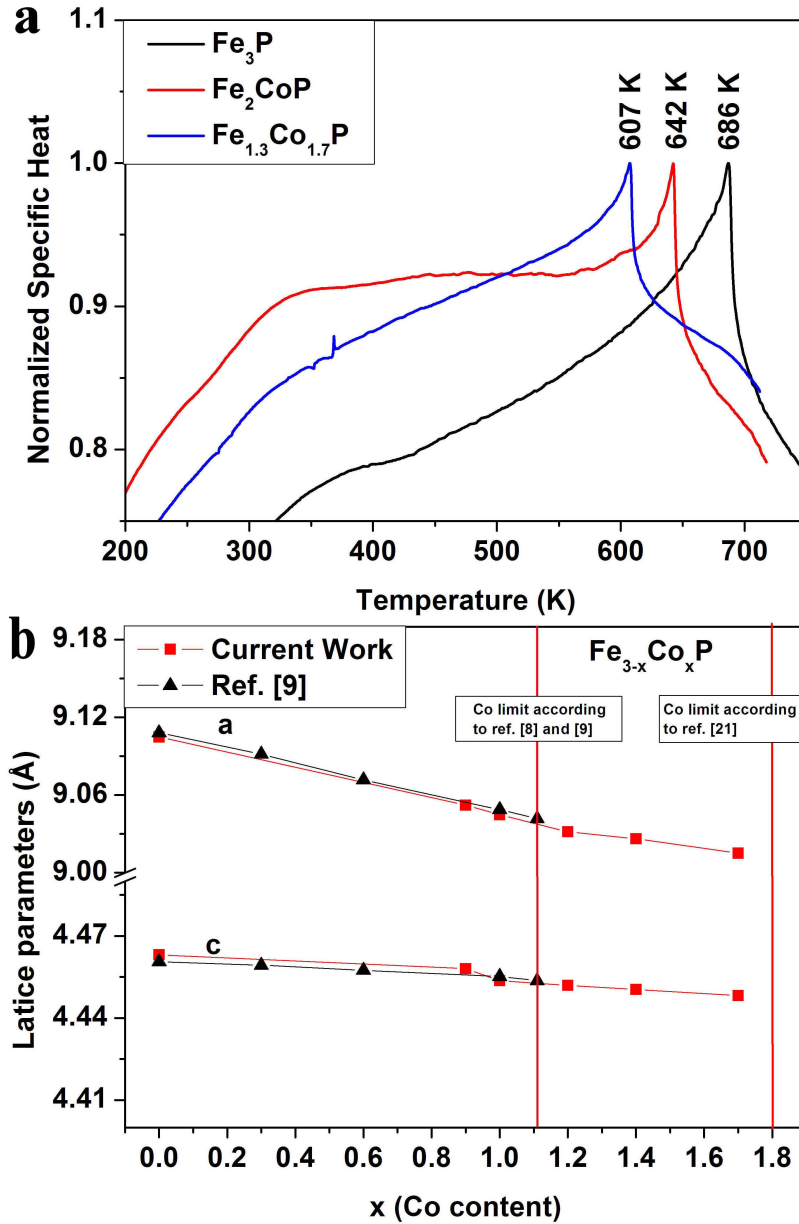


Figure 6.3 a) Normalized DSC measurements for the samples Fe₃P, Fe₂CoP and Fe_{1.3}Co_{1.7}P, demonstrating the decrease in T_C with increasing Co content. b) Evolution of the lattice parameters *a* and *c* with increasing Co content in the samples produced for the current work and compared with the values given by Hui-ping et al. [9].

6.3.3 Sulfur substitution in (Fe,Co)₃(P,Si)

Given the undesired results of Si substitution in the P rich side of the (Fe,Co)₃(Si,P) system, one final attempt was made to further tune down the extremely

high T_C of these compounds by resorting to sulfur substitution, given the periodic table proximity of this element with elemental phosphorus.

All samples used for this study were produced and characterized in the same way as all others belonging to the $(\text{Fe,Co})_3(\text{Si,P})$ system. The used S was 99.5% pure powder from Alfa Aesar.

X-ray diffraction patterns revealed that all S containing samples show the tetragonal $I\bar{4}$ structure, without the occurrence of any second phase. The same S substitution causes a decrease in both lattice parameters a and c , with $a=9.0263 \text{ \AA}$ and $c=4.4504 \text{ \AA}$ for $\text{Fe}_{1.6}\text{Co}_{1.4}\text{P}$, and $a=9.0192 \text{ \AA}$ and $c=4.4499 \text{ \AA}$ for $\text{Fe}_{1.6}\text{Co}_{1.4}\text{P}_{0.9}\text{S}_{0.1}$.

All S containing samples show a high magnetization value of $110 \text{ Am}^2/\text{kg}$. Similarly to other Fe and P rich samples T_C was still beyond the reach of our magnetometers, but DSC measurements indeed demonstrate a slight decrease in the transition temperature. DSC measurements further display an unexpected second unidentified transition around 372 K, as shown in Figure 6.4. In this new $(\text{Fe,Co})_3(\text{P,S})$ system the critical temperature, similarly to the $(\text{Fe,Co})_3\text{P}$ system, decreases with increasing Co content.

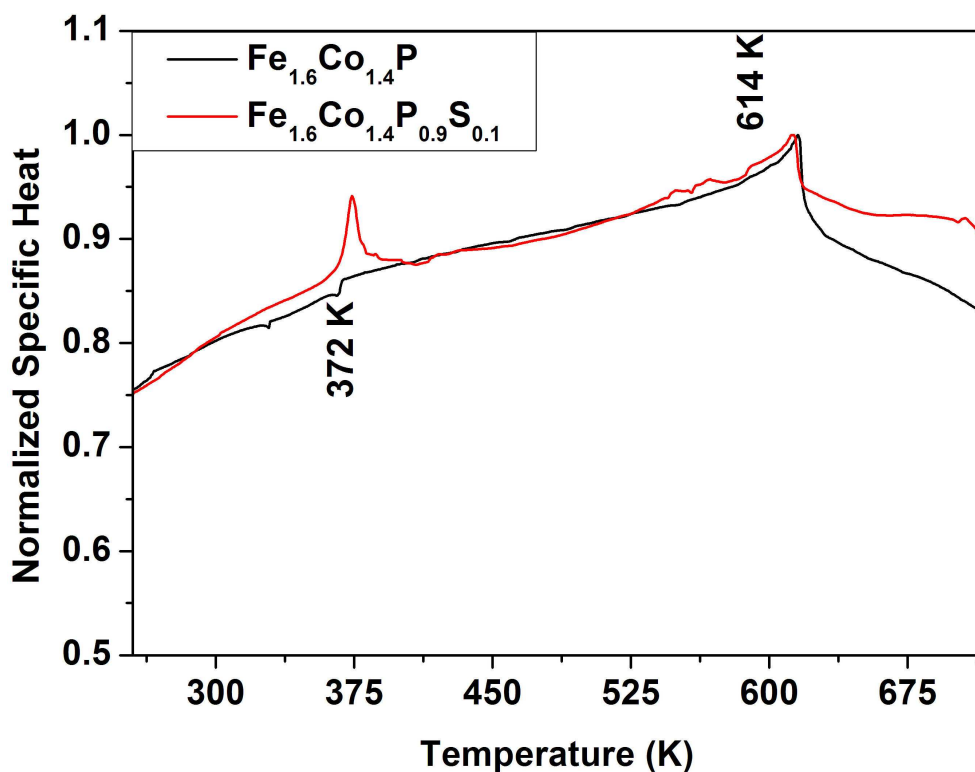


Figure 6.4 Comparison between the normalized specific heat of the $\text{Fe}_{1.6}\text{Co}_{1.4}\text{P}$ and the $\text{Fe}_{1.6}\text{Co}_{1.4}\text{P}_{0.9}\text{S}_{0.1}$ samples, demonstrating the slight decrease in T_C with S substitution and the occurrence of a new and unidentified transition around 372 K.

6.4 Results on the (Mn,Co)₃(Si,P) system

Early in this study it became obvious that this system did not in fact exist as a single-phase material, which might explain the limited number of compositions within this system studied by previous authors [11-14]. All samples produced in this system, even those belonging to the restricted (Mn,Co)₃Si system, displayed a large number of secondary phases. This made it impossible to ascertain if any of these materials effectively belonged to the (Mn,Co)₃(Si,P) system.

The reason behind this difficulty to achieve a single-phase sample, even in compositions known to exist, might be explained by the extremely rich and complex phase diagram of the Mn-Co-P system [24], demonstrated in Figure 6.5. The complex phase diagram makes this an extremely sensitive system to work with.

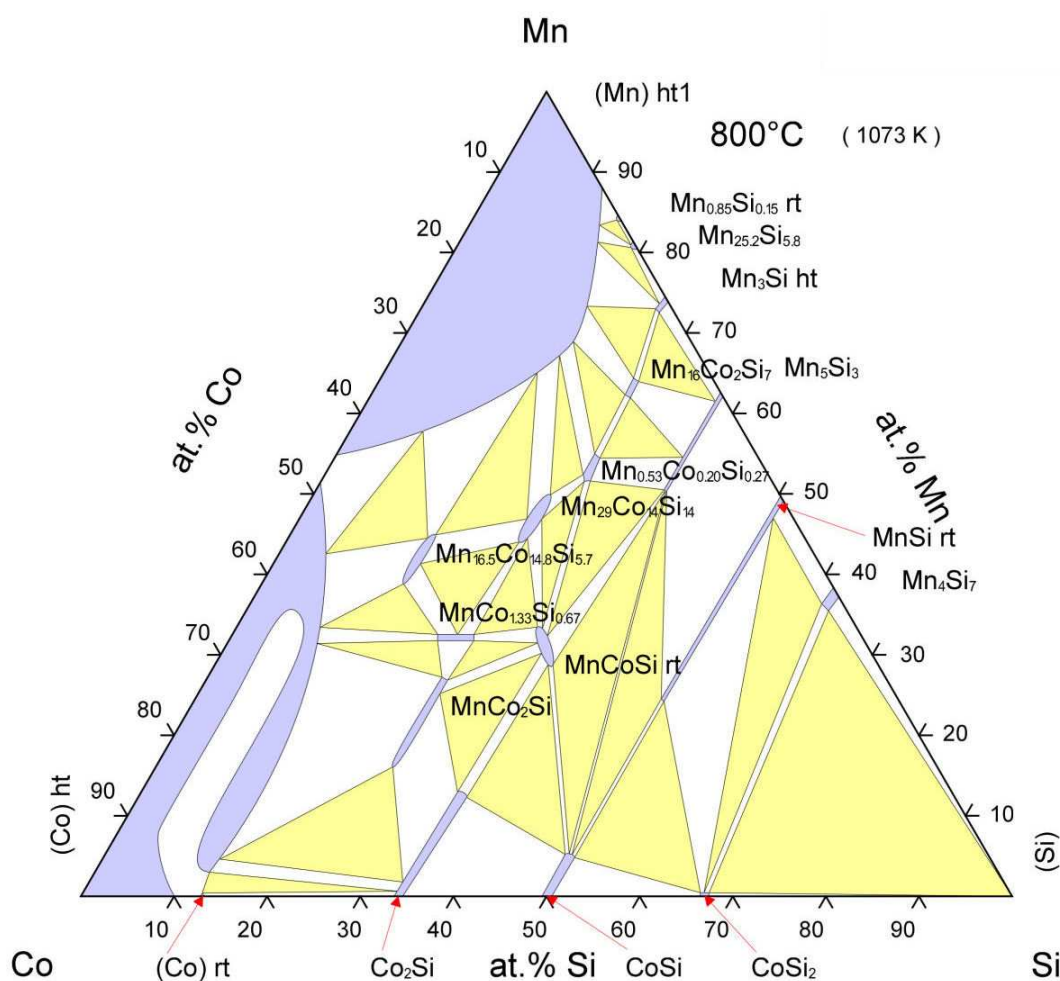


Figure 6.5 The complex phase diagram of the Mn-Co-P system, an insight into the difficulty of achieving a single phased sample in this system (Figure taken from [25]).

6.4.1 Inverse magnetocaloric effect

Samples produced with $0.1 < P < 0.5$ and $1.2 < Co < 1.6$, display multiple phases and exhibit a clear and significant magnetic transition from either an antiferromagnetic or ferrimagnetic to a ferromagnetic phase, or alternatively from antiferromagnetic to a ferrimagnetic phase. As shown in Figure 6.6, this leads to an increase of magnetization for increasing temperature resulting in an inverse magnetocaloric effect.

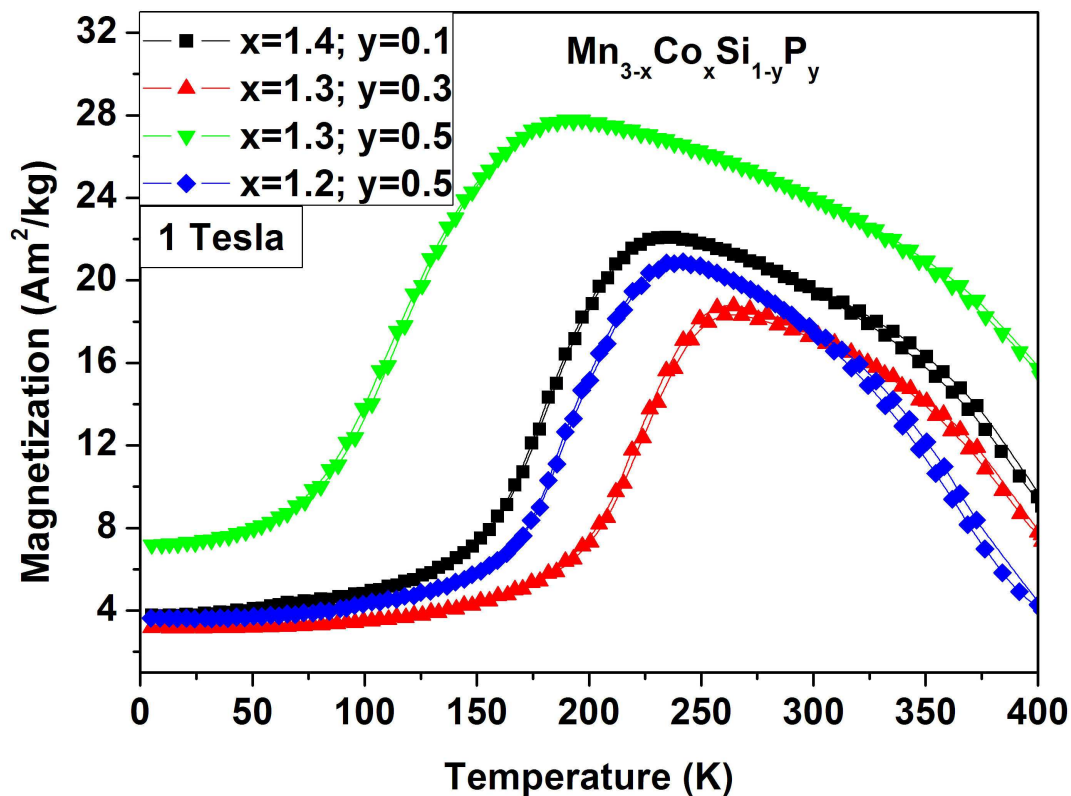


Figure 6.6 Example of some of the produced samples displaying an inverse magnetocaloric effect. The non linear evolution of both transition temperature and overall magnetization with the change in both the Mn\Co and Si\P ratios is symptomatic of the apparently random occurrence of secondary phases in this system of compounds.

In this process, contrary to the usual magnetocaloric effect, where a material heats up with the adiabatic application of an external magnetic field, a material cools down by the application of a magnetic field [26-28]. This effect is usually observed in magnetic transitions between antiferro-ferromagnetic, collinear and non-collinear antiferromagnetic or antiferro-ferrimagnetic phases [26].

In terms of applications this effect is most often considered as a possible heat sink for a functioning magnetic refrigeration device [29, 30], meaning that when a field is applied to a regular magnetocaloric material, the heat released can be effectively dumped into the inverse magnetocaloric material which cools down with the application of the same field. Alternatively a magnetocaloric refrigerator design has been suggested by Zhang *et al.* [31], resorting to both regular magnetocaloric and inverse magnetocaloric materials, in which cooling may be achieved by both the application and removal of a magnetic field in the refrigeration cycle, making up a more efficient refrigerator.

Popular in this field of research are the RhFe [26, 30-32], La-Ca-MnO₃ [30] and Ni-Mn Heulers alloys [26, 27].

In order to isolate the phase that produces these interesting results, EDS measurements were performed on a set of samples. In this way we established that the phase of interest corresponds to Mn_{1.1}Co_{0.8}Si_{0.2}P_{0.8}.

A Mn_{1.1}Co_{0.8}Si_{0.2}P_{0.8} sample was produced and characterized in exactly the same terms as the ones belonging to the (Mn,Co)₃(Si,P) system.

X-ray diffraction measurements revealed the sample was single phase and crystallizes in the orthorhombic *Pnma* structure, displayed in Figure 6.7. This structure is the same as the (Co,Fe)₂P secondary phase found in the (Fe,Co)₃(Si,P) system.

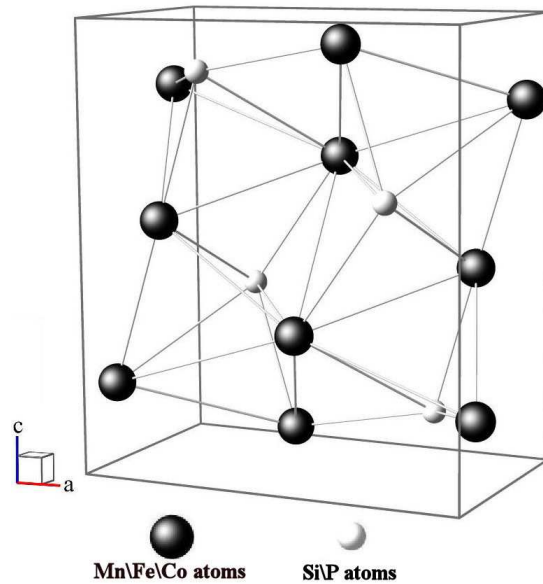


Figure 6.7 *Pnma* orthorhombic structure of the (Co,Fe)₂P system found as a secondary phase in the (Fe,Co)₃(Si,P) samples and the Mn_{1.1}Co_{0.8}Si_{0.2}P_{0.8} compound found in the (Mn,Co)₃(Si,P) system.

This compound revealed a remarkably high magnetic transition compared with many compounds previously investigated for their inverse magnetocaloric effect [26, 27, 31]. The magnetization, reaching above 70 Am²/kg, as shown in Figure 6.8, makes this compound an extremely exciting candidate for new inverse magnetocaloric effect systems.

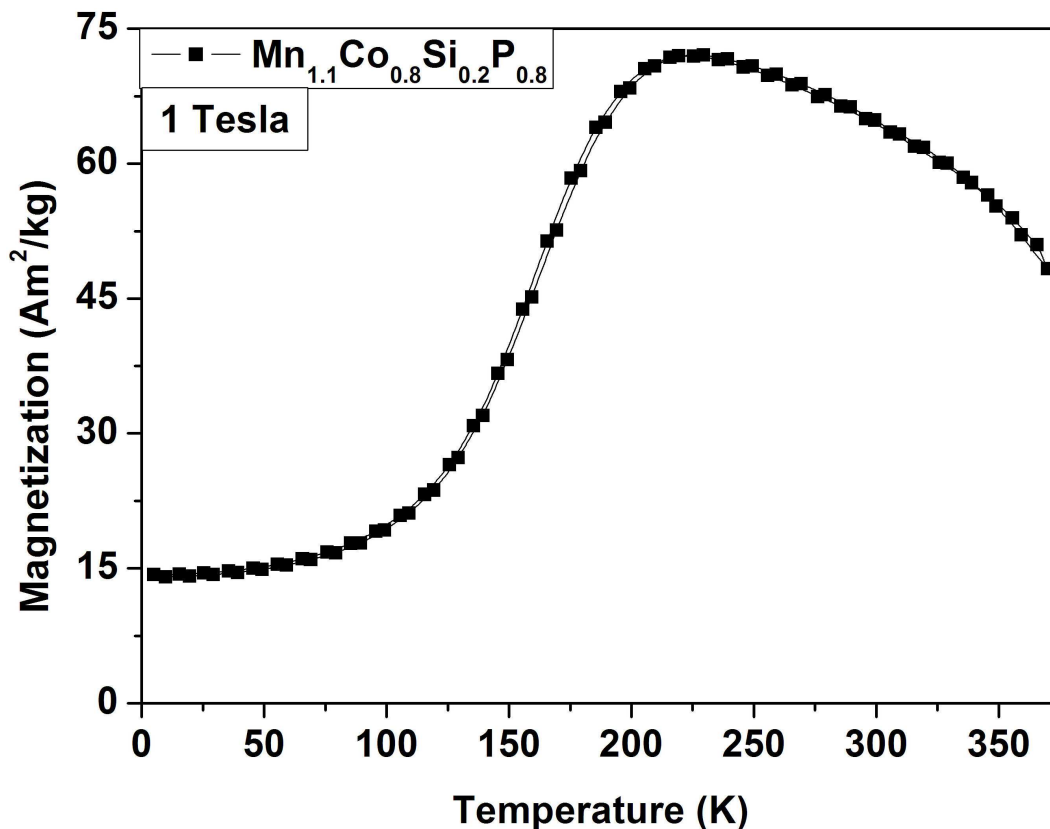


Figure 6.8 Magnetization vs temperature curve for the $\text{Mn}_{1.1}\text{Co}_{0.8}\text{Si}_{0.2}\text{P}_{0.8}$ compound, demonstrating an extremely high inverse magnetic transition.

6.5 Conclusions

The initial motivation to explore the magnetocaloric potential of the novel *P6/mmm* hexagonal phase discovered in the $(\text{Mn,Fe})_3(\text{Si,P})$ system (Chapter 5) led to a systematic study of the magnetic and structural properties of the $(\text{Fe,Co})_3(\text{Si,P})$ and $(\text{Mn,Co})_3(\text{Si,P})$ systems.

Our results on the $(\text{Fe,Co})_3(\text{Si,P})$ system strongly suggest that this quaternary system does not exist as a single-phase compound. While we were very successful in producing samples belonging to the ternary $(\text{Fe,Co})_3\text{Si}$ and $(\text{Fe,Co})_3\text{P}$ systems, the addition of P or Si to these always gave rise to multi-phase samples. This result

motivated us to further explore methods to tune T_C in the $(\text{Fe,Co})_3\text{P}$ system that did not resort to Si substitution, leading us to a promising and unexpected result with the S substitution instead.

All samples belonging to this new $(\text{Fe,Co})_3(\text{P,S})$ system have a slightly lower T_C than those not containing S, and showed a new and unexpected secondary transition around 370 K.

Similar to the $(\text{Fe,Co})_3(\text{Si,P})$ system, the $(\text{Mn,Co})_3(\text{Si,P})$ system does not seem to exist as a single-phase compound. Even the compositions previously studied by other groups proved to be extremely difficult to produce as single-phase samples. The detection of an inverse magnetocaloric effect in some of these multiple phase samples led to the discovery of a new system with remarkable properties for inverse magnetocaloric effect applications, showing a high magnetic transition temperature for an antiferromagnetic or ferrimagnetic to ferromagnetic phase, or alternatively from an antiferromagnetic to a ferrimagnetic phase.

In both of these systems the hexagonal $P6/mmm$ phase was not found.

References

- [1] S. Wurmehl, G. H. Fecher, H. C. Kandpal, V. Ksenofontov, C. Felser and Hong-Ji Lin, Appl. Phys. Lett. 88 (2006) 032503.
- [2] K. Hamaya, N. Hashimoto, S. Oki, S. Yamada, M. Miyao, and T. Kimura, Phys. Rev. B 85 (2012) 100404.
- [3] S. Wurmehl, G. H. Fecher, V. Ksenofontov, F. Casper, U. Stumm, C. Felser, Hong-Ji Lin and Y. Hwu, J. Appl. Phys. 99 (2006) 08J103.
- [4] V. Niculescu, T. J. Burch, K. Raj and J. J. Budnick, J. Magn. Mater. 5 (1977) 60.
- [5] V. Niculescu, J. I. Budnick, W. A. Hines, K. Raj, S. Pickart and S. Skalski, Phys. Rev. B 19 (1979) 453.
- [6] L. Hongzhi, Z. Zhiyong, M. Li, X. Shifeng, L. Heyan, Q. Jingping, L. Yangxian and W. Guangheng, J. Phys. D Appl. Phys. 40 (2007) 7121.
- [7] Y. Nishino, Shin-ya Inoue, S. Asano and N. Kawamiya, Phys. Rev. B 48 (1993) 13607.
- [8] M. Goto, H. Tange, T. Tokunaga, H. Fujii and T. Okamoto, Jpn. J. Appl. Phys. 16 (1977) 2175.

- [9] Hui-ping Liu, P. James, A. Broddefalk, Y. Andersson, P. Granberg and O. Eriksson, *J. Magn. Magn. Mater.*, 189 (1998) 69.
- [10] R. J. Gambino, T. R. McGuire, and Y. Nakamura, *J. Appl. Phys.* 38 (1967) 1253.
- [11] R. Grasin, E. Vinteler, A. Bezerghceanu, C. Rusu, R. Pacurariu, I. G. Deac and R. Tetean, *Acta Phys. Pol. A* 118 (2010) 648.
- [12] B. Hülsen, M. Scheffler and P. Kratzer, *Phys. Rev. B* 79 (2009) 094407.
- [13] G. Gökoğlu and O. Gülseren, *Eur. Phys. J. B* 76 (2010) 321.
- [14] S. Picozzi, A. Continenza and A. J. Freeman, *Phys. Rev. B* 66 (2002) 094421.
- [15] S. Ishida, T. Masaki, S. Fujii and S. Asano, *Physica B* 245 (1998) 1.
- [16] B. Balke, G. H. Fecher, H. C. Kandpal, C. Felser, K. Kobayashi, E. Ikenaga, Jung-Jin Kim, and S. Ueda, *Phys. Rev. B* 74 (2006) 104405.
- [17] S. V. Oryshchyn, T. I. Berezyuk, Y. B. Kuz'ma, *Russ. J. Inorg. Chem.* 32 (1987) 295.
- [18] Z. Yao, S. Gong, J. Fu, Yue-Sheng Zhang and Kai-Lun Yao, *Solid State Commun.* 150 (2010) 2239.
- [19] . Fruchart, A. Roger and J. P. Senateur, *J. Appl. Phys.* 40 (1969) 1250.
- [20] S. Kumar, S. Chander, A. Krishnamurthy, B. K. Srivastava, *J. Magn. Magn. Mater.* 237 (2001) 135.
- [21] S. Kumar, A. Krishnamurthy and B. K. Srivastava, *J. Phys. D Appl. Phys.* 41 (2009) 055001.
- [22] V. Raghavan, *Indian Inst. Met.* 3 (1988) 51.
- [23] Co-Fe-P, ternary phase diagram, isothermal section, in *Springer Materials – The Landolt-Börnstein Database*
(http://www.springermaterials.com/docs/VSP/datasheet/lpf-c/00925000/LPFC_925042.html).
- [24] Y. B. Kuz'ma, E. I. Gladyshevskii, *Russ. J. Inorg. Chem.* 9 (1964) 373.
- [25] Co-Mn-Si, ternary phase diagram, isothermal section, in *Springer Materials – The Landolt-Börnstein Database*
(http://www.springermaterials.com/docs/VSP/datasheet/lpf-c/00925000/LPFC_925257.html).
- [26] T. Krenke, E. Duman, M. Acet, E. F. Wassermann, X. Moya, L. Mañosa and A. Planes, *Nat. Mater.* 4 (2005) 450.
- [27] T. Krenke, E. Duman, M. Acet, X. Moya, L. Mañosa, and A. Planes, *J. Appl. Phys.* 102 (2007) 102.
- [28] P. J. von Ranke, N. A. de Oliveira, B. P. Alho, E. J. R. Plaza, V. S. R. de Sousa, L. Caron and M. S. Reis, *J. Phys.: Condens. Mat.* 21 (2009) 056004.

- [29] R. J. Joenk, *J. Appl. Phys.* 34 (1963) 1097.
- [30] A. Biswas, T. Samanta, S Banerjee and I. Das, *J. Phys. Condens. Mat.* 21 (2009) 506005.
- [31] X. Zhang, B. Zhang, S. Yu, Z. Liu, W. Xu, G. Liu, J. Chen, Z. Cao and G. Wu, *Phys. Rev. B* 76 (2007) 132403.
- [32] S. A. Nikitin, G. Myaligulyev, A. M. Tishin, M. P. Annaorazov, K. A. Asatryan and A. L. Tyurin, *Phys. Lett. A* 148 (1990) 363.

Chapter 7

Magnetic and magnetocaloric exploration of Fe rich $(\text{Mn,Fe})_2(\text{P,Ge})$

7.1 Introduction

As mentioned in Chapter 5, much of the MCE materials research performed in Delft focuses on promising Fe_2P -type systems. Among these is the $(\text{Mn,Fe})_2(\text{P,Ge})$ system that has shown great promise, having a highly tunable transition temperature, low thermal hysteresis and high magnetization [1].

This system, however, has the drawback of being considerably more expensive due to the use of germanium, which limits its potential use in commercial magnetic refrigeration devices.

The results presented by Trung *et al.* [1], and more recently by Dung *et al.* on the $(\text{Mn,Fe})_{1.95}(\text{P,Si})$ system [2], do reveal that increasing the Fe composition in these systems triggers an increase in their transition temperature, which may then be compensated by a decrease in Ge or Si content.

Obviously, among these two systems, $(\text{Mn,Fe})_{1.95}(\text{P,Si})$ stands out as the cheapest and safest, possessing remarkable magnetic and magnetocaloric properties. Unfortunately, the dramatic change in the a and c parameters observed in its crystal lattice during its first-order magneto-elastic transition implies that these materials may display a potentially crippling brittleness when they are thermally (or magnetically) cycled [2], which is an added difficulty for their commercial application.

This has led to the motivation to investigate Fe rich $(\text{Mn,Fe})_2(\text{P,Ge})$ samples in more detail, as the characteristics of this system's magneto-elastic transition suggest a more stable mechanical behavior, and the above mentioned results seem to point to the

fact that Ge content can be significantly reduced if Fe is increased, possibly making this system commercially viable.

The Fe rich part of the $(\text{Mn,Fe})_2(\text{P,Ge})$ system's phase diagram appears to have been largely disregarded, as all recent publication only focus on the Mn-rich samples, as shown in Figure 7.1.

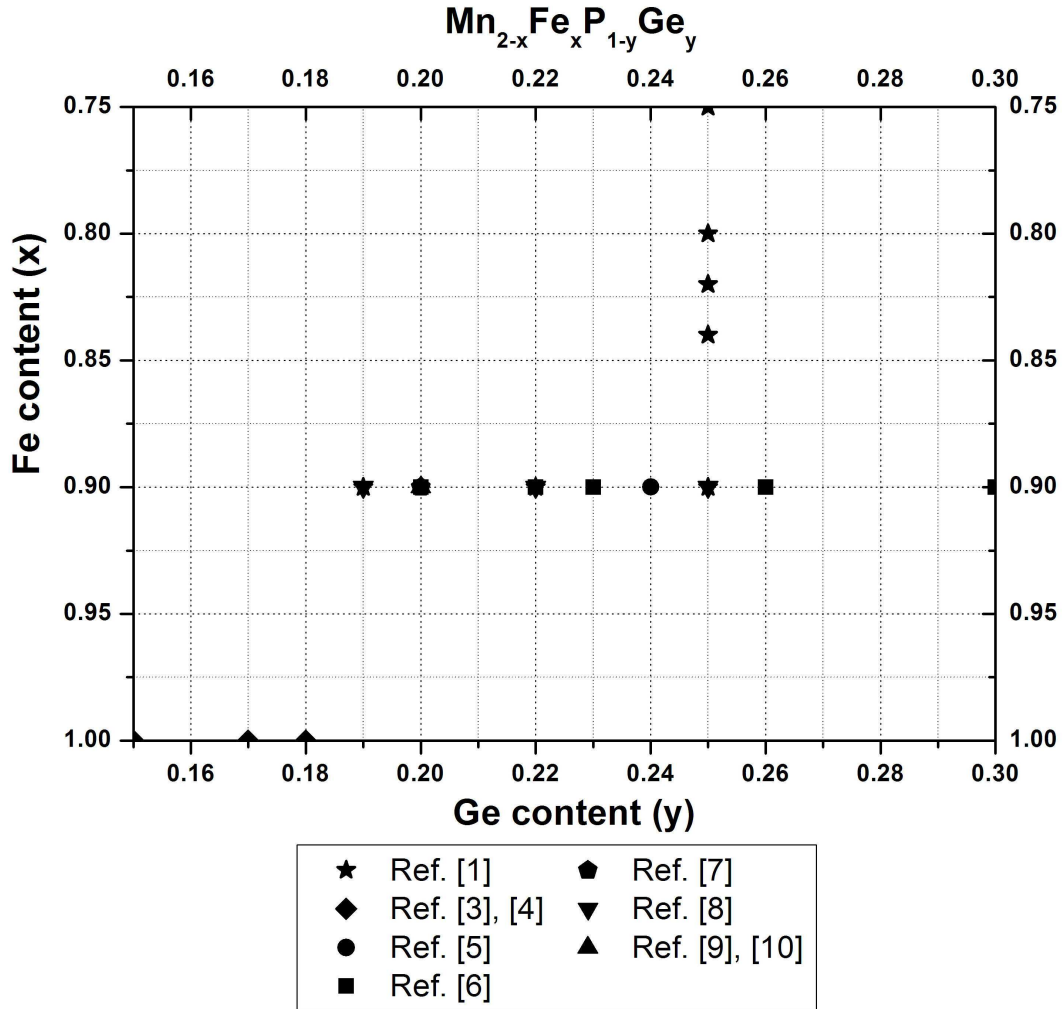


Figure 7.1 Studied compositions of recently published papers on the $(\text{Mn,Fe})_2(\text{P,Ge})$ system.

For this purpose various Fe-rich samples belonging to the $(\text{Mn,Fe})_2(\text{P,Ge})$ system, and the closely related $(\text{Mn,Fe})_{1.95}(\text{P,Ge})$ system, have been produced to evaluate their transition temperatures and overall magnetic properties.

7.2 Material overview

Both the $(\text{Mn,Fe})_2(\text{P,Ge})$ and the $(\text{Mn,Fe})_{1.95}(\text{P,Ge})$ systems crystallize in the Fe_2P -type hexagonal structure ($P\bar{6}2m$ space group) [1, 7]. The Fe and Mn transition metal atoms occupy the $3f$ -site at the tetrahedral $(x_1, 0, 0)$ position and the $3g$ -site at the pyramidal $(x_2, 0, 1/2)$ position. The non-metal P and Ge atoms can both occupy the $1b$ -site at the $(0, 0, 1/2)$ position and in the $2c$ -site at the $(1/3, 2/3, 0)$ position.

Considering the parent compound Fe_2P , when Mn atoms are added, to replace Fe, they preferably occupy the $3g$ -sites, coplanar with the P and Ge atoms at the $1b$ -site, while the Fe atoms preferably occupy the $3f$ -sites, coplanar with the P and Ge atoms at the $2c$ -site [11]. For $(\text{Fe,Mn})_2(\text{P,Ge})$ the Mn and Fe atoms occupy separate planes, as depicted in Figure 7.2.

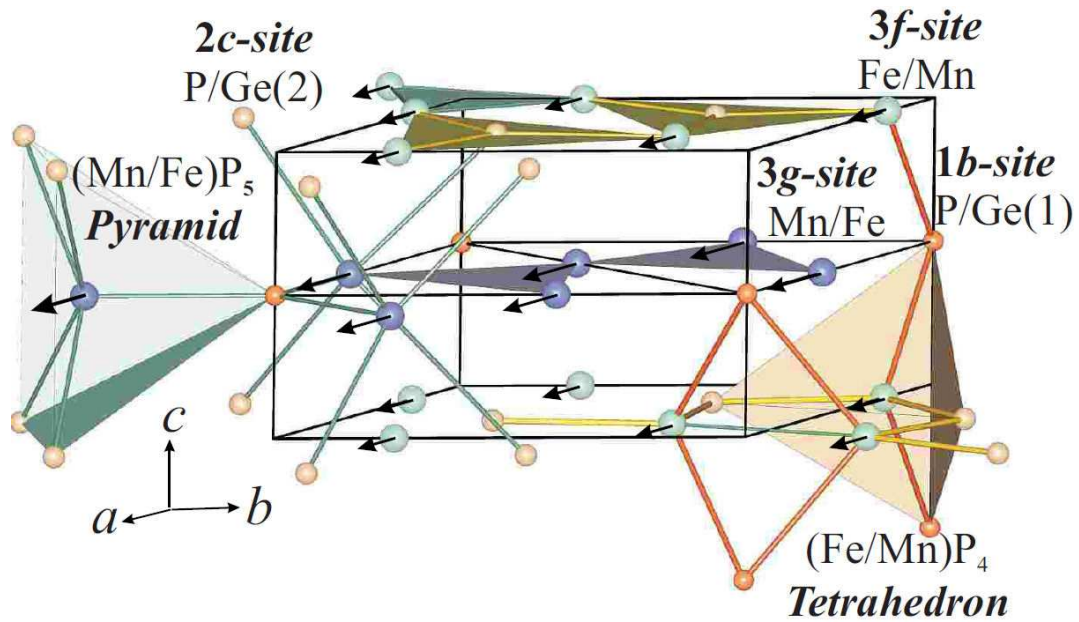


Figure 7.2 Crystal structure of the $(\text{Mn,Fe})_2(\text{P,Ge})$ system presenting its several atomic sites; the arrows represent the magnetic moments of Mn and Fe atoms while the system is in its Ferromagnetic state [11].

This system is paramagnetic at high temperatures and ferromagnetic at low temperatures [11]. Its T_C is easily tunable over a broad temperature range ($150 \text{ K} < T_C < 450 \text{ K}$) by careful adjustment of both Mn/Fe and P/Ge ratios [1].

Accompanying the magnetic transition at T_C , this system also undergoes a contraction of the lattice parameter c and an expansion of a [11], which can be identified in X-ray diffraction data as a shift in both the (300) and the (002) peak

towards higher and lower angles, respectively. This phenomenon is illustrated in Figure 7.3.

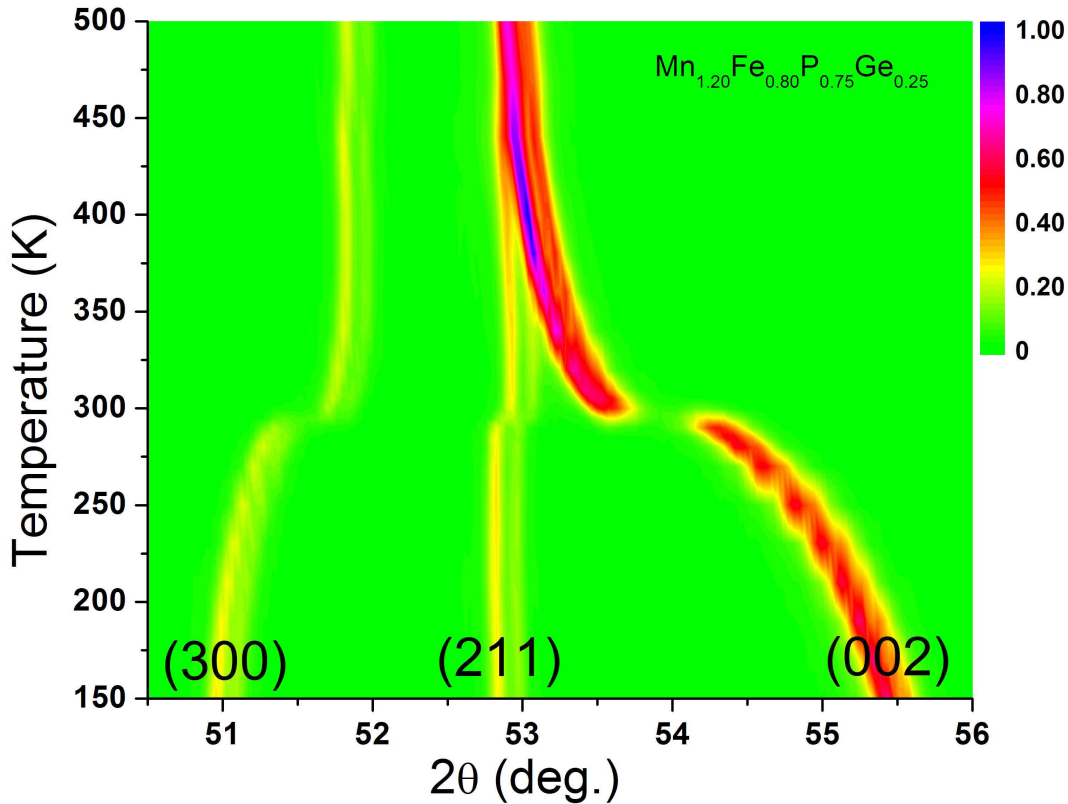


Figure 7.3 Contour plot of the angle change in the (300), (211) and (002) peaks versus temperature for $\text{Mn}_{1.2}\text{Fe}_{0.8}\text{P}_{0.75}\text{Ge}_{0.25}$, illustrating the sharp discontinuity in lattice parameters accompanying the magnetic transition [12].

7.3 Sample preparation and characterization

All $(\text{Mn,Fe})_2(\text{P,Ge})$ and $(\text{Mn,Fe})_{1.95}(\text{P,Ge})$ samples were prepared from the appropriate amounts of 99+% iron powder, 99% red phosphorous powder, 99.5% binary Fe_2P powder, 99.999% Ge chips and 99.9% manganese chips reduced at 600 °C under a hydrogen atmosphere in order to remove oxides.

The samples were ball milled as described in Chapter 3, then compacted into 10 mm pellets with a pressure of 150 kgf/cm² and sealed into quartz tubes with an atmosphere of 200 mbar of argon. Finally these were annealed in a vertical resistive furnace at 1100 °C for 10 hours, homogenized at 1000 °C for 60 hours and then quenched to room temperature in water.

This particular heat treatment was selected based on the study performed by N. T. Trung on the influence of annealing procedures in the $(\text{Mn,Fe})_2(\text{P,Ge})$ system, that indicates that this heat treatment produced samples with the sharpest magnetic transitions [13].

The magnetic and DSC measurements were performed on all samples and homogeneity and crystal structure were checked using X-ray diffraction as described in Chapter 3.

7.4 Result and discussion

7.4.1 $(\text{Mn,Fe})_2(\text{P,Ge})$ system

Throughout the studied compositional range, all samples belonging to both the $(\text{Mn,Fe})_2(\text{P,Ge})$ and the $(\text{Mn,Fe})_{1.95}(\text{P,Ge})$ systems presented the Fe_2P -type hexagonal structure, with the occasional occurrence of a minor MnO peak in their X-ray diffraction patterns. The lattice parameter a was found to increase with Ge addition and decrease with Fe, while the c parameter decreases with Ge and increases with Fe.

The T_C of these systems was found to be quite easy to manipulate and tune with changes in both Fe and Ge content. For the $(\text{Mn,Fe})_2(\text{P,Ge})$ system, the diagram in Figure 7.4 was assembled.

The results displayed in Figure 7.4 show that in this compositional range T_C is easily tunable, but does not change linearly with Fe or Ge concentration, in contrast to what had previously been reported by Trung *et al.* [1] and Brück *et al.* [14] for Mn-rich $(\text{Mn,Fe})_2(\text{P,Ge})$ compounds.

Novel in this system is the detection of an anomalous magnetic behavior at low Ge concentrations, not consistent with regular full Ferromagnetic behavior. If pushed to even lower Ge contents, this turns into full Antiferromagnetic behavior, limiting the lowest usable Ge content in this system. This novel magnetic region seems to be influenced by the Fe content, as increasing Fe pushes the occurrence of this behavior further into low Ge concentrations, eventually vanishing from our samples. A similar behavior to this seems to have been also observed by Tegus *et al.* [15, 16], both in the $(\text{Mn,Fe})_2(\text{P,As,Ge})$ and $(\text{Mn,Fe})_2(\text{P,As})$ systems for samples with low As and Ge content. The exact nature of this behavior has not yet been established, but given the contraction of the lattice parameter a and expansion of c (also observed in $(\text{Mn,Fe})_2(\text{P,As})$ [16]) this phenomenon should be associated with intra-layer interactions between atoms.

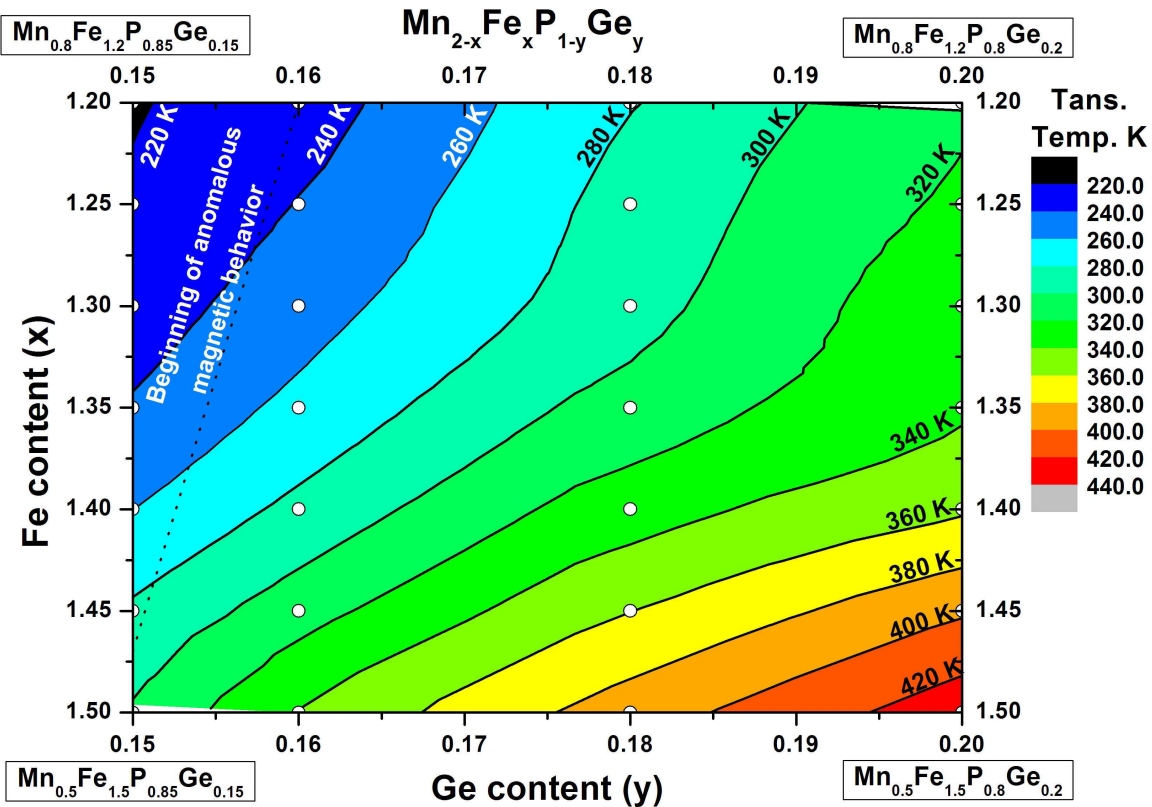


Figure 7.4 Evolution of T_C with both Fe and Ge content in the $(\text{Mn,Fe})_2(\text{P,Ge})$ system. The open dots mark the compositions of the samples used in this study. The bar on the right of the figure represents the transition temperature of the composition range.

As can be seen in Figure 7.4, our initial hypothesis to reduce Ge by increasing Fe content, while maintaining T_C around room temperature, was correct. This process has, however, also brought on an undesirable widening of the typically sharp transition between the Ferromagnetic and the Paramagnetic states in this system, which no longer displays the characteristics of a first order phase transition.

Such an occurrence is extremely unfortunate for the prospect of applying Fe-rich $(\text{Mn,Fe})_2(\text{P,Ge})$ samples to any practical magnetic cooling device. Figure 7.5 illustrates the above mentioned results.

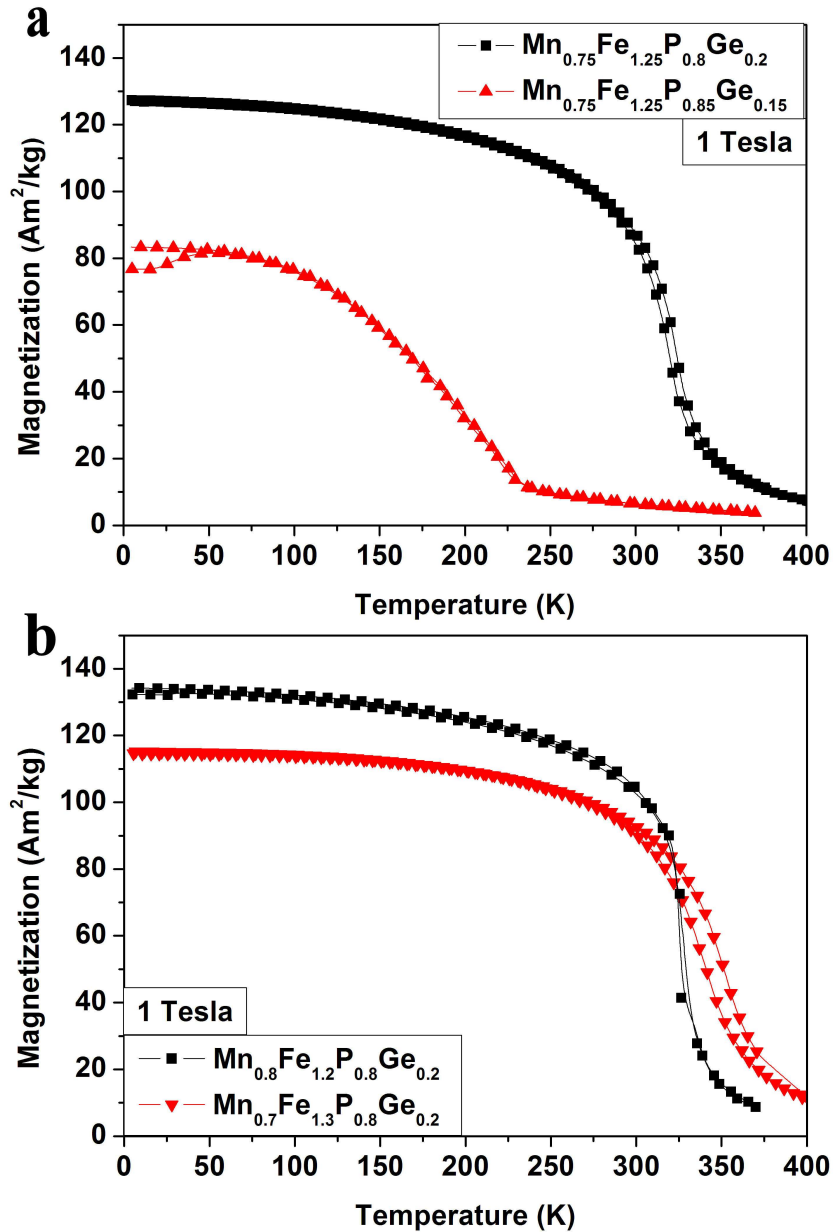


Figure 7.5 a) Comparison between the Ferromagnetic and the anomalous magnetic behavior observed in low Ge content samples in the $(\text{Mn}, \text{Fe})_2(\text{P}, \text{Ge})$ system; b) Comparison between two samples with different Fe contents demonstrating the decrease in transition sharpness promoted by the increase of Fe.

The loss of the first-order behavior of the magneto-elastic transition also implies a disappearance of the discontinuity previously observed in the Mn-rich magnetic and structural properties. This can be best observed by monitoring the (003) and (002) peaks in the X-ray diffraction patterns of the Fe-rich $(\text{Mn}, \text{Fe})_2(\text{P}, \text{Ge})$ samples.

While in the Mn rich side of the diagram we observe a discontinuity in the temperature evolution of these two peaks around the transition temperature, exemplified in Figure 7.3, we now observe a very smooth and gradual variation with temperature in both of them, as seen in Figure 7.6.

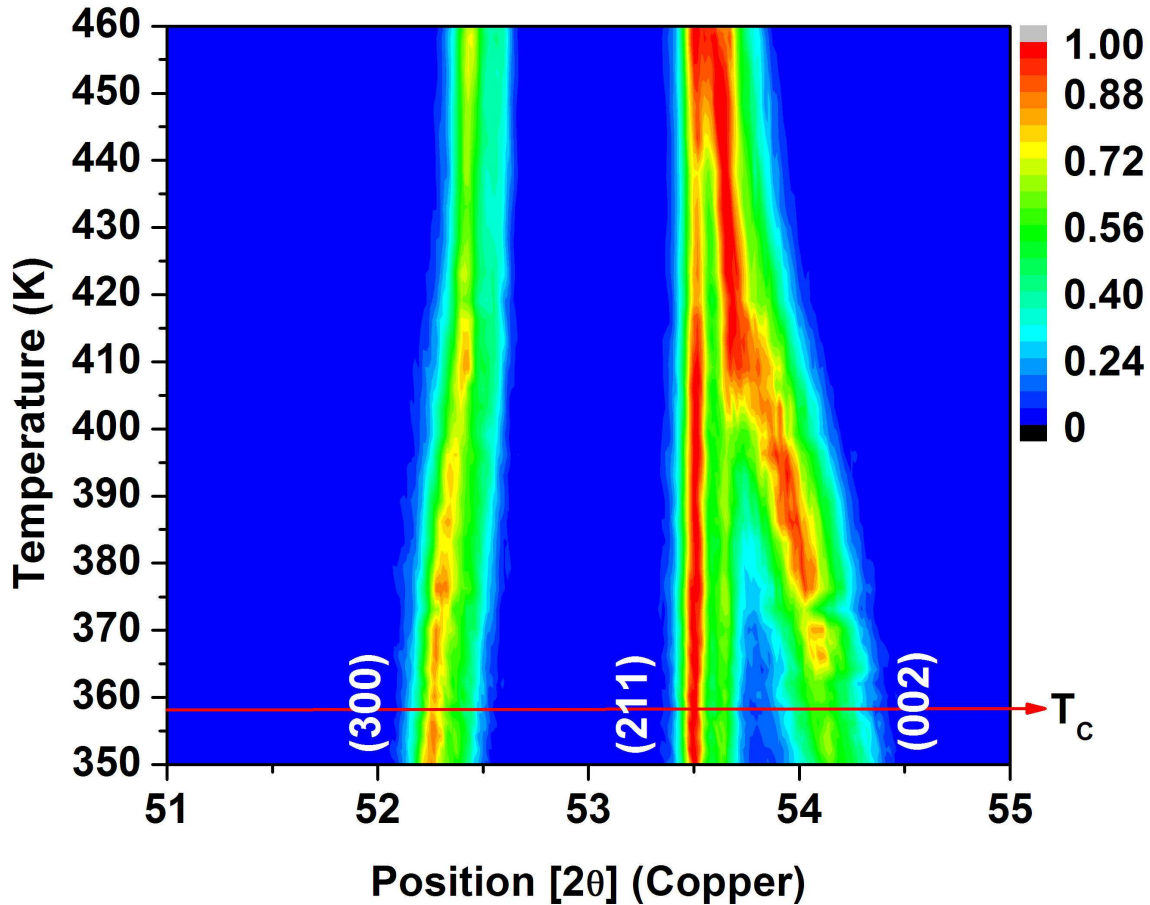


Figure 7.6 Contour plot of the angle change in the (300), (211) and (002) peaks versus temperature for the $\text{Mn}_{0.6}\text{Fe}_{1.4}\text{P}_{0.8}\text{Ge}_{0.2}$ sample, demonstrating the slow and smooth character of the magneto-elastic transition. The transition temperature of this sample has been determined as being 358 K by DSC measurements. The bar on the right of the figure represents the normalized peak intensity.

7.4.2 $(\text{Mn,Fe})_{1.95}(\text{P,Ge})$ system

In contrast to the $(\text{Mn,Fe})_2(\text{P,Ge})$ system the $(\text{Mn,Fe})_{1.95}(\text{P,Ge})$ system does not seem to be so negatively influenced by the increase of Fe content, as it maintains a usable sharp transition up to high Fe concentrations.

This stability has enabled us to reduce the Ge content down to Ge=0.12 (less than half of the value used by Trung *et al.* [1]). Lowering the Ge concentration beyond

this point was found to trigger antiferromagnetic behavior in this system. This concentration is therefore considered as the lowest possible Ge content in which this system still displays a sharp Ferro-Paramagnetic transition, as indicated in Figure 7.7.

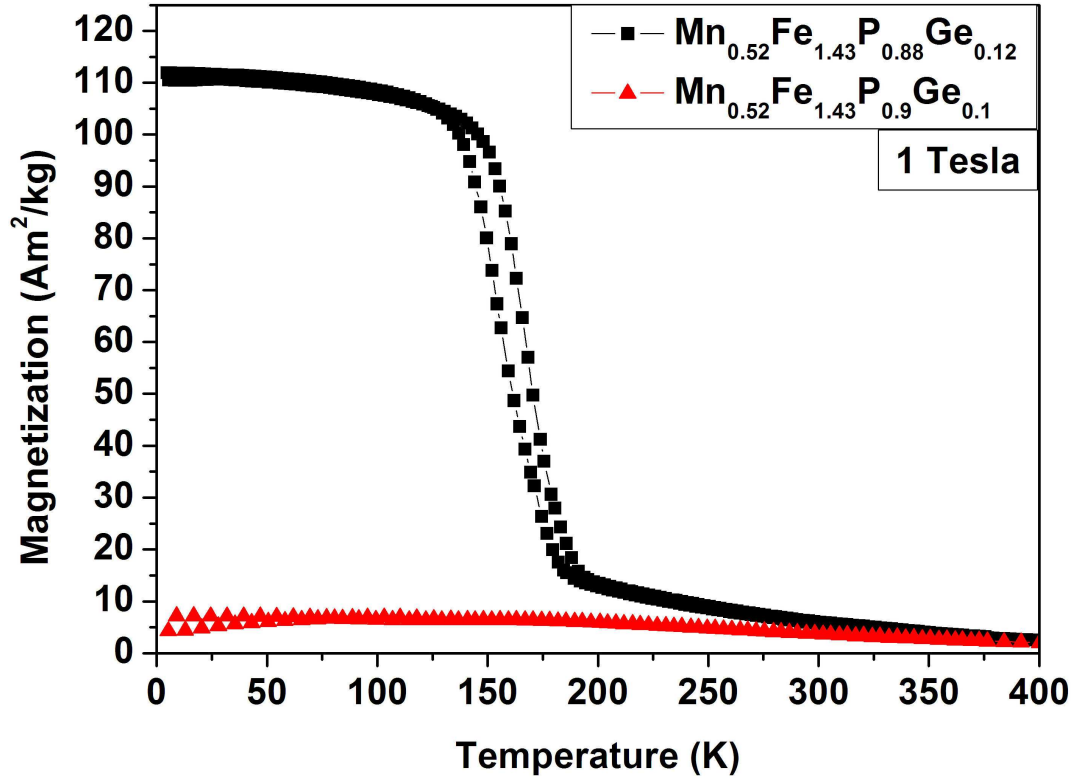


Figure 7.7 Comparison between the Ge=0.12 and Ge=0.1 magnetization versus temperature measurements in the $(\text{Mn,Fe})_{1.95}(\text{P,Ge})$ system.

Having determined a usable minimum Ge concentration, we were able to tune T_C by changing Fe content, in accordance with the behavior observed for the $(\text{Mn,Fe})_2(\text{P,Ge})$ system displayed in Figure 7.4. This, however, turned out to be challenging, as in this concentration range properties such as sharpness or magnetic behavior are extremely sensitive to small compositional changes. In this sense, while maintaining Ge=0.12, we have determined the Fe maximum (and consequently the maximum T_C) in which this system still displays usable characteristics for a magnetic cooling device, as shown in Figure 7.8a.

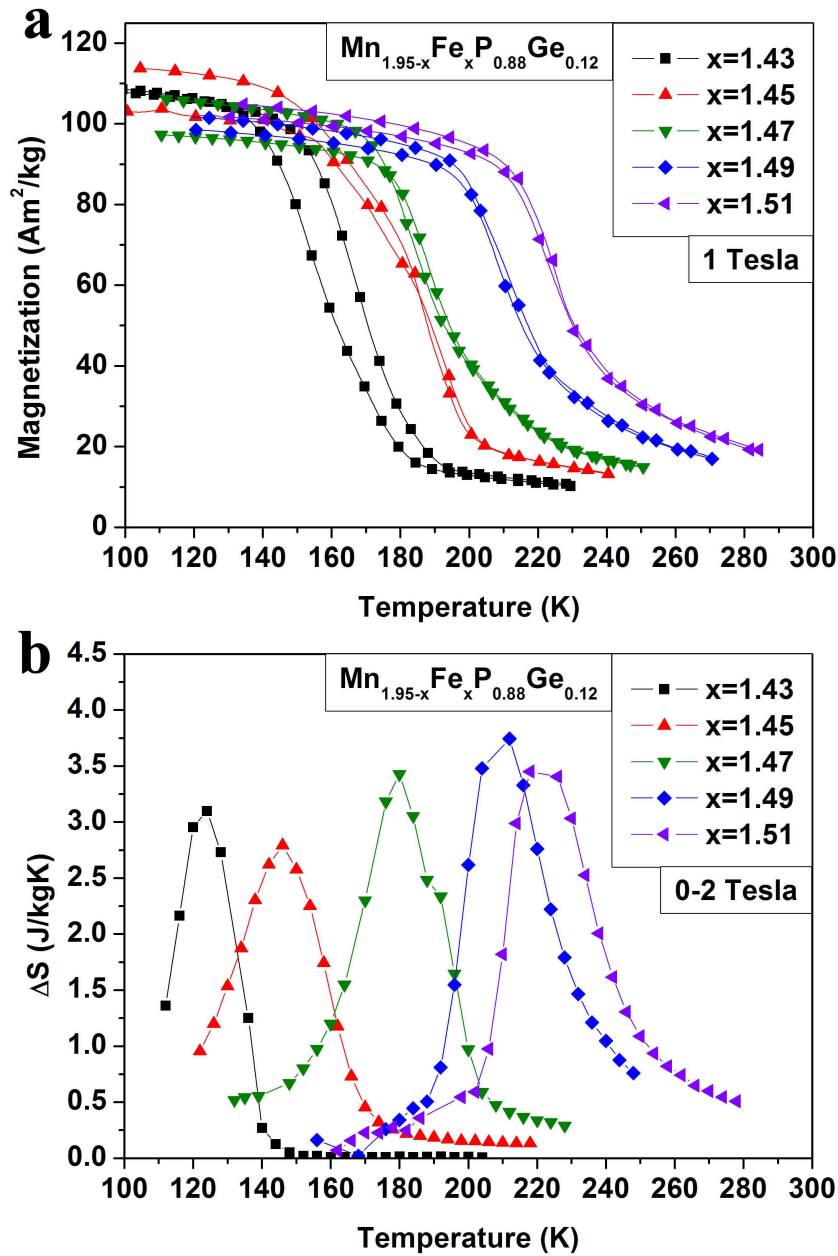


Figure 7.8 a) Magnetization versus temperature curves for $\text{Mn}_{2-x}\text{Fe}_x\text{P}_{0.88}\text{Ge}_{0.12}$ samples for an applied magnetic field of 1 Tesla, demonstrating the change in T_C with increasing Fe content; b) Magnetic entropy change for $\text{Mn}_{2-x}\text{Fe}_x\text{P}_{0.88}\text{Ge}_{0.12}$ samples for an applied magnetic field of 2 Tesla.

We have thus determined a maximum T_C of about 225 K for a maximum Fe content of 1.51, for the determined Ge minimum (0.12).

Due to the partial loss of magnetic transition sharpness (when compared with Mn-rich compounds), the magnetic entropy change calculated for these samples, displayed in Figure 7.8b, is not as high as those measured previously by Trung *et al.* [1], but are comparable with those observed for pure Gd metal [17].

Although these results may seem less ideal than the previously mentioned ones from Trung *et al.* [1], they represent a trade off between cheaper samples and improved mechanical properties, which nonetheless still possess many possible applications in low temperature applications or in magnetocaloric material cascading in practical cooling devices.

7.5 Permanent magnet potential

Surprisingly, during the course of this study certain limited compositional areas of Mn and Ge poor $(\text{Mn,Fe})_{1.95}(\text{P,Ge})$ have been found to possess very exciting magnetic properties, which may indicate a definite potential for future permanent magnet applications.

The applicability for permanent magnets in modern society are widespread. These are used in a massive array of modern appliances, from the mundane to the cutting edge in science and industry: everything from motors and generators, dynamos, microwave generators, loudspeakers, communications and electronics, aeronautics, electric cars, nuclear industry, satellite electric power systems, measuring instruments and sensors, medical devices (MRI), latching and holding devices, separation equipment (such as water and oil purifiers) and so on [18-21].

Among the families of materials used for such application we can cite the Alnico magnets (Al-Ni-Co) [18, 21, 22], the Ba or Sr hexaferrites, characterized by lower flux densities and higher coercivities than the Alnicos [21] and, as the most modern and widely used, the rare earth-transition metal magnets (on which we can group Sm-Fe, Nd-Fe-B and Sm-Co magnets) [18, 20, 22-24].

Given the current demand for high-performance magnets the most widely used are the rare earth-transition metal compounds, particularly the Nd-Fe-B, as can be observed in Figure 7.9. These are relatively expensive materials, as a consequence of the limited yearly rare earth production rate [19, 25]. Such a situation logically makes the research on novel permanent magnet materials that do not contain rare earth elements an exciting and extremely relevant field of investigation.

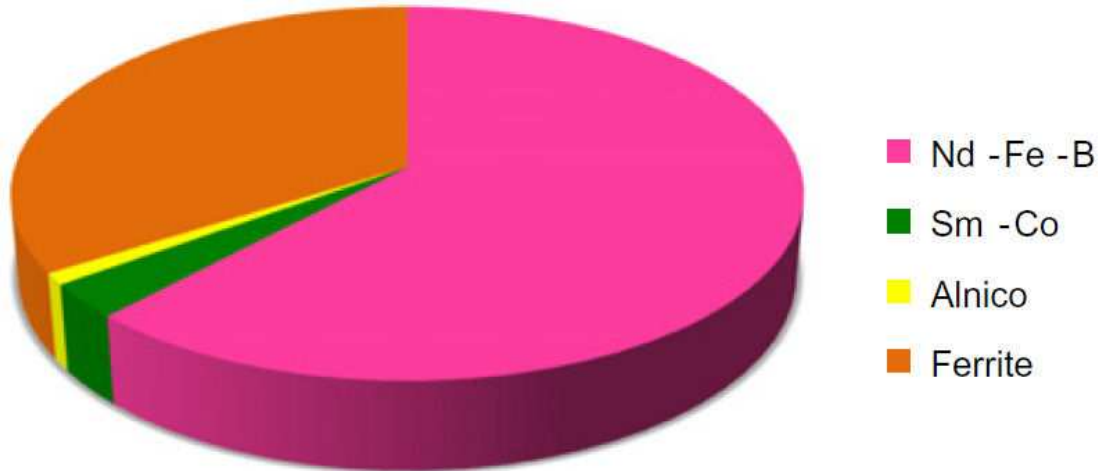


Figure 7.9 Breakdown of the permanent magnet world market [19].

The magnetization versus temperature in field cooled (FC) and zero field cooled (ZFC) conditions for the $\text{Mn}_{0.1}\text{Fe}_{1.85}\text{P}_{0.9}\text{Ge}_{0.1}$ sample show a striking difference in magnetic behavior. The FC curve displays a considerably higher magnetization than the ZFC curve. Given that this sample consisted of an irregular multigrain powder, such a behavior may indicate the presence of strong magnetic anisotropy in this compound.

This observation suggests that there is an easy direction in this compound along which the magnetic moments will preferably align, an essential property of a permanent magnet.

As the relevant intrinsic properties that should be displayed by a material to make it relevant for permanent magnet applications can be listed as (1) a high saturation magnetization, (2) strong magneto-crystalline anisotropy with a uniaxial crystal structure, (3) a high T_C [26] and (4) a high coercivity field, such a result naturally becomes relevant.

Pure Fe_2P is in fact currently studied as a possible alternative to the current rare earth based magnets, given that it is a cheap compound which exhibits a considerable magnetic anisotropy [25, 27]. This property, however, is not sufficient for an effective application, as a significant drawback of this material is its low T_C , (about 217 K [28]), and attempts have been made to raise this value by elemental substitution (such as P by Si). This however frequently results in the loss of the hexagonal $P\bar{6}2m$ structure in favor of the orthorhombic $Imm2$ structure [27], as shown in Figure 7.10.

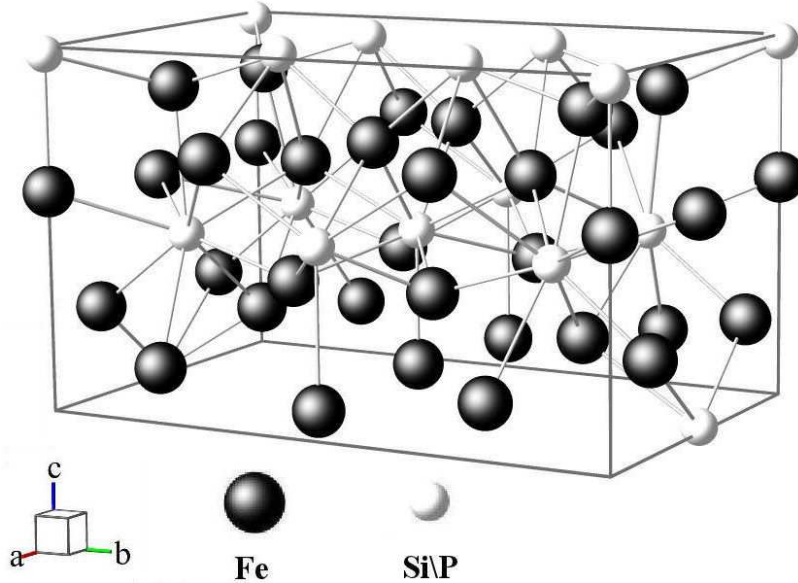


Figure 7.10 *Imm2* orthorhombic structure found for the $\text{Fe}_2(\text{Si,P})$ system.

The mentioned $\text{Mn}_{0.1}\text{Fe}_{1.85}\text{P}_{0.9}\text{Ge}_{0.1}$ sample, which contains small amounts of both Mn and Ge, was found to have a high T_C , while still maintaining the desired $P\bar{6}2m$ hexagonal structure. Such a combination of factors indeed changes the outlook on Fe_2P based permanent magnets, as for the first time we have a reliable direction in which to explore the possibility of future magnetic applications.

In order to further study this phenomenon, two different types of magnetization versus field measurements were performed. All samples that display this discrepancy between FC and ZFC measurements were reduced to a fine powder and, firstly, mixed with varnish, to solidify the powder with random grain orientation (random powder). For comparison, the same process was followed but the varnish solidified while the powder was under a magnetic field, meaning that the grains were able to align with this field (field oriented powder). Figure 7.11 displays the results from these measurements.

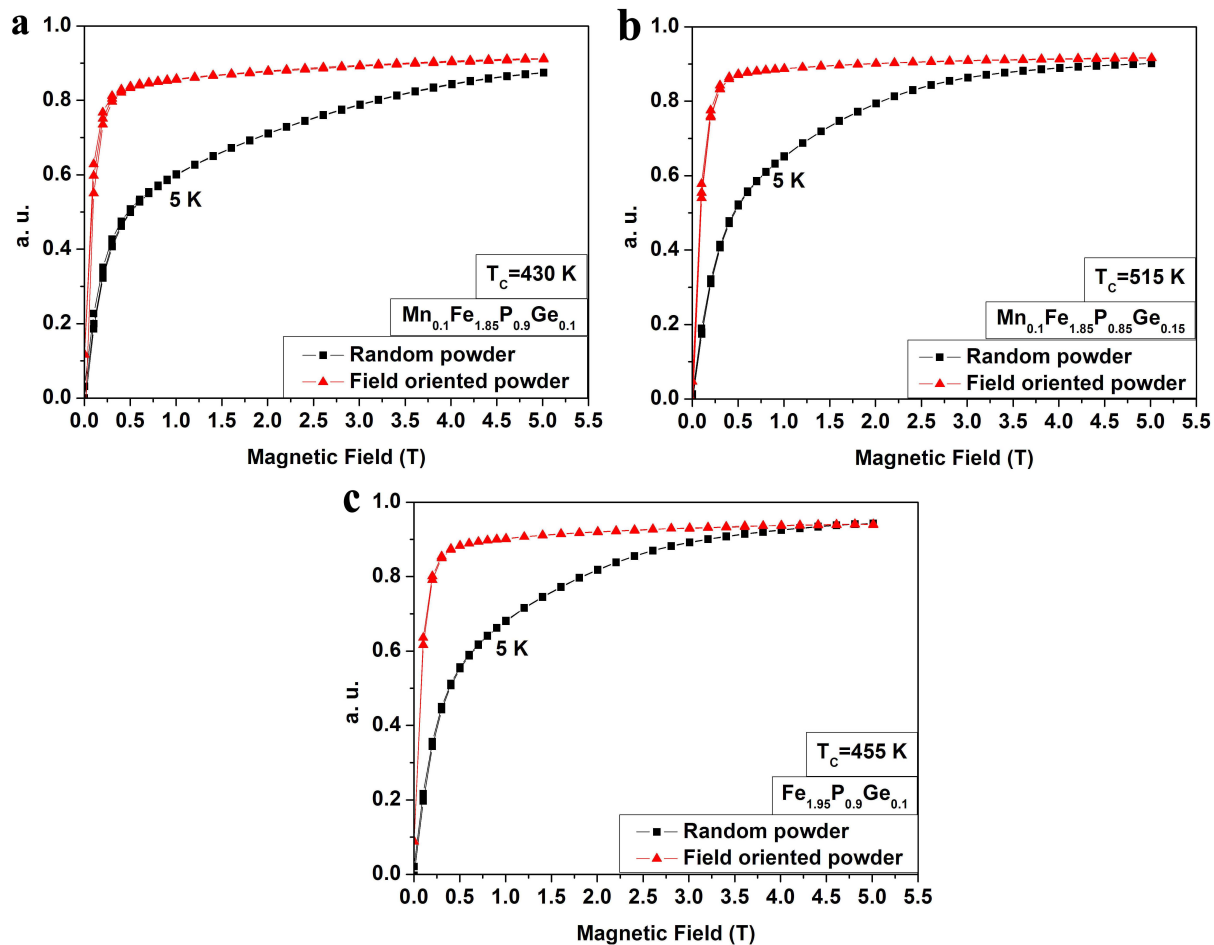


Figure 7.11 a) Magnetization versus applied magnetic field at 5 K for the $\text{Mn}_{0.1}\text{Fe}_{1.85}\text{P}_{0.9}\text{Ge}_{0.1}$ sample. As can be observed there is a clear difference in magnetic behavior between the field aligned and the randomly aligned sample, indicating the presence of strong magnetic anisotropy; b) Magnetization versus applied magnetic field at 5 K for the $\text{Mn}_{0.1}\text{Fe}_{1.85}\text{P}_{0.85}\text{Ge}_{0.15}$ sample, demonstrating a similar, but not as pronounced, magnetic anisotropy as the $\text{Mn}_{0.1}\text{Fe}_{1.85}\text{P}_{0.9}\text{Ge}_{0.1}$ sample; c) Magnetization versus applied magnetic field at 5 K for the $\text{Fe}_{1.95}\text{P}_{0.9}\text{Ge}_{0.1}$ sample, also demonstrating the same clear difference in magnetic behavior but giving a good insight on the influence of the small Mn content present on the $\text{Mn}_{0.1}\text{Fe}_{1.85}\text{P}_{0.9}\text{Ge}_{0.1}$ sample

The clear difference in magnetic behavior between the random powder and the field-oriented powder suggests a strong anisotropy, associated with an easy axis that allows for a rapid magnetic saturation.

Analyzing the results depicted in Figure 7.11 it can be concluded that indeed Ge is a fundamental element in the occurrence of this behavior. Comparing the $\text{Mn}_{0.1}\text{Fe}_{1.85}\text{P}_{0.9}\text{Ge}_{0.1}$ and the $\text{Mn}_{0.1}\text{Fe}_{1.85}\text{P}_{0.85}\text{Ge}_{0.15}$ samples, we notice a reduction in magnetic anisotropy in the later, while completely removing Ge appears to simply remove the occurrence of this behavior [29], giving room for other already studied

states of metamagnetism and antiferromagnetism related to the presence of small amounts of Mn in this system [27, 30].

The small amount of Mn in these samples does seem to play some part in this behavior given that the $\text{Fe}_{1.95}\text{P}_{0.9}\text{Ge}_{0.1}$ sample, while still possessing a clear magnetic behavior difference, reaches its saturation magnetization much more rapidly in its random powder measurement than in the other samples. This indicates that the small amount of Mn present in the other two samples does contribute to the large magneto-crystalline anisotropy.

This field alignment was further verified by X-ray diffraction. Measurements were conducted on the random powder and on the magnetic field aligned powder of the $\text{Mn}_{0.1}\text{Fe}_{1.85}\text{P}_{0.85}\text{Ge}_{0.15}$ sample, as shown in Figure 7.12.

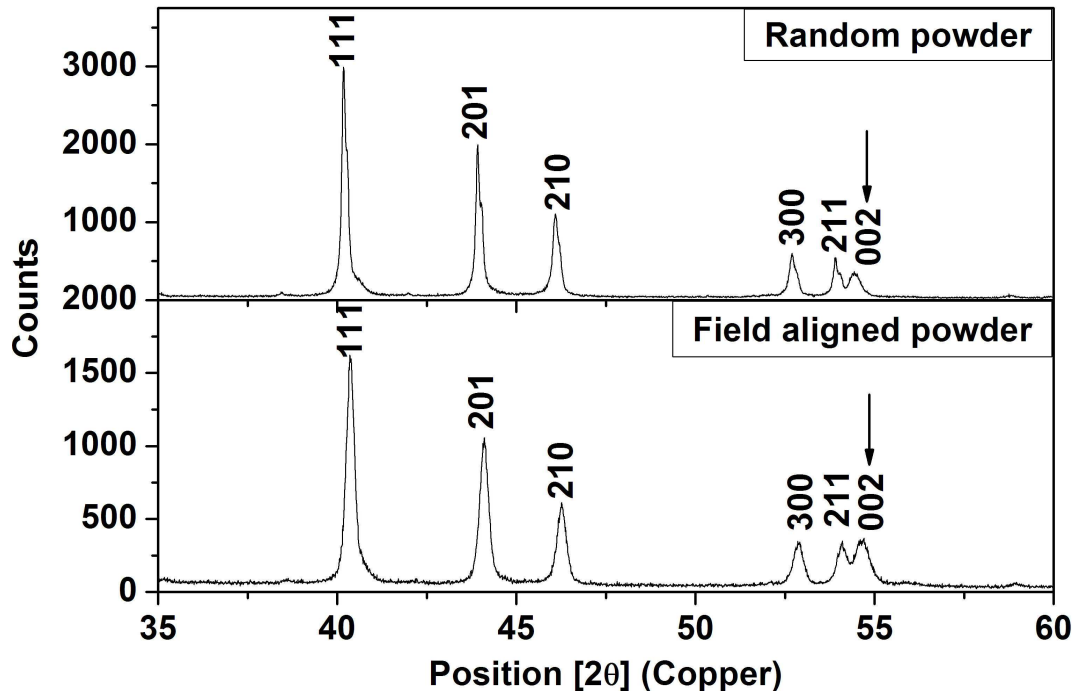


Figure 7.12 X-Ray diffraction measurements of $\text{Mn}_{0.1}\text{Fe}_{1.85}\text{P}_{0.85}\text{Ge}_{0.15}$. The top graph shows a regular randomly aligned powder and the bottom one a field aligned powder, in which it is possible to observe an increase in the intensity of the (002) reflection, indicating an alignment along the c -direction.

These X-ray diffraction measurements, which show a typical hexagonal Fe_2P structure, reveal a clear increase in the (002) peak intensity relatively to the other peaks, which indicates the presence of an easy axis along the c -direction, once again underlying the presence of magnetic anisotropy in this sample and its possible viability as a permanent magnet.

The only drawbacks of this surprising discovery so far are the obvious lack of coercivity, or a broad hysteresis loop, a property which plays a crucial role in the ability of a magnet to resist thermal demagnetization, and the relatively low T_C of 430 K for the $\text{Mn}_{0.1}\text{Fe}_{1.85}\text{P}_{0.9}\text{Ge}_{0.1}$ sample. This T_C value, although much higher than that of pure Fe_2P [28], is still too low for practical permanent magnet applications.

This is the first time that such a concrete permanent magnet potential has been observed in an Fe_2P -type system. Such an observation cannot be overlooked, and it may now open new and exciting opportunities for novel permanent magnet alloys in this rich family of materials. Further study and research is highly desirable.

7.6 Conclusions

Given their attractive mechanical properties, a study on the $(\text{Mn,Fe})_2(\text{P,Ge})$ and $(\text{Mn,Fe})_{1.95}(\text{P,Ge})$ systems was conducted with the purpose of making such systems economically viable for magnetic cooling applications.

The mapping of a limited compositional range of the $(\text{Mn,Fe})_2(\text{P,Ge})$ system revealed a strong non-linear T_C dependence with both Fe and Ge contents, giving rise to the possibility to reduce the amount of expensive Ge by the increase of the Fe content. Such a map also offers an understanding on the general behavior of Fe_2P -type systems at high Fe concentrations.

The magnetic behavior of Fe-rich $(\text{Mn,Fe})_2(\text{P,Ge})$ is quite complex, with the discovery of an unidentified magnetic phase at low Ge concentrations. Unexpectedly, the increase in Fe content also gives rise to a decrease in the Ferro-Paramagnetic transition sharpness, symptomatic with the disappearance of the first-order behavior of this transition, an unfortunate characteristic that makes this system unviable for MCE applications.

The $(\text{Mn,Fe})_{1.95}(\text{P,Ge})$ system maintains a sharp transition with a high magnetic moment at high Fe concentrations, with the possibility of lowering Ge content down to 0.12, and thereby effectively reducing the cost of this system to under half of the originally studied compositions. Given the difficult balance of magnetic properties and element concentrations, T_C cannot, however, be raised above 225 K, but it is nonetheless easily tuned below this temperature, in a region where there aren't many attractive magnetocaloric materials.

Remarkable and exciting properties were detected in a limited concentration range of Mn and Ge poor $(\text{Mn,Fe})_{1.95}(\text{P,Ge})$, which may indicate a tangible possibility

to use Fe₂P-type alloys for permanent magnet applications. This result points to a new and exciting field of permanent magnet research.

References

- [1] N. T. Trung, Z. Q. Ou, T. J. Gortenmulder, O. Tegus, K. H. J. Buschow, and E. Brück, *Appl. Phys. Lett.* 94, 102513 (2009).
- [2] N. H. Dung, L. Zhang, Z. Q. Ou, and E. Brück, *Appl. Phys. Lett.* 99, 092511 (2011).
- [3] H. Yabuta, K. Umeo, T. Takabatake, K. Koyama and K. Watanabe, *J. Phys. Soc. Jpn.* 75 (2006) 113703.
- [4] H. Yabuta, K. Umeo, T Takabatake, L. Chen, Y. Uwatoko, *J. Magn. Magn. Mater.* 310 (2007) 1826.
- [5] A. Yan, K. H. Müller, L. Schultz, and O. Gutfleisch, *J. Appl. Phys.* 99 (2006) 08K903.
- [6] W. Dagula, O. Tegus, B. Fuquan, L. Zhang, P. Z. Si, M. Zhang, W. S. Zhang, E. Brück, F. R. de Boer and K. H. J. Buschow, *IEEE T. Magn.* 41 (2005) 2778.
- [7] M. Yue, Z. Q. Li, X.B. Liu, H. Xu, D. M. Liu, J. X. Zhang, *J. Alloy. Compd.* 493 (2010) 22.
- [8] M. T. Sougrati, R. P. Hermann, F. Grandjean, G. J. Long, E. Brück, O. Tegus, N. T. Trung and K. H. J. Buschow, *J. Phys.: Condens. Mat.* 20 (2008) 475206.
- [9] M. Yue, Z. Q. Li, X. L. Wang, D. M. Liu, J. X. Zhang, and X. B. Liu, *J. Appl. Phys.* 105 (2009), 07A915.
- [10] M. Yue, Z. Q. Li, H. Xu, Q. Z. Huang, X. B. Liu, D. M. Liu, and J. X. Zhang, *J. Appl. Phys.* 107 (2010), 09A939.
- [11] D. Liu, M. Yue, J. Zhang, T. M. McQueen, J. W. Lynn, X. Wang, Y. Chen, J. Li, R. J. C., Xubo L., Z. Altounian, and Q. Huang, *Phys. Rev. B* 79 (2009) 014435.
- [12] N. H. Dũng, *Moment Formation and Giant Magnetocaloric Effect in Hexagonal Mn-Fe-P-Si Compounds*, Delft University of Technology (2012), PhD Thesis, Chapter 8.
- [13] N. T. Trung, *First-order phase transitions and giant magnetocaloric effect*, Delft University of Technology (2010) PhD thesis, Chapter 4.
- [14] E. Brück, O. Tegus, L. Zhang, X. W. Li, F.R. de Boer and K.H.J. Buschow, *J. Alloy. Compd.* 383 (2004) 32.
- [15] E. Brück, *J. Phys. D: Appl. Phys.* 38 (2005) R381.

- [16] O. Tegus, B. Fuquan, W. Dagula, L. Zhang, E. Brück, P. Z. Sia, F. R. de Boer, K. H. J. Buschow, *J. Alloy. Compd.* 396 (2005) 6.
- [17] Tegusi, *Novel Materials for Magnetic Refrigeration*, University of Amsterdam (2003), PhD Thesis, Chapter 5.
- [18] J. M. D. Coey, *J. Magn. Magn. Mater.* 248 (2002) 441.
- [19] J. M. D. Coey, *Scripta. Mater.* 67 (2012) 524.
- [20] Z. Zhang, X. Song, Y. Qiao, W. Xu, J. Zhang, M. Seyring and M. Rettenmayr, *Nanoscale* 5 (2013) 2279.
- [21] J. E. Gould, *IEEE T. Magn.* 5 (1969) 812.
- [22] S. Sugimoto, *J. Phys. D: Appl. Phys.* 44 (2011) 064001.
- [23] M. Sagawa, S. Fujimura, N. Togawa, H. Yamamoto, and Y. Matsuura, *J. Appl. Phys.* 55 (1984) 2083.
- [24] J. M. D. Coey, *J. Magn. Magn. Mater.* 140 (1995) 1041.
- [25] M. Costa, O. Grånäs, A. Bergman, P. Venezuela, P. Nordblad, M. Klintonberg and O. Eriksson, *Phys. Rev. B* 86 (2012) 085125.
- [26] S. J. Collocott, J. B. Dunlop, H. C. Lovatt and V. S. Ramsden, *Mater. Sci. Forum* 315-317 (1999) 77.
- [27] L. Severin, L. Häggström, L. Nordström, Y. Andersson and B. Johansson, *J. Phys.: Condens. Mat.* 7 (1995) 185.
- [28] O. Beckman, L. Lundgren, P. Nordblad, P. Svedlindh, A. Törne, Y. Andersson and S. Rundqvist, *Phys. Scripta* 25 (1982) 679.
- [29] B. K. Srivastava, T. Ericsson, L. Häggström, H. R. Verma, Y. Andersson and S. Rundqvist, *J. Phys. C Solid State* 20 (1987) 463.
- [30] R. Fruchart, A. Rogers and J. P. Senateur, *J. Appl. Phys.* 40 (1969) 1250.

Chapter 8

In field microcalorimetry measurements on polycrystalline Fe₂P

8.1 Introduction

As exemplified by the previous Chapters, the core theme of the material research performed on magnetocaloric materials in Delft is focused on Fe₂P-type alloys [1-7].

The remarkable magnetocaloric potential found in these compounds is linked to the realization that they maintain many of the same properties as the parent compound Fe₂P, but can easily be tuned towards more practical ends given its particular sensitivity to stoichiometric changes and synthesis methods.

The magnetic properties of Fe₂P itself have been widely studied in the past, for permanent magnet applications, as mentioned in Chapter 7, or for pure academic interest. Still, a great deal of uncertainty and speculation has hovered over this compound precisely given its extreme sensitivity to stoichiometry and to external magnetic fields, which give rise to incompatible and disparate results in different publication [8, 9].

Given the importance currently placed on this compound there is a need for a complete assessment and understanding of the specific heat of Fe₂P under a magnetic field. These measurements are inspired by the recent work performed by Caron *et al.* [10].

8.2 Material overview

Fe₂P crystallizes in the already discussed hexagonal $P\bar{6}2m$ structure. We have two magnetic sub-lattices, both occupied by Fe (Fe-I in the tetragonal $3f$ and Fe-II in the pyramidal $3g$ site) and P (the dissimilar $2c$ and $1b$ sites) atoms [10, 11]. In this arrangement Fe-I and Fe-II have a total moment around $2.9 \mu_B/\text{f.u.}$, with Fe-I having a moment close to $1 \mu_B/\text{f.u.}$ and Fe-II close to $2 \mu_B/\text{f.u.}$ [10, 12-14]. Information regarding moment orientation can be found in Chapter 7 section 5.

Besides its first order ferro to paramagnetic transition at 217 K, this compound also exhibits a metamagnetic transition at relatively low magnetic fields suggesting two magnetic solutions to be nearly degenerate in energy [15].

Under high pressures (1.5 GPa), this compound turns antiferromagnetic [16]. Senateur *et al.* claim it actually undergoes a structural transition to the $Imm2$ structure (Figure 7.10) with the application of high temperatures and external pressure (8 GPa and 800°C) [17].

This compound displays a great structural sensitivity to alloying with a third element in terms of T_C , magnetic moment tuning [15, 18] and structural changes, which frequently gives rise to the already mentioned orthorhombic $Imm2$ structure and metamagnetic and antiferromagnetic states [15, 18].

Previous heat capacity measurements have shown that the already mentioned first-order phase transition is the only observable magnetic contribution, manifesting itself as a sharp and symmetric peak at T_C [19].

Focusing on data for the polycrystalline samples displayed in the study by Caron *et al.* [10], for fields below 0.05 T this transition presents the characteristics of a first-order transition, which rapidly changes into a broader second-order transition when the external applied field is increased, a phenomenon that is also accompanied by an increase in T_C , as displayed in Figure 8.1.

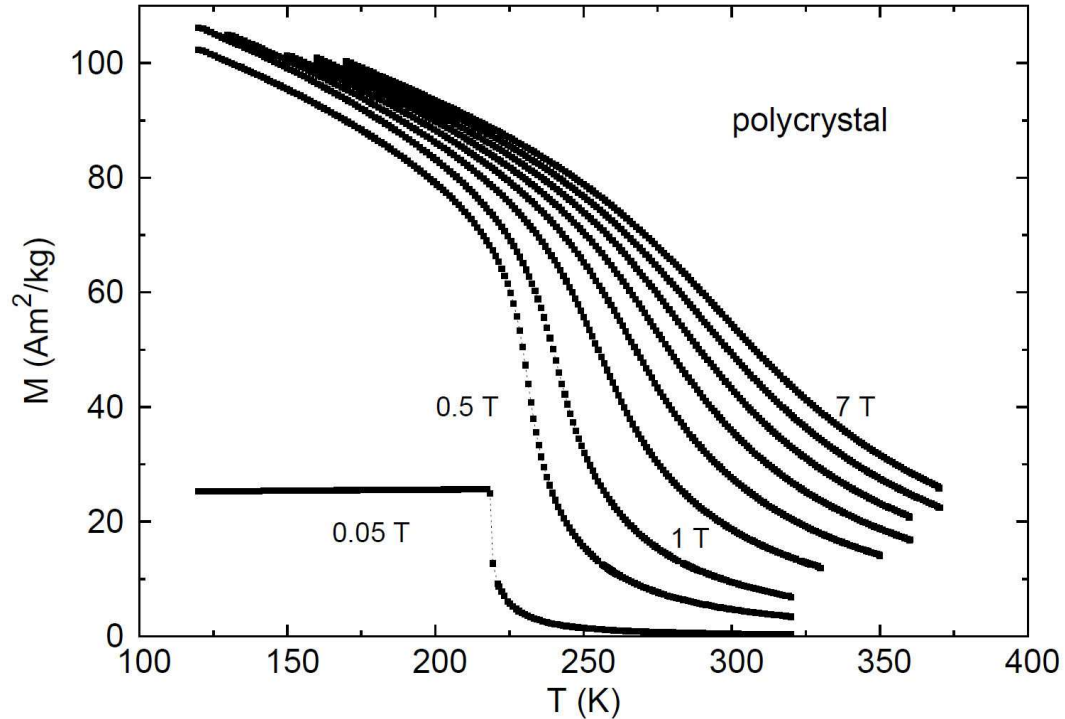


Figure 8.1 Magnetization vs temperature at various fields for polycrystalline Fe₂P [10].

In order to acquire a deeper understanding on the nature of this transition (fundamental to the work developed in Delft), the objective of the current study is to re-investigate the results presented in Figure 8.1, using the microcalorimetry setup described in Chapter 4.

8.3 Experimental procedure

The sample used for this study was the same Fe₂P sample produced by the drop synthesis technique as described by Carlsson *et al.* [20], which was also used by Caron *et al.* [10] in the acquisition of the data displayed in Figure 8.1. The used copper reference consisted of a small 99.9% pure spherical particle from Alfa Aesar.

The details of both these samples can be found in Table 8.1.

Table 8.1 Details regarding the sample and reference used in the measurements for the current chapter.

	Mass (mg)	Error (mg)	Grease (mg)	Error (mg)
Sample	0.21	0.02	Grease mass was too small to be registered by our balance, none the less we should consider a maximum value of 0.02 mg, the balance error.	
Reference	0.23	0.02		

The measurement procedure consisted of a continuous ramp with a heating rate of 0.2 K/min with a constant applied magnetic field, ranging from 0 T to 0.8 T with steps of 0.1 T.

8.4 Results and discussion

The results obtained from the above mentioned measurements revealed to be a challenge to interpret. From 0 to 0.3 T the observed transition displayed the characteristics of a first-order phase transition, although a slight decrease in the specific heat peak and sharpness is detectable with increasing field, as demonstrated in Figure 8.2. While this particular magnetic behavior falls in line with the results previously obtained by Caron *et al.* [10] (shown in Figure 8.1), the transition temperature did not seem to be influenced by the application of an external magnetic field, maintaining a stable and strangely high value of 231 K.

This temperature inconsistency may be due to instrumental issues. The Lakeshore 331 Temperature Controller possesses a thermal correction algorithm consisting of reversing the polarity of the current source every other reading, a procedure referred to as “Reversal Mode”. In this way the average of the positive and negative sensor readings cancel the thermal EMF (electro motive force) voltage, enabling for more accurate measurements. Unfortunately, our original temperature calibration (displayed in Figure 4.3) was done without resource to the “Reversal Mode” function, which, on certain temperature ranges, may give rise to substantial temperature uncertainties.

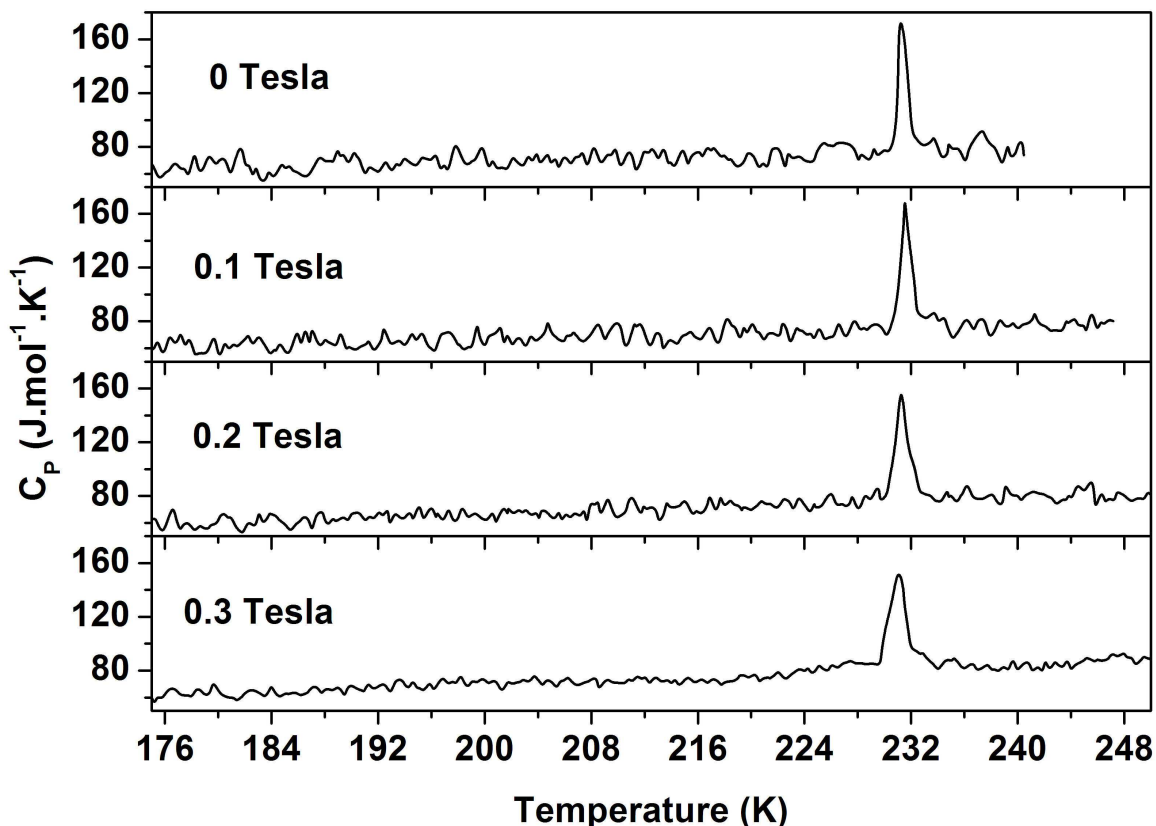


Figure 8.2 Fe₂P specific heat measurements taken in the experimental setup described in Chapter 4, with magnetic fields between 0 and 0.3 Tesla. The specific heat values for solid copper used to calculate the contribution of our reference and isolate the Fe₂P behavior in our data were taken from ref. [21].

For field values of 0.4 and 0.5 T there was a significant reduction in the sharpness and height of the transition peak, indicating the change from a first-order transition to a second-order transition, with T_C remaining constant. Only for a field of 0.6 T did the transition temperature finally move up to 232.5 K.

Measurements performed with higher fields proved to be unreliable as the transition peak became smaller than our instrumental noise.

The behavior described above can be observed in Figure 8.3.

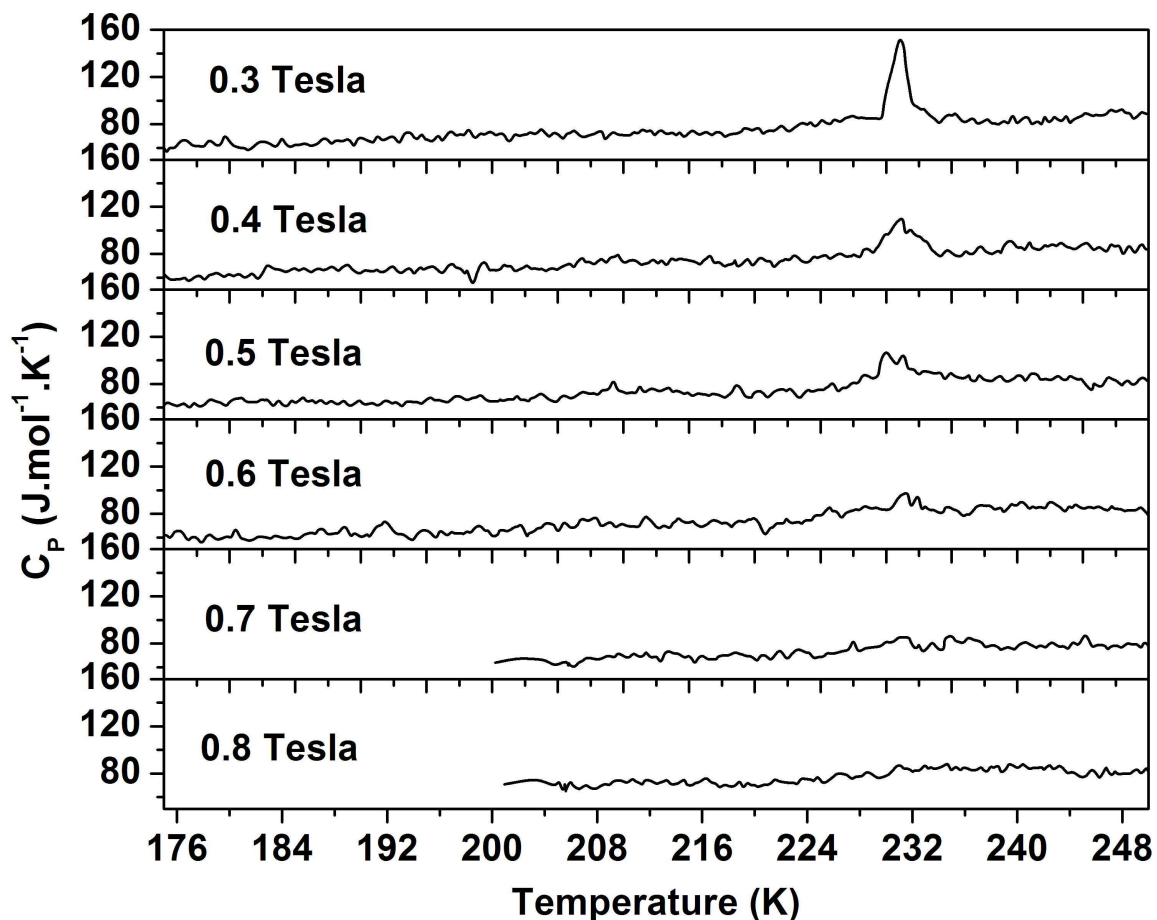


Figure 8.3 Fe_2P specific heat measurements taken in the experimental setup described in Chapter 4, with magnetic fields between 0.3 and 0.8 Tesla. The specific heat values for solid copper used to calculate the contribution of our reference and isolate the Fe_2P behavior in our data were taken from ref. [21].

These results can be interpreted in the light of Caron *et al.* [10], but only if we consider that they show the results of a single crystal sample with an applied magnetic field along its hard direction (perpendicular to the c axis).

This is a surprise, as the sample used was supplied to us as being polycrystalline. Further analysis of the results by Caron *et al.* [10] does suggest that this might not be the case. Figure 8.4 shows magnetization as a function of the magnetic field on polycrystalline and single-crystalline Fe_2P , both parallel and perpendicular to its easy direction.

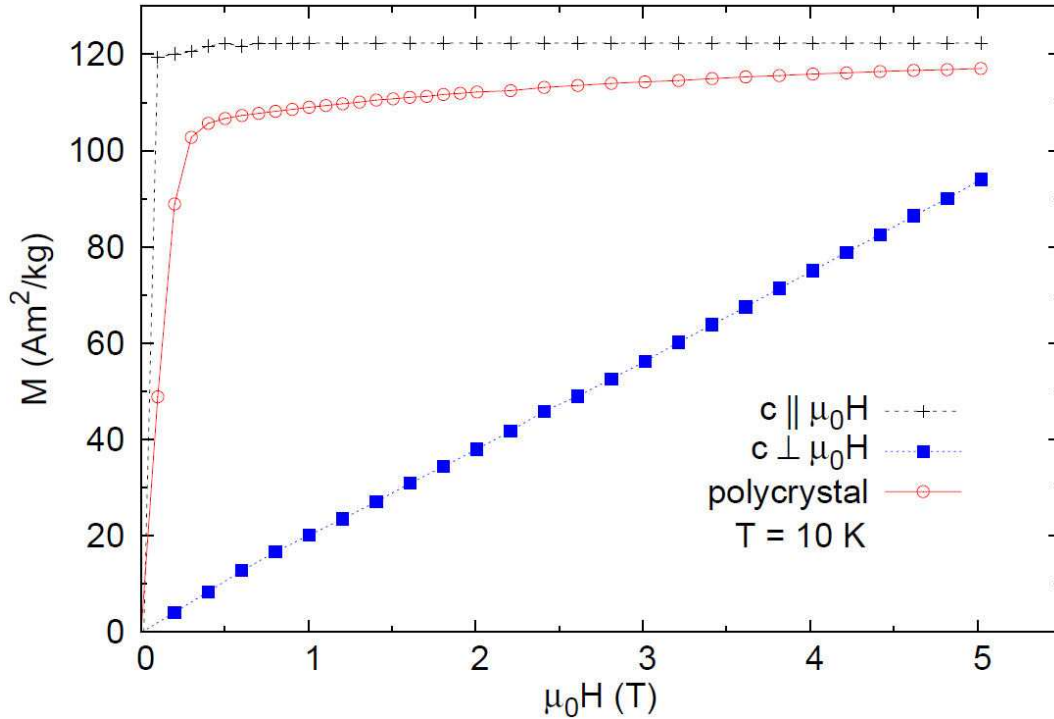


Figure 8.4 Magnetization vs magnetic field measurements on polycrystalline and single crystal Fe₂P, both parallel and perpendicular to its easy direction [10].

It should be noted that the results given by polycrystalline Fe₂P mimic the ones by the single crystal measured with a field parallel to the easy axis, which, should the sample in question be truly polycrystalline, is not expected.

What seems to be the case is that all samples taken to be polycrystalline are in fact single crystals or near-single crystals, which, given their small size, have a clearly predominant easy direction. Should our case be that of a truly polycrystalline sample, considering that this would have its various grains/crystals aligned along every possible direction, one would expect an initial magnetization value of 50% of that of a pure single crystal. The values for the polycrystalline sample in Figure 8.4 on the other hand amount to nearly 83% of the magnetization of the single crystal, signifying that the various grains/crystals composing this sample have an average misalignment of 34 degrees with the applied magnetic field.

Should this hypothesis be correct, it sheds a great deal of light on our current specific heat measurements, as they then represent measurements with an applied field along the hard axis (figures 8.2 and 8.3).

This difference in orientation between the applied magnetic field and the easy axis of the samples can be easily explained by the particularities of sample mounting in

both equipments used. The measurements of Figure 8.4, a were taken in a MPMS XL SQUID, on which samples are mounted “vertically”, with the applied magnetic field along the c axis of a single crystal, while the XEN-39328 microcalorimetry chips used for Figures 8.2 and 8.3 mount samples “horizontally”, which, when inserted into the AMI Cryostat of the experimental setup, places the easy axis perpendicular to the applied magnetic field, as demonstrated in Figure 8.5.

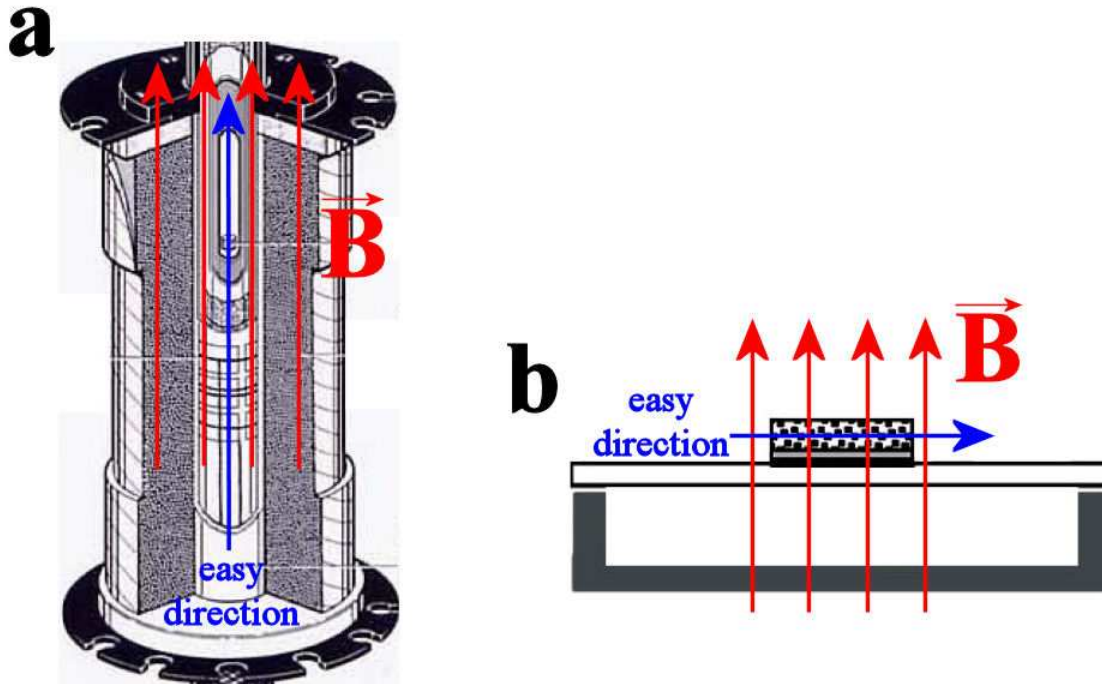


Figure 8.5 a) “Vertical” sample mounting on a MPMS XL magnetometer, placing the easy axis of a single crystal along the applied magnetic field direction (image taken from [22]); b) “Horizontal” sample mounting on the XEN-39328 microcalorimetry chips, placing the easy axis of a single crystal perpendicular to the applied magnetic field (image taken from [23]).

It should further be noted that our equipment and sample handling protocol is not prepared to make distinctions between easy and hard directions, and such a measurement was unintended.

8.5 Conclusions

In order to further investigate and understand the properties of Fe_2P , the parent compound of much of the material research being done in Delft on magnetocaloric materials, a series of microcalorimetry measurements were performed in a polycrystalline Fe_2P sample in the experimental setup described in Chapter 4.

Our results were unexpected and could only be understood if we consider that the sample measured was a single grain positioned in the equipment along its hard axis.

References

- [1] N. T. Trung, Z. Q. Ou, T. J. Gortenmulder, O. Tegus, K. H. J. Buschow and E. Brück, *Appl. Phys. Lett.* 94, 102513 (2009).
- [2] N. T. Trung, J. C. P. Klaasse, O. Tegus, D. T. Cam Thanh, K. H. J. Buschow and E. Brück, *J. Phys. D: Appl. Phys.* 43 (2010) 015002.
- [3] N. H. Dung, L. Zhang, Z. Q. Ou, and E. Brück, *Appl. Phys. Lett* 99 (2011) 092511.
- [4] N. H. Dung, Z. Q. Ou, L. Caron, L. Zhang, D. T. Cam Thanh, G. A. de Wijs, R. A. de Groot, K. H. J. Buschow, and E. Brück, *Adv. Energy Mater.* 1 (2011) 1215.
- [5] E. Brück, N. T. Trung, Z. Q. Ou and K. H. J. Buschow, *Scripta Mater.*, 67 (2012) 590.
- [6] N. H. Dung, L. Zhang, Z. Q. Ou, L. Zhao, L. van Eijck, A. M. Mulders, M. Avdeev, E. Suard, N. H. van Dijk, and E. Brück, *Phys. Rev. B* 86 (2012) 045134.
- [7] N. H. Dung, L. Zhang, Z. Q. Ou and E. Brück, *Scripta Mater.* 67 (2012) 975.
- [8] H. Fujii, T. Hokabe, T. Kamigaichi and T. Okamoto, *J. Phys. Soc. Jpn.* 43 (1977) 41.
- [9] L. Lundgren, G. Tarmohamed, O. Beckman, B. Carlsson and S. Rundqvist, *Phys. Scripta* 17 (1978) 39.
- [10] L. Caron, M. Hudl, V. Höglin, N. H. Dung, C. P. Gomez, M. Sahlberg, E. Brück, Y. Andersson, and P. Nordblad, *Phys. Rev. B* (to be published).
- [11] S. Rundqvist and F. Jellinek, *Acta Chem. Scand.* 13 (1959) 425.
- [12] D. Scheerlinck and E. Legrand, *Solid State Commun.* 25 (1978) 181.
- [13] J. Tobola, M. Bacmann, D. Fruchart, S. Kaprzyk, A. Koumina, S. Niziol, J. L. Soubeyroux, P. Wolfers and R. Zach, *J. Magn. Magn. Mater.* 157 (1996) 708.
- [14] M. Costa, O. Grånäs, A. Bergman, P. Venezuela, P. Nordblad, M. Klintonberg and O. Eriksson, *Phys. Rev. B* 86 (2012) 085125.
- [15] L. Severin, L. Häggström, L. Nordström, Y. Andersson and B. Johansson, *J. Phys.: Condens. Matter* 7 (1995) 185.

- [16] H. P. Scott, B. Kiefer, C. D. Martin, N. Boateng, M. R. Frank and Y. Meng, *High Pressure Res.* 23 (2008) 375.
- [17] J. P. Senateur, A. Rouault, R. Fruchart, J. J. Capponi, M. Perroux, *Mat. Res. Bull.* 2 (1976) 631.
- [18] R. Fruchart, A. Rogers and J. P. Senateur, *J. Appl. Phys.* 40 (1969) 1250.
- [19] O. Beckman, L. Lundgren, P. Nordblad, P. Svedlindh, A. Törne, Y. Andersson and S. Rundqvist, *Phys. Scripta* 25 (1982) 679.
- [20] B. Carlsson, M. Gölin and S. Rundqvist, *J. Solid State Chem.* 8 (1973) 57.
- [21] N. Dass, *J. Phys. Soc. Japan* 28 (1970) 251.
- [22] M. McElfresh, *Fundamentals of Magnetism and Magnetic Measurements – Featuring Quantum Design’s Magnetic Property Measurement System*, printed by Quantum Design (1994).
- [23] A. A. Minakov, S. B. Roy, Y. V. Bugoslavsky and L. F. Cohen, *Rev. Sci. Instrum.*, 76 (2005) 043906.

Addendum

Instruction Manual for the use and handling of the microcalorimetry setup described in Chapter 4

A.1 Hardware overview

The total sum of all equipment involved in the current microcalorimetry instrument can firstly be divided into two categories:

1) The setup

This consists of the AMI cryostat, equipped with a 9 Tesla 2 inch bore superconducting magnet, and the home made insert fitted for microcalorimetry measurements, represented in Figure A.1.

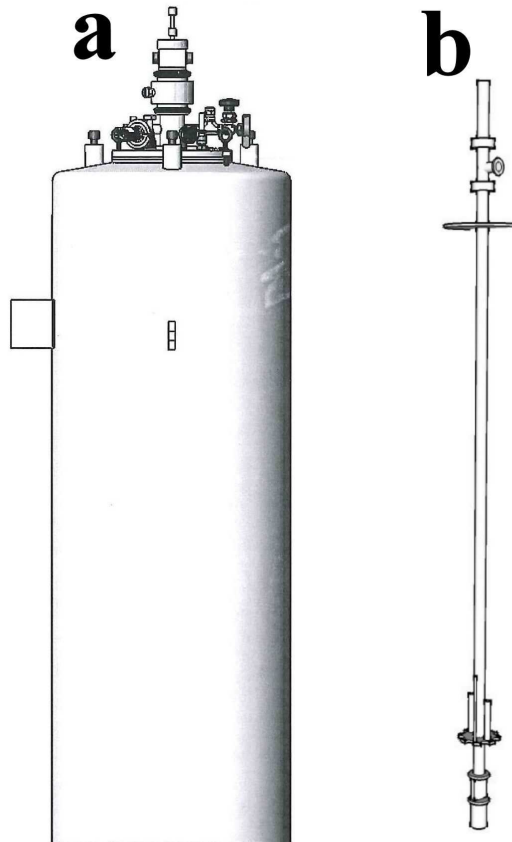


Figure A.1 a) Schematic representation of the AMI cryostat; b) Schematic representation of the home made insert.

2) The outside of the setup

This consists of the several measurement and control modules, namely:

Lakeshore 331 Temperature Controller – both used to measure the sample space temperature and supply power to the sample space heater(s), represented in Figure A.2;



Figure A.2 Lakeshore 331 Temperature Controller.

Keithley 2400 (Source Meter) – used to supply and measure voltage to the Xensor microcalorimetry chips heaters used in the setup, represented in Figure A.3. In the current case (relaxation measurement) it supplies a square wave.



Figure A.3 Keithley 2400 Source Meter.

Keithley 2000 (Multimeter) – used to measure the response of the Xensor microcalorimetry chip thermopiles to the square wave supplied by the Keithley 2400, the *de facto* relaxation measurements, represented in Figure A.4. It also measures the voltage across the chip heaters, which is mostly meant as a diagnosis tool.

Particular module used is also equipped with a Model 2001-SCAN 10-Ch Scanner Card which allows the instrument to change between different channels and measure different signals.



Figure A.4 Keithley 2000 6½-Digit Multimeter.

Keithley 2002 (Multimeter) – used to measure the difference between the thermopile voltages of the two Xensor microcalorimetry chips, represented in Figure A.5. Mostly meant as a diagnosis tool.



Figure A.5 Keithley 2002 8½-Digit High Performance Multimeter.

The above four modules are connected to a PC via a GPIB bus that enables for their remote control with the main interface software (see section A.3.1).

Model 430 Power Supply Programmer (AMI field control module) – used to apply and remove magnetic fields up to 9 Tesla, represented in Figure A.6. Capable of both setting magnetic field ramps and stable continuous fields.



Figure A.6 Model 430 Power Supply Programmer.

Model 4Q0625PS (AMI power Supply) – power supply for the 9 Tesla superconducting magnet, represented in Figure A.7. Controlled by the Model 430 Power Supply Programmer.

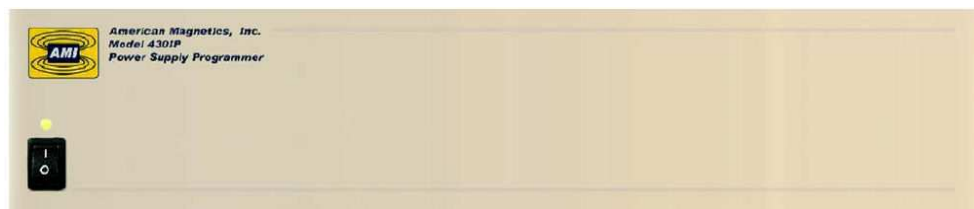


Figure A.7 Model 4Q0625PS.

Model 185 (liquid nitrogen meter) – used to monitor the liquid nitrogen level inside the AMI cryostat, represented in Figure A.8.

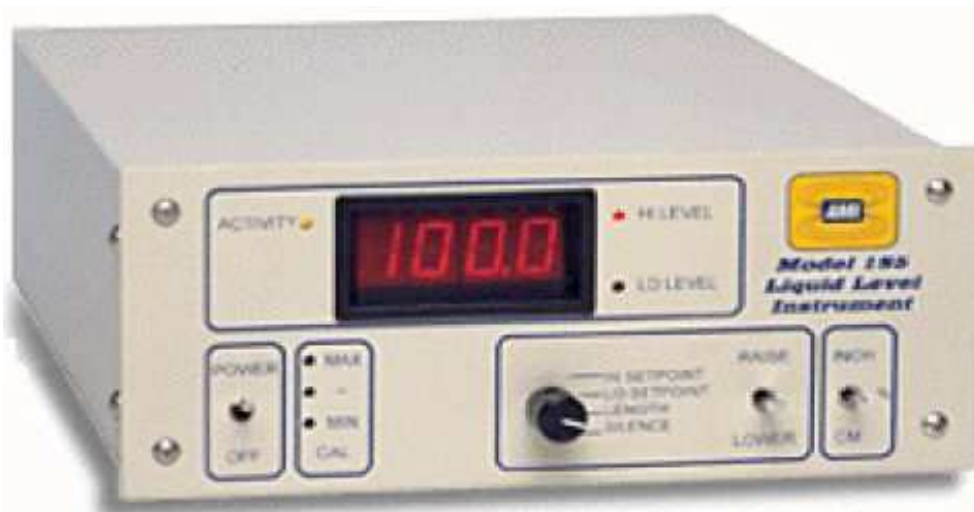


Figure A.8 Model 185 Liquid Nitrogen Level Monitor

Model 135 (liquid helium meter) – used to monitor the liquid helium level inside the AMI cryostat, represented in Figure A.9.



Figure A.9 Model 135 Liquid Helium Level Monitor

A.2 Wiring

The understanding of the relation between the inside and outside of the setup is entirely dependent on the wiring of the whole microcalorimetry instrument, as this runs from the very tip of the movable insert up to the measurement and control modules.

There are several wiring “clusters” in the setup that should be understood:

- 1) The movable insert head;
- 2) The insert body;
- 3) The 16 pin plugs on the top of the insert;
- 4) The 16 pin cable plugs on the outside of the setup;
- 5) The wires that finally immerge from the cables and feed into our measuring equipment on the outside of the setup

A.2.1 Insert head

This should be regarded as the “heart” of the whole microcalorimetry instrument. It is here that all measurements and data acquisition happens.

For further clarification, the insert head can be divided into the following subsections:

- 1) The sample space containing the microcalorimetry chip socket platform, the calorimetry chips and a temperature dependent carbon glass resistor;

- 2) The insert head extension, which is merely a carefully measured elongated piece of metal meant to center the sample space in the magnetic field produced by the 9 Tesla superconducting magnet;
- 3) The insert head plug, where all the wiring from the sockets/chips and the resistor connect to.

These divisions are demonstrated in Figure A.10.

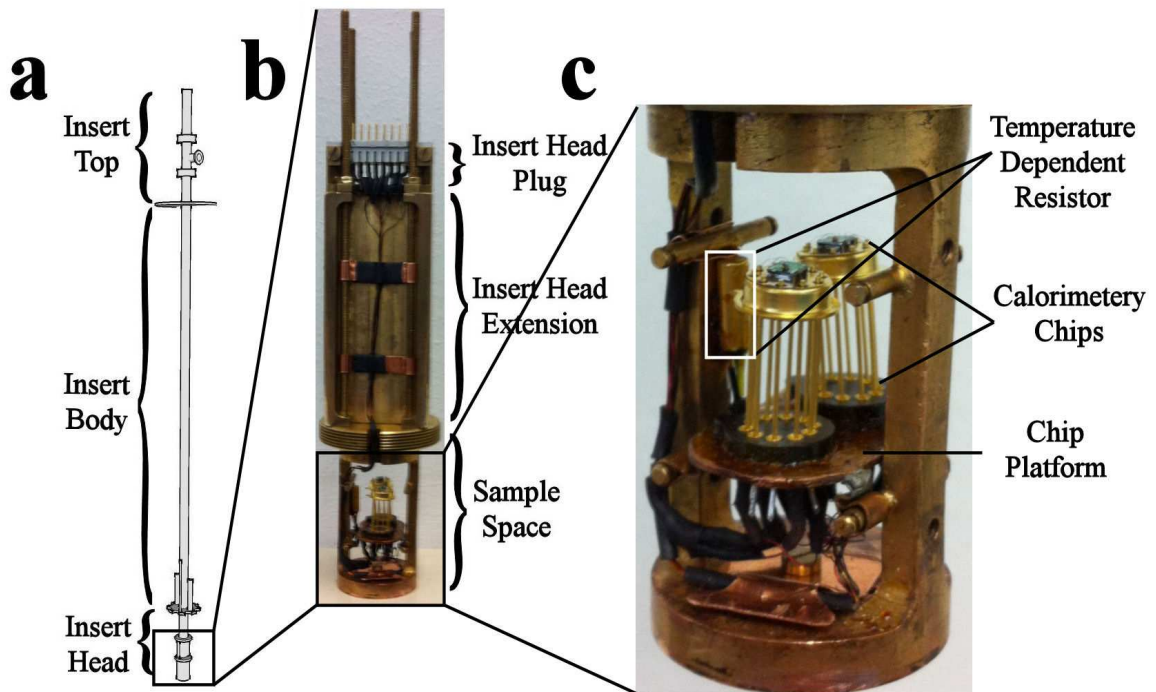


Figure A.10 a) Insert subdivisions; b) insert head subdivision; c) sample space layout.

The platform on which the two removable Xensor microcalorimetry chips are meant to fit into is wired according to Figure A.11, with the respective legend given in Table A.1.

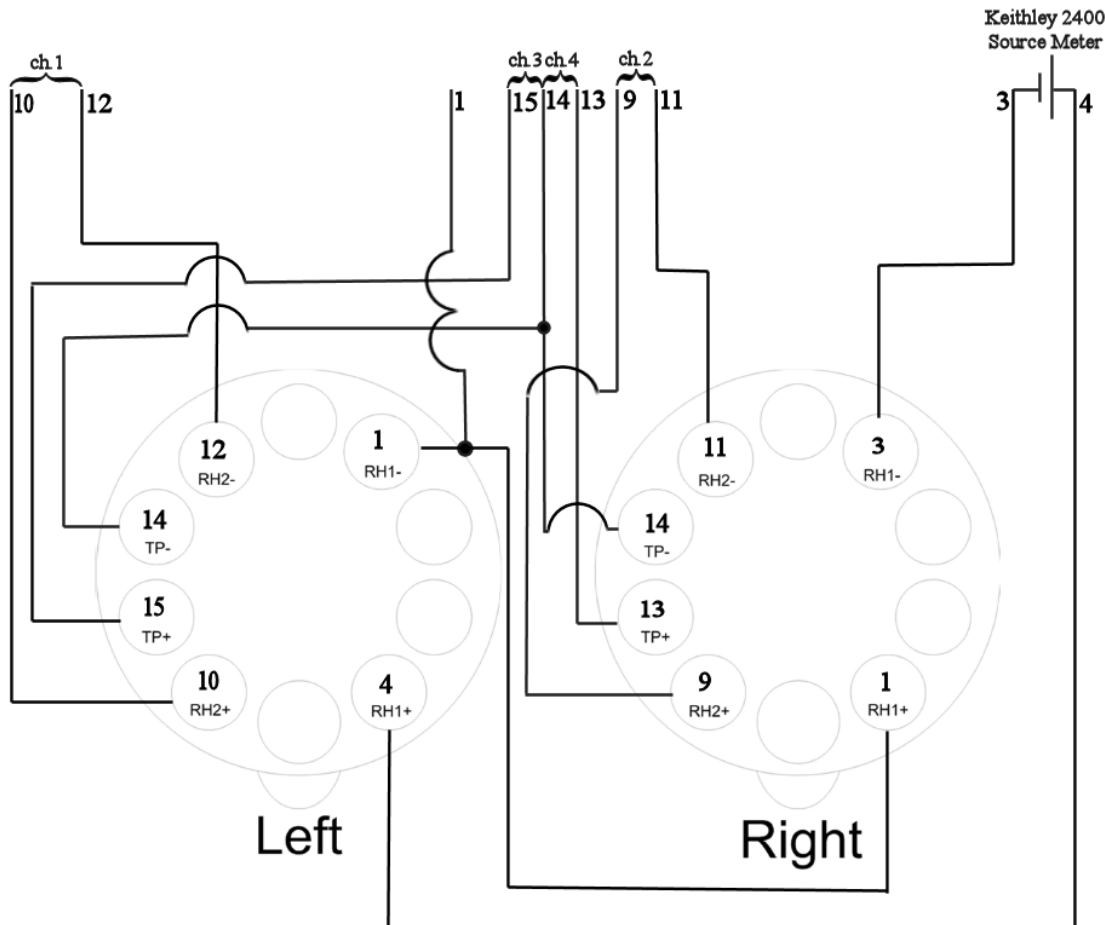


Figure A.11 Chip platform wiring. The definition of “Right” and Left” presented in this scheme will, from this point on, be used to distinguish both the chip sockets and the chips installed in the setup. Note that this wiring was planed in accordance with the layout of Xensor microcalorimetry chips mounted on TO-5 frames.

Table A.1 Legend for Figure A.11

Chip terminals legend	
TP+ / TP-	Positive/negative poles of the chip thermopile (source of calorimetric data)
RH1+ / RH1-	Positive/negative poles of the chip heater current
RH2+ / RH2-	Positive/negative poles of the chip heater voltage
Sample space wire legend	
Wires 3 and 4	Wires connecting the chip sockets to the Keithley 2400 (Source Meter) on the outside of the setup, the source of the square wave which is fed into the chip heaters and consequently heats up the samples in the chips, enabling for the performance of relaxation measurements.

Table A.1 (cont.) Legend for Figure A.11

Wire 1	Middle point between the right RH1+ and the left RH1-. It does nothing in the current setup and it is not connected to any equipment on the outside of the cryostat, it is used merely for diagnosis purposes.
Wires 10, 12, 9 and 11	Wires connecting RH2- and RH2+ of the left and right chips respectively to the Keithley 2000 (Multimeter) on the outside of the setup, making up channels 1 and 2 in this equipment respectively.
Wires 15, 14 and 13	Wires connecting the calorimetry chip's thermopiles to the Keithley 2000 (Multimeter) on the outside of the setup, making up channels 3 and 4 respectively. These are the channels carrying the information of the thermal response of the samples mounted on the two chips to the heat pulses provided by the chip heaters, making them the sources of measured information.

Parallel to the previously described wires is the temperature control equipment.

This is divided into a small resistor inside the sample space (see Figure A.10c) and the sample space heater(s). The resistor and the heater(s) are connected to the Lakeshore 331 Temperature Controller on the outside of the setup.

The wiring details of this part of the setup are displayed in Figure A.12, with the respective legend given in Table A.2.

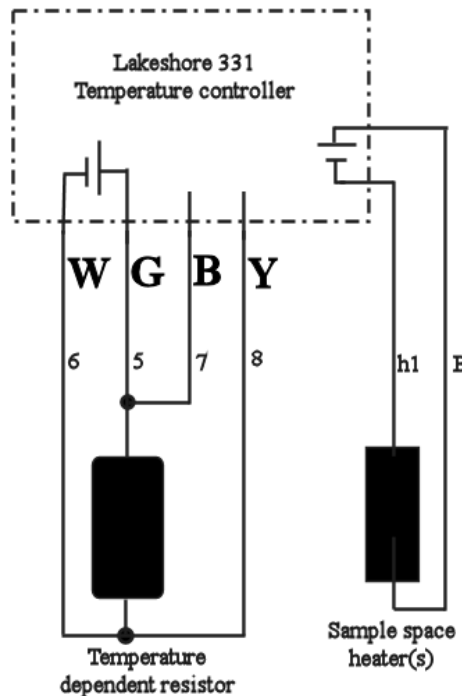


Figure A.12 Wiring for the resistor and sample space heater(s).

Table A.2 Legend for Figure A.12

W, G, B and Y	Color code for the 5, 6, 7 and 8 wires, meaning Green, White, Black, and Yellow
Wires 5, 6, 7 and 8	Wires connecting the temperature dependent resistor to the Lakeshore 331 Temperature Controller on the outside of the setup, enabling for a four point temperature measurement.
h1 and B wires	Wires connecting the sample space heater(s) to the Lakeshore 331 Temperature Controller on the outside of the setup. It should be relevant to note that the sample space heater(s) wiring is not directly related to the movable insert head, as it is a parallel and semi-independent system whose wires are merely bundled together with the ones from the insert head on the insert body. Also, one should not to confuse the chip heaters with the sample space heater(s), as these control the temperature of the sample space, while the chip heaters merely provide a heat pulse to the sample/reference which enables for the performance of relaxation measurements.

All the wires described above, except those referring to the samples space heater(s) (h1 and B), connect the chip sockets and resistor to the 16 pin insert head plug. The wire numeration used in the above Figures and Tables relates to this point as displayed in Figure A.13.

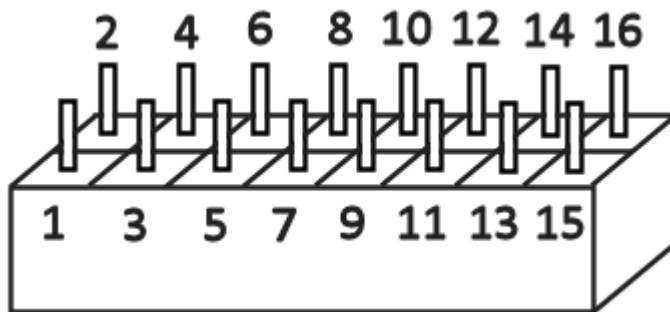


Figure A.13 Wire layout on the insert head plug. Not all pins in this plug are used in the current setup.

A.2.2 Insert body and top

Rising from the insert head, the sample space wires are bundled together with the sample space heater wires and travel along the body of the insert to two cable plugs, D1 and D2, on the insert top.

Each of these plugs has 16 pins, meaning that the wires coming from the insert head and heaters are distributed among both of them, being that some wires are actually repeated on both plugs. The layout of these plugs is displayed in Figure A.5.

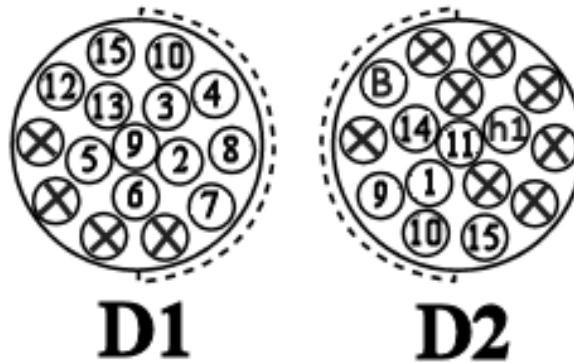


Figure A.14 Wire layout on the plugs at the top of the insert.

A.2.3 Insert cables

Connecting the D1 and D2 plugs to the several measurement modules on the outside of the setup are two cables, equality designated as D1 and D2 according to the their corresponding plug. The wire layout in these, as is logical, is a mirror image of Figure A.14, and is displayed in Figure A.15.

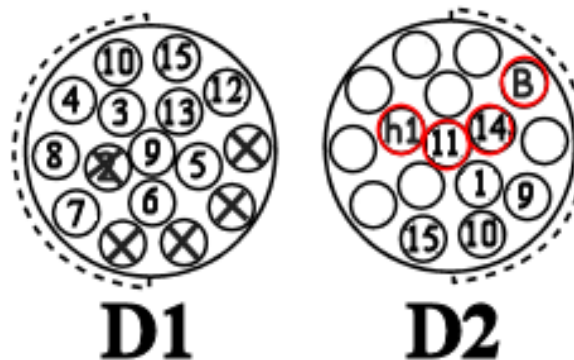


Figure A.15 Wire layout on the D1 and D2 cables. Given the number of repeated wire connection in the D1 and D2 insert plugs, the red circles in the D2 cable indicate the pins which are being used in this cable.

The D1 and D2 cables finally connect the insert plugs, and the wires emerging from the sample space, to the external measurement modules.

Observing these: into the Lakeshore 331 Temperature Controller one should have two separate wires (wires B and h1) and a four wire cable (consisting of wires 5, 6, 7 and 8); into the Keithley 2400 one should have two wires (wires 3 and 4); into the Keithley 2002 two wires (these are duplicates of wires feeding into the Keithley 2000, and are mainly used for diagnosis purposes) and all remaining wires should feed into the Keithley 2000, making up channels 1 through 4.

A.3 Software overview

There are several programs and routines that have to be used between the steps of data acquisition and achieving a final presentable result. These are listed below:

- 1) The microcalorimetry instrument interface software (Labview program)
- 2) The data visualization and extraction software (Labview program)
- 3) The calorimetric data calculation software (Matlab routine)
- 4) Data plotting and handling software (Origin or any other versatile data plotter)

A.3.1 Interface software

This program should be installed in a computer onto which the three Keithley modules and the Lakeshore 331 Temperature Controller are connected via a GPIB bus. It is designated as “Calorimetry.vi”, and upon opening it one should be confronted with a panel such as Figure A.16

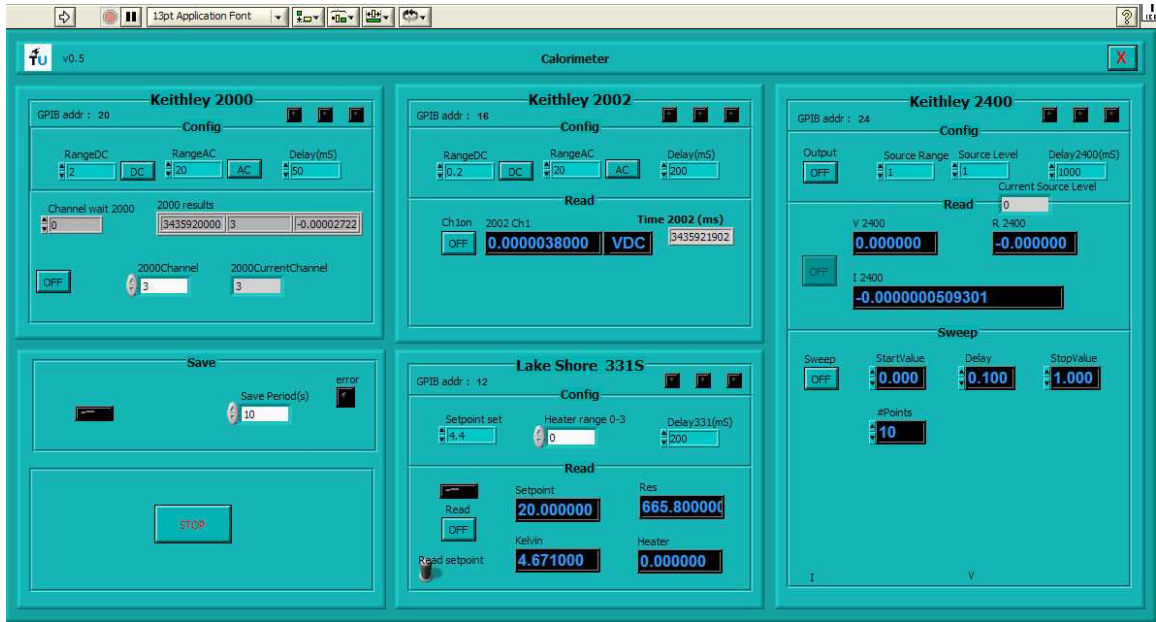


Figure A.16 Front panel of the interface software.

This interface is built up of 5 blocks, one for each of the external measurement modules (the four AMI modules are technically control modules, not measurement modules), clearly identified on their headings, and an extra one for data saving issues. All relevant information given by the front panels of the modules during a measurement is also given by these blocks.

The Keithley 2000 block is displayed in detail in Figure A.17, with the respective legend given in Table A.3.

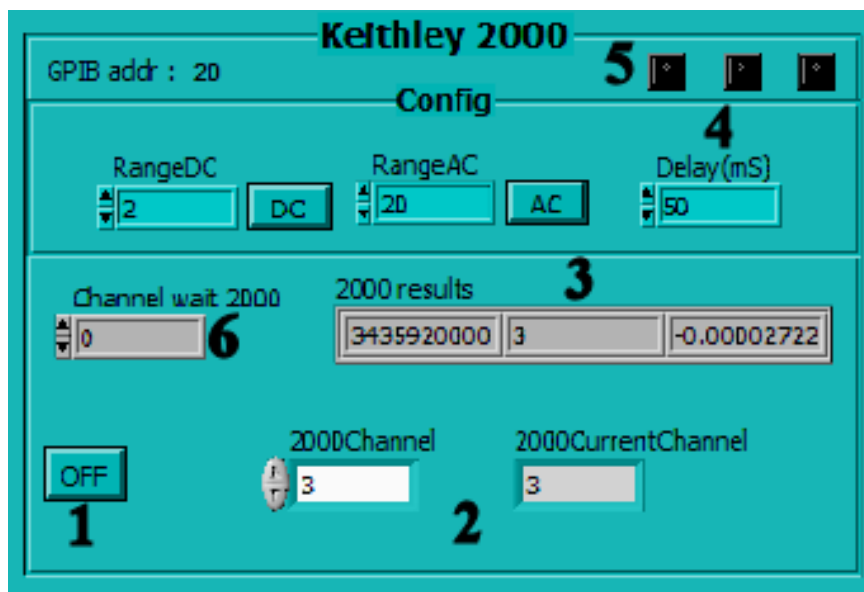


Figure A.17 Keithley 2000 interface software block.

Table A.3 Legend for Figure A.17

1	On\Off button
2	Indication of the channel currently being measured by the setup. During a measurement these two displays will oscillate between 3 and 4, with a slight lag between them, as one indicates the channel switching in the software and the other the channel switching in the hardware.
3	From left to right: time, channel and voltage response from that same channel. This, except time, should be equally displayed on the front panel of the Keithley 2000.
4	Measurement frequency, how often this equipment measures. This box is present in every equipment block, but it is of an essential importance on this block as the calculation of the relaxation measurements performed requires a large number of data point.
5	“Wellness” indicators, lighting either in green, yellow or red. Under normal circumstances these should light green, otherwise they indicate an error. These are present in every equipment block.
6	“Pause” indicator. Should any number be introduced in this box the software will pause the whole system for that amount of time whenever it changes channel. This was built so as to prevent the measuring of aberrant first measurements caused by channel switching. Given that the calculations to follow resort merely to the temperate relaxation curve, this number is not important.

The Keithley 2002 block is displayed in detail in Figure A.18, with the respective legend given in Table A.4. This module doesn't play a significant role in the current measurement procedure.

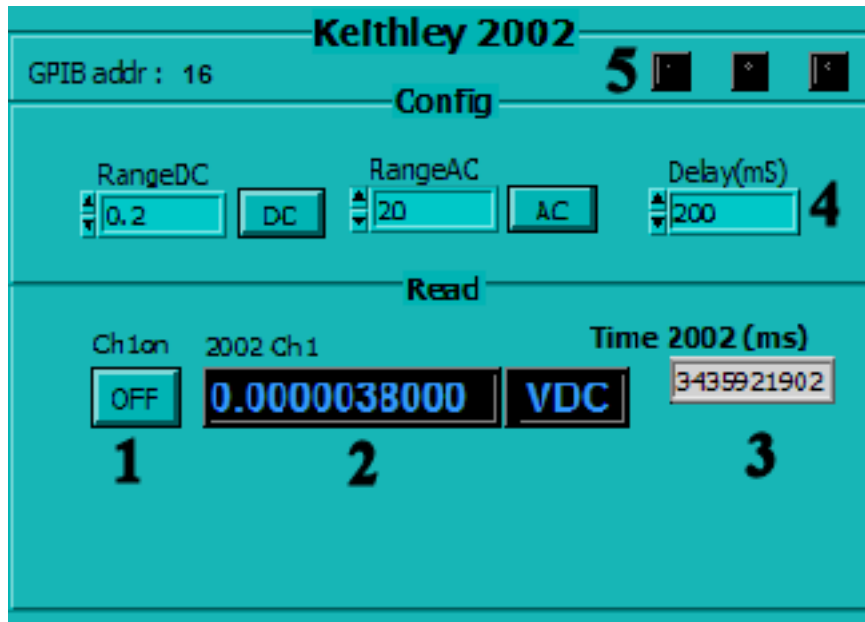


Figure A.18 Keithley 2002 interface software block.

Table A.4 Legend for Figure A.18

1	On\Off button.
2	Difference between the thermopile voltages of the two Xensor microcalorimetry chips. This is equally displayed on the front panel of the Keithley 2002.
3	Time indicator. This value is measured by an external “clock”, and as such is the same for all measurement modules. It is through this value that the data sets measured by each module are fitted together.
4	Measurement frequency, how often this equipment measures. This box is present in every equipment block.
5	“Wellness” indicators, lighting either in green, yellow or red. Under normal circumstances these would light green, otherwise they indicate an error. These are present in every equipment block.

The Lakeshore 331 Temperature Controller block is displayed in Figure A.19, with the respective legend given in Table A.5. This block is crucial on all temperature dependent measurements and it is the one where one may more directly operate and control the setup during a measurement, as all the others modules are fairly automated.



Figure A.19 Lakeshore Temperature 331 Controller interface software block

Table A.5 Legend for Figure A.19

1	On\Off bottom.
2	Read setpoint switch. This switch determines if the measurement is reading and recording the setpoint temperature and the resistance of the carbon glass temperature dependent resistor from the Lakeshore 331 Temperature Controller module.
3	Sample space temperature in Kelvin. This should be equally displayed on the front panel of the Lakeshore 331 Temperature Controller.
4	Setpoint temperature reading, the temperature the Lakeshore 331 Temperature Controller is aiming at during heating\cooling or a during a temperature ramp. This should be equally displayed on the front panel of the Lakeshore 331 Temperature Controller.
5	Resistance value of the carbon glass temperature dependent resistor inside the sample space. This value indicates the temperature at which the sample space is at via the calibration curve presented in Figure 4.3. This should be equally displayed on the front panel of the Lakeshore 331 Temperature Controller.
6	Heater output in percentage. This should be equally displayed on the front panel of the Lakeshore 331 Temperature Controller.
7	Remote setpoint temperature setter. This allows you to remotely enter a new setpoint temperature value into the Lakeshore 331 Temperature Controller during a measurement.

Table A.5 (cont.) Legend for Figure A.19

8	Remote Heater range setter. This allows for a remote control the heater setting of the Lakeshore 331 Temperature Controller (0 – Off; 1 – Low; 2 – Medium; 3 – High) during a measurement.
9	Measurement frequency. This it is present in every equipment block;
10	“Wellness” indicators, lighting either in green, yellow or red. Under normal circumstances these would light green, otherwise they indicate an error. These are present in every equipment block.
11	Saving light. This is an indicator of when you are recording your data.

The Keithley 2400 block is displayed in Figure A.20, with the respective legend given in Table A.6.

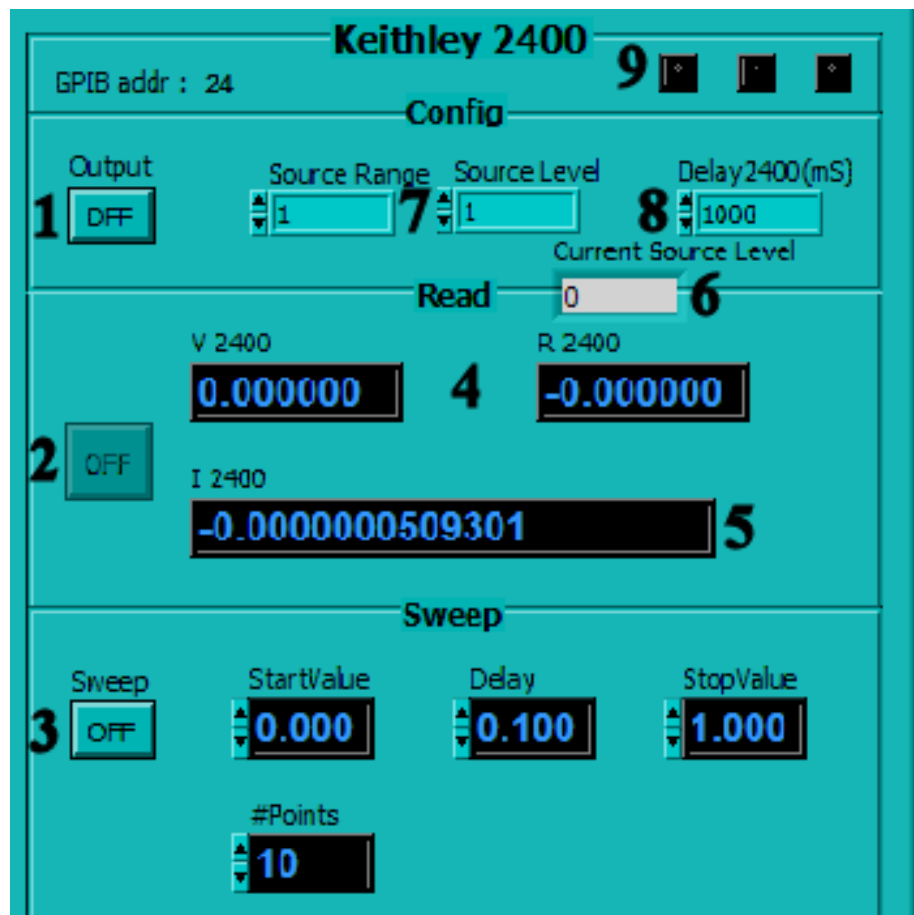


Figure A.20 Keithley 2400 interface software block

Table A.6 Legend for Figure A.20.

1	On\Off button of the square wave generator;
2	On\Off button of the reading functionality of the source meter (can only be turned on when either buttons 1 or 3 are turned on);
3	On\Off button of the sweep function. In the current setup there is no foreseeable use for this feature.
4	Xensor microcalorimetry chip resistance and voltage registered in response to the wave generated by this module.
5	Intensity registered in response to the square wave generated. This should be equally displayed on the front panel of the Keithley 2400;
6	Source level indicator. See next point;
7	Source level and source range setters. These refer to the characteristics of the square wave being generated by the Keithley 2400 (currently an 1 V square wave). Should these values need to be changed this can only be done with some knowledge of Labview.
8	Measurement frequency. This it is present in every equipment block;
9	“Wellness” indicators, lighting either in green, yellow or red. Under normal circumstances these would light green, otherwise they indicate an error. These are present in every equipment block.

The saving block is displayed in Figure A.21, with the respective legend given in Table A.7

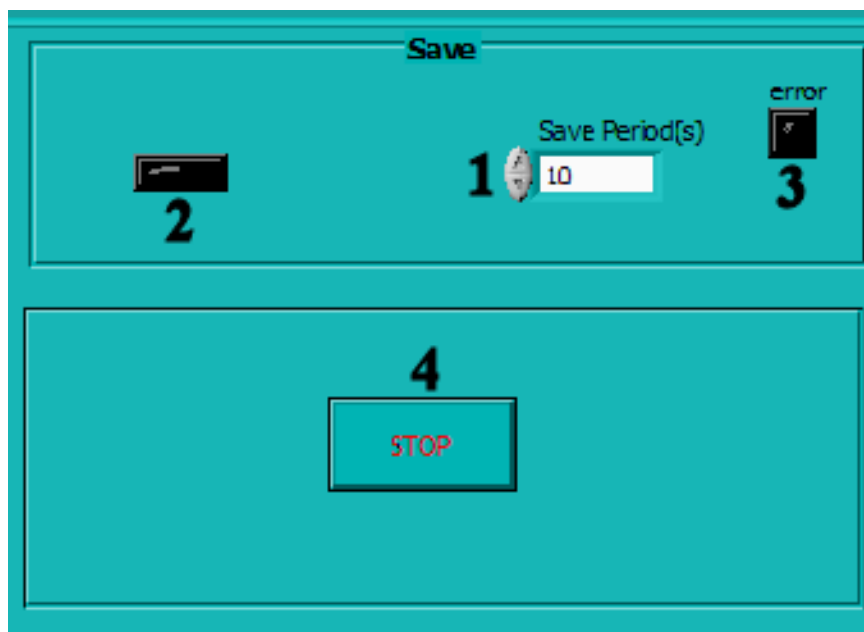


Figure A.21 Saving interface software block

Table A.7 Legend for Figure A.21.

1	Global save periodicity. This box is directly related to an unexplained inbuilt error of LabView. This translates itself as the fact that a measurement file needs to be closed and opened occasionally, so as there may be a release of computer memory. If this does not happen, given the long nature of the measurements performed in this setup, the computer will run out of memory, crash and lose the measurement.
2	Global saving light. This light should flash according to the global save periodicity.
3	Error light.
4	Global stop button. This shuts down the whole interface software.

A.3.2 Data visualization and extraction software

This program does not need to be installed in the same computer onto which the three Keithley modules and the Lakeshore 331 Temperature Controller are connected via a GPIB bus. It is designated as “Calorimetry read.vi”, and upon opening it one should be confronted with a panel such as Figure A.22, with the respective legend given in Table A.8

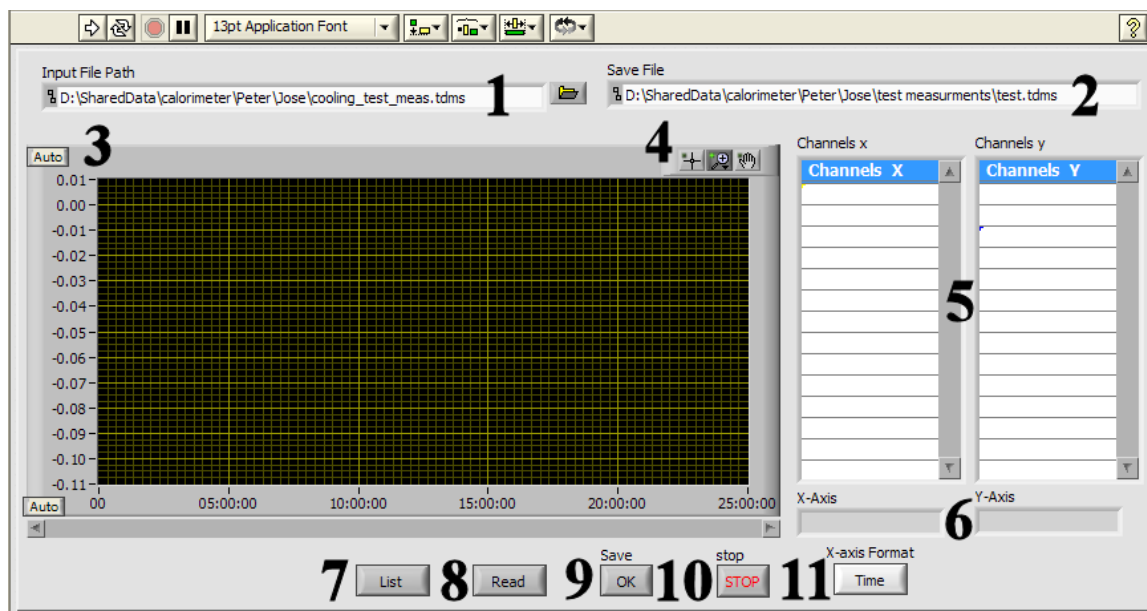


Figure A.22 Front panel of the data visualization software.

Table A.8 Legend for Figure A.22.

1	Input file box. This refers to the original “tdms” file produced by the Calorimetry.vi, the data acquisition software.
2	Output file box. This refers to the path, name and file type you produce with this software.
3	Data visualization panel. This displays the two data sets you define as X and Y in points 5 and 6.
4	Visualization tools.
5	Double listing of all the data contained in the “tdms” file produced by the Calorimetry.vi.
6	Data selected from the double listing in point 5 as X and Y.
7	Lists all the data contained in the “tdms” file produced by the Calorimetry.vi selected in point 1 on point 5.
8	Plots the data selected as the X and Y-axis in point 6 into the visualization panel.
9	Saves the data displayed in the visualization panel in a two column file as specified by the path, name and file type in point 2.
10	Global stop button. This shuts down the whole data extraction software.
11	X-axis format. This switches between the definition “Time” and “Decimal” allowing for the selection of the appropriate data format on the visualization panel.

This is an extensively versatile and powerful piece of software, which allows for the visualization and extraction of any two sets of data measured by any of the modules connected to the control PC during a measurement. As such, its adequate use enables not only the extraction of the data necessary for the calculation of specific heat, but also the detailed monitoring of all the events which might have happened with the different modules during a measurement.

A.3.3 Calculation software

These consist of two Matlab routines, which do not need to be run in the same computer onto which the three Keithley modules and the Lakeshore 331 Temperature Controller are connected via a GPIB bus, but merely in one where Matlab is installed.

The first of these routines, entitled “grabtau.m” uses two data sets that are extracted from your measurement “tdms” file, the Keithley 2000 voltage reading vs time and the Keithley 2400 voltage reading vs time, and it calculates the specific heat ratio between the sample and reference in order of time.

The second routine, entitled “capacity_temperature_matcher.m”, resorts to an additional data set, the Lakeshore 331 Temperature Controller sample space temperature reading vs time, and it matches the specific heat ratio calculated by the “grabtau.m” routine with temperature. Both these routines were written by Peter van Dommelen as part of his Bachelor end project, and they are shown below (with the exception of the plotting code lines).

grabtau.m:

```
clear all;

% ### Parameters ###

filename = 'channel.csv'; %first column time, second
column thermopile voltage measurements
pif_filename = 'switch.csv'; %first column time, second
column chip heater output in volts
csv_seperator = ','; %the seperator in the .csv files
```

```

nSkip = 8; %number of data points to skip to get rid of
the high slope

nLength = 100; %number of data points the fit length is

nMinimal = 100; %number of data points one curve should be
atleast

fitorder = 1; %2 works, but 1 is better for theoretical
and practical reasons

use_pif_as_switching_time = 1; %0 or 1

delta_bar = 0.00001; %some small value

nGraphPre = 20; %on the worst fit graph, how many data
points to show before the fit
nGraphPost = 100; %on the worst fit graph, how many data
points to show after the fit

tCycleTime = 90; %for use in the graphs: amount of time
one cycle takes

show_analysis = 1; %0 or 1
show_cycle = 1; %0 or 1
remove_old_figures = 1; %0 or 1

seebeck = 0.002060; %V/K for both. ROUGH estimation
approx_power = 0.00018; %W per chip for both. Estimated

% ### Define data variables ###
data = dlmread(filename, csv_seperator);
data_time = data(:,1);
data_value = data(:,2);
data_length = length(data_time);
data_abs = abs(data_value); %absolute value

```

```

data_delta = [0 ; (data_abs(2:data_length) -
data_abs(1:data_length-1))]; %change
data_log = log(data_abs); %logarithm

pif = dlmread(pif_filename, csv_seperator);
pifstart = find(pif(2:1:end, 2) < pif(1:1:end-1, 2));
%find indices where heater voltage goes down
pifstop = find(pif(2:1:end, 2) > pif(1:1:end-1, 2)); %find
indices where heater voltage goes up
pifstop = pifstop(find(pifstop(:) > pifstart(1))); %skip
first if stop comes before start
pifstarttime = pif(pifstart(:), 1);
pifstoptime = pif(pifstop(:), 1);

% ### Find step down curves ###

startdownwards = [find(data_delta < -delta_bar) ;
data_length ];

downwards = [];
for index=1:min(size(pifstarttime), size(pifstoptime)+1)
    start = find(data_time > pifstarttime(index), 1,
'first');
    stop = start + 5000;
    if (length(start) == 1 && length(stop) == 1 &&
stop > start)
        downwards = [ downwards ; start stop ];
%indices at which the downward curve starts and stops
    end
end

% ### Find fit parameters from curves ###

resultdown = [];
linlogmax = [];
error = [];

```

```

high = [];
for index=1:size(downwards)
    timedown = data_time(downwards(index,
1)+nSkip:downwards(index, 1) + nLength);
    logdown = data_log(downwards(index,
1)+nSkip:downwards(index, 1) + nLength);
    P = polyfit(timedown, logdown, fitorder);

    resultdown = [resultdown ; P]; %fit parameters
    if (use_pif_as_switching_time == 1)
        linlogmax = [linlogmax ; polyval(P,
pifstarttime(index)) ];
    else
        linlogmax = [linlogmax ; polyval(P,
data_time(downwards(index, 1))) ];
    end
    high = [high ; mean(data_abs(downwards(index, 1)-
5:downwards(index, 1)))]];

    error = [error ; mean((polyval(P, timedown) -
logdown).^2)]; %error used in showing worst fit
end

% ### Calculate initial voltage and decay time ###
linmax = exp(linlogmax); %inverse of the logarithm

corrA = linmax(1:2:end);
corrB = linmax(2:2:end);
if (fitorder == 1)
    slopeA = resultdown(1:2:end, 1);
    slopeB = resultdown(2:2:end, 1);
else
    slopeA = 2*resultdown(1:2:end, 1) .*
data_time(downwards(1:2:end, 1) - nSkip) +
resultdown(1:2:end, 2);

```

```

    slopeB = 2*resultdown(2:2:end, 1) .*
data_time(downwards(2:2:end, 1) - nSkip) +
resultdown(2:2:end, 2);
end

decayA = -1./slopeA;
decayB = -1./slopeB;

highA = high(1:2:end);
highB = high(2:2:end);

temp_corr_A = corrA / seebeck;
temp_corr_B = corrB / seebeck;

% ### Calculate average results ###

heat_resistance_correction_A = corrA ./ highA;
heat_resistance_correction_B = corrB ./ highB;

heat_resistance_A = temp_corr_A ./ approx_power;
heat_resistance_B = temp_corr_B ./ approx_power;

valA = decayA ./ heat_resistance_A;
valB = decayB ./ heat_resistance_B;

moving_valB = 0.5*(valB(1:end-1)+valB(2:end));
ratio = valA(2:end-1) ./ moving_valB;
average = mean(ratio);
std_deviation = std(ratio);
relative_std_deviation = std_deviation / average;

heat_capacity_A_and_B = [mean(valA) mean(valB)] %print
results
heat_capacity_A_and_B_stat_dev = [std(valA) std(valB)]
%print deviations

```

```
ratio_std_relstd = [average std_deviation  
relative_std_deviation] %print ratio
```

capacity_temperature_matcher.m :

```
% ### Parameters ###  
  
amount_to_average = 10;  
  
filename = 'temperature.csv'; %first column time, second  
column thermopile voltage measurements  
csv_seperator = ';'; %the seperator in the .csv files  
  
% ### Define data variables ###  
data = dlmread(filename, csv_seperator);  
t_time = data(:,1);  
t_value = data(:,2);  
  
t_index = zeros(size(ratio_time));  
for index=1:length(ratio_time)  
    time = ratio_time(index);  
    t_index(index) = find(t_time > time, 1, 'first');  
end  
  
ratio_temperature = zeros(size(t_index));  
for index=1:length(t_index)  
    i = t_index(index);  
    ratio_temperature(index) = mean(t_value(i-  
amount_to_average/2:i+amount_to_average/2));  
end
```

A.3.4 Data display

The software used for this step in particular is not specific to the microcalorimetry instrument and data, and as such will not be discussed in detail at this point. A regular software like Origin is more than enough to handle this step.

A.4 Measurement preparation protocol

What follows are step by step instruction for the handling and mounting of both measurement and references samples on Xensor microcalorimetry chips and their subsequent fitting with the insert and 9 Tesla Cryostat.

At this point there will be no concern with actually measurement, merely sample and chip handling.

*
* *

0. Should you already have two microcalorimetry chips mounted with a reference and measurement sample, skip to point 7.

1. Select two microcalorimetry chips from the reserve. This should be done with a considerable degree of attention as a simple naked eye examination of a chip may be enough to detect a broken calorimetric membrane or disconnected wires, see Figure A.23.

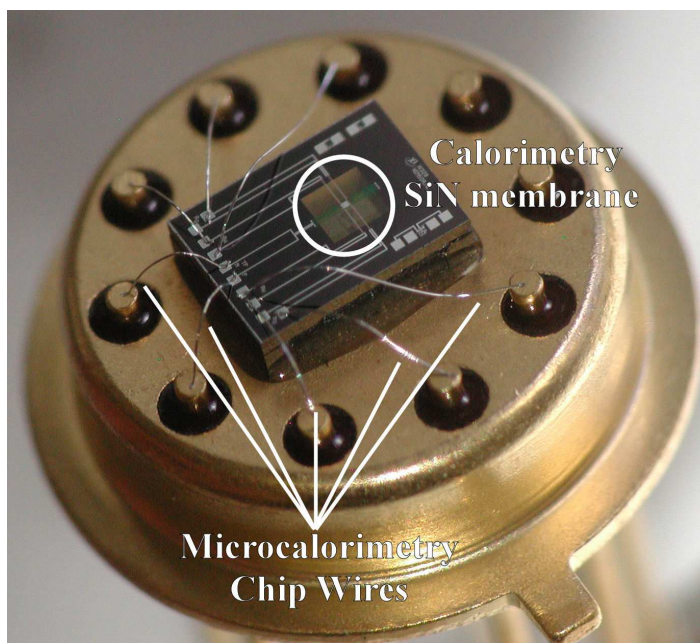


Figure A.23 Close up of a XEN-39328 microcalorimetry chip, evidencing the SiN membrane and chip wires.

2. Take the two selected chips to a microscope and confirm their physical integrity.
3. Fit both chip on the chip platform on the insert head and mount it on the insert. At this point there is no need to mount any shields or heaters.
4. On the Keithley 2000 press the bottom reading “DCV” (making sure the “REM” definition is off), and using the arrows check the values from channel 1 trough 4, they all should read 0 V, with the occurrence of some minor noise. While doing this also check the Keithley 2002, the numbers it displays are not important, but, should everything be as it should, on no channels should you ever read an Overflow.

Press the “ Ω 2” button and once again check channel 1 trough 4. You should read about 1.2 K Ω on channels 1 and 2, and about 30 K Ω on channels 3 and 4. These are the resistance values of the XEN-39328 chip heaters and thermopiles respectively (should the chip model used not be this one please check these values with the manufacturer). On the Keithley 2002 this should read as a string of unimportant numbers in channels 1 and 2 and as an Overflow on channels 3 and 4.

Figure A.24 illustrates the position of the above mentioned buttons on the Keithley 2000.

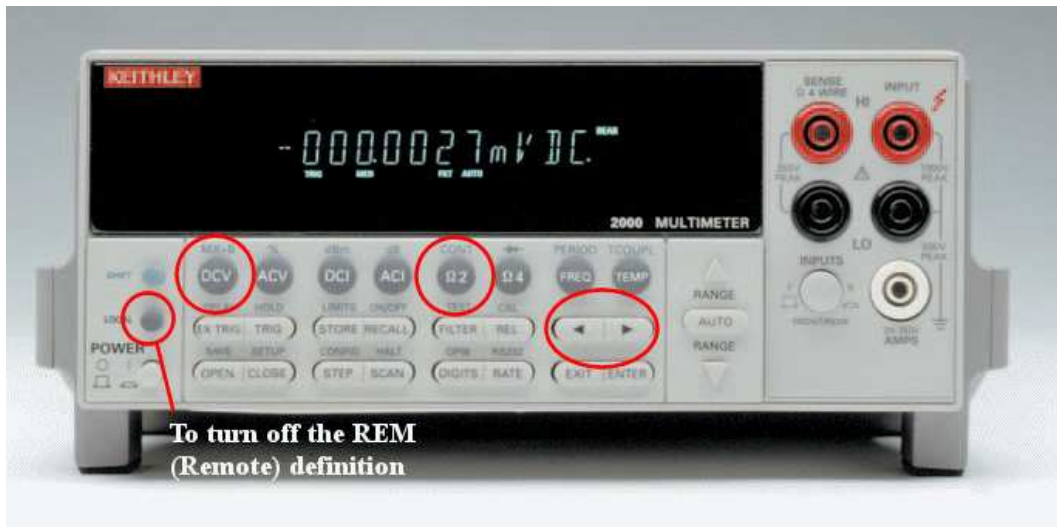


Figure A.24 Location of all the buttons mentioned above in the Keithley 2000 front panel

Check the Lakeshore 331 Temperature Controller, you should read a temperature value of about 300 K and a resistance value of around 12.8 Ω .

5. Should any of these values fail you have an error.

If this is a consistent error on either channel 1 and 3 or channel 2 and 4 then it is most likely chip related, the left chip for 1 and 3 and the right chip for 2 and 4. If this is the case confirm that you have positioned the chips correctly (the small elongated patch on the chip should match with the one on the socket). If all seems right re-examine the integrity of the chip SiN membrane and try to switch the chip positions and see if the error “follows” one of the chips. If this happens go back to point 1, and repeat this procedure with one chip.

If the problem is not localized, there is the possibility that both chips are malfunctioning, but you are most likely facing a wiring problem.

If the problem is with the values in the temperature controller you most likely have a wiring problem, as the thermometer itself is just a simple resistor.

These issues will not be dealt with in the current manual, as they boil down to adequately using a hand held multimeter and wire soldering.

6. If all seems well dismount the insert head and carefully remove both chips.

Take the chips to a balance and take the following steps with one at a time:

1) Weight the chip, take note of its mass and tare the balance to 0;

2) With a tip of a thin tweezer take an excitingly small amount of grease (Apiezon N if you're planning on doing a low temperature measurements and Apiezon H for high temperature measurements) and slightly touch the SiN calorimetry membrane so as a small droplet is left on its surface;

Should you notice that during this process some grease has extended beyond the membrane and into the chip frame, then this chip has become inadequate, go back to point 1, and follow this procedure with one chip;

Should you see that during this process the membrane has broken as a result of over pressure from the tweezer, then this chip has become inadequate, go back to point 1, and follow this procedure with one chip;

3) Weight the chip with the grease, take note of its mass and tare the balance to 0. An ideal grease amount should be so small as the balance will not be able to register it;

4) With a thin tweezer transport a small particle of sample/reference to the chip membrane and weight the chip.

5) Do this as many times as required until you have the desired mass on the chip (betewn 0.2 to 0.8 mg). Take note of this mass.

Should you see that during this process some grease has extended beyond the membrane and into the chip frame, then this chip has become inadequate, go back to point 1, and follow this procedure with one chip;

Should you see that during this process the membrane has broken as a result of over pressure from the tweezer, then this chip has become inadequate, go back to point 1, and follow this procedure with one chip;

7. After both chips are ready take them to a microscope to determine with certainty if any grease has extended beyond the membrane and into the chip frame or if the SiN has broken as a result of over pressure from the tweezer.

If you see that this has happened go back to point 1, and follow this procedure with one chip;

8. Once again place the two chips in the chip platform in the insert head and make a simple mount on the insert body. Repeat point 4 and 5.

9. Dismount the insert head. Take the two heaters and check their resistance, you should read around 91 Ω on the smaller inner heater and 65 Ω on the larger outer heater.

10. Mount the insert head on the insert body and repeat point 4 and 5. Attach bolts to the long insert head screws to secure it and connect one end of the heater current divider to the inner heater.

Screw the outer heater onto the insert head, connect the second end of the current divider to it and connect it to the heater wiring coming from the insert body.

The current divider should not be dismissed, as it has been determined that one single heater cannot withstand the “High” setting of the Lakeshore 331 Temperature Controller and, should you want to make a measurement above 80 K you cannot avoid using the “High” setting.

11. Repeat point 4 and 5.

In the Lakeshore 331 Temperature Controller press the “Setpoint” button (making sure the “Remote” definition is off) and insert a setpoint which is higher than the sample space temperature reading. Press the “Heater Range” button and select one of the power ranges of the heater using the arrow buttons (restrain from using the “High” setting), press Enter. At this point you should read a percentage value under the

resistance value of the carbon glass temperature dependent resistor; this is the percentage of the maximum output of the heater setting you have selected and that the Lakeshore 331 Temperature Controller is supplying to the heaters in order to raise the temperature of the setup to your selected setpoint. If you see this it means your heaters are working accordingly and you can press the “Heater off” button. If instead you read “Open” you have an error.

Make sure the heater wires are correctly connected to the back of the Lakeshore 331 Temperature Controller. If all seems well dismount the two heaters and re-measure their resistance, if their values are good then you have a wiring problem somewhere on the outside of the insert head.

Figure A.25 illustrates the position of the above mentioned buttons on the Lakeshore 331 Temperature Controller.

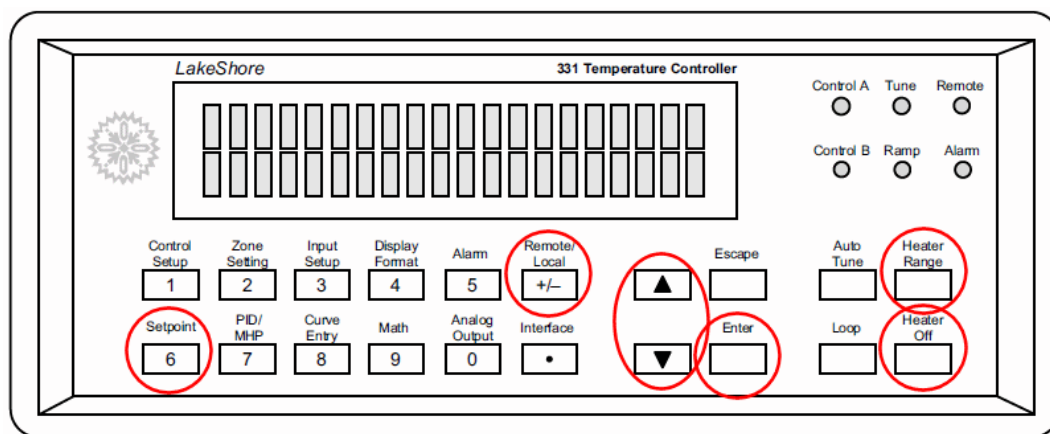


Figure A.25 Location of all the buttons mentioned above in the Lakeshore 331 Temperature Controller front pannel.

12. Take the large outer shield that covers the insert head and thoroughly clean its top part.

Using Apeazon N or H (depending on the nature of your measurement) coat the outer indented ring on the top of this shield. Cut a piece of Indium wire of 18.5 cm and carefully fit it to the outer ring. This is meant to function as an O-ring for the vacuum created in the sample space during a measurement.

13. Carefully attach the outer shield to the insert body trying your best to make sure the indium gets pressed homogeneously all around the shield by slowly tightening its screws in opposing pairs.

14. Repeat point 4, 5 and 11.

15. Is there either liquid Nitrogen or Helium inside the cryostat?

No – Gently lower the insert into the cryostat, taking special attention to tilt it as little as possible. As soon as it is lowered, and before you screw it shut, repeat point 4, 5 and 11.

Screw it shut and attach the vacuum pump to the insert top. Start pumping and gently open the vacuum valve so as not to create a pressure chock which might dislodge your chips or damage the setup. After you have created some vacuum (10^{-3} or 10^{-4}) repeat point 4, 5 and 11.

Make a test measurement of a few minutes to make sure everything is responding as it should (see section A.5).

Fill the liquid nitrogen tank and repeat point 4, 5 and 11.

Fill the liquid helium tank and repeat point 4, 5 and 11.

Yes – Gently attach the vacuum pump to the insert top avoiding tilting it too much. Start pumping and gently open the vacuum valve so as not to create a pressure chock that might dislodge your chips or damage the setup. After you have created some vacuum (10^{-3} or 10^{-4}) repeat point 4, 5 and 11.

Make a test measurement of a few minutes to make sure everything is responding as it should (see section A.5).

Open the cryostat and gently lower the insert into it, screw it shut and repeat point 4, 5 and 11.

A.5 Measurement protocol

What follows are step by step instructions for the performance of both temperature and magnetic field dependent specific heat measurement in the microcalorimetry instrument currently described. At this point there will be no concern with data handling or calculation, merely data acquisition.

Should you have performed all of the instructions given in section A.4 correctly then all should boil down to adequately operating the Calorimetry.vi interface software.

A.5.1 Software handling

Open the Calorimetry.vi. Before turning any of the blocks on go through the following steps:

1. Check the save time in the saving block. This should read 10 seconds.
2. Check the saving time on the Keithley 2400 block (the Delay box), this should at least read 1000 ms, or, 1 second.
3. Check the saving rate in the Keithley 2000 block (the Delay box), this should at least read 50 ms. This value is extremely relevant.
4. Check the “Read Setpoint” switch on the Lakeshore 331 Temperature Controller block, this should be turned up.
5. Check the current work folder for any previous measurement files, these will be named “meas.tdms” and “meas.tdms_index”. Since the data recording is done on a substitution basis it is essential that these be removed. Ignoring this will result in files with mixed data from various different measurements.

Should all of the above have been observed, and given the semi-automated nature of most of the measurement blocks, you should be ready to start a measurement.

Turn the Labview program on and in a rapid sequence, turn all the measurements blocks on. The order and speed in which you do this is not necessarily fundamental, as during the subsequent data analysis all the data from the various blocks will be align among itself in order of Time. This Time, it is important to note, is set by an autonomous “clock”, and as such it will always be the same and coherent for all blocks.

None the less, the order given in Figure A.26 has been determined as the one which is less likely to give you problems related to unfinished modules processes in the long run.

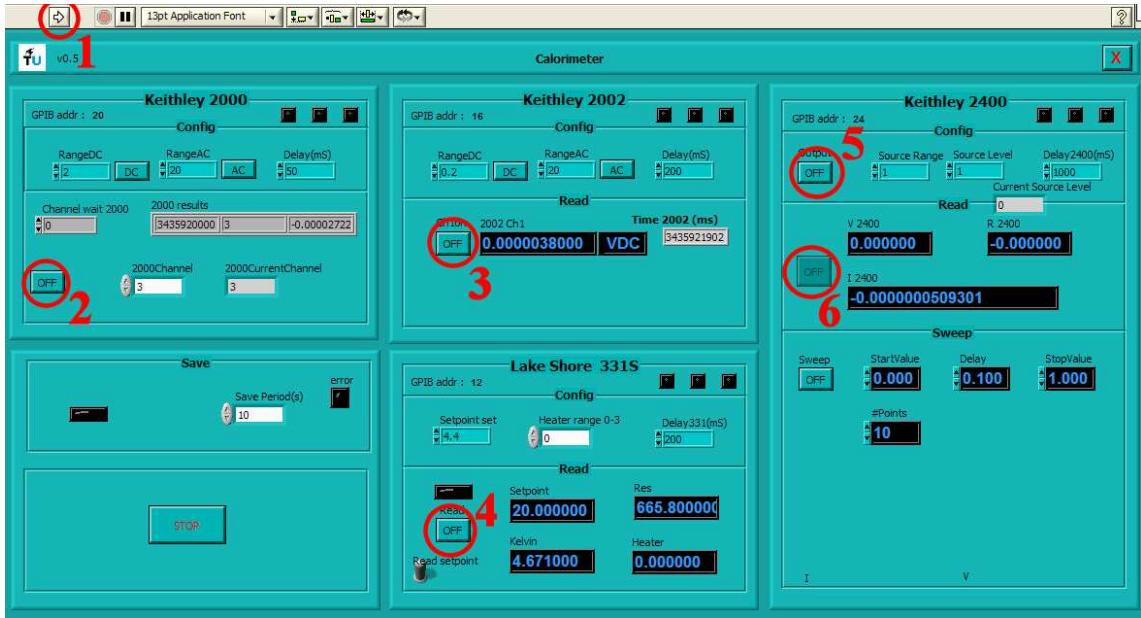


Figure A.26 Suggested sequence for turning the different measurement blocks on.

Once you have done this the interface software should display an arrangement similar to Figure A.27.

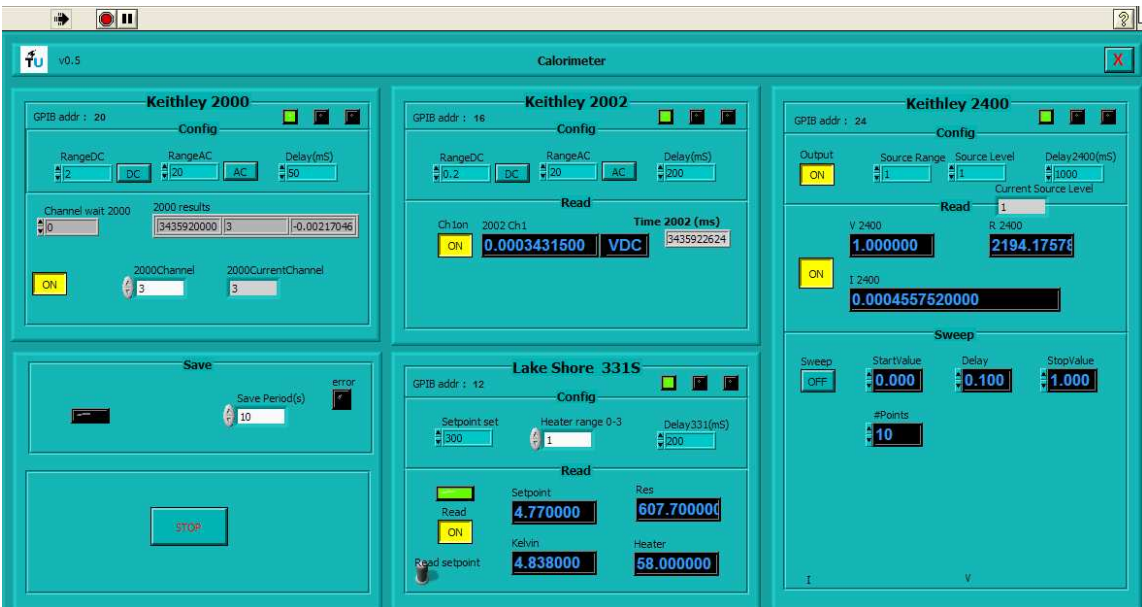


Figure A.27 A functioning and measuring software interface

Carefully check each block and their corresponding modules for malfunctions with the following steps:

1. All “wellness” lights should be green;
2. The overall save light should flash every 10 seconds (if this is the defined time);
3. The save light in the Lakeshore 331 Temperature Controller block should be flashing at a high rate;
4. There should be values in the four boxes of the Lakeshore 331 Temperature Controller block, and these should correspond to the values being presented in the 331 front panel, as exemplified by Figure A.28.



Figure A.28 Comparison between the Lakeshore 331 Temperature Controller block and front panel during a working measurement.

5. The Keithley 2000 should be switching between channels 3 and 4 in a rate of about 30 seconds, and you should be seeing a very clear voltage response to the wave being generated by the Keithley 2400 (see below) on both the Keithley 2000 block and the Keithley 2000 front panel, as exemplified by Figure A.29.

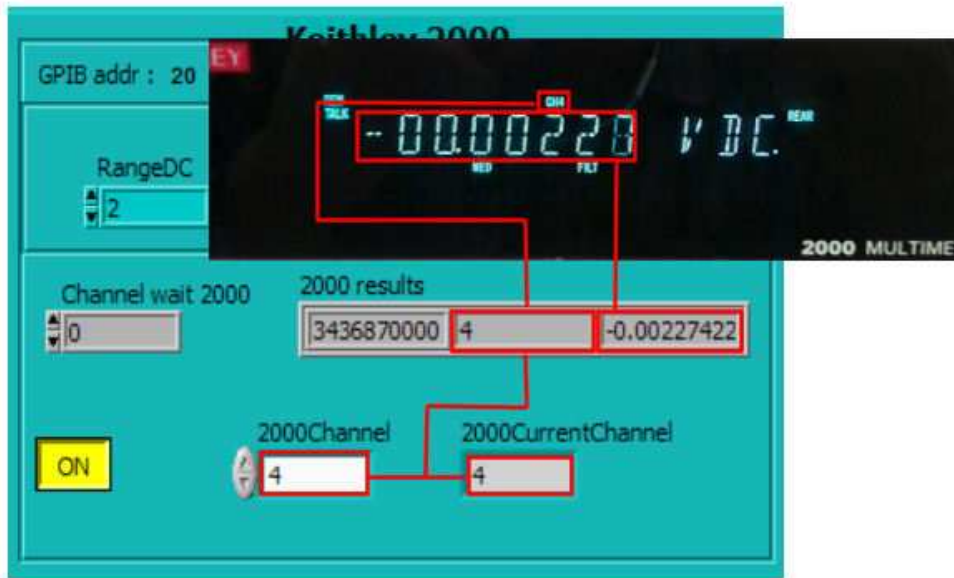
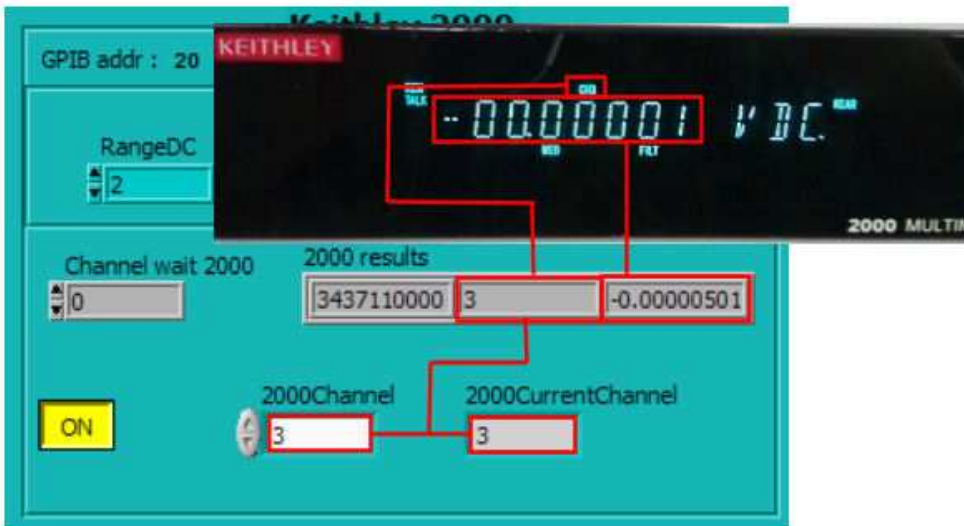
a**b**

Figure A.29 a) Comparison between the Keithley 2000 software block and front panel, while on channel 4 and under the influence of a wave from the Keithley 2400; b) Comparison between the Keithley 2000 software block and front panel, while on channel 3 and not under the influence of a wave from the Keithley 2400.

6. The Keithley 2400 front panel should be switching between 0 mA and a concrete value (this will depend on your chip resistance), as exemplified by Figure A.30.

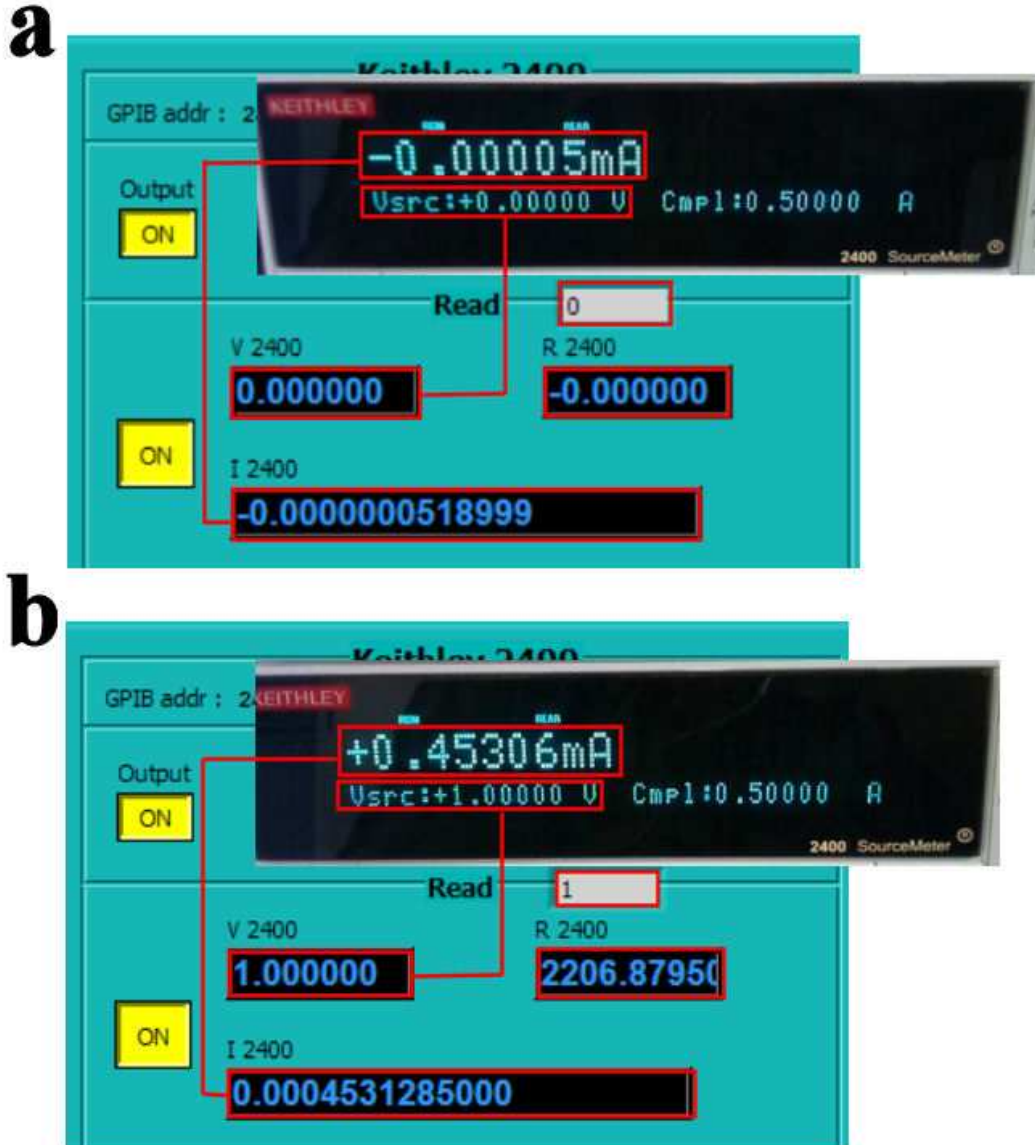


Figure A.30 a) Comparison between the Keithley 2400 software block and front panel, while not producing a square wave; b) Comparison between the Keithley 2400 software block and front panel, while producing a square wave.

7. There should be new “meas.tdms” and “meas.tdms_index” files in the work folder;

Should all of these be observed the measurement is working on all accounts.

A.5.2 Temperature sweeps

The above instructions hold true for measuring in the abstract sense, but a great deal more needs to be added to them in order to perform a useful calorimetric measurement

In order to perform a temperature sweep you will have to work in part with the interface software and with the actual physical Lakeshore 331 Temperature Controller, as the interface does not possess all the necessary tools to do this remotely.

To set a temperature ramp follow the below instructions:

1. Be sure that the Remote light of the Lakeshore 331 Temperature Controller is turned off, if not, turn it off by pressing the “Remote\Local” button.
2. Be sure that the “Ramp” light is turned off. If it is not press the “Control Setup” button followed by “Enter” until you read “Setpoint Ramp On”. Press one of the arrow buttons so this reads “Setpoint Ramp Off” and press “Enter”.

The two points above are preliminaries in order to simplify the next steps.

3. Press the “Setpoint” button and using the number pad insert the initial temperature for your ramp (this should be the temperature the sample space is in).
4. Repeat the steps in point 2 so as to turn the “Setpoint Ramp Off” into “Setpoint Ramp On”. When you do this you will read “Ramp Rate” on the Lakeshore 331 Temperature Controller display. Using the numerical pad enter your ramp rate and press “Enter”. The ramp light should now turn back on.
5. Go to the interface software and be sure that the “Setpoint Set” in the Lakeshore 331 Temperature Controller block is the same as your initial ramp setpoint, which you should be reading in the front Lakeshore 331 Temperature Controller panel.
6. Start the measurement as described in section A.5.1.

This will cause the Remote function of the Lakeshore 331 Temperature Controller to turn on, blocking you from being able to do anything on the physical module.

7. Change the “Setpoint Set” on the Lakeshore 331 Temperature Controller software block to the final temperature you wish for your ramp and press the arrow up in the “Heater Range” software box, turning the sample space heater(s) on. You should now observe that you are not only performing a measurement but also that the setpoint in the 331 is changing according to the ramp you defined (the blue ramp light on the Lakeshore 331 Temperature Controller should be intermittent at this point), while a certain heater power is being charged to the sample space heater(s) so as to maintain this same rate in your sample space.

Figure A.31 illustrates the position of the above mentioned buttons on the Lakeshore 331 Temperature Controller and its corresponding software block.

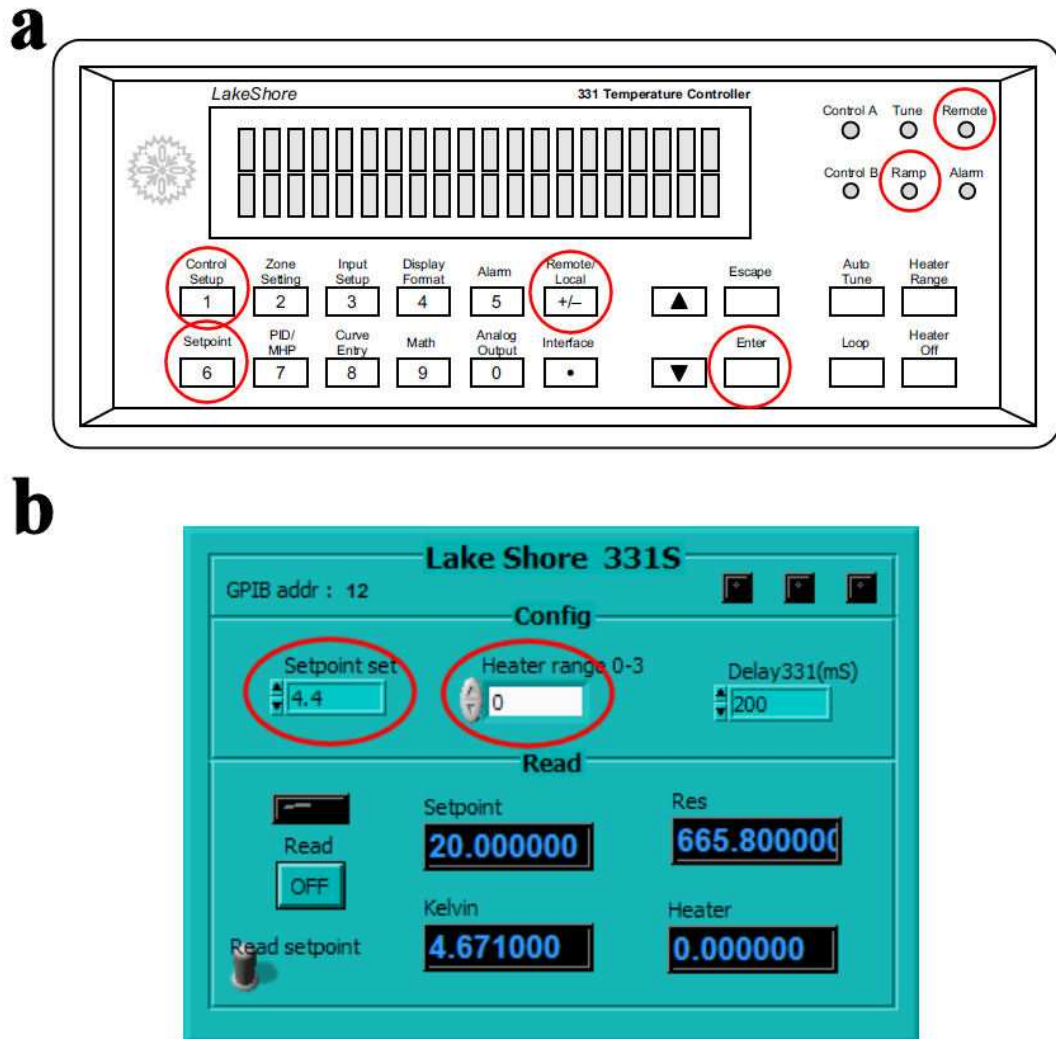


Figure A.31 a) Location of all buttons mentioned in the above instruction for the performance of a temperature ramp in the Lakeshore 331 Temperature Controller front panel; b) Location of the Setpoint set and Heater range boxes needed to perform a remote temperature ramp.

It should be noted that a single heater range will not be sufficient to reach the whole range of temperatures which are achievable by the setup and, depending on the nature of the measurement being performed, there might be the necessity to change this range in mid measurement.

There are two ways of handling this problem: the manual solution and the Zone Setting solution.

- The manual solution is straight forward: arrange your measurements in such a way as it will be possible to do the heater range change manually.

Remembering that 100% of any heater range is 10% of the next one, simply do this change when you know that the heater setting you are defining is able to pick up from where the previous one left off. For example: when you reach 10% of the Low setting, you should be able to switch to the Medium, which will then translate itself as 1% of this setting, being the same also valid for the transition between Medium and High.

Since you are doing a measurement, this change needs to be done in the software interface.

- The zone setting solution is a much more convenient way of solving this issue, even if it requires some additional work. As this feature of the Lakeshore 331 Temperature Controller is not specific to the current microcalorimetry instrument you should refer to this module's User's Manual for more details.

A.5.3 Magnetic fields

Currently the magnetic field control modules are not in any way related to all the rest of the control and measurement modules and software discussed so far. This means that there is no possible remote control of this equipment and that the calorimetry measuring and field control systems should be regarded as completely separate and independent. As such, the application of a magnetic field on the sample space, while this is inside the cryostat, needs to be done manually and externally, after which one may proceed to with a measurement as described above.

Given that the application of a magnetic field by the Model 430 Power Supply Programmer is not specific to the current microcalorimetry instrument you should refer to this module's User's Manual for more details.

Currently this instrument is not fitted for the registration of magnetic field sweeps.

A.5.4 Stopping a measurement

Depending on your measurement there may be various degrees of complexity to this step in particular.

Approaching the interface software press all the “On” buttons in exactly the opposite order as indicated in Figure A.26, with the exception of the Labview on/off button which should be substituted by the large STOP button on the interface software saving block, as indicated in Figure A.32.

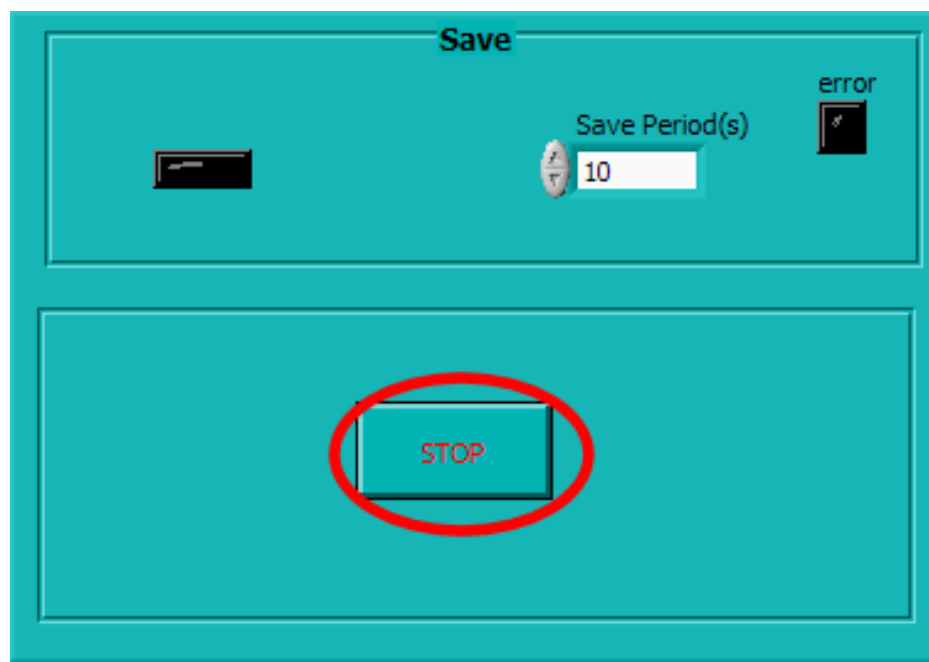


Figure A.32 Location of the STOP button on the Saving block of the interface software

The above process may take a few minutes to conclude (depending on the length of the measurement). Besides this you should also turn off the heater output of the Lakeshore 331 Temperature Controller, as shutting down the interface software will not do this automatically. Press “Remote/Local” followed by the “Heater Off” button on the Lakeshore 331 Temperature Controller to do this (depending on what method you used to perform your temperature ramp you may or may not need to do this step, particularly if you used Zone settings).

Finally remove the applied magnetic field following the instructions given in the Model 430 Power Supply Programmer User's Manual.

A.6 Data management

What follows are step by step instruction for the handling of the data file produced during a specific heat measurement in the current microcalorimetry instrument.

*
* *

0. To prevent data loss or confusion, it is advisable to move the produced “meas.tdms” and “meas.tdms_index” files to a new folder specifically meant for working on this measurement;

1. Open the “Calorimeter Read.vi”;

2. Turn this program on using the LabView “On” button and, opening the “Input file Path”, selecting the “meas.tdms” file relative to the measurement you wish to work on.

3. Press the “List” button on the bottom of the software panel. This should list all the information recorded in your measurement file in the two columns entitled “Channel X” and “Channel Y”, according to module and data type as shown in Figure A.33.

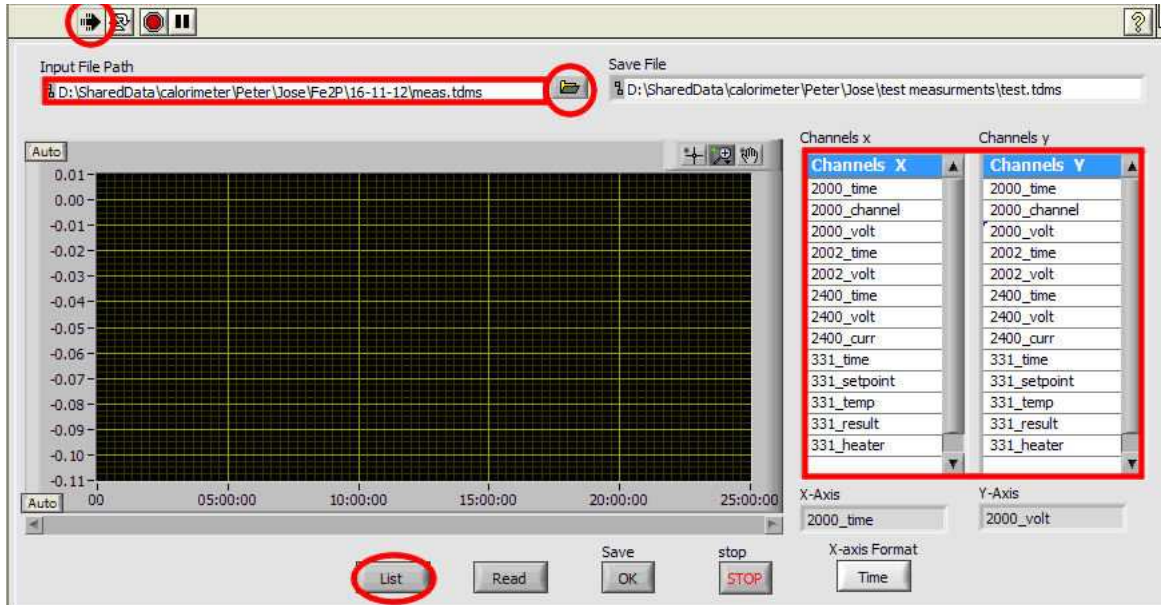


Figure A.33 Location of the functions mentioned in the above instruction for the “Calorimeter Read.vi.

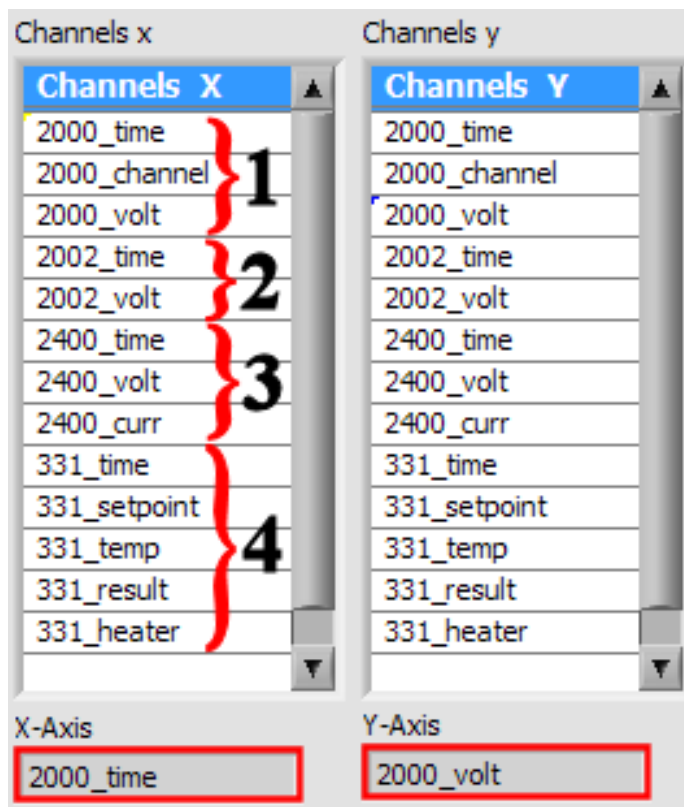


Figure A.34 Detail on the X and Y columns on the Calorimeter read.vi.

4. As mentioned above (section A.3.2), the “Channel X” and “Channel Y” columns list the data contained in the “tdms” file produced by the Calorimetry.vi during a measurement, originating from the various measurements performed by the several modules.

A detail of these columns is given in Figure A.34, with the respective legend given in Table A.9.

Table A.9 Legend for Figure A.34.

Block 1 (data recorded by the Keithley 2000)	2000_time	Time registered by the Keithley 2000 software block, this is measured from an external “clock” and is consistent in all modules.
	2000_channel	Registry of the channel in which the Keithley 2000 is measuring, a string of values of either 3 or 4.
	2000_volt	Voltage response from the Keithley 2000’s channel 3 and 4, the response from the two calorimetry chip thermopiles.
Block 2 (data recorded by the Keithley 2002)	2002_time	Time registered by the Keithley 2002 software block, this is measured from an external “clock” and is consistent in all modules.
	2002_volt	Voltage measured by the Keithley 2002, the voltage difference between channels 3 and 4.
Block 3 (data recorded by the Keithely 2400)	2400_time	Time registered by the Keithley 2400 software block, this is measured from an external “clock” and is consistent in all modules.
	2400_volt	Voltage supplied by the source meter, a string of values of either 0 or 1.
	2400_curr	Current measured by the Keithley 2400 in response on the 1 volt wave supplied to the chips.

Table A.9 (cont.) Legend for Figure A.34.

Block 4 (data recorded by the Lakeshore 331 Temperature Controller)	331_time	Time registered by the Lakeshore 331 Temperature Controller software block, this is measured from an external “clock” and is consistent in all modules.
	331_setpoint	Setpoint temperature set and registered by the Lakeshore 331 Temperature Controller.
	331_temp	Sample space temperature registered by the Lakeshore 331 Temperature Controller.
	331_result	Resistance value of the temperature depended carbon glass resistor used to monitor the temperature inside the sample space.
	331_heater	Heater output supplied and measured by the Lakeshore 331 Temperature Controller.

With resource to this program you can select and visualize any two sets of data by selecting one as the X and other as the Y axis and pressing the button “Read”, which will plot the two data sets in the large display.

5. To continue with you data handling you will need to extract the following sets of data:

1)

X Axis: 2000_time	Y Axis: 2000_volt
----------------------	----------------------

The chip voltage response measured by the Keithley 2000 vs time.

2)

X Axis: 2400_time	Y Axis: 2400_volt
----------------------	----------------------

The voltage supplied by the Keithley 2400 Source meter vs time.

3)

X Axis: 331_time	Y Axis: 331_temp
---------------------	---------------------

The sample space temperature measured by the Lakeshore 331 Temperature Controller vs time.

In order to extract these data sets from the general “meas.tdms” file, while they are on display, press the “Ok” button below “Save”. Attention should be paid to the Output file box, as the file produced should have the termination “csv”. These functions are shown in Figure A.35.

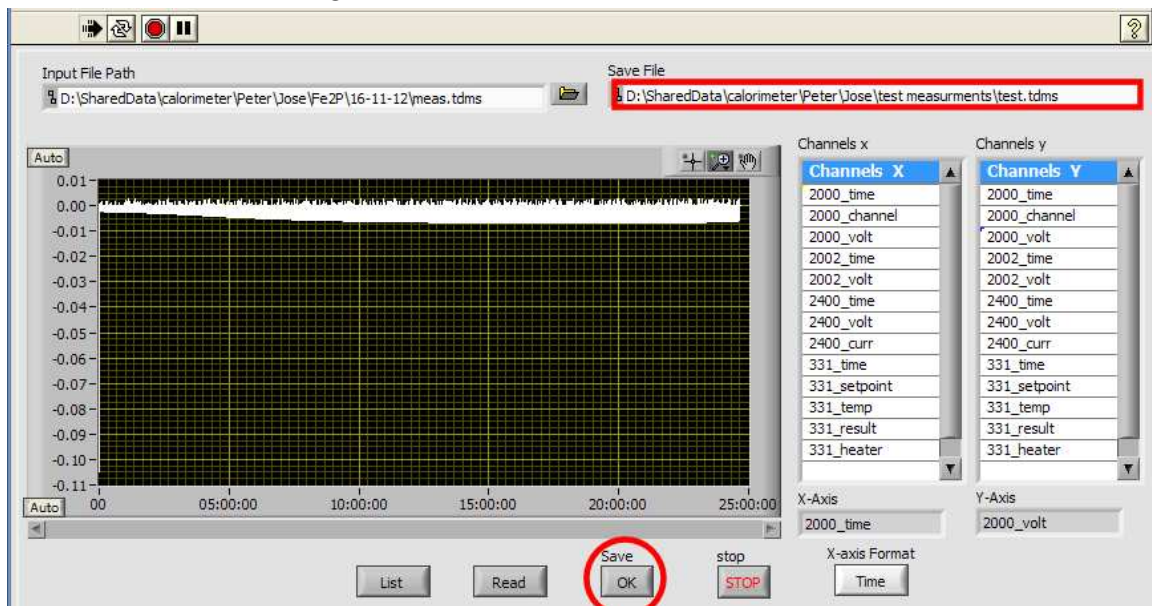


Figure A.35 Location of the functions mentioned in the above instruction for the “Calorimeter Read.vi.

The default names for these data sets, which will be used from this point on, are the following:

- 1) 2000_time vs 2000_volt: “channel.csv”
- 2) 2400_time vs 2400_volt: “switch.csv”
- 3) 331_time vs 331_temp: “temperature.csv”

6. Open the channel.csv (do not use MS Excel).

Analyze the first data points in this file and delete those that clearly do not make sense, as shown in Figure A.36.

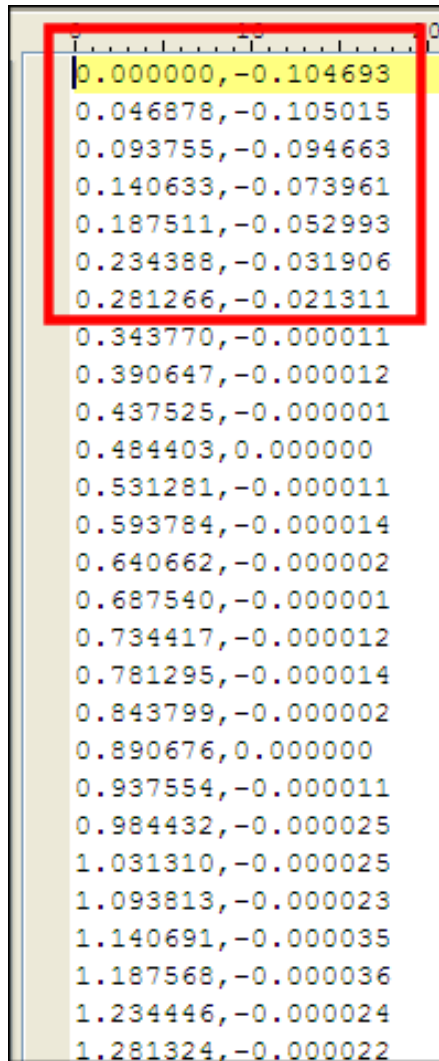


Figure A.36 Initial data points that should be deleted in the channel.csv file.

7. Open Matlab and set your work folder to the folder where you have your data files, making sure the two “grabtau.m” and “capacity_temperature_matcher.m” routines are also placed in this folder.

8. Run the “grabtau.m”.

9. This should open two image windows, Image 1 with an assortment of graphs and Image 2 with a small selection of your chip thermopile responses (not important).

Image 1 should be the one you pay more attention to, and it consists of a number of graphs, detailed in Figure A.37, with the respective legend given in Table A.10.

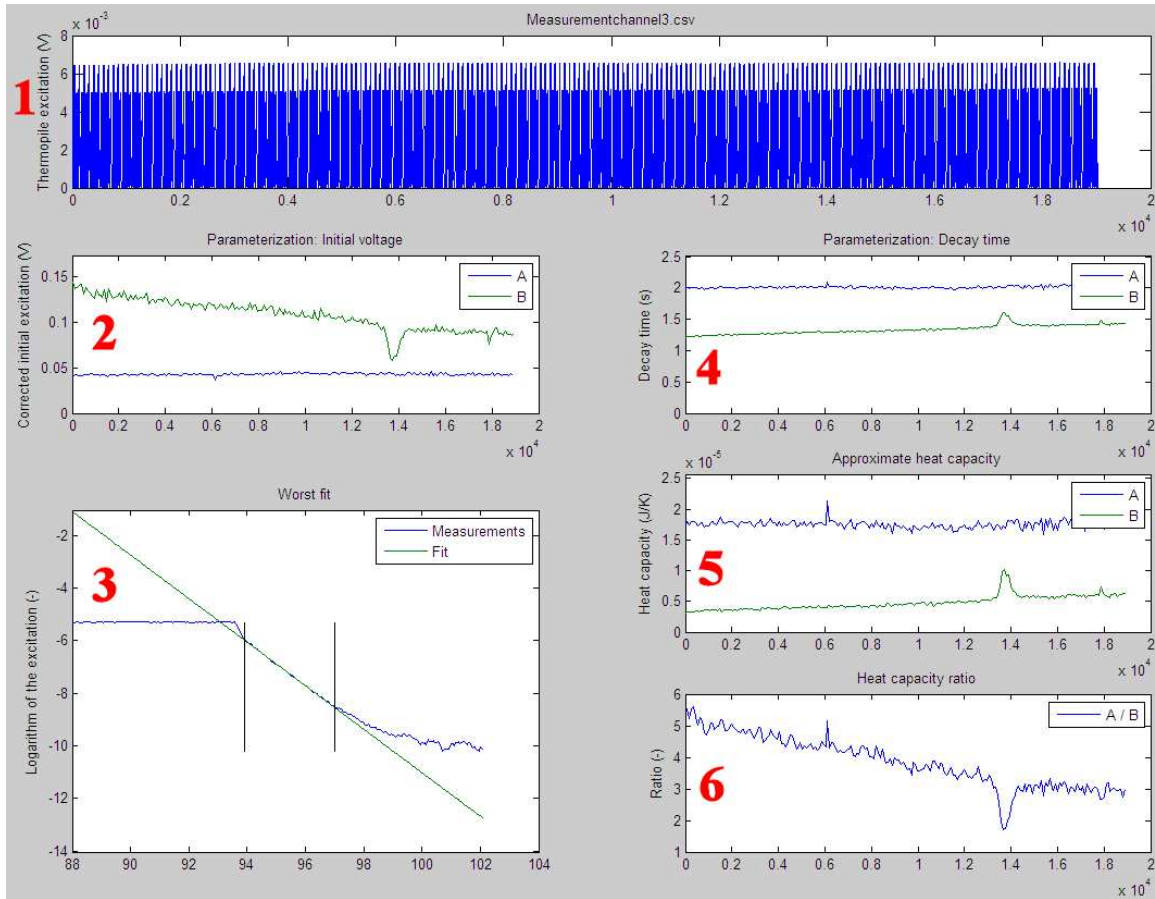


Figure A.37 Detail on Image 1 produced by the routine “grabtau.m”.

Table A.10 Legend for Figure A.37

1	Relaxation curves, the chips thermopile voltage response as measured by the Keithley 2000 vs time.
2	Results from the fits worked out from the relaxation curves for both sample and reference chip vs time.
3	Worst relaxation curve fit.
4	Relaxation time of all the relaxation curves for both sample and reference chip vs time.
5	Heat capacity for both sample and reference chip vs time.
6	Heat capacity ratio between sample and reference chip vs time.

10. Run the “capacity_temperature_matcher.m”

11. This should finally open one image window with the result from point 6 in Figure A.37 vs temperature.

12. To further proceed you will need to export or copy the two vectors used in the plot made by the “capacity_temperature_matcher.m” into a suitable data plotting and handling program (such as Origin).

13. Having the two data sets isolated in such a program, you may now proceed with simple calculus steps on the appropriate columns, taking into consideration sample and reference mass and specific heat in order to isolate the calorimetric values of your actual sample. Arriving at your final result as exemplified in Figure A.38.

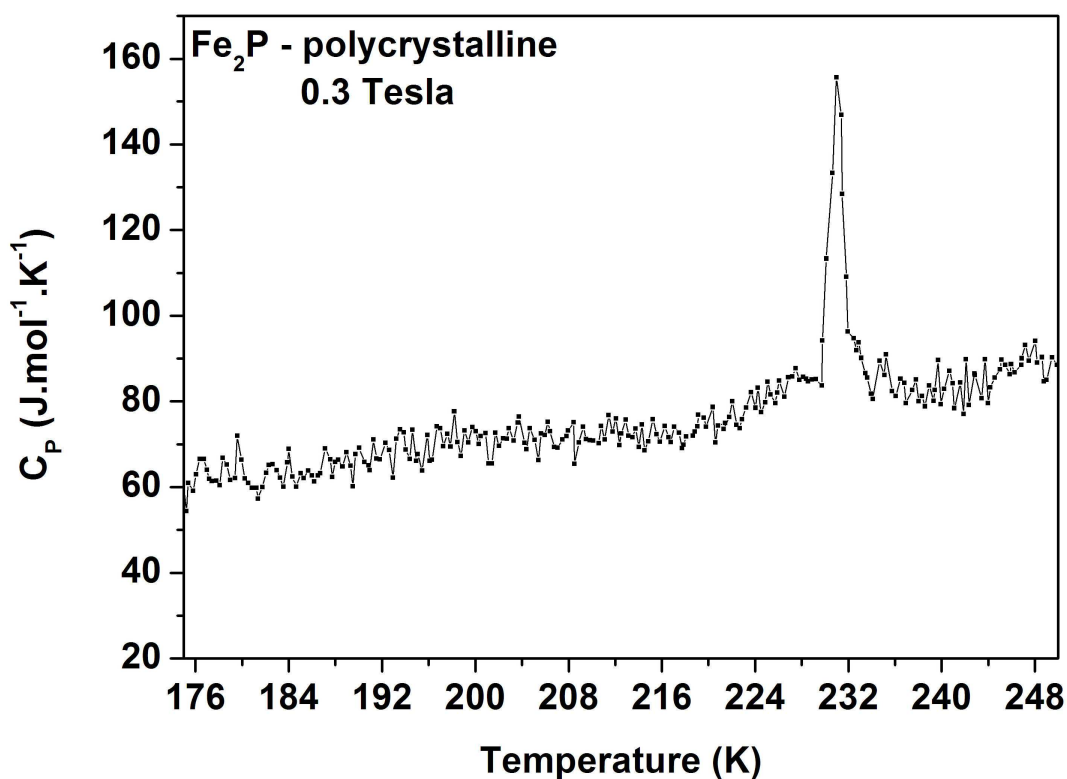


Figure A.38 Isolated specific heat measurement for polycrystalline Fe₂P under an external magnetic field of 0.3 Tesla.

Summary

Given the potentiality of Fe_2P based alloys for magnetocaloric application, this thesis covers various offshoot material systems related to this rich family of compounds, such as the $(\text{Mn,Fe})_3(\text{Si,P})$, $(\text{Mn,Co})_3(\text{Si,P})$ and the $(\text{Fe,Co})_3(\text{Si,P})$. Also covered is the assembly of a microcalorimetry setup meant for the study of certain fundamental qualities of these systems, as well as an economical optimization of the $(\text{Mn,Fe})_2(\text{P,Ge})$ system.

After a general and contextualizing introduction in Chapter 1, it proceeds in Chapter 2 with the coverage of theoretical aspects of the magnetocaloric effect, as well as the description of magnetic anisotropy phenomenon, both concepts being fundamental for the understanding of the results presented in the subsequent chapters.

Experimental procedures for sample preparation and characterization are detailed in Chapter 3, with the details of the experimental microcalorimetry setup being offered in Chapter 4. This specific heat measuring instrument, with the capacity for the application of magnetic fields up to 9 Tesla, resorts to microcalorimetry chips from the company Xensor Integration.

With this instrument is it possible to perform specific heat measurements with applied magnetic fields up to 9 Tesla in milligram samples. This offers the possibility to calculate the actual adiabatic temperature change of a material, as well as providing reliable and precise information on any phase transition that may be influenced by the application of a magnetic field.

In Chapter 5 the $(\text{Mn,Fe})_3(\text{Si,P})$ system is fully explored with X-ray diffraction, DSC and magnetization measurements. This system has been determined to be inadequate for magnetocaloric applications, but the research performed allowed for the assembly of a magnostructural map of this system.

Besides the already known cubic phase for $\text{Mn}_{3-x}\text{Fe}_x\text{Si}$ system and the tetragonal and orthorhombic phases for the $\text{Mn}_{3-x}\text{Fe}_x\text{P}$ system, a novel hexagonal phase has been observed for $\text{Mn}_{3-x}\text{Fe}_x\text{Si}_{1-y}\text{P}_y$, within the approximate range of $0.2 < x < 2.0$ and $0.2 < y < 0.9$. Magnetization measurements both confirm and further detail the already known properties of the $\text{Mn}_{3-x}\text{Fe}_x\text{Si}$ and $\text{Mn}_{3-x}\text{Fe}_x\text{P}$ systems.

Given the interesting character of an antiferro-forremagnetic transition present in Si rich samples with Fe content ranging from 1.2 to 2.3, a study on the effect of interstitial Boron was also performed on this system. This resulted in the shift of this transition from 50.5 to 57 K for the B content of 0.05, with all higher concentration resulting in the occurrence of secondary phases.

Chapter 6 is an attempt at studying the novel hexagonal phase discovered in Chapter 5 by the introduction of Co into $(\text{Mn,Fe})_3(\text{Si,P})$ system, creating in this way the $(\text{Mn,Co})_3(\text{Si,P})$ and $(\text{Fe,Co})_3(\text{Si,P})$ systems. Results on both these systems were inconclusive, as both of them do not seem to exist as a single phase. Still, the exploration of the several secondary phases found in our $(\text{Mn,Co})_3(\text{Si,P})$ samples revealed the existence of the $(\text{Mn,Co})_{1.9}(\text{Si,P})$ system which displayed an extremely relevant inverse magnetocaloric effect.

A Si-free T_C tuning attempt performed in the $(\text{Fe,Co})_3\text{P}$ system revealed the existence of the $(\text{Fe,Co})_3(\text{S,P})$ system, which displays a tunable T_C with S content as well as a novel transition of an uncertain nature at 370 K.

Chapter 7 explores the Fe rich side of the $(\text{Mn,Fe})_2(\text{P,Ge})$ magnetocaloric system.

The transition temperature of this system is extremely easy to tune with careful manipulation of Fe and Ge content as well as stoichiometrical proportions, which gives rise to the real possibility of lowering the Ge content in this family of compounds, and thus make it economically viable for practical magnetocaloric applications.

While the $(\text{Mn,Fe})_2(\text{P,Ge})$ system suffered a significant loss of transition sharpness with reducing Ge content, the same was not verified in the $(\text{Mn,Fe})_{1.95}(\text{P,Ge})$ system, and at the lowest possible Ge content (which coincides with the lowest possible monetary cost) T_C was found to be tunable below a temperature of 225 K, with the magnetic entropy changes in this area oscillating between 3 and 3.5 J/kg.K for a field of 2 Tesla.

Novel and unexpected magnetic properties observed in this system suggest an exciting potential for permanent magnet application in a certain low Mn and Ge concentrations.

Chapter 8 displays the microcalorimetry results on pure Fe_2P measured on the experimental setup described in Chapter 4. These demonstrate the gradual loss of the 1st order character of this compound's magnetic transition with increasing applied field, arriving at a critical value of 0.4 T, when the transition becomes completely 2nd order. Further temperature shift in this transition of about 1.5 K is observed at an applied field of 0.6 T.

These results were in truth quite unexpected and could only be clarified if we consider that the sample measured is a near single crystal, positioned in the equipment along its hard axis. Further measurements are required in order to clarify this issue

Finally the Addendum is a detailed step by step operator's manual for the experimental setup described in Chapter 4 and used in Chapter 8. This manual details all relevant aspects of this setup, from hardware to software, covering handling, wiring, sample preparation and measurement and data calculation.

Samenvatting

Gegeven de mogelijkheden van Fe_2P gebaseerde legeringen voor magnetocalorische toepassingen, behandelt dit proefschrift verscheidene verwante materiaal systemen gerelateerd aan deze rijke familie van verbindingen zoals $(\text{Mn,Fe})_3(\text{Si,P})$, $(\text{Mn,Co})_3(\text{Si,P})$ en de $(\text{Fe,Co})_3(\text{Si,P})$. Eveneens behandeld is de opbouw van een microcalorimetrie opstelling bedoeld zekere fundamentele eigenschappen van deze systemen te bestuderen, en eveneens een economische optimalizatie van het $(\text{Mn,Fe})_3(\text{P,Ge})$ systeem.

Na een algemene en contextualiserende introductie in hoofdstuk 1, vervolgt het in hoofdstuk 2 met de behandeling van theoretische aspecten van het magnetocalorisch effect, evenals de beschrijving van het magnetisch anisotropie fenomeen, waarbij beide concepten fundamenteel zijn voor begrip van de resultaten gepresenteerd in de volgende hoofdstukken.

Al de experimentele procedures voor monster bereiding en karakterisatie worden gedetailleerd gegeven in hoofdstuk 3, met de details van de experimentele microcalorimetrie in hoofdstuk 4. Dit soortelijke warmte meetinstrument, met de mogelijkheid van het toepassen van een magnetisch veld tot 9 Tesla, hangt af van microcalorimetrie chips van het bedrijf Xensor Integration.

Met dit instrument is het mogelijk soortelijke warmte metingen te doen in een magnetisch veld tot 9 Tesla aan milligram monsters. Dit biedt de mogelijkheid de ware adiabatische temperatuur verandering van een materiaal te berekenen, evenals betrouwbare en precieze informatie te geven over enige fase overgang die beïnvloed wordt door een magnetisch veld.

In hoofdstuk 5 het $(\text{Mn,Fe})_3(\text{Si,P})$ systeem is volledig onderzocht met Röntgen Diffractie, DSC en magnetisatie metingen. Van dit systeem is vastgesteld dat het niet geschikt is voor magnetocalorische toepassingen, maar het gedane onderzoek liet toe een magnetostructurele kaart van het systeem samen te stellen.

Naast de reeds bekende cubische fase voor $\text{Mn}_{3-x}\text{Fe}_x\text{Si}$ systeem en de tetragonale orthorhombische fasen van het $\text{Mn}_{3-x}\text{Fe}_x\text{P}$ systeem, een nieuwe hexagonale fase voor $\text{Mn}_{3-x}\text{Fe}_x\text{Si}_{1-y}\text{P}_y$ werd gevonden in het gebied met ongeveer $0.2 < x < 2.0$ en $0.2 < y < 0.9$. Magnetisatie metingen bevestigen, en detailleren, de al bekende eigenschappen van de $\text{Mn}_{3-x}\text{Fe}_x\text{Si}$ en $\text{Mn}_{3-x}\text{Fe}_x\text{P}$ systemen.

Gegeven het interessante karakter van de antiferro-ferromagnetische overgang zoals aanwezig in Si rijke monsters met een Fe gehalte van 1.2 tot 2.3, een studie van het effect van interstitieel borium werd ook gedaan op dit systeem. Dit resulteerde in het verschuiven van de overgang van 50.5 naar 57 K bij een B gehalten van 0.05, terwijl bij alle hogere concentraties secundaire fases ontstonden.

Hoofdstuk 6 is een poging de nieuw ontdekte hexagonale fase in het $(\text{Mn,Fe})_3(\text{Si,P})$ systeem te bestuderen door de introductie van Co het eerder bestudeerde systeem, en op deze manier $(\text{Mn,Co})_3(\text{Si,P})$ en $(\text{Fe,Co})_3(\text{Si,P})$ te creëren. Resultaten waren voor geen van deze systemen overtuigend, aangezien ze geen van beide als enkele fase lijken te bestaan. Nochtans, de exploratie van verscheidene secundaire fases zoals gevonden in de $(\text{Mn,Co})_3(\text{Si,P})$ monsters onthulden het bestaan van het $(\text{Mn,Co})_{1.9}(\text{Si,P})$ systeem dat een extreem relevant invers magnetocalorisch effect liet zien.

Een poging Si-vrij T_C af te stemmen in het $(\text{Fe,Co})_3\text{P}$ systeem liet het bestaan van een $(\text{Fe,Co})_3(\text{S,P})$ systeem zien, welke een afstembare T_C heeft met S gehalte, evenals een nieuwe overgang van onbekende aard bij 370 K.

Hoofdstuk 7 exploreert de Fe rijke kant van het $(\text{Mn,Fe})_2(\text{P,Ge})$ magnetocalorische systeem .

De overgangs temperatuur van dit systeem is buitengewoon eenvoudig af te stemmen door een zorgvuldige manipulatie van het Fe en Ge gehalte en de stoichiometrische verhoudingen, wat leidt tot de reële mogelijkheid de prijs van de benodigde Ge te verlagen en de verbinding economisch haalbaar te maken voor praktische magnetocalorische toepassingen.

Terwijl het $(\text{Mn,Fe})_2(\text{P,Ge})$ systeem lijdt onder een significant verlies aan scherpte van de overgang bij verlagen van het Ge gehalte, werd dat niet vastgesteld bij het $(\text{Mn,Fe})_{1.95}(\text{P,Ge})$ systeem, en bij het laagst mogelijke Ge gehalte (die samenvalt met de laagste mogelijke financiële kosten), was de T_C af te stemmen onder een temperatuur van 225 K, met de magnetische entropie verandering schommelend tussen 3 en 3.5 J/Kg.K bij een veld van 2 Tesla.

Nieuwe en onverwachte magnetische eigenschappen die in dit systeem zijn waargenomen suggereren een opwindend potentieel voor permanente magneet toepassingen in een bepaalde Mn en Ge arme concentraties.

Hoofdstuk 8 geeft de microcalorimetrie resultaten aan zuiver Fe_2P , gemeten met de experimentele installatie zoals beschreven in hoofdstuk 4. Deze laten het geleidelijke verlies van het 1e orde karakter van de overgang van deze verbinding zien bij een toenemend toegepast magnetisch veld, welke bij een kritische waarde van 0.4T

arriveert als de overgang geheel 2e orde is. Een verdere temperatuur verschuiving van deze overgang van ongeveer 1.5 K wordt waargenomen bij een veld van 0.6 T.

Deze resultaten waren eigenlijk nogal onverwacht en worden alleen duidelijk als we overwegen dat het gemeten monster vrijwel een enkel kristal is, gepositioneerd in de opstelling langs de harde as. Meer metingen zijn nodig op deze zaak op te helderen.

Tenslotte is de Addendum een gedetailleerde stap voor stap bedienings handleiding voor de experimentele installatie zoals beschreven in hoofdstuk 4 en gebruikt in hoofdstuk 8. Deze handleiding beschrijft in details alle relevante aspecten van de opstelling, van hardware tot software, en dekt het hanteren, de bedrading, monster behandeling en meting en gegevens verwerking.

Acknowledgements

As it is somewhat of a cliché, I can never expect to thank all the people who have helped me along these four years of PhD work. Furthermore, all those who are relevant and close to my heart know who they are, and they shouldn't have the necessity to have their names publicized on a book practically no one will ever read. None the less, I believe traditions exist for a reason and I'll make an effort to follow yet one more.

As is polite, I should naturally start with my supervisor, Prof. Ekkes Brück. Whether these were expressed or not, we often disagreed on many topics, but you always showed yourself patient and graceful with my shortcomings... more than I probably would if I was ever in your position. We once again fall into a cliché here, I will always be thankful for having been given the opportunity to study in this strange and faraway land I have come to love. And this is not because of the academic or scientific work I developed here, but rather because coming to the Netherlands enabled me to achieve more of myself than I would care to divulge.

Niels should also be mentioned at this point. Although you were technically my co-supervisor (this was actually something I only discovered during my second year) I think we very rarely had any work related conversations. Even still, you are a most pleasant and intelligent man, and all our intercalations, be them work related or not, were always exceedingly interesting and entertaining.

Of course that now, following the proper etiquette, I should mention my colleagues of the Delft magnetocalorics research group. From the very beginning you were all welcoming and certainly aided with my learning curve. Ou, I think we shared too many hotel rooms; Trung, your good mood and hard work were always an inspiration; Anton, know that you are my favorite Dutchman; François, it felt good to finally not be the only European student around here (Luana doesn't count); Luana, it is hard to express how much of a luxury it was to be able to speak my own language and know that there would be someone who would (almost) understand it; Yibole, if niceness was a disease you would be a terminal case; Miao, you're a good man, and I can tell that deep down you're a fighter; Maurits, an advice no Japanese master will ever give you: the perfect technique is not the strongest; Van Thang, I'm sorry about the monster you're inheriting from me; Giacomo, you were only here for a short time, but it was a most pleasant short time; Jurgen Buschow, your massively experienced insights are priceless; Bert, you were always available to tell some interesting vacation

story... whether we wanted to hear it or not; Theo, you came here as the archetypical Dutch student, and I am happy I had the opportunity to watch you grow out of that socially imposed shell of mental mediocrity and into something of higher aspirations. I wish you all the luck in Canada.

Of course I cannot in any way forget my three students: Xinmin, Peter and Mischa. I have discussed student supervision with many of my PhD and Post-doc colleagues and considering the stories they told me it seems like I completely lucked out with you three. Your work was valuable beyond words, and I am glad and proud to have known you and to have been able to put your names on three papers. I wish you all rich and fruitful lives. And even if what I write next may be considered inelegant, I still feel like I have to write it: Peter, I honestly don't think this thesis would exist if it wasn't for the massive load of work you took on. Even if I was your supervisor I am humble enough to say that I owe you.

Logically now, I must pass a review of my PhD and Pos-doc colleagues, both present and absent: Swapna, you are a trustworthy and honest person if there ever was one (sometimes even too much...), with you we always know where we stand, and don't let anyone ever tell you this isn't a virtue; Anca, you're too sweet, and I'm happy I got to see some of that sweetness come into the world as a whole new person; Markus, you're my friend, that has been settled, but do know that you were very close to being punched in the face a number of times; Anna, relax, leaving your desk to have lunch with your friends isn't a sin; Shasha, you are the only girl I know who can successfully wear a leopard pattern shirt, and if for nothing else, since you came into the office at least somebody would always greet me with an enthusiastic "Good Morning" everyday (you also liked my Bacalhau à Brás, so that's another virtue right there); Inês, with you around there was a clear upgrade in conversation, I could finally curse and swear and somebody would understand (Luana doesn't count); Fengjiao, you're a ray of sunshine: Romain, I got the feeling you went through some rough times during your PhD, but I'm happy to see that you came out on top: Gijs, it was good to know somebody else who remembers the Muppets (and the movie Krull). With all of you lunch time was always a pleasure.

Of course, one cannot forget the many professionals and technicians of FAME who were always willing to give a hand (when time permitted it): Fred, I probably bothered you more than anybody else and yet, unlike Anton, who tried to physically run away, you were always patient, courteous and well-disposed. Much like Peter I owe you a great deal, you are a professional of extraordinary skill and I hold you in the highest possible regard; Jouke, you were always surprisingly available for any and all

informatics problems anyone had, and even though I don't think this was ever in your job description, you always went out of your way to help in anyway you could; Michel, I never got this... why do you sit on a giant inflatable ball? Kees, it was nice to know that somebody else thought the ICDD were a bunch of lazy bums; Paul, you are a gentleman; our hard working secretaries Nicole and Ilse, a big thank you.

Besides all of these there was, of course, a constant stream of Bachelor and Master student passing by this place that helped ease the heavy work days. Naming them all would be an ungrateful task but I would still like to take the time to remember a hand full of which I was particularly fond of: Chris (van Soest), whatever it is that makes the average Dutch youngster into a jackass, you managed to make that into something cool; Cassandra, *flos sanctorum*; Hanan, you are a bright and sweet person and don't think you don't have what it takes to fight for that happy ending.

Stepping outside of Delft, I would like to mention Peter Foreshaw and Punita from Amsterdam University. I know our meetings were brief and recent, but our conversations gave me the strength to keep on pushing against the current. I honestly hope we meet again in the proper and adequate circumstances.

Leaving the academies and going into the streets, I would also like to thank Don Azito and the whole Amsterdam 'la Botanica' crowd, both living and dead. It would be inelegant of me to start naming you, particularly in this context, but know that with your friendship, openness and light you helped me more than you can ever imagine. I managed to find my way out of some dark places thanks to you. LUZ!

Also, the tip of my hat and a gentleman's "thank you" to the Devil for having always stayed on that side of the mirror (except that one time). And finally to my Saints and Eguns, even with all my sins, for some reason I could never really understand, someone in Heaven has always loved me.

Chega agora aquela parte em que se escreve algo na língua original do estudante em questão. E por favor note-se que não o faço por muito, apenas porque me parece que tal fica sempre elegante e misterioso aos olhos de quem a não sabe ler... quer dizer, eu vi umas teses escritas por vietnamitas e aquilo impressiona muito, só é pena que o português não tenha mais assentos e sinais gramaticais.

Ainda assim, já que aqui estou, mais vale agradecer àquelas pessoas que não saberão ler nada do que lá vai em cima, o que não é grande perda, diga-se de passagem.

Ora, acho que o óbvio será começar pelos meus santos pais: eu sei, a todos os momentos da minha vida, que o vosso amor e apoio são incondicionais e se alguma vez pareci emocionalmente distante foi precisamente por ter esse facto como certo.

João... na verdade não me ajudaste neste trabalho mas ajudaste de maneiras muito significantes em muitos outros que decidi arcar contra os meus próprios concelhos. E isto ao ponto de eu dizer “pá, já chega!”, o que no fundo apenas quer dizer que foste sempre prestável de mais.

No fundo, fora isto, não mantive amizades com estudantes Portugueses por estas bandas. Em tempos tentei, mas rápido me apercebi que a qualidade de gente da minha terra que por esta terra anda tinha orientações diferentes das minhas. Da vossa boca apenas ouvi referencias a pulhice, sua canalhada pueril da puta que vos pariu.

E assim sendo, apenas me posso referir àqueles outros Portugueses que não caiem nesta categoria, ou seja, aqueles que não estão neste país ou aqueles que estão já há anos demais para o seu próprio bem (mas não todos, que um dia vi um velho no aeroporto que merecia uma chapada na boca).

Fábio pá, ainda que do outro lado do Mar do Norte, o contacto que mantivemos ao longo destes anos foi para mim uma referência essencial. Nestas outras lides não teria chegado onde cheguei sem a tua ajuda... e o cornetim ainda não se ouviu na praça.

O guitarrista Nuno: aprender guitarra consigo foi por vezes um oásis no meio do deserto. Ainda que saiba que não fui o aluno exemplar, consegui realizar um sonho de longa data quando finalmente dos meus dedos tirei os “Verdes Anos”. Não sei o que é que no meu futuro haverá de guitarra, mas sei que me vou sempre lembrar das nossas aulas (disso e de me ter que levantar às 6 da manhã para a apanhar a porra do comboio para Haarlem e ainda ter que pedalar meia hora até sua casa)

Por fim, julgo não ter que me repetir para o Diabo, visto que, com excepção de Euskara, ele fala todas as línguas (a menos que lhe chamemos Akerbeltz).

Bom... e agora que aqui estou, tomo a oportunidade para me dar a uns ares de rebeldia, pois apercebo-me que no fundo poderei escrever quase tudo o que bem me apeteça neste ponto que, a menos que alguém faça uma tradução (tu sabes quem és) quase ninguém vai perceber (pelo menos não as pessoas que poderão fazer algo sobre isso). Posso ter posto a alma no penhor, mas até á data ela ainda é minha, e, caso isso ainda não tenha sido feito evidente, ela é a alma de um grandessíssimo punk.

Assim sendo, passo de seguida a transcrever as proposições desta tese que foram recusadas pelas altas instâncias e que eram infinitamente melhores e mais inteligentes que as oficias:

- Entre outras coisas, o método científico está desenhado para remover o indivíduo circunstancial do processo de investigação científica, no entanto, é notável ver a quantidades de egos que florescem neste meio.
- O paradigma (pós)moderno do investigador profissional procura produzir um indivíduo ignorante, amoral e desumanizado. Tal fera é um perigo iminente para toda a humanidade e deverá ser abatida à primeira vista.
- A relevância da política inter-institucional ameaça eclipsar real mérito científico.
- Ciência Russa não é ciência normal.
- Dado o tempo que os seres humanos existem neste mundo como tal, é estranho que a morte seja ainda encarada como uma surpresa e uma tragédia.
- Bergson pode ser considerado brilhantes, mas o seu “Matière et mémoire” é uma obra ignorante e mal informada, uma grosseira má interpretação e subestimação do que é a consciência, e apenas poderia ter sido escrita por um Francês.
- O Diabo é o reflexo de um homem à noite.
- Em práticas Goéticas, os dois paradigmas opostos de mera projeção mental subjetiva, popularizada pela introdução de Crowley ao “The Book of the Goetia of Solomon the King”, e a existência objetiva de uma entidade exterior ao carista, largamente proclamada pelo corrente Revivalismo Mágico, são ambos conceitos egocêntricos. A maioria das mentes não tem capacidade para projetar uma alucinação coerente que possa ser interpretada como um demônio e a maioria das pessoas não são assim tão notáveis que um demônio realmente se queira dar ao trabalho de falar com elas.

List of Publication

Papers

Published before the current PhD:

1) **J. V. Leitão**, D. L. Rocco, J. S. Amaral, M. S. Reis, V. S. Amaral, R. P. Fernandes, N. V. Martins and P. B. Tavares, “Influence of the Magnetic Anisotropy on the Magnetic Entropy Change of Ni₂Mn(Ga,Bi) Memory Shape Alloy”, *IEEE Transactions on Magnetics* 44 (2008) 3036.

2) D. L. Rocco, J. S. Amaral, **J. V. Leitão**, V. S. Amaral, M. S. Reis, R. P. Fernandes, A. M. Pereira, J. P. Araújo, Nuno V. Martins, P. B. Tavares and A. A. Coelho, “Percolation processes and spin-reorientation of PrNi_{5-x}Co_x”, *Physical Review B* 79 (2008) 014428.

3) E. J. R. Plaza, V. S. R. de Sousa, P. J. von Ranke, A. M. Gomes, D. L. Rocco, **J. V. Leitão** and M. S. Reis, “A comparative study of the magnetocaloric effect in RNi₂ (R = Nd, Gd, Tb) intermetallic compounds”, *Journal of Applied Physics* 105 (2009) 013903.

4) D. L. Rocco, J. S. Amaral, **J. V. Leitão**, V. S. Amaral, M. S. Reis, Soma Das, R. P. Fernandes, J. P. Araújo, A. M. Pereira, P. B. Tavares, Nuno V. Martins and A. A. Coelho, “High refrigerant capacity of PrNi_{5-x}Co_x magnetic compounds exploiting its spin reorientation and magnetic transition over a wide temperature zone”, *Journal of Physics D: Applied Physics* 42 (2009) 055002.

Published during the current PhD

1) **J. V. Leitão**, You Xinmin, L. Caron and E. Brück, “Magnetostructural study of the (Mn,Fe)₃(P,Si) system”, *Journal of Alloys and Compounds* 520 (2012) 52.

2) **J. V. Leitão**, P. van Dommelen, F. Naastepad, E. Brück, “Description of a Differential Setup For Relaxation Microcalorimetry”, *5th International Conference on Magnetic Refrigeration at Room Temperature Proceedings* (2012) 263.

3) **J. V. Leitão**, M. van der Haar, A. Lefering, E. Brück, “Magnetic and Magnetocaloric Exploration of Fe rich (Mn,Fe)₂(P,Ge)”, *Journal of Magnetism and Magnetic Materials* 334 (2013) 49.

4) **J. V. Leitão**, P. van Dommelen, F. Naastepad, E. Brück, “Description of a Differential Setup For Relaxation Microcalorimetry”, *International Journal of Refrigeration*, 2013 (Special issue based on selected articles presented on the Thermag V)

(Accepted and in press)

Others

X-ray diffraction patterns accepted for the International Center for Diffraction Data (ICDD), 15th of November 2012

1) Fe₃P

2) Fe₃Si

3) Mn₃P

4) Mn₃Si_{0,2}P_{0,8}

5) Mn_{0,5}Fe_{2,5}Si

6) Mn_{0,6}Fe_{2,4}Si

7) Mn_{0,7}Fe_{2,3}Si

8) Mn_{0,8}Fe_{2,2}Si

9) Mn_{0,9}Fe_{2,1}Si

10) Mn_{2,5}Fe_{0,5}P

11) MnFe₂Si

Non physics related publications

Published before the current PhD:

1) **José Leitão**, “Um Argumento pela ideia de Pátria”, *Nova Águia* 1 (2008) 37.

2) **José Leitão**, “Vadios e Poetas – Uma consideração sobre a mística Agostiniana”, *Nova Águia* 3 (2009) 35.

Published during the current PhD

- 1) **José Leitão**, “Ipsissimus Pessoa”, *Nova Águia* 7 (2011) 99.
- 2) **José Leitão**, “On Pessoa – A Heterodox Exposition”, *Mandragora - Further Explorations in Esoteric Poesis*, Scarlet Imprint, Croydon, UK 2012.
- 3) **José Leitão**, “Clavis Cyprianus”, *Nova Águia* 10 (2012) 92.
- 4) **José Leitão**, “The Grimoire of Saint Cyprian or The Prodigies of the Devil”, *Conjure Codex*, Hadean Press, Vol.1 n.2 (2013) 78.
- 5) **José Leitão**, “Deambulação”, *Nova Águia* 11 (2013) 47.
- 6) **José Leitão**, “The folk and oral roots of the Portuguese «Livro de São Cipriano»”, *Sharing Cultures 2013 Proceedings* (2013) 265.
- 7) **José Leitão**, “The folk and oral roots of the Portuguese «Livro de São Cipriano»”, *International Journal of Heritage and Sustainable Development* (invited publication based on the proceedings of the Sharing Cultures 2013 conference)
(Submitted)
- 8) **José Leitão** (translation and comments), *The Book of Saint Cyprian - The Sorcerer’s Treasure*, Hadean Press.
(Accepted for publication in Spring 2014 and currently in editing).
- 9) **José Leitão**, “Nauts and Nymphs”, *Clavis – Journal of Occult Arts, Letters and Experience*
(submitted)
- 10) **José Leitão**, “Unapologetically Catholic – Use and Practicality of the Cult of the Saints”
(Under preparation)

11) **José Leitão** (translation and comments), *Bibliotheca Valenciana – The Collected Works of Jeronimo Cortez*
(Under preparation)

Corriculum Vitæ

José Carlos Vieira Leitão was born in 1984 in Leiria, Portugal. In 2002 he entered into the University of Aveiro where he took his bachelor degree in theoretical physics, finishing in 2007 under the supervision of Prof. Vitor Amaral and Dr. Mario Reis. In that same year he followed a Master degree in this same university, also in theoretical physics, finishing in 2008, having his final project on the magnetocaloric effect once again supervised by Prof. Vitor Amaral and Dr. Mario Reis.

In 2009 he was accepted as a PhD student in the Delft University of Technology under the supervision of Prof. Ekkes Brück., with his assigned project being a mix of magnetocaloric material exploration and the assembly of an experimental setup, and whose result are presented in the current thesis.

Parallel to his daytime academic career, he regularly publishes essays and papers in literature and philosophical periodical journal, having also broken into the worlds of occult publishing. His particular interest in Portuguese and Ibero-Afro-American forms of spirituality and transcendence has also led him to further lecture and publish in academic anthropological seminars.

Epilogue

Inquietação

*A contas com o bem que tu me fazes
A contas com o mal por que passei
Com tantas guerras que travei
Já não sei fazer as pazes*

*São flores aos milhões entre ruínas
Meu peito feito campo de batalha
Cada alvorada que me ensinas
Oiro em pó que o vento espalha*

*Cá dentro inquietação, inquietação
É só inquietação, inquietação
Porquê, não sei
Porquê, não sei
Porquê, não sei ainda*

*Há sempre qualquer coisa que está pra
acontecer
Qualquer coisa que eu devia perceber
Porquê, não sei
Porquê, não sei
Porquê, não sei ainda*

*Ensinas-me fazer tantas perguntas
Na volta das respostas que eu trazia
Quantas promessas eu faria
Se as cumprisse todas juntas*

*Não largues esta mão no torvelinho
Pois falta sempre pouco para chegar
Eu não meti o barco ao mar
Pra ficar pelo caminho*

*Cá dentro inquietação, inquietação
É só inquietação, inquietação*

*Porquê, não sei
Porquê, não sei
Porquê, não sei ainda*

*Há sempre qualquer coisa que está pra
acontecer
Qualquer coisa que eu devia perceber
Porquê, não sei
Porquê, não sei
Porquê, não sei ainda*

*Cá dentro inquietação, inquietação
É só inquietação, inquietação
Porquê, não sei
Mas sei
É que não sei ainda*

*Há sempre qualquer coisa que eu tenho
que fazer
Qualquer coisa que eu devia resolver
Porquê, não sei
Mas sei
Que essa coisa é que é linda*

José Mário Branco